TESIS DE LA UNIVERSIDAD
DE ZARAGOZA
2024
461

Chiara Celotto

In silico characterization of atrial electrical activity modulation by the autonomic nervous system for atrial fibrillation management

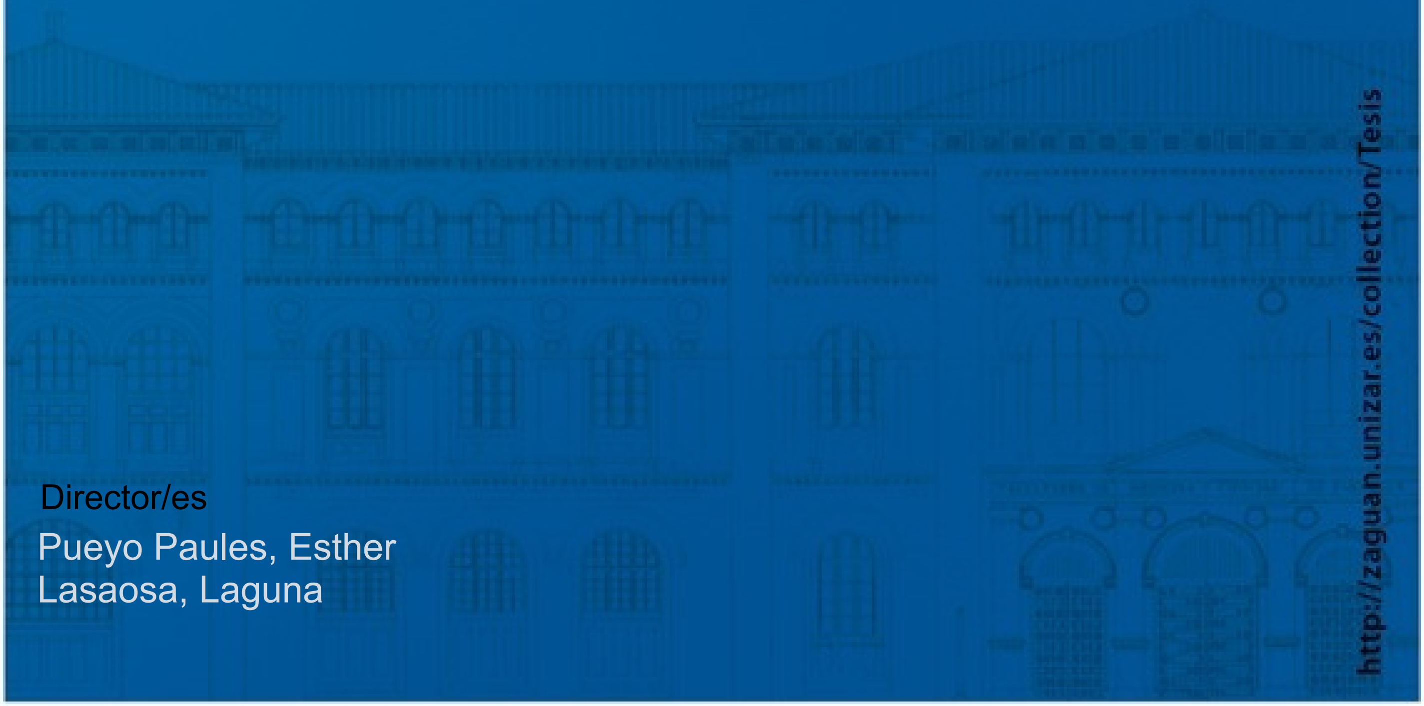

Director/es
Pueyo Paules, Esther
Lasaosa, Laguna

ISSN 2254-7606

Prensas de la Universidad
Universidad Zaragoza

Universidad de Zaragoza
Servicio de Publicaciones

ISSN 2254-7606

Tesis Doctoral

IN SILICO CHARACTERIZATION OF ATRIAL ELECTRICAL ACTIVITY MODULATION BY THE AUTONOMIC NERVOUS SYSTEM FOR ATRIAL FIBRILLATION MANAGEMENT

Autor

Chiara Celotto

Director/es

Pueyo Paules, Esther
Lasaosa, Laguna

UNIVERSIDAD DE ZARAGOZA
Escuela de Doctorado

Programa de Doctorado en Ingeniería Biomédica

2023

Instituto Universitario de Investigación
en Ingeniería de Aragón
Universidad Zaragoza

Ph.D. Thesis

In silico characterization of atrial electrical activity modulation by the autonomic nervous system for atrial fibrillation management

---

Celotto Chiara

SUPERVISORS:
Esther Pueyo Paules
Pablo Laguna Lasaosa

Zaragoza, July 2023

Ph.D. Thesis

In silico characterization of atrial electrical activity modulation by the autonomic nervous system for atrial fibrillation management

Celotto Chiara

I3A Institute, University of Zaragoza, IIS Aragón, Zaragoza, Spain

SUPERVISORS:

Esther Pueyo Paules
Associate Professor
I3A Institute, University of Zaragoza, IIS Aragón, Zaragoza, Spain

Pablo Laguna Lasaosa
Full Professor
I3A Institute, University of Zaragoza, IIS Aragón, Zaragoza, Spain

Zaragoza, July 2023

In silico characterization of atrial electrical activity modulation by the autonomic nervous system for atrial fibrillation management

Chiara Celotto 2023

This thesis was supported by the Government of Aragon through the research projects T39_23R (Reference Group BSICoS) and LMP94_21, and by Ministerio de Ciencia e Innovación through projects PID2019-105674RB-I00 and TED2021-130459B-I00, a fellowship from the European Union's Horizon 2020 research and innovation programme under the Marie Skłodowska-Curie grant agreement No.766082: "MultidisciplinarY training network for ATrial fibRillation monItoring, treAtment and progression" (MY-ATRIA). Some parts of this thesis have been developed during secondments at the Department of Physiology of the University of Lisbon (Lisbon, Portugal), the Department of Biomedical Engineering at Lund University (Lund, Sweden), and the Department of Chemistry at the Polytechnic University of Milan (Milan, Italy).

Summary and Conclusions

Cardiovascular diseases are the leading cause of mortality and morbidity in industrialized societies. Among these diseases, atrial fibrillation (AF) stands out as the most common arrhythmia encountered in clinical practice. It is estimated that by 2050, AF will affect 6-12 million people in the USA and by 2060, 17.9 million people in Europe. AF significantly increases the risk for heart failure, stroke and overall mortality and it negatively impacts the quality of life and healthcare costs. The development of arrhythmias, including AF, involves three key elements: an arrhythmogenic substrate, a trigger and modulating factors. The Autonomic nervous system (ANS) has been proved to be a crucial modulator in this process, with both its parasympathetic and sympathetic ANS branches playing a pivotal role in initiating and sustaining AF.

Given the complex relationship between AF and the ANS, the primary objective of this thesis is to improve the understanding of the mechanisms by which the ANS promotes and modulates AF and pave the way for the development of new treatment strategies. To achieve this goal, we developed comprehensive *in silico* computational models incorporating theoretical descriptions of electrophysiology, cholinergic and β-adrenergic stimulation and the effects of electrical remodeling resulting from the arrhythmia. These models encompass scales from the cellular to the whole atria level, with the multi-dimensional models also considering structural remodeling and providing a geometrical representation of ANS innervation. By combining theoretical computational research with the analysis of clinical and experimental atrial signals, the research presented in this thesis establishes a foundation for future investigations aimed at guiding the search for more effective anti-arrhythmic therapies targeting the ANS.

The first part of this thesis focuses on characterizing the autonomic influence on the modulation of f-waves, i.e. the AF electrical activity reflected on the surface electrocardiogram (ECG). In particular, the f-wave frequency is analyzed as a means to non-invasively assess ANS activity during AF. This research could be the basis for future developments of personalized treatment approaches based on specific ANS dysregulation patterns, with such approaches having the potential to be beneficial in managing AF.

In Chapter 3, we aimed to assess the impact of vagal stimulation on the respiratory modulation of fibrillatory frequency in persistent AF (psAF) patients. The objective was to explore the possibility of using this relationship as a surrogate measure to quantify the vagal input in such patients. To achieve this, we combined the analysis of data obtained from a clinical study involving ECG recordings of psAF patients during controlled respiration with computational modeling and simulation. In these simulations, we mimicked the parasympathetic modulation induced by respiration by introducing cyclic variations in the concentration of acetylcholine (ACh), the parasympathetic neurotransmitter. Both 2D tissue models and 3D biatrial models considering different innervation patterns were employed in this investigation. We found that temporal variations in the fibrillatory frequency followed the simulated temporal ACh(t) pattern in all cases. The temporal mean of the fibrillatory frequency ($\overline{\mathrm{F}}_{\mathrm{f}}$) depended on the fibrillatory pattern, on the percentage of ACh release nodes and on the mean ACh concentration over time. The magnitude of the respiratory modulation of the fibrillatory frequency ($\Delta \mathrm{F}_{\mathrm{f}}$) depended on the percentage of ACh release nodes and on the peak-to-peak ACh range $\Delta\mathrm{ACh}$. The spatial pattern of ACh release did not have an impact on $\overline{\mathrm{F}}_{\mathrm{f}}$ and only a mild impact on $\Delta \mathrm{F}_{\mathrm{f}}$ for the highest tested spatial ACh percentage.

In Chapter 4 of this thesis, we delved into the correlation between autonomic influences and alterations in the modulation of the fibrillatory frequency during head-up tilt (HUT) and head-down tilt (HDT) tests. These tests are commonly used in medical settings to assess the autonomic function, providing valuable information about the ability of the ANS to regulate blood pressure and heart rate in response to postural changes. Similarly, we sought to assess if the same test could be adopted in AF to evaluate the autonomic modulation of atrial electrical activity. We used computational modeling and simulation to test different combinations of sympathetic and parasympathetic stimulation. The simulation outcomes were then compared to the analysis of clinical ECGs obtained from psAF patients who underwent a tilt test protocol. Collectively, the findings of this study indicate that the increase in the fibrillatory rate following the HUT maneuver and the decrease in the fibrillatory rate following the HDT maneuver can be primarily attributed to enhanced and diminished sympathetic activity, respectively. Furthermore, it appears that parasympathetic stimulation exerts a modulatory effect on the sympathetic effects rather than being the primary driving force behind the observed trends in atrial function.

Managing AF is challenging due to its complex and uncertain underlying mechanisms. Rhythm control strategies focus on restoring and maintaining sinus rhythm. This can be achieved through a combination of treatment approaches, including electrical or pharmacological cardioversion, antiarrhythmic drug therapy (ADT) and catheter ablation. Chapter 5 and Chapter 6 of this thesis focus on AF therapies, particularly addressing signal processing of atrial electrograms (EGMs) to improve cardioneuroablation procedures and theoretically investigating the efficacy of new pharmacological therapies targeting ion channels and neural components.

In Chapter 5, we developed a method to locate atrial parasympathetic innervation sites using EGM measurements. The ablation of the intrinsic cardiac autonomic ganglia, called ganglionated plexi (GPs), individually or in combination with pulmonary vein isolation, has been associated with a decreased risk of AF recurrence. However, accurate location of GPs is required for ablation to be effective. We developed computational models to simulate non-AF, paroxysmal AF (PxAF) and psAF tissues. In GPs, predominance of parasympathetic activity has been shown, so parasympathetic effects were incorporated by increasing the concentration of ACh in randomly distributed islands within the tissue. Different sizes of ACh islands and fibrosis geometries were considered, including uniform diffuse and non-uniform diffuse fibrosis. Unipolar EGMs in a 16x16 electrode mesh were generated from the simulation. The study revealed that the amplitude of the atrial EGM repolarization wave reflects the presence or absence of ACh release sites, with larger positive amplitudes indicating that the electrode is placed over an ACh region. Statistical analysis was employed to determine optimal thresholds for identification of ACh sites. The method successfully identified ACh sites in all types of tissues, with higher accuracy in the absence of fibrosis or with uniform diffuse fibrosis. The proposed algorithm proves robust against noise and electrode-to-tissue distance variations.

Chapter 6 focuses on the analysis of antiarrhythmic pharmacological therapies in combination with β-adrenergic signaling to treat cholinergic AF. The parasympathetic neurotransmitter ACh causes a reduction in action potential (AP) duration (APD) and an increase

in resting membrane potential (RMP), both of which contribute to enhance the risk for reentry. In this chapter, we used computational modeling and simulation to examine the impact of SK channel block (SKb) and β-adrenergic stimulation by Isoproterenol (Iso) on countering the negative effects of cholinergic activity in human atrial cell and 2D tissue models. The steady-state effects of Iso and/or SKb on AP shape, APD at 90% repolarization (APD_{90}) and RMP were evaluated. The ability to terminate stable rotational activity in cholinergically-stimulated 2D tissue models of AF was also investigated. A range of SKb and Iso application kinetics, which reflect varying drug binding rates, were taken into consideration. The results showed that SKb alone prolongs APD_{90} and is able to stop sustained rotors in the presence of ACh concentrations up to 0.01 μM. Iso terminates rotors under all tested ACh concentrations, but results in highly-variable steady-state outcomes depending on the baseline AP morphology. Importantly, the combination of SKb and Iso results in greater APD_{90} prolongation and shows promising anti-arrhythmic potential by stopping stable rotors and preventing re-inducibility.

In conclusion, this thesis develops cardiac computational modeling and simulation techniques to provide insights into the mechanisms of AF under the influence of the ANS and presents innovative methodologies for its treatment. Specifically, this research sheds light on the modulation of fibrillatory frequency by the ANS, enhancing our understanding of the potential underlying mechanisms behind macroscopic observations. Furthermore, it paves the way for the possibility of non-invasively assessing autonomic activity from EGM signals. In addition, from a therapeutic perspective, this thesis develops a method to determine the location and dimensions of GPs from an electrogram grid to aid in cardioneuroablation procedures. Finally, it investigates potential pharmacological therapies, identifying the combination of SK channel blockade and Iso as a potential therapy for treating cholinergically-induced AF.

Keywords: Acetylcholine, Atrial fibrillation, Autonomic nervous system, Cardiorespiratory modulation, Catheter ablation, Computational simulation, Electrograms, f-waves, Ganglionated Plexi, Isoproterenol, Repolarization EGM, Small-conductance calcium-activated potassium channels, Tilt Test.

Resumen y Conclusiones

Las enfermedades cardiovasculares son la principal causa de mortalidad y morbilidad en las sociedades industrializadas. Entre estas enfermedades, la fibrilación auricular (FA) destaca como la arritmia más común en la práctica clínica. Se estima que para el año 2050 la FA afectará a entre 6 y 12 millones de personas en Estados Unidos y para el año 2060, a 17.9 millones de personas en Europa. La FA aumenta significativamente el riesgo de insuficiencia cardíaca, accidentes cerebrovasculares y mortalidad en general, y afecta negativamente a la calidad de vida y los costes económicos de la atención médica. El desarrollo de arritmias, incluida la FA, implica tres elementos clave: un sustrato arritmogénico, un desencadenante y factores moduladores. El sistema nervioso autónomo (SNA) ha demostrado ser un modulador crucial en este proceso, con sus ramas parasimpática y simpática desempeñando un papel fundamental en la iniciación y mantenimiento de la FA.

Dada la compleja relación entre la FA y el SNA, el objetivo principal de esta tesis es mejorar la comprensión de los mecanismos por los cuales el SNA promueve y modula la FA, y abrir el camino para el desarrollo de nuevas estrategias de tratamiento. Para lograr este objetivo desarrollamos modelos computacionales *in silico* que incorporan descripciones teóricas de la electrofisiología, la estimulación colinérgica y β-adrenérgica, y los efectos de la remodelación eléctrica resultante de la arritmia. Estos modelos abarcan desde la escala celular hasta el nivel de las aurículas completas. Los modelos multidimensionales consideran, además, la remodelación estructural y proporcionan una representación geométrica de la inervación del SNA.

Mediante la combinación de investigación computacional teórica y el análisis de señales auriculares clínicas y experimentales, la investigación presentada en esta tesis sienta las bases para futuras investigaciones destinadas a guiar la búsqueda de terapias antiarrítmicas más efectivas que se centren en el SNA.

La primera parte de esta tesis se centra en caracterizar la influencia autonómica en la modulación de las ondas f, es decir, de la actividad eléctrica de la FA reflejada en el electrocardiograma (ECG) de superficie. En particular, se analiza la frecuencia de las ondas f como un medio para evaluar de manera no invasiva la actividad del SNA durante la FA. Esta investigación tiene potencial para sentar las bases de futuros tratamientos personalizados basados en patrones específicos de disfunción del SNA, que podrían ser beneficiosos en el manejo de la FA.

En el Capítulo 3, nuestro objetivo fue evaluar el impacto de la estimulación vagal en la modulación de la frecuencia fibrilatoria en pacientes con FA persistente (psFA). El objetivo era explorar la posibilidad de utilizar esta relación como una medida subrogada para cuantificar la actividad vagal en dichos pacientes. Para lograr esto combinamos el análisis de datos obtenidos de un estudio clínico que involucraba registros de ECG de pacientes con psFA sometidos a respiración controlada, con modelos y simulaciones computacionales. En estas simulaciones, imitamos la modulación parasimpática inducida por la respiración al introducir variaciones cíclicas en la concentración de acetilcolina (ACh), el neurotransmisor parasimpático. Se emplearon modelos de tejido en 2D y modelos biauriculares en 3D en los que se consideraron diferentes patrones de inervación.

Encontramos que las variaciones temporales en la frecuencia fibrilatoria seguían el patrón temporal simulado de $\mathrm{ACh(t)}$ en todos los casos. La media temporal de la frecuencia fibrilatoria ($\overline{\mathrm{F}}_\mathrm{f}$) dependía del patrón fibrilatorio, del porcentaje de nodos de liberación de ACh y de la concentración media de ACh a lo largo del tiempo. La magnitud de la modulación respiratoria de la frecuencia fibrilatoria ($\Delta\mathrm{F}_\mathrm{f}$) dependía del porcentaje de nodos de liberación de ACh y del rango pico a pico de ACh, $\Delta\mathrm{ACh}$. El patrón espacial de liberación de ACh no tuvo un impacto en $\overline{\mathrm{F}}_\mathrm{f}$ y sólo tuvo un leve impacto en $\Delta\mathrm{F}_\mathrm{f}$ para el porcentaje espacial de ACh más alto analizado.

En el Capítulo 4 de esta tesis, profundizamos en la correlación entre la actividad del SNA y las alteraciones en la modulación de la frecuencia fibrilatoria durante las pruebas de tabla basculante cabeza arriba (HUT) y cabeza abajo (HDT). Estas pruebas se utilizan comúnmente en entornos médicos para evaluar la función autonómica, proporcionando información valiosa sobre la capacidad del SNA para regular la presión arterial y la frecuencia cardíaca en respuesta a cambios posturales. Del mismo modo, buscamos evaluar si la misma prueba se podría utilizar en la FA para evaluar la modulación autonómica de la actividad eléctrica auricular.

Para ello utilizamos modelos y simulaciones computacionales con el fin de probar diferentes combinaciones de estimulación simpática y parasimpática. Los resultados de las simulaciones se compararon con el análisis de ECG clínicos obtenidos de pacientes con psFA que se sometieron a un protocolo de prueba de tabla basculante. En conjunto, los hallazgos de este estudio indican que el aumento en la tasa fibrilatoria después de la maniobra de HUT y la disminución en la tasa fibrilatoria después de la maniobra de HDT pueden atribuirse principalmente a una actividad simpática aumentada y disminuida, respectivamente. Además, parece que la estimulación parasimpática ejerce un efecto modulador sobre los efectos simpáticos en lugar de ser la fuerza impulsora principal detrás de las tendencias observadas en la función auricular en respuesta a maniobras autonómicas.

El manejo de la FA es un desafío debido a sus mecanismos subyacentes complejos e inciertos. Las estrategias de control del ritmo se centran en restablecer y mantener el ritmo sinusal. Esto puede lograrse mediante una combinación de enfoques de tratamiento, que incluyen cardioversión eléctrica o farmacológica, terapia farmacológica antiarrítmica (TFA) y ablación por catéter. El Capítulo 5 y el Capítulo 6 de esta tesis se centran en las terapias para la FA, abordando en particular el procesamiento de señales de electrogramas (EGM) auriculares para mejorar los procedimientos de cardioneuroablación e investigar teóricamente la eficacia de nuevas terapias farmacológicas dirigidas a canales iónicos y componentes neurales.

En el Capítulo 5, desarrollamos un método para localizar los lugares de inervación para-simpática auricular utilizando mediciones de EGM. La ablación de los ganglios autonómi-cos cardiacos intrínsecos, llamados plexos ganglionares (PG), individualmente o en combinación con el aislamiento de las venas pulmonares, se ha asociado con un menor riesgo de recurrencia de la FA. Sin embargo, se requiere una ubicación precisa de los PG para que la ablación sea efectiva.

Para este estudio desarrollamos modelos computacionales con los que simulamos la actividad eléctrica en tejidos sin FA, con FA paroxística (pxFA) y con psFA. Se ha demostrado que en los PG hay predominio de actividad parasimpática, por lo que se incorporaron efectos parasimpáticos mediante el aumento de la concentración de ACh en islas distribuidas aleatoriamente dentro del tejido. Se consideraron diferentes tamaños de islas de ACh y distintas distribuciones fibróticas, incluyendo fibrosis difusa uniforme y fibrosis difusa no uniforme. Se generaron EGMs unipolares en una malla de 16x16 electrodos a partir de la simulación.

El estudio reveló que la amplitud de la onda de repolarización del EGM auricular refleja la presencia o ausencia de lugares de liberación de ACh, siendo las amplitudes positivas más grandes indicativas de que el electrodo se encuentra sobre una región de ACh. Se empleó análisis estadístico para determinar umbrales óptimos para la identificación de los lugares de liberación de ACh. El método identificó exitosamente dichos lugares en todos los tipos de tejidos, con una mayor precisión en ausencia de fibrosis o con fibrosis difusa uniforme. El algoritmo propuesto demuestra ser robusto contra el ruido y las variaciones en la distancia electrodo-tejido.

El Capítulo 6 se centra en el análisis de terapias farmacológicas antiarrítmicas en combinación con la señalización β-adrenérgica para tratar la FA colinérgica. El neurotransmisor parasimpático ACh provoca una reducción en la duración del potencial de acción y un aumento en el potencial de membrana en reposo, contribuyendo ambos a aumentar el riesgo de reentrada.

En este capítulo, utilizamos modelos y simulaciones computacionales para examinar el impacto del bloqueo de los canales SK (SKb), que son canales de potasio activados por calcio con conductancia baja. Exploramos también la estimulación β-adrenérgica mediante isoproterenol para contrarrestar los efectos negativos de la actividad colinérgica en modelos auriculares humanos. Los resultados mostraron que la combinación de SKb e isoproterenol fue capaz de restaurar el potencial de reposo y la duración del potencial de acción a los niveles observados en ausencia de actividad colinérgica, lo que indica una posible estrategia terapéutica para contrarrestar los efectos adversos de la actividad colinérgica en la FA.

En resumen, esta tesis ofrece una comprensión más profunda de los mecanismos de modulación autonómica en la FA y presenta avances en el desarrollo de nuevas estrategias terapéuticas basadas en el SNA, ya sea individualmente o en combinación con fármacos que bloquean canales iónicos que se encuentran en las aurículas. Los resultados obtenidos a través de modelos computacionales y análisis de señales clínicas y experimentales proporcionan información valiosa para futuras investigaciones y el desarrollo de tratamientos

más efectivos y personalizados para la FA.

Palabras clave: Ablación por catéter, Acetilcolina, Canales de potasio activados por calcio de baja conductancia, Electrogramas, Fibrilación auricular, Isoproterenol, Modulación cardiorespiratoria, Ondas f, Plexos ganglionares, Prueba de tabla basculante, Repolarización de EGM, Simulación computacional, Sistema nervioso autónomo.

Acknowledgements

This thesis is the result of years of work, and this achievement would not have been possible without the help and support of many people.

First of all, I would like to sincerely thank my supervisors, Esther Pueyo and Pablo Laguna, for their exceptional guidance during my doctoral journey. Esther, Pablo, I am truly grateful for your encouragement, patience, and for the countless hours you invested in me. I feel privileged to have learned from you and to have been inspired by your passion for research. You are truly extraordinary scientists, but, above all, extraordinary people.

A special mention goes to Carlos Sánchez, who not only served as an exceptional (albeit unofficial) supervisor, but who also deserve credit for making great efforts to help me improve my castellano. Carlos, thank you a lot for all your help and precious advices throughout those years.

Next, I want to express my heartfelt appreciation to the entire BSICoS group. A special thanks to the old friends who welcomed me when I first arrived here and to the new ones who joined along the way: Alba, Carmen, Clara, Cristina, David, Diego, Flavio, Hassaan, Javi, Jorge Mario, Kostas, Maxi, Neurys, Pablo, Saúl, Spyros. From the bottom of my heart, thank you for being a part of my journey and for making it truly unforgettable.

I would also like to thank the University of Zaragoza, especially the staff at I3A, for all their assistance and support.

I cannot thank enough the entire MY-ATRIA group, the supervisors, and all my fellow ESRs: Jordan, Rebecca, Giorgio, Muhamed, Javier, Ricardo, Hesam, Mostafa, Guadalupe, Luca, and Jennifer. Every gathering we attended, from the summer and winter schools to the conferences and secondments, provided not only scientific stimulation but, most importantly, a lot of fun memories that I will cherish dearly.

A special thank you goes to José Felix Rodríguez and Frida Sandberg for hosting me during the secondments and contributing to my work with their supervision and expertise.

To Jenny, with whom I have shared every step of the way: you have been an incredible colleague, roommate, and friend. We have pushed and encouraged each other, and it would

have been much more challenging without you.

To my dear friends, Ale, Giorgia, Cancy, Giulia, Jes, Manu, and Rosy, I just want to say how incredibly grateful I am for your unwavering friendship all these years. Thank you for your visits during my time away, thank you for the countless voice notes that kept me company, and thank you for always being there to welcome me back.

Most importantly, I want to express my heartfelt gratitude to my parents. Your unconditional love and constant encouragement have been the driving force behind all I have accomplished in life. I am forever grateful for your presence in my life and for the support and sacrifices you have made to help me pursue my dreams.

Finally, to Andrea. I am deeply thankful for your patience, understanding, and support. You have been my rock during challenging times, always believing in me and lightening the heavy moments with laughter. I consider myself incredibly fortunate to have you by my side. The love and support we share are treasures that I hold dear.

Contents

List of Tables

List of Figures

Nomenclature

$\mathcal{C}$	Courtemanche
$\mathcal{G}$	Grandi
$\mathcal{S}$	Skibsbye
2D	two-Dimensional
3D	three-Dimensional
ACh	Acetylcholine
ADT	Antiarrhythmic Drug Theraphy
AF	Atrial Fibrillation
ANS	Autonomic Nervous System
AP	Action Potential
APD	Action Potential Duration
APD$_{90}$	Action Potential Duration at 90 % Repolarization
AV	Atrioventricular
BB	Bachmann Bundle
cAMP	Cyclic AMP
CANS	Cardiac Autonomic Nervous System
CL	Cicle Length
CS	Coronary Sinus
CT	Crista Terminalis
CTBB	Crista Terminalis and Bachmann Bundle
CV	Conduction velocity
DAD	Delayed Afterdepolarization
EAD	Early Afterdepolarization
ECANS	Extrinsic Cardiac Autonomic Nervous System
ECG	Electrocardiogram
EGM	Electrogram
ERP	Effective Refractory Period
$\mathrm{F_f}$	f-wave frequency
FEM	Finite Element Method
FO	Fossa Ovalis

GJs	Gap Junctions
GPs	Ganglionated Plexi
HF	Heart Failure
HFS	High Frequency Stimulation
HH	Hodgkin Huxley model
HR	Heart Rate
ICANS	Intrinsic Cardiac Autonomic Nervous System
IRE	Irreversible Electroporation
Iso	Isoproterenol
IST	Isthmus
LA	Left Atrium
LAA	Left Atrial Appendage
MVR	Mitral Valve Ring
OAC	Oral Anticoagulants
ODE	Ordinary Differential Equation
pEGM	unipolar electrogram for a “punctual” electrode
PKA	Protein Kinase A
PLB	Phospholamban to SERCA Ratio
PLLA-GP	Posterolateral Left Atrial GP
PM	Pectinate Muscles
PMLA-GP	Posteromedial Left Atrial GP
PRA-GP	Posterior Right Atrial GP
psAF	Persistent Atrial Fibrillation
PVI	Pulmonary Veins Isolation
PVs	Pulmonary Veins
pxAF	Paroxysmal Atrial Fibrillation
RA	Right Atrium
RAA	Right Atrial Appendage
RF	Radiofrequency
RMP	Resting Membrane Potential
RyR	Ryanodine Receptors
SA	Sinoatrial
SERCA	Sarcoplasmic Reticulum Calcium ATPase
SKb	SK Channels block
SLA-GP	Superior Left Atrial GP
SLN	Sarcolipin to SERCA ratio
SNR	Signal-to-noise Ratio
SR	Sinus Rhythm
SRA-GP	Superior Right Atrial GP
TAT	Total Activation Time
TVR	Tricuspid Valve Ring
TW	Time Window
WL	Wavelength of Reentry

Chapter 1

Introduction

1.1 Motivation

Atrial fibrillation (AF) is the most common cardiac dysrhythmia affecting millions of patients worldwide [1–3]. AF increases the risk for heart failure (HF) [4, 5], stroke [6, 7] and death [4, 8]. On top of being associated with reduced life expectancy, it has substantial adverse effects on the quality of life and significantly increases the costs of care [1, 8, 9]. AF is a progressive disease often initially manifested by intermittent episodes terminating spontaneously and eventually leading to sustained forms of AF in some patients [10].

The prevalence of AF increases with advancing age [11]. As the older adults become a proportionately larger segment of the population worldwide [11–14], predictions estimate that AF will affect 6-12 million people in the USA by 2050 and 17.9 million in Europe by 2060 [15].

The imbalance of the autonomic nervous system (ANS) represents an important pathophysiological mechanism for AF genesis and maintenance [16–18]. Autonomic imbalance is not only a modulating factor of AF, but both the triggers and the substrate of the arrhythmia can be influenced by such an imbalance [19, 20]. The relationship between AF and the ANS is complex and multifaceted and further research is needed to fully elucidate the underlying underpinnings of this relationship and to help guiding the development of new treatment strategies for AF. Drugs that specifically target ANS activity and/or modulate atrial refractoriness may be effective in preventing AF recurrence. Transcatheter biatrial ablation of ganglionated plexi (GPs) has been suggested as an adjunct to pulmonary vein isolation (PVI) to treat AF, even if with heterogeneous results [21–27]. Furthermore, identifying patients with specific ANS dysregulation patterns could aid in the development of personalized treatment approaches for AF.

In this thesis, computational modeling and simulation is used to improve the understanding of the mechanisms by which the ANS promotes and modulates AF and to explore new potential AF therapies. Particularly, new pharmacological therapies targeting ion channels and neural components as well as strategies to improve cardioneuroablation procedures have been investigated.

1.2 The heart

1.2.1 Anatomy and function

The human heart is a vital organ responsible for circulating blood throughout the body. It comprises two similar sides, the left and right, each consisting of an upper chamber called the atrium and a lower chamber called the ventricle. The heart's electrical and mechanical functions are responsible for ensuring proper blood circulation. This relies on rhythmic contraction and relaxation movements, known as systole and diastole, respectively.

The heart has four valves that regulate blood flow between the atria and ventricles, known as atrioventricular (mitral and tricuspid) valves, and between the ventricles and the arteries and veins that supply blood to the lungs and other body parts, known as pulmonary and aortic valves. All of the heart valves facilitate forward blood flow while preventing backward flow.

The right atrium (RA) receives deoxygenated blood from the entire body except for the lungs via the superior and inferior vena cavae. Deoxygenated blood from the heart muscle itself drains into the RA through the coronary sinus. From there, the blood flows through the tricuspid valve and fills the right ventricle, the primary pumping chamber of the right heart. The right ventricle pumps blood through the right ventricular outflow tract, across the pulmonary valve, and into the pulmonary artery, which distributes it to the lungs for oxygenation. In the lungs, blood gets oxygenated as it passes through the capillaries, where it gets close enough to the oxygen in the alveoli of the lungs. The four pulmonary veins (PVs), two from each lung, collect the oxygenated blood, and they all open into the left atrium (LA), which acts as a collection chamber for oxygenated blood. The oxygenated blood then flows from the LA into the left ventricle, which is the primary pumping chamber of the left heart. The left ventricle pumps and sends freshly oxygenated blood to the systemic circulation through the aortic valve. Figure 1.1 (A) illustrates the different chambers of the heart and the course of blood through them.

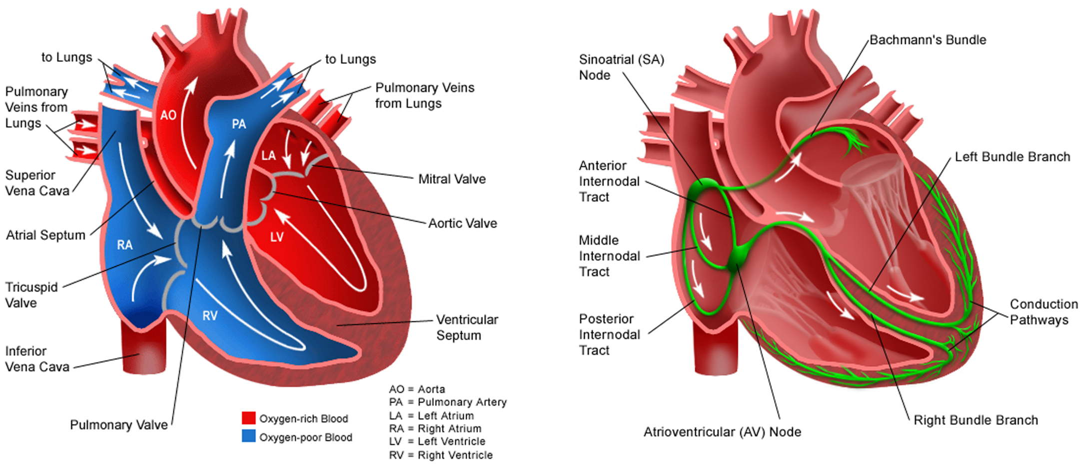

(a) (b)

Figure 1.1: Anatomic overview of the heart: chambers and blood flow (a) and conduction network (b). Extracted from [28]

.

The cardiac conduction system is responsible for initiating, conducting and controlling the heart rhythm, which is the ordered pattern of electrical impulses that governs the beating of the heart. The normal heart rhythm is known as sinus rhythm (SR), which is characterized by a regular and coordinated pattern of electrical impulses that result in the contraction and relaxation of the heart muscle. In the absence of ANS influence, the heart beats at a rate of about 100-120 beats per minute [29]. Abnormal heart rhythms, known as arrhythmias, can occur when the electrical impulses become irregular, too fast or too slow.

The heart's muscular fibers, composed of thousands of aligned muscle cells known as cardiomyocytes, contract and relax synchronously in a healthy heart. The cardiac cycle is initiated by a mass of self-excitable cells located in the RA called the sinoatrial node (SAN), also known as the natural pacemaker of the heart. The SAN generates electrical impulses autonomously, thanks to a property called autorhythmicity, at a rate that is modulated by the ANS. A second system of specialized fibers is responsible for distributing these electrical impulses throughout the myocardium. The electrical signal generated by the SAN cause the atria to contract and travels to the atrioventricular (AV) node, where the impulse is delayed to allow the atrial contraction to further increase the blood volume in the ventricles before the systole takes place. From the AV node the impulse continues to the bundle of His. The bundle of His divides into the right and left bundle branches and finally reaches the Purkinje network. The Purkinje network rapidly propagates the impulse to the different layers of cardiac muscle, achieving a coordinated contraction of the ventricles. The cardiac conduction system is illustrated in Figure 1.1 (B).

1.2.2 Cellular electrical activity

The cellular membrane of cardiomyocytes is a semi-permeable membrane composed of a lipid bilayer made up of two layers of phospholipids. The membrane contains various proteins, including ion channels, transporters, receptors and enzymes. These proteins play crucial roles in maintaining the function of the cardiomyocyte, such as regulating the flow of ions and nutrients into and out of the cell, transmitting signals between cells and facilitating metabolic processes.

The movement of ions through ion channels is passive and is controlled by two forces: the electrical gradient, which is the difference in potential between the inside and outside of the cell, and the chemical gradient, which is the difference in ion concentrations between the extracellular and the intracellular media.

In contrast, pumps and exchangers move ions against the gradient, using energy from ATP hydrolysis or electrochemical gradients. The activation of pumps and exchangers is regulated by various factors, including changes in intracellular and extracellular ion concentrations, changes in membrane potential and the presence of specific ligands.

During the resting state of a cardiomyocyte, the concentrations of ions inside and outside the cell are different. The resting membrane potential (RMP) is around -65 to -80 mV for atrial myocytes, which means that the inside of the cell is negatively charged compared to the outside. The concentration of ions inside the cell includes a high concentration of potassium (K^+) ions and a low concentration of sodium (Na^+) and calcium (Ca^{2+}) ions. The concentration of ions outside the cell includes a high concentration of Na^+ and Ca^{2+} ions and a low concentration of K^+ ions.

The action potential (AP) of an atrial cardiomyocyte refers to the sequence of electrical events that occur when the cell is stimulated. It is a rapid and brief change in the membrane potential of the cell, characterized by a depolarization phase followed by a repolarization phase. The AP time course is divided into five phases (Figure 1.2). The minimum stimulation current required to generate an AP when the cell is at its resting state is called the diastolic threshold. The five phases are described in the following:

- **Phase 0** is characterized by a rapid cell depolarization. The inward flux of sodium ions through voltage-gated sodium channels causes a sharp increase in the transmembrane potential. This influx of sodium ions generates the fast sodium current (I_{Na}).

- **Phase 1**, also known as the AP dome, is marked by inactivation of the sodium channels and by the activation of the outward transient potassium current (I_{to}), which begins to repolarize the cell, causing a transient reduction in the transmembrane potential.

- **Phase 2** is the plateau phase, marked by a balance between the inward flux of calcium ions through L-type calcium channels and the slow opening of outward potassium channels. The inward calcium ion flux creates slow calcium currents (I_{CaL}) that compensate for the outward delayed rectifier potassium current (I_{Kur}), resulting in a relatively stable transmembrane potential. This phase lasts for several hundred milliseconds and is essential for efficient heart contraction and blood pumping.

  The late sodium current (I_{NaL}) is a small inward current that flows through sodium channels during the plateau phase. It is generated by a small fraction of sodium channels that remain open during the plateau phase, even after the initial rapid depolarization. These channels do not inactivate as rapidly as the majority of sodium channels that are responsible for the upstroke of the AP, thus allowing a small inward flow of sodium ions that contributes to prolong the plateau phase.

- **Phase 3** is the repolarization phase, in which the transmembrane potential returns to the resting potential due to calcium channel inactivation and potassium channel opening. Outward potassium currents, such as the rapid delayed rectifier potassium current (I_{Kr}) and the slow delayed rectifier potassium current (I_{Ks}), act to get the cell back to its resting state. The inward rectifier potassium current (I_{K1}) helps to shape the final stages of repolarization by slowly closing and causing the repolarization of the cell to slow down and eventually reach a plateau before returning to its resting state. Inward rectifier potassium channels are so named because they allow potassium ions to flow more easily into the cell than out of the cell, rectifying the potassium current and allowing more potassium ions to enter than leave. I_{K1} channels can conduct much larger inward currents at membrane voltages negative to the K^+ equilibrium potential than outward currents at voltages positive to it because the conductance is larger at potentials more hyperpolarized than E_K and is smaller at depolarized potentials [30, 31].

- **Phase 4** is the final phase of the atrial AP, during which the transmembrane potential reaches its resting value (-65 and -80 mV). At this phase, the cell remains in its resting state when there is no external stimulation. The Na^+/K^+ ATPase pump plays a crucial role in maintaining this state by actively transporting sodium ions out of the cell and potassium ions into the cell. Additionally, I_{K1} channels are still open, allowing potassium ions to flow out of the cell and contributing to the maintenance of the RMP.

Apart from these mechanisms, other currents also play a role in the atrial AP. Chloride currents help to balance the outward potassium currents during repolarization, thereby ensuring that the cell remains at a stable RMP. The voltage-gated chloride channels open in response to the depolarization of the cell membrane, whereas the calcium-activated chloride channels open in response to an increase in intracellular calcium levels.

The Na^+/Ca^{2+} exchanger is responsible for regulating the levels of calcium inside atrial myocytes. During the resting phase of the AP, the concentration of calcium is low inside the cell, and the Na^+/Ca^{2+} exchanger is responsible for removing any calcium that enters the cell. The equilibrium potential for Na^+/Ca^{2+} exchange current is generally slightly negative to 0 mV. Thus, near the resting potential the $\mathrm{Na^+/Ca^{2+}}$ exchanger works in the normal mode and generates an inward current. As the AP begins, voltage-gated calcium channels open, allowing calcium to flow into the cell and trigger muscle contraction. During the first part of the plateau, the $\mathrm{Na^+/Ca^{2+}}$ exchanger works in the reverse mode and briefly generates an outward current prior to returning to the normal mode, when the increase in intracellular calcium levels activates the $\mathrm{Na^+/Ca^{2+}}$ exchanger, which removes calcium from the cell in exchange for sodium ions that are present outside the cell.

Finally, the small conductance calcium-activated potassium (SK) channels generate the calcium-activated potassium current (I_{SK}). These channels, which represent a subfamily of all calcium-activated potassium channels, have a small single channel conductance of the order of 10 pS and are activated by an increase in intracellular calcium levels during the depolarization phase of the AP. As intracellular calcium levels increase, these channels open, allowing potassium ions to flow out of the cell, thus contributing to the repolarization of the cell membrane.

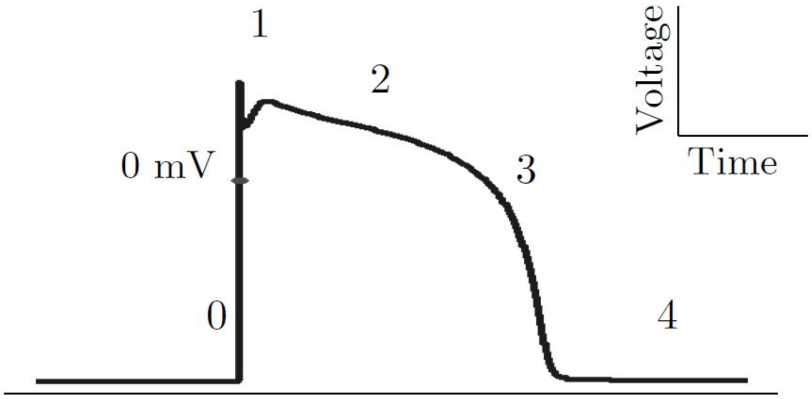

Figure 1.2: Schematic representation of a cardiac AP with the ionic currents involved in each AP phase. Adapted from [32]

AP profiles remarkably vary between different regions of the heart due to tightly controlled variations in gene expression and regulation. Typically, the human atrial AP exhibits a triangular morphology, which is distinct from the spike-and-dome shape with a more prominent plateau phase seen in the ventricular AP [33, 34]. The human atrial AP duration (APD) at 90% repolarization (APD_{90}) at 1 Hz is highly variable, ranging from 150 to

500 ms, and may be influenced by recording conditions and ionic concentrations [34–37]. Additionally, the human atrial RMP is more depolarized, ranging from -65 to -80 mV, than the human ventricular RMP [34–37]. The more depolarized RMP in atrial cells compared to ventricular cells is mainly due to differences in the density of the inward rectifier K^+ current, $\mathrm{I_{K1}}$ [38]. Maximum upstroke velocities for atrial APs have been experimentally reported to vary between 150 and 300 V/s, in contrast to the higher values of 300-400 V/s reported for human ventricular cells [34–37].

During the AP, three states of refractoriness can be identified: 1) the absolute refractory period, which is the time when a stimulus, regardless of its strength, will not generate another AP due to the membrane not being sufficiently repolarized and $\mathrm{Na^+}$ channels being inactivated; 2) the relative refractory period, requiring a stronger stimulus to initiate an AP; and 3) normal excitability.

1.2.3 Cardiac electromechanical coupling

Cardiac electromechanical coupling refers to the process that links electrical signals in the heart to mechanical contraction of the myocardium. During the AP, the opening of voltage-gated calcium channels in the cellular membrane of the cardiomyocytes leads to an influx of $\mathrm{Ca^{2+}}$ into the cell. This calcium influx triggers the opening of $\mathrm{Ca^{2+}}$-sensitive ryanodine receptors (RyR) in the sarcoplasmic reticulum, an internal membrane system within the cardiomyocyte that stores and releases calcium ions. The opening of RyRs leads to an increase in the intracellular $\mathrm{Ca^{2+}}$ concentration in the sarcoplasm, which binds to troponin, thus allowing the interaction of the two contractile proteins actin and myosin. This leads to the mechanical contraction of the cardiomyocyte.

The above described process is coordinated by the T-tubules, which ensure that the membrane gets close to the sarcoplasmic reticulum in the sarcoplasm and the AP reaches all regions of the cell. This allows spatially and temporally synchronous release of $\mathrm{Ca^{2+}}$ from the sarcoplasmic reticulum, thus facilitating the rapid and coordinated contraction of the cell.

Following mechanical contraction, the sarcoplasmic reticulum calcium ATPase (SERCA) pump restores the cytoplasmic Ca^{2+} concentration by introducing Ca^{2+} into the sarcoplasmic reticulum [39].

1.2.4 Electrical conduction in the heart

The electrical conduction in the heart relies heavily on the specialized cardiac conduction system and the connectivity between cells. In the cardiac muscle, cells are separated by intercalated discs. Gap junctions (GJs) form when adjacent cell membranes fuse at these discs. GJs are structures that connect adjacent cells, allowing for electrical coupling and exchange of small molecules, ions or metabolites. Each GJ is made up of two hemichannels, or connexons, each composed of six proteins called connexins, which combine with the connexons of neighboring cells to create a functional channel in the intercellular space. This allows ions to move along the longitudinal axes of the muscle fibers. The electrical impulse travels from one cardiac cell to a neighboring one through these junctions. As a result, the cardiac muscle functions as a closely interconnected group of cells and, when one cell is stimulated, the AP spreads to the rest of the cells [40].

1.2.5 Cardiac arrhythmias

Cardiac arrhythmias encompass a wide range of heart rhythm disorders, ranging from benign irregularities to life-threatening complications. Arrhythmias can arise in hearts with an underlying heart disease or other medical conditions, including hypertension, hyperthyroidism and structural heart defects. Lifestyle factors such as stress, smoking, excessive alcohol consumption and drug abuse can also contribute to their development. If left untreated, cardiac arrhythmias can lead to serious complications, such as HF, stroke and sudden cardiac death.

There are two main types of cardiac arrhythmias depending on where they are originated: ventricular and supraventricular arrhythmias. Ventricular arrhythmias, which occur in the lower chambers of the heart, can be fatal and require immediate medical attention. Supraventricular arrhythmias, which originate above the ventricles, such as in the atria or the AV node, are typically less severe. Nevertheless, without proper treatment, supraventricular arrhythmias can lead to significant complications too. Treatment for this type of arrhythmias may involve medication, lifestyle intervention or procedures like ablation or cardioversion.

Some common types of supraventricular arrhythmias include supraventricular tachycardia, which is a rapid heart rate (HR) originating above the ventricles that can be caused by factors like stress, caffeine or heart disease. Atrial flutter occurs when the atria contract at an excessively high rate, usually between 250 and 350 beats per minute, leading to a rapid HR and decreased blood flow to the body. AF, the most common type of supraventricular arrhythmia, occurs when the atria quiver or fibrillate instead of contracting properly. AF increases the risk for blood clot formation and stroke (explained in detail in section 1.3).

1.2.6 Electrograms and electrocardiograms

Electrograms (EGMs) and electrocardiograms (ECGs) are important tools for diagnosing and monitoring heart rhythm abnormalities.

Electrograms An intracardiac EGM measures localized electrical activity in the heart using invasive electrodes placed on the heart wall. The EGM signals can be bipolar or unipolar depending on the position of the electrodes.

A unipolar EGM records electrical activity from an electrode at a point on the heart surface with respect to a reference electrode located remotely. Unipolar EGMs have straightforward morphology interpretation and their shape is independent of the wavefront direction [41]. They are rather sensitive to electrical signals generated at a distance from the electrode, such as remote activation caused by activity of distant heart cells or electrical disturbances. The EGM recorded at the origin of activation is consistently negative because the electrode remains in the negative area of the extracellular potential field during the propagation of the activation front. However, at a site where the activation front passes the electrode, the EGM shows a biphasic deflection: during the initial phase of the front's approach, the electrode is in the positive part of the potential field, resulting in a positive deflection of the EGM; when the front is exactly over the electrode, the EGM amplitude becomes zero; as the front moves past the electrode, the EGM becomes negative once again because the electrode is now in the negative part of the potential field (Figure 1.3, bottom panel). This sequence results in a biphasic deflection for the EGM, a positive deflection followed by a negative one. when the electrode is situated at a site where activation comes to an end, it is positioned within the positive region of the potential field and therefore the signal will be positive [41].

A bipolar EGM records electrical activity between two points on the heart's surface. Both the recording and reference electrodes are placed in contact with the surface of the heart. Bipolar electrograms are sharper than unipolar ones because differentiation of the signal promotes the high-frequency components in the signal (Figure 1.3, top panel). Morphology and amplitude of a bipolar electrogram depend on the direction of the wavefront [41]. The degree of time shift between the two (unipolar) signals depends on the direction of the wavefront and is nearly zero if activation moves perpendicular to the line between the electrode positions. If the distance between the two electrodes is small, the EGM signal is more sensitive to near-field components, while if they are far apart, the signal collects information from a larger heart region.

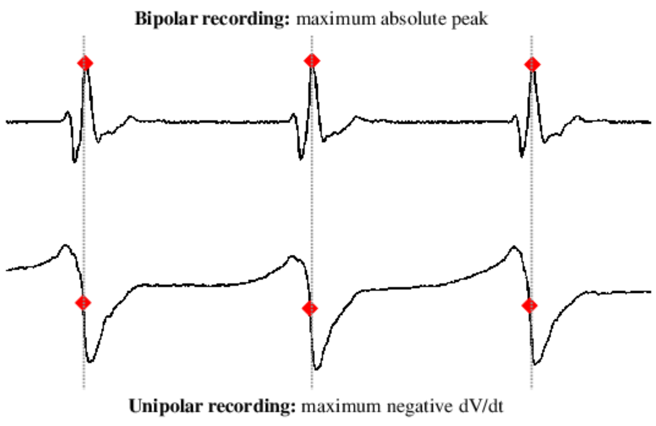

Figure 1.3: Comparison between bipolar (top) and unipolar (bottom) EGM signals. Extracted from [42].

EGM recordings are a useful tool for analyzing activation patterns, identifying regions with impaired electrical propagation and guiding interventions such as surgical ablation procedures.

Electrocardiograms The ECG is obtained by placing electrodes at specific locations on the body surface and represents a summation of voltage gradients generated within the heart. A standard 12-lead ECG is recorded using 10 surface electrodes, which include 6 precordial leads (V1-V6), 3 bipolar limb leads (I, II, and III), and 3 augmented limb leads (aVR, aVL, and aVF).

The limb electrodes, placed in each of the arms and legs, allow the recording of standard limb leads I, II and III, and the augmented limb leads aVR, aVL and aVF. The chest electrodes are positioned at specific locations on the chest and are used to record precordial leads V1, V2, V3, V4, V5 and V6. The standard limb leads are bipolar as they measure differences between a positive and a negative electrode in the limbs, whereas the augmented and precordial leads are unipolar as they measure differences between a positive electrode and a combination of electrodes that act as a negative electrode.

The ECG signal consists of a series of waves and intervals that represent the electrical activity of the heart during one cardiac cycle. These waves and intervals are labeled with letters of the alphabet, which are commonly referred to as ECG landmarks. The classical ECG form includes the P wave, the QRS complex and the T wave. The P wave represents the sequential activation of the right and left atria, while the QRS complex represents the activation of the right and left ventricles, with the left ventricle having a greater contribution due to its larger mass. Atrial repolarization is masked within the QRS complex, which almost exclusively represents ventricular depolarization due to the ventricles' considerably larger mass, leading to a greater contribution to the ECG signal. The T wave represents ventricular repolarization.

Other segments and intervals in the ECG signal include the QT interval, which comprises the duration of ventricular depolarization and repolarization. The time interval between ventricular depolarization and repolarization is, under physiological conditions, an isoelectric period represented in the ECG by the ST segment. The RR interval is the elapsed time between two consecutive heartbeats. Figure 1.4 illustrates the correspondence between the ECG waveforms and the action potentials of cells from different regions of the heart. As can be observed, the electrical activities of all cells in the heart contribute to the ECG signal.

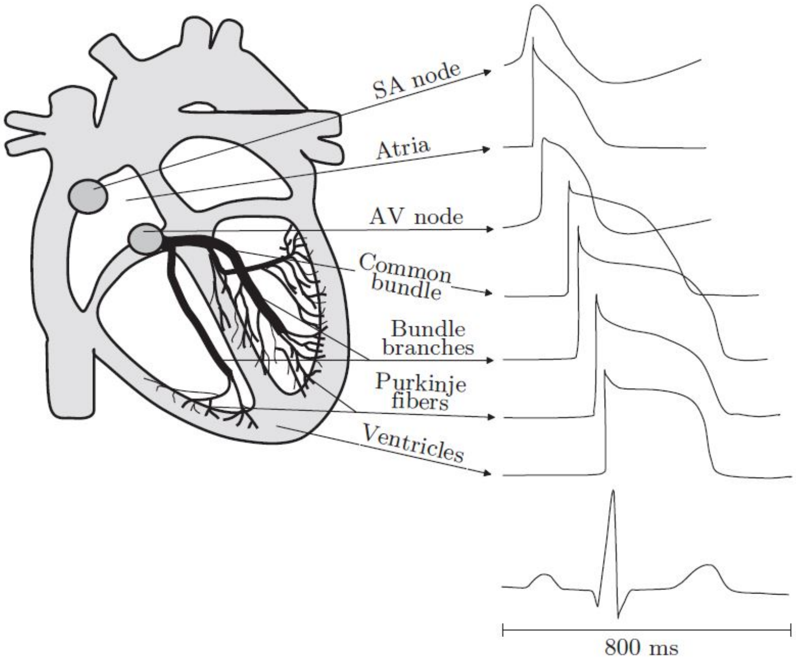

Figure 1.4: Schematic representation of the APs recorded in various cardiac tissues and the correspondence with the ECG waves and intervals. Reproduced from [43].

1.2.7 Autonomic nervous system

Homeostasis refers to the regulation and maintenance of an organism's internal environment, including factors such as pH levels, temperature, and nutrient levels. The ANS plays a crucial role in controlling and maintaining homeostasis. It automatically detects changes in the internal environment and adjusts physiological processes accordingly to keep the body's conditions within a narrow range that is compatible with life.

In order to ensure optimal organ function, the heart must adapt to changes in both internal and external stimuli. This adaptation is regulated by the ANS, which modulates HR and contractility through the interplay of sympathetic and parasympathetic inputs.

Dysregulation of autonomic heart function has been implicated in numerous cardiac disorders, such as HF, hypertension and arrhythmias. Therefore, understanding the role of the ANS in regulating heart function is crucial for developing effective treatments and interventions to prevent or manage these conditions.

The autonomic control of the heart is mediated by the highly integrated intrinsic and extrinsic cardiac autonomic nervous system (CANS) [44, 45]. The CANS maintains homeostasis through two branches: the sympathetic nervous system, which is the primary mechanism in control of the “fight-or-flight” response, and the parasympathetic nervous system, which is involved in rest and recuperation.

Sympathetic and parasympathetic autonomic nervous system The efferent autonomic signals are transmitted through two major subdivisions of the ANS known as the sympathetic nervous system and the parasympathetic nervous system [40]. Both systems are tonically active, providing some degree of nervous input to a given tissue at all times.

Sympathetic tone is associated with the fight-or-flight response to confront threats. In a relaxing environment, the parasympathetic tone is more dominant and is associated with the rest and digest state. As sympathetic and parasympathetic systems typically have opposing effects, if one system increases its activity while the other decreases it, the result is a rapid and precise control of a tissue’s function.

Focusing also on the circulatory system, parasympathetic tone activation results in lower HR and a decrease in blood pressure due to a lower cardiac output, although parasympathetic activity has more limited effects on blood vessels than sympathetic activity. During sympathetic activation, HR and muscle contractility increase, leading to a higher stroke volume. Additionally, sympathetic innervation causes vasoconstriction of blood vessels, giving rise to an increase in blood pressure due to increased cardiac output and vascular resistance.

ANS neurons mainly release two neurotransmitters, acetylcholine (ACh) and norepinephrine, which are secreted by cholinergic and adrenergic fibers, respectively [40]. Unlike skeletal motor nerves that contain a single neuron pathway, sympathetic nerves have preganglionic and postganglionic neurons in each innervated tissue pathway. Both systems have cholinergic preganglionic neurons, but the majority of postganglionic neurons in the parasympathetic system are cholinergic, while those in the sympathetic system are adrenergic. Thus, except for a few cases, ACh is secreted by terminal nerve endings of the parasympathetic system, while norepinephrine is secreted by the sympathetic nerve endings.

Extrinsic and intrinsic cardiac autonomic nervous system The CANS is described as a multiple-level hierarchy, consisting of central components, intrathoracic extracardiac components and intrinsic cardiac components. The extrinsic components of the CANS (ECANS), comprising the central and intrathoracic levels, are composed of brain or spinal conglomerations of neuron bodies, such as the vagosympathetic trunk, that are connected to the heart through their axons. The intrinsic CANS (ICANS) consists of a neural network formed by nerve axons, interconnecting neurons and clusters of autonomic ganglia called GPs [46, 47].

Regarding the ECANS, a subdivision into sympathetic and paraysmpathetic components is made. The sympathetic fibers are mostly derived from major autonomic ganglia located along the cervical and thoracic spinal cord, including the superior cervical ganglia that communicate with cervical nerves C1-3, the stellate (cervicothoracic) ganglia that communicate with cervical and thoracic nerves C7-8 to T1-2, and the thoracic ganglia [48, 49]. Parasympathetic preganglionic fibers are mostly carried within the vagus nerve and are divided into superior, middle and inferior branches. The majority of parasympathetic nerve fibers converge at a distinct fat pad known as the “third fat pad”, between the superior vena cava and the aorta, to then connect to the SAN and AV node [50]. This is illustrated in Figure 1.5.

The ICANS represents the final relay center for the coordination of regional cardiac function and is composed of sensory (afferent), interconnecting (local circuit) and motor (adrenergic and cholinergic efferent) neurons. These neurons communicate with intrathoracic extracardiac ganglia, forming a distributive network that processes both afferent and efferent neuronal impulses for cardiac control, under the influence of the central nervous system and circulating catecholamines [**Bassil˙PulmonaryVein**, 51–53]. The ICANS regulates several aspects of cardiac function, such as HR, atrial and ventricular refractoriness, conduction, contractility and blood flow [54]. The ICANS appears to function interdependently as well as independently of the ECANS, as confirmed by its retention of nearly full control of cardiac physiology after autotransplantation [52, 53].

The exact shape and structure of the neural network in the myocardium are not fully known, but some works have documented the presence of between 500 and 1500 ganglia of different sizes in the atrial and ventricular myocardium [46]. These ganglia may contain 200 to 1000 neurons [46, 52, 55], including efferent neurons, afferent neurons and local interneurons that receive inputs from both efferent and afferent neurons. Although the vast majority of ganglion cells are cholinergic, most ganglia also contain adrenergic nerve fibers [56]. Depending on age, the number of intrinsic ganglia per heart can significantly fluctuate. For instance, the mean number in human adult hearts is 700, while in human fetuses, neonates, infants and children, the mean is larger than 900 [56]. The vast majority of these ganglia are organized into GPs on the surface of the atria and ventricles [52] and are more abundant epicardially than endocardially [57]. Although their location, shape and size can vary, intrinsic cardiac ganglia are usually distributed at specific regions in many mammals, including humans [46, 58, 59].

In particular, with regards to the atria, five major atrial GPs have been reported to be embedded in epicardial fat pads located near the PVs [46, 52]. They have been named based on clinical anatomy: the superior right atrial GP (SRA-GP), located on the posterior superior surface of the RA close to the junction of the SVC and RA; the superior left atrial GP (SLA-GP), located on the posterior surface of the LA between the PVs; the posterior right atrial GP (PRA-GP), located on the posterior surface of the RA adjacent to the interatrial groove; the posteromedial left atrial GP (PMLA-GP), located on the posterior medial surface of the LA; and the posterolateral left atrial GP (PLLA-GP), located on the posterior lateral surface of the LA base on the atrial side of the atrio-ventricular groove.

Ionic mechanisms of parasympathetic and sympathetic stimulation Autonomic effects on cardiac function are mediated by the release of neurotransmitters, namely norepinephrine from sympathetic nerves and ACh from parasympathetic nerves. Both neurotransmitters bind to G protein-coupled receptors.

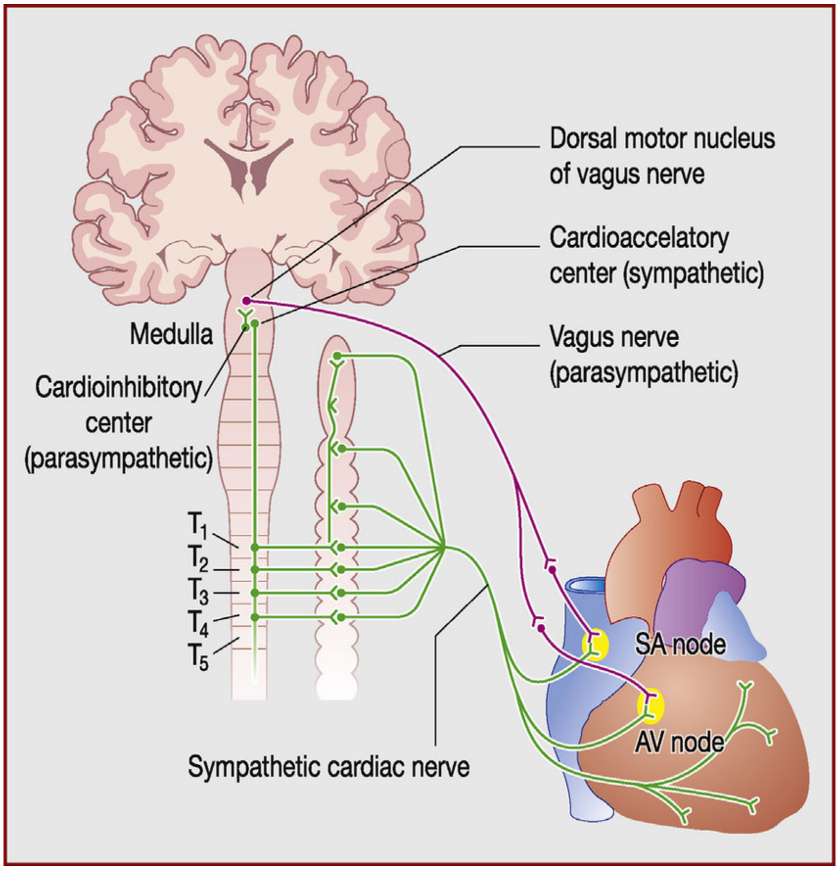

Figure 1.5: Anatomy of the sympathetic and parasympathetic innervation of the heart. Extracted from [19].

Norepinephrine specifically binds to the β-adrenoceptors of cardiac cells, which in turn activate the stimulatory G protein α-subunit. This activates adenylyl cyclase, an enzyme that converts ATP to cyclic AMP (cAMP). cAMP activates protein kinase A (PKA), which phosphorylates a number of downstream targets, including ion channels and enzymes in cardiac cells. Among such targets are L-type calcium channels, which, when phosphorylated by PKA, increase their activity. This results in increased intracellular calcium levels, contractility and HR. Other targets are RyRs, which, when phosphorylated by PKA, increase the release of calcium from the sarcoplasmic reticulum, leading to increased contractility. PKA also phosphorylates phospholamban, which relieves its inhibitory effect on the SERCA pump, leading to increased calcium reuptake by the sarcoplasmic reticulum and relaxation of the heart muscle. PKA also phosphorylates troponin I, which reduces its affinity for calcium, leading to increased contractility. Dysregulation of this pathway can

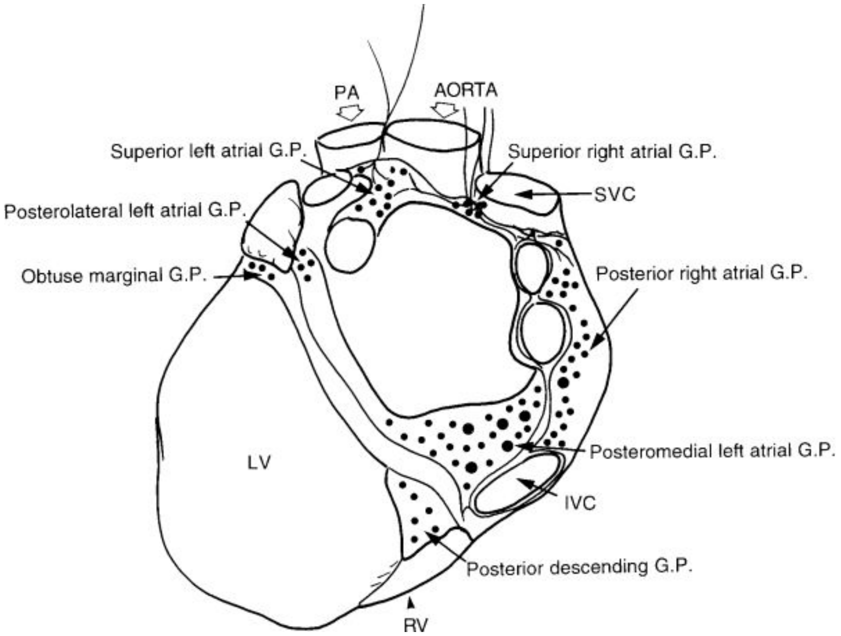

Figure 1.6: Posterior view of the human heart illustrating the locations of major atrial GPs, extracted from [52].

lead to cardiovascular diseases, including HF and arrhythmias. In the SAN cells, the effect of norepinephrine is to accelerate their pacemaker activity.

Similarly, ACh binds to muscarinic receptors in atrial myocytes, activating the inhibitory G protein α-subunit. Additionally, ACh exerts its effects through G-$\beta\gamma$-mediated activation of the G protein-activated inwardly rectifying potassium channels. The resulting ACh-activated potassium current, I_{KACh}, causes shortening of the APD and hyperpolarization of the RMP, with concentration-dependent effects. The intrinsic pacemaker activity of SAN cells is decelerated by ACh-mediated stimulation of the muscarinic receptors due to an induced decrease in cAMP levels and a reduction in the funny current (I_f) that contributes to spontaneous SAN depolarization. This results in a decrease in the firing rate of the SAN and a decrease in HR. Finally, ACh is able to inhibit GJs communication, with a consequent reduction in the conduction velocity (CV) across the atrium. This may favor proarrhythmicity by enhancing vulnerability to reentry.

1.3 Atrial fibrillation

1.3.1 Incidence and diagnosis

AF is currently the most prevalent sustained arrhythmia encountered in clinical practice, affecting over 43.6 million individuals worldwide [3, 60]. AF is a supraventricular arrhythmia characterized by rapid and irregular activation of the atria at a rate of 5 to 10 Hz, producing an irregular ventricular response [61]. Ectopic activity and/or areas of slow conduction can facilitate the persistence of reentrant activity. AF is associated with frequent symptoms and reduced quality of life and, although it is not typically life-threatening, it constitutes a major risk factor for stroke and mortality from cardiovascular and all causes [62–64].

Age is the most significant risk factor for AF. The population of adults aged over 65 years is expected to double from 12% in 2010 to 22% in 2040 [65] and the risk of developing AF increases with age, ranging from 0.7% in subjects aged 55-59 years to almost 18% in patients aged 85 years and above [11]. Due to the aforementioned increase in global life expectancy and the longer survival of the population with chronic conditions, the incidence and prevalence of AF have reached epidemic proportions [63, 66–68]. Based on data from the Framingham Heart Study, the prevalence of AF has tripled over the last 50 years [66]. In the United States alone, at least 3-6 million people have AF, and the numbers are projected to reach approximately 6-16 million by 2050 [12, 14]. In Europe, the prevalence of AF in 2010 was around 9 million among individuals older than 55 years and is expected to reach 14-18 million by 2060 [15, 69, 70]. It is estimated that by 2050, AF will be diagnosed in at least 72 million individuals in Asia, with approximately 3 million experiencing AF-related strokes [71]. Furthermore, about one-third of the total AF population is asymptomatic [72], indicating that the global AF burden is likely underestimated.

Despite multifaceted research efforts, the prevention of AF and its related complications remains challenging [73]. Diagnosis of AF is based on ECG rhythm documentation. On the ECG, AF can be observed from the replacement of consistent P waves, produced by a coordinated atrial depolarization during atrial systole, with rapid oscillations or fibrillatory waves (”f waves”) that vary in size, shape and timing due to the asynchronous depolarization of atrial tissue. The frequency of these fibrillatory waves, known as the f-wave frequency, is generally accepted as a surrogate marker for local refractoriness and is extensively studied in clinical contexts [74].

Another characteristic of the ECG in AF is the irregular and often faster HR or RR intervals, due to the high level of disorganization of ventricular impulses resulting from the AV node's filtering role. To establish the diagnosis of AF, conventionally, an ECG tracing of at least 30 seconds showing heart rhythm with no discernible P waves and irregular RR intervals is required [38]. Figure 1.7 displays the ECG tracings typically observed during SR and AF, with the rhythm becoming irregular and the P waves being replaced with f-waves in the case of AF.

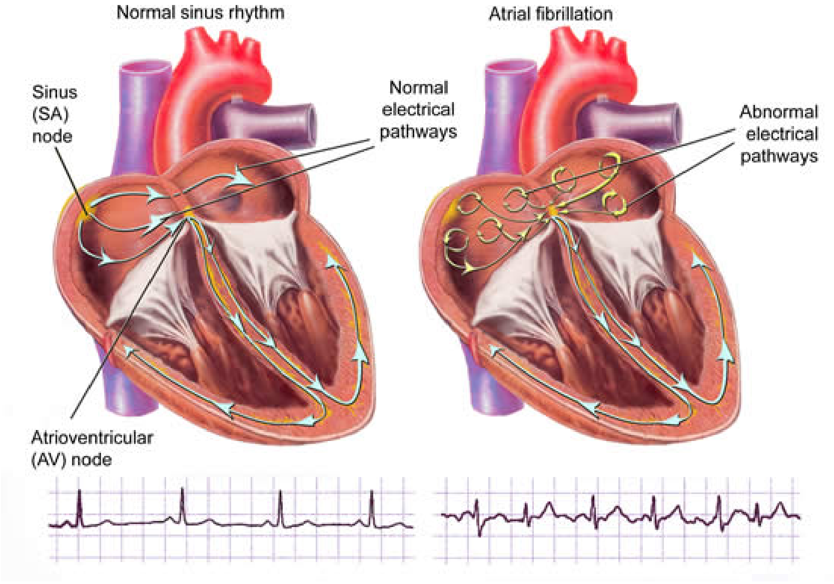

Figure 1.7: Examples of ECGs in normal SR (left) and in AF (right). Extracted from [75].

1.3.2 Types of atrial fibrillation

AF is a progressive disease often initially manifested by intermittent episodes terminating spontaneously and eventually leading to sustained forms of AF for a subset of patients [10]. However, progression varies considerably among patients and the exact mechanism by which some patients progressed while others did not remains elusive.

Current clinical AF classification is based on the duration of AF episodes and form of termination [3, 76] as follows:

- First diagnosed AF: This type of AF occurs when the arrhythmia is diagnosed for the first time, irrespective of the duration of the episode or the presence and severity of related symptoms.

- Paroxysmal AF (pxAF): It is a self-terminating AF ending in most cases within 48 hours that, by definition, may continue for up to 7 days.

- Persistent AF (psAF): This type of AF lasts longer than 7 days, including cardioverted episodes, either with drugs or by direct electrical cardioversion. Persistent AF can be the first sign or can occur after some paroxysmal episodes.

- Long-standing persistent AF: It is a continuous AF with a duration greater than one year, usually leading to permanent AF, in which cardioversion has failed or has not been attempted.

- Permanent AF: This type of AF happens when cardioversion fails or the arrhythmia relapses within 48 hours.

1.3.3 Pathophysiology

AF is a highly complex arrhythmia whose pathophysiology has been proposed to be based on a “pathophysiological triangle” (see Figure 1.8). This triangle highlights the interplay of three key factors in the development and perpetuation of AF: triggers for arrhythmia initiation, a fibrotic substrate for its maintenance and numerous modulators [77].

The pathophysiological triangle underscores the multifactorial nature of AF and emphasizes the importance of addressing all three factors in the management of the arrhythmia. Treatment strategies for AF may involve addressing structural changes, altering electrical activity and mitigating triggers or risk factors.

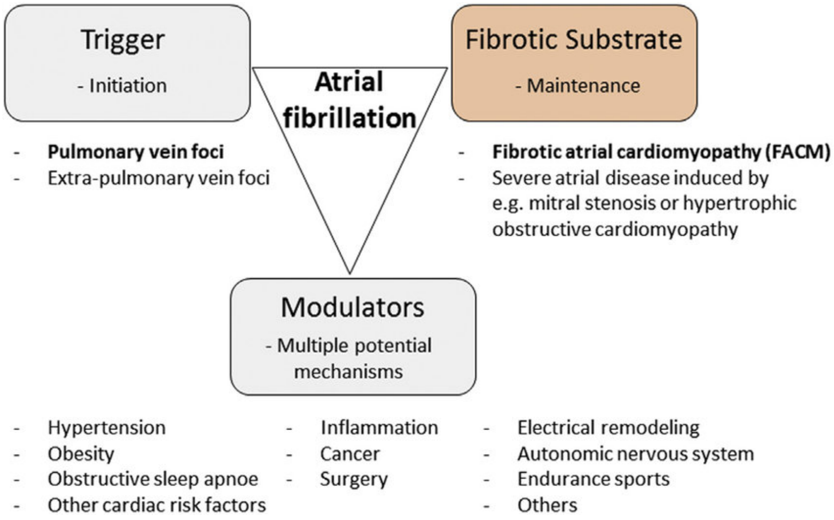

Figure 1.8: The pathophysiological triangle in AF. Extracted from [77].

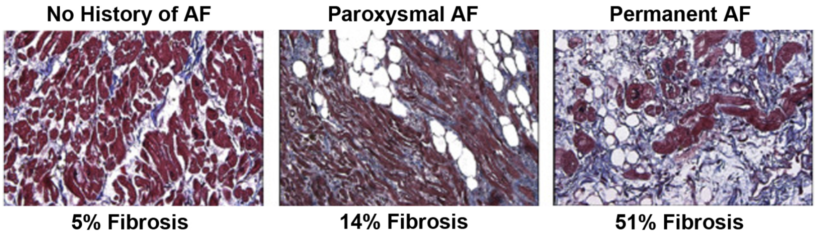

Figure 1.9: Masson's trichrome staining showing the amount of fibrosis (blue) increasing with AF burden. Modified with permission from [78].

Substrate Atrial structural and functional changes may develop as a result of pathological systemic processes in cardiac conditions, including hypertension, valvular disease, HF, or AF itself [79]. Electrical remodeling, including changes in APD and ionic mechanisms, occurs over a period of one to two weeks [61]. In contrast, structural remodeling occurs over longer periods of atrial tachypacing (months) and is mostly irreversible [61, 80]. Structural remodeling in AF can manifest in various ways, including enlargement of the atrial chamber, cardiomyocyte hypertrophy, increased mismatch between the orientations of epicardial and endocardial myofibers, changes in atrial wall thickness, and most importantly, increased fibrotic or connective tissue content [81–83]. Fibrosis is the hallmark of structural remodeling in AF, generally being significantly higher in AF patients compared to patients in SR and in psAF compared to pxAF [78] (Figure 1.9). However, different studies have shown large inter-individual variability in the fibrotic load in both pxAF and psAF, with some individual cases of pxAF patients showing massive fibrosis and of psAF patients showing only mild fibrosis [78, 84–86].

Fibrosis remodeling is a multiscale process that occurs from the subcellular to tissue levels. It has been associated with GJs remodeling [87, 88], fibroblast proliferation [89, 90] and excess collagen deposition [89, 91], all of which interfere with cardiac electrical propagation and slow conduction. Fibroblasts comprise around 10-15% of the myocardium volume, despite far outnumbering cardiomyocytes [92]. While fibroblasts were traditionally considered passive structural cells, recent studies have shown that they can exhibit APs when electrically coupled to cardiomyocytes through GJ channels [93, 94]. Fibroblasts have been recognized to play a crucial role in modulating the electrical function of the myocardium [95–98]. They can act as current sources or sinks during cardiomyocyte excitation, thus disturbing normal electrical propagation. Their proliferation has been associated with abnormal automaticity in the atria, where fibroblast-cardiomyocyte coupling can induce a depolarizing current during the diastolic phase and elicit APs [99]. Additionally, fibroblasts can exert electrophysiological influences on neighboring myocytes [100], leading to changes in AP shape, RMP, AP upstroke velocity and CV [101–103].

Electrophysiological remodeling also contributes to the development of a substrate that facilitates the tendency for persistence of AF [61]. It induces changes in the biophysical properties of the Na^{+}, Ca^{2+} and K^{+} currents, which lead to a shortening of the APD [38, 61, 104–107]. The peak amplitude of $[\mathrm{Ca}^{2+}]_i$ is reduced in atrial myocytes from psAF patients compared to those from healthy individuals, although the sarcoplasmic reticulum Ca^{2+} content is unaltered [38, 108]. Additionally, $[\mathrm{Ca}^{2+}]_i$ decays more slowly in psAF compared to that in SR [38, 108].

Electrical remodeling during AF affects various ionic currents. The main affected ionic currents are:

- $\mathrm{I_{Na}}$: In patients with psAF, the peak $\mathrm{I_{Na}}$ density slightly decreases in the atrial myocardium [109]. The steady-state activation shifts rightwards by about 10 mV [107]. Furthermore, $\mathrm{I_{NaL}}$, the late sodium current component, is significantly increased in psAF patients [109].

- I_{CaL}: A reduction of about 50% in I_{CaL} density in psAF compared to that in SR is one of the most consistent findings in humans and animal models of AF [38, 61, 104, 105, 110, 111]. No changes have been reported in channel activation and inactivation properties [104].

- I_{to} and I_{Kur}: Human psAF has been strongly associated with a reduction in I_{to} density [105, 107, 112–115] and with downregulation of its α-subunit Kv4.3 [116]. Different works have described a reduction in I_{Kur} in psAF [113, 115, 117], along with a diminished expression of Kv1.5 in some studies [113, 118]. However, other studies have reported no changes in I_{Kur} density [105, 107, 114]. The inconsistency in I_{Kur} function may result from different strategies to identify I_{to} and I_{Kur}, i.e. peak and late current [117]. The reduction in I_{to} and I_{Kur} could explain the slight prolongation in the earlier phases of the action potential [38].

- I_{Ks}: Caballero and colleagues were the first to demonstrate that psAF significantly increases the amplitude of I_{Ks} in both atria [112]. They suggested that the increase in I_{Ks} could contribute to psAF-induced shortening of APD and could further promote fibrillatory conduction, especially with its accumulation at higher pacing frequencies, as shown in neonatal rat ventricular myocytes in which I_{Ks} was overexpressed [119].

- I_{K1}: Increases in both current density [35, 104, 120] and mRNA levels of I_{K1} [35] have been reported in human psAF. Increased I_{K1} causes a more negative RMP in psAF versus SR human atrial myocytes [35, 38].

- I_{SK}: In the atria of patients with psAF, the density of this Ca^{2+}-activated K^+ current was found to be reduced when compared to those in SR. When assessed pharmacologically, the contribution of this current to APD in psAF was not significant [121].

- Na^+/Ca^{2+} exchange current (I_{NaCa}): Abnormal function and increased expression of the exchange protein have been reported in human psAF and in a sheep model of psAF [35, 36, 38, 61, 108, 110, 122–124]. The increase in I_{NaCa} may be an adaptive response to cellular Ca^{2+} loading and helps to reduce the Ca^{2+} overload induced by rapid atrial pacing. Na^+ overload, which induces Ca^{2+} influx via the reverse-mode of the exchanger, has been implicated in Ca^{2+} overload and related arrhythmogenesis. Additionally, an increase in the forward-mode Ca^{2+} extrusion has been linked to delayed afterdepolarizations (DADs) [61, 124].

- RyR: In myocytes from AF hearts, leaky RyR channels can cause spontaneous Ca^{2+}-release events known as Ca^{2+} sparks and Ca^{2+} waves, as reported in several studies [61, 108, 124–127]. Remarkably, these events can occur despite unaltered sarcoplasmic reticulum Ca^{2+} content.

- SERCA: Human psAF has been associated with a decrease in SERCA activity and reduced SERCA protein expression, which can explain the slower decay of $[\mathrm{Ca}^{2+}]_\mathrm{i}$ in psAF compared to SR [38, 61].

Triggers Pathophysiological variability is likely to influence how AF is initiated and sustained. In fact, AF has been postulated to have multiple and diverse mechanisms in different patients or even in the same patient at different times [61, 128, 129]. Ectopic firing refers to the initiation of electrical impulses from regions outside the SAN. In some cases, other areas of atrial tissue can spontaneously depolarize and create electrical impulses, leading to abnormal heart rhythms. Several factors can enhance automaticity in atrial tissue, including aging, structural heart disease, hypertension, diabetes, hyperthyroidism and certain medications. Focal ectopic and triggered activity at the cellular level can be caused by early and delayed afterdepolarizations (EADs and DADs) and have been associated with reentry initiation and, in some instances, maintenance of AF [130]. EADs occur during phase 2 or 3 of action potential repolarization, while DADs occur after repolarization is complete or nearly complete. When afterdepolarizations are large enough to reach the threshold potential for activating an inward current, they can give rise to APs referred to as "triggered."

Voltage fluctuations during repolarization are the primary source of EADs. EADs can increase the dispersion of refractoriness by locally prolonging the APD, making the tissue susceptible to reentry. Arrhythmias caused by EADs have been shown not to be induced by overdrive or premature stimulation, but can be initiated by slowing the basic HR. During diastole, spontaneous release of Ca^{2+} generates DADs, which can lead to conduction block by locally depolarizing the RMP [131]. The amplitude of DADs increases with a decrease in the cycle length at which AP occurs until the afterdepolarization reaches the threshold to cause triggered activity. Triggered activity caused by DADs is more easily induced by rapid pacing than by a single premature stimulus.

Maintenance AF is likely sustained by reentrant activity, with irregular fibrillatory activity caused by the main reentrant wavefront breaking into multiple chaotic daughter wavelets due to inhomogeneity in atrial structure, refractoriness and CV [132]. Moreover, the mechanisms that sustain AF may change over time as the atria remodel electrically and structurally and AF progresses from paroxysmal to persistent and then permanent forms. Several studies have demonstrated more frequent reentrant drivers of AF in patients with longstanding arrhythmia, supporting this concept [133].

Functional reentry has been described by the leading circle model, in which circus movement of a unidirectional wavefront results in constant centripetal activation of the center of the circuit, rendering it continuously refractory. This refractory area then forms a functional barrier that can sustain reentry similar to a fixed anatomic barrier, such as a scar, as first described by Allessie et al. in 1977 [134]. Rotors, also known as spiral waves, are a specific type of functional reentry. Unlike circular waves, the wavefront of a rotor has a curved or spiral shape, and the wavefront and wavetail meet at a focal point called a phase singularity (PS). Rotors can theoretically and experimentally form when a wavefront interacts with a barrier, such as a scar or functional myocardial electrical inhomogeneity or anisotropy. When a wavefront passes through a barrier, it can bend and break into two daughter wavelets in a process known as vortex shedding (similarly to the flow of turbulent water around an obstacle in a river). In contrast to the leading circle model, the wavefront velocity in a rotor is not constant, and tissue at the core of a rotor is not truly refractory. This means that a reentrant circuit in the leading circle model must remain fixed in space because the center of the circuit is completely unexcitable, while a rotor is able to move through space, which affects rotor behavior and sustainability significantly. In some cases, rotors will anchor in place, often in areas around the pulmonary veins and in areas of heterogeneous atrial tissue, forming stable rotors [135]. Figure 1.10 illustrates the different mechanisms of AF triggering and maintenance.

Rapidly firing foci can not only initiate arrhythmia but also perpetuate it. In AF, both rapid focal firing and reentry may be operative [76]. In both scenarios, wave fronts are generated and may encounter refractory tissue, causing them to break up during propagation. The result is the irregular or fibrillatory conduction observed in AF [136].

In 1959, Moe et al. introduced the ‘multiple wavelet hypothesis’ of AF, which expanded the concept of reentry to include multiple simultaneous atrial reentrant circuits with separate initiating and sustaining factors. According to this theory, if a critical number of reentrant wavefronts existed in an appropriate atrial substrate (which depends on a combination of factors including atrial size and mass, CV and tissue refractory period), these wavefronts could continually re-excite the atria, resulting in chaotic, fibrillatory conduction [137]. Moe et al. showed that it was unlikely for a large number of simultaneous wavefronts to all die out simultaneously, making it probable that AF would perpetuate. However, if the number of simultaneous wavelets was small and/or below a critical value (between 15 and 30 in Moe’s computer model) [138], all reentrant wavefronts would be simultaneously extinguished, leading to AF termination [138].

Patients with psAF tend to exhibit more complex patterns of atrial activation. They have multiple wavelets propagating around multiple arcs of functional conduction block, which are predominantly oriented perpendicular to the tricuspid annulus, and areas of random and complete reentry. This suggests a critical role for tissue anisotropy in the pathogenesis of AF.

Modulators: role of the ANS in AF The pathophysiology of AF is complex and involves various modulators that act through multiple potential mechanisms (Figure 1.8).

Hypertension is the most common cardiovascular risk factor associated with AF, with hypertensive patients having a 1.7-fold higher risk of developing AF compared to normotensive individuals [140]. Additionally, interactions between AF and HF [141] and coronary artery disease [142] have been demonstrated. Diabetes mellitus is also an independent risk factor for AF, particularly in younger patients [143], with a prevalence of AF twice as high in patients with diabetes compared to those without [144]. Obstructive

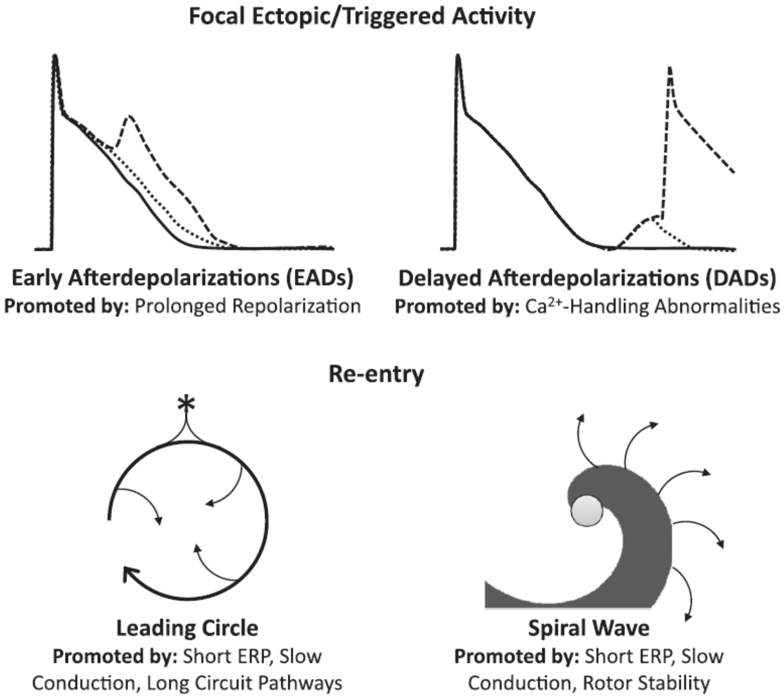

Figure 1.10: Major arrhythmogenic mechanisms include focal ectopic/triggered activity and re-entry. Focal ectopic/triggered activity is mediated by early and delayed afterdeplarizations, which are promoted by prolonged repolarization and Ca^{2+}-handling abnormalities, respectively. Conceptual interpretations of functional re-entry include leading circle and spiral wave. Extracted from [61].

sleep apnea (OSA), the most common form of sleep-disordered breathing, is highly associated with an increased risk of cardiovascular events and mortality [145]. A prospective analysis has shown that approximately 50% of AF patients had OSA compared with 32% of the control group [146]. Lifestyle choices such as obesity [147, 148], excessive alcohol consumption [149, 150] and vigorous physical activity mainly related to long-term or endurance sport participation [151] have also been shown to increase the risk of incident AF.

Furthermore, several studies have linked the onset and perpetuation of AF to the ANS [152–154]. Research has shown that fluctuations in both the sympathetic and parasympathetic branches of the ANS are involved in atrial tachyarrhythmias [155–159].

Activation of the adrenergic system can promote focal activity in various ways, including through EAD- or DAD-associated triggered activity. Also, α-adrenergic stimulation or

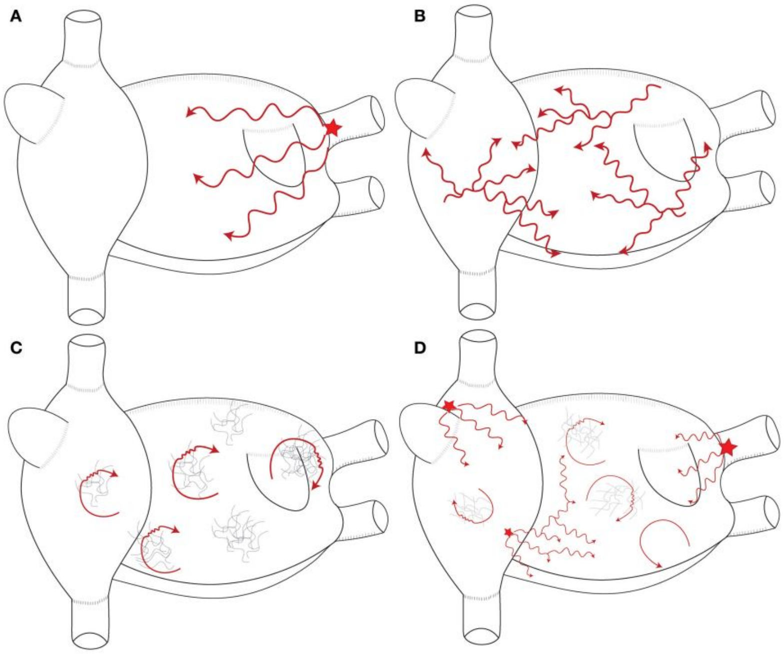

Figure 1.11: Schematic representation of the mechanisms maintaining AF. (A) Single stable focal or reentrant source (star) with fibrillatory conduction. (B) Multiple wavelets: multiple waves propagate randomly and give birth to new daughter wavelets. (C) Multiple reentries (red arrows) around areas of scar and fibrosis. (D) Combination of the different mechanisms that sustain AF in humans. These mechanisms are typically meandering and last for few consecutive beats. Extracted from [139].

increased funny current produced by β-adrenergic activation can result in a decrease in $\mathrm{I_{K1}}$ and enhanced automaticity [160].

Hyperactivity of the parasympathetic branch is specifically associated with the onset of pxAF [161]. It is believed that higher autonomic centers can inhibit GPs, and loss of this inhibitory tone may result in possible hyperactivity of GPs. This hyperactivity could contribute to increased susceptibility to AF [162–164], as autonomic signals from GPs to the heart have significant electrophysiological effects, including alterations in atrial refractory periods [165, 166] and the vulnerability of atrial tissue to AF induction [165, 167, 168].

The release of ACh from cholinergic neurons in atrial GPs can activate the $\mathrm{I_{KACh}}$ current, which facilitates the formation of reentries by shortening the wavelength of reentry (WL), defined as the distance traveled by the depolarization wave during the effective refractory period (ERP) [169] and estimated as the product of CV and ERP. In fact, ACh shortens APD and hyperpolarizes the RMP in a concentration-dependent manner. Hyperpolarization of the RMP leads to a reduction in the maximum upstroke velocity of the AP [169], which can also slow CV. A reduction in WL facilitates reentrant activity by decreasing the distance covered by the depolarization wave during the ERP.

It is important to note that the heterogeneous spatial distribution of parasympathetic nerve endings and the rapid breakdown of ACh by acetylcholinesterase at its release site make the effects of cholinergic stimulation on atrial refractoriness largely spatially heterogeneous. This heterogeneity further contributes to increased AF vulnerability, as shown in previous studies [121, 152, 170].

1.3.4 Therapies for arrhythmia treatment

Managing AF has been challenging due to its complex and not fully understood underlying mechanisms. AF increases the risk of stroke five-fold as the incomplete contractions of the atria may cause blood to coagulate and form clots. However, the risk of stroke in AF is not uniform and varies depending on various risk factors, including congestive HF, hypertension, age, diabetes mellitus, previous stroke or vascular disease, age between 65-75 years, and female sex. Hence, the administration of oral anticoagulants (OAC) for stroke prevention is recommended for patients with one or more of these risk factors.

After considering the use of OAC to prevent stroke, the next step involves managing symptoms (for symptomatic patients) and deciding between two options: rate control or rhythm control [171]. The choice between these treatments depends on various factors such as age, symptoms, medical history and overall health. Therefore, a personalized approach is necessary to achieve the best outcomes for AF patients.

Rate control Rate control consists in increasing the degree of block at the level of the AV node. There are two methods to achieve rate control.

The first method is based on using drugs to increase the degree of block that the AV node offers, thus decreasing the number of impulses that are conducted into the ventricles so as to maintain a HR of $\leq$110 bpm, unless symptoms necessitate stricter rate control [172]. These medications include β-blockers [3], calcium channel blockers [173], digoxin [174] or a combination of them. They effectively decrease the number of impulses that conduct down into the ventricles [173, 175, 176].

If medication fails, the second method consists in AV node ablation, with pacemaker implantation being attempted to control ventricular rate. This procedure has a low complication rate and low long-term mortality risk [177, 178]. However, it will render patients pacemaker-dependent for the rest of their lives.

Rhythm control The rhythm control strategy focuses on restoring and maintaining SR, especially in AF patients who remain symptomatic despite rate control therapy. This can be achieved through a combination of treatment approaches, including electrical or pharmacological cardioversion, antiarrhythmic drug therapy (ADT) and catheter ablation [179–184].

Pharmacological and electrical cardioversion Pharmacological cardioversion to SR is recommended for haemodynamically stable patients. While it is less effective than electrical cardioversion, restoring SR in approximately 60-80% of patients with recent-onset AF versus the 80%-90% restoration rate of electrical cardioversion, it does not require sedation. Flecainide, propafenone, vernakalant and amiodarone are some examples of effective antiarrhythmic drugs for pharmacological cardioversion [185–188]. For severely haemodynamically compromised patients, synchronized direct current electrical cardioversion is the method of choice to quickly and effectively convert AF to SR [3]. The standard device for electrical cardioversion is the biphasic defibrillator with anterior-posterior electrode positions for more effective rhythm restoration [179, 189].

Antiarrhythmic drugs The goal of ADT is to reduce AF-related symptoms [3]. While clinically successful, ADT may only reduce rather than eliminate AF. Compared to no therapy, ADT approximately doubles SR maintenance [190], but it is less effective than other therapies like AF catheter ablation [191, 192]. To reduce the risk of side effects, such as adverse events, proarrhythmic events and even death, a shorter duration of ADT is preferred [190, 193, 194]. For example, short-term treatment with flecainide for four weeks was well-tolerated and prevented up to 80% of AF recurrences when compared to long-term treatment [195]. The main ADT available to prevent AF include amiodarone, dronedarone, flecainide, sotalol and dofetilide [190].

There are three classes of antiarrhythmic drugs: Class I, II and III. Class I antiarrhythmics block the sodium channels in the heart, which slows down the conduction of electrical impulses and reduces the excitability of the heart. Sodium channel blockade can terminate AF and prevent its re-induction by slowing conduction and making reentry unfavorable. Proposed mechanisms of AF rotor termination with sodium channel blockade include an increase in rotor size so that the rotor extinguishes at tissue boundaries, reduced anchoring of the rotor which promotes meander of the core and eventual termination, reduced rotational frequency, and a reduction in the number of daughter wavelets that can generate new rotors to sustain AF [196]. Class II antiarrhythmics are β-blockers, which block the β-receptors in the heart and reduce the sympathetic tone. This slows down the HR and reduces the force of contraction of the heart. Examples of Class II antiarrhythmics include propranolol, metoprolol and atenolol. Class III antiarrhythmics block the potassium channels that drive AP repolarization, leading to an increase in APD and WL [197, 198]. Examples of Class III antiarrhythmics include amiodarone, sotalol and dofetilide.

Catheter ablation Over the years, catheter ablation has become a common treatment for patients with AF [181]. This procedure is particularly beneficial for patients who have not responded well to ADT or those who experience severe symptoms [3, 181, 199].

The first catheter ablation procedure used to treat AF was based on the surgical Maze procedure [200, 201]. This involved creating multiple linear lesions in the RA using radiofrequency (RF) energy. The Maze procedure aimed to compartmentalize the atria by creating scar tissue on the heart's surface to eliminate reentrant wavelets and restore SR or an atrial rhythm within the atrial myocardium [200].

Since the pioneering work of Haïssaguerre and colleagues [202], which showed that a rapidly firing focus in or close to the PVs can be a trigger for pxAF, PVI has become the most widely used ablation approach for treating AF [203]. PVI can be achieved by creating lesions around the pulmonary veins using RF ablation, cryoballoon ablation or the relatively new electroporation ablation technique.

RF point-by-point myocardial ablation is a thermal-mediated method that creates tissue necrosis and ablation lesions by generating localized heat. Lesions are created in a point-by-point manner, typically guided by a 3D electro-anatomical mapping system [204]. Factors that affect lesion size include electrode size, temperature, electrode-tissue contact, power and duration of RF energy delivery [205, 206]. To improve catheter-tissue contact, catheters have been developed that can measure contact force between the catheter tip and tissue during ablation [207, 208]. Despite being the most commonly applied technique for achieving PVI, point-by-point RF ablation remains technically challenging, even in experienced centers.

Multielectrode circumferential RF ablation catheters were designed to simplify and expedite PVI procedures. Currently available multielectrode PV ablation catheters have nine to ten electrodes arranged in a circular configuration when deployed. These catheters can be guided to the PV ostium by fluoroscopy to allow for both mapping and ablation. The circumferential placement of the electrodes allows for the creation of a circular ablation lesion at the PV ostium after multiple applications, eventually resulting in PVI.

In cryoballoon ablation, PVI is achieved by freezing tissue using a pressurized balloon that occludes the PV ostium and injecting liquid nitrous oxide as refrigerant into the balloon. Operators use fluoroscopic guidance to place the device at each pulmonary vein antrum. Freezing tissue below -40°C causes irreversible cell death due to the freezing of intracellular water, resulting in irreversible disruption of organelles and cell membranes [209].

The balloon design allows circumferential ablation in a single shot and, while cryoballoon procedures have shown reduced hospitalizations and lower complication rates than RF ablation, both types of energy have similar AF termination and maintenance outcomes [210, 211]. The most commonly reported complication in cryoballoon ablation is phrenic nerve injury with a reported incidence between 2 and 5%, fortunately often of temporary nature [212, 213].

Irreversible electroporation (IRE), also referred to as pulsed field ablation, is a novel nonthermal ablative modality in which ultrarapid (< 1 s) electrical pulses are applied to target tissue. This approach destabilizes cell membranes by forming irreversible nanoscale pores and leakage of cell contents, culminating in cell apoptosis (programmed cell death) [214]. Importantly, various tissues have specific characteristic thresholds to field strengths that induce necrosis by electroporation. Myocardial tissue has the lowest threshold and is thus the most sensitive tissue for irreversible electroporation. Therefore, unlike any other energy source, IRE spares collateral structures such as the esophagus, arteries and nerves while effectively ablating myocardial tissue.

Potential benefits of IRE include the tissue selectivity of the ablation and the rapid delivery of energy, which could result in shorter procedure times. The first-in-human experience with IRE ablation for PVI in patients with AF was recently reported [215]. The feasibility of achieving acute PVI by IRE ablation was shown using different catheter designs, including a 14-polar circular catheter [216] and an over-the-wire catheter with a deployable basket containing 20 separate electrodes [217].

IRE depends on current density, while RF tissue heating depends on the square of current density and therefore decreases with the fourth power of distance with unipolar RF ablation. These differences suggest that circular electroporation application may penetrate deeper and create larger lesions than unipolar RF application. In addition, the contact between the electrode and the tissue is less critical in electroporation since the current density decays linearly, whereas the direct resistive RF heating decays with the fourth power.

Figure 1.12 depicts the PVI procedures using cryoballoon ablation and RF ablation.

Despite being the most common ablation procedure to treat AF, PVI has unsatisfactory long-term results, particularly for psAF [218]. Two potential explanations could clarify this phenomenon. First, recurrent AF may occur due to PV reconnection, which means that sustained PVI is not achieved. Second, failure to eliminate the trigger (or substrate) in standard PVI may contribute to the high recurrence rate after ablation, with the trigger possibly being the GPs surrounding the PVs. Autonomic modification or denervation might contribute to the effectiveness of standard PV-directed ablation because the linear lesions from this procedure run through areas with high GP concentrations [219].

GP ablation has been associated with a decreased risk of AF recurrence [23, 25, 220–226], either as an addition to PVI [23, 24, 26, 227–230] or as a stand-alone procedure [26, 231]. Although the success rates in eliminating AF are similar for PVI and GP ablation individually, combining the two has been shown to have a significantly higher success rate [26, 47, 227]. The hitherto largest randomized, multicenter trial reported by Katritsis et al. [227] enrolled 242 patients with pxAF and compared the efficacy of PVI, GP ablation alone and PVI followed by GP ablation. This study found that freedom from AF was achieved in 56%, 48%, and 74% of patients after 2 years of follow-up, respectively.

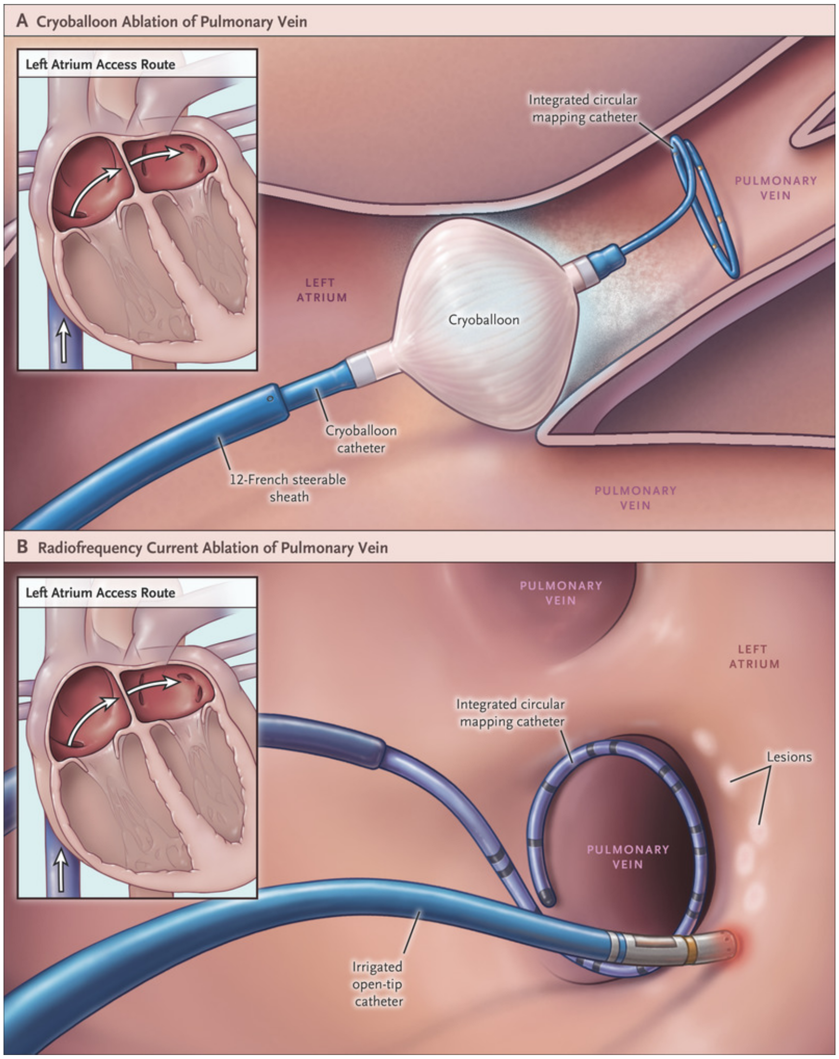

Figure 1.12: PVI procedures using cryoballoon ablation (top) and RF ablation (bottom). Extracted from [213].

1.3.5 Unmet needs

Understanding the electrophysiological mechanisms that initiate and sustain AF is crucial for developing safer and more effective therapies. The role of the ICANS in atrial excitability is complex and its understanding is currently incomplete. Computational simulation is a powerful tool to investigate the mechanisms by which the ANS can influence the initiation and development of AF. It enables reproducible control of the tested conditions, conduction of virtual interventions not feasible clinically or experimentally and in-depth mechanistic research.

ADT and catheter ablation are the main treatments for pxAF, but the short- and long-term clinical efficacy of these treatments remains controversial. Studies have shown that the control rate of AF recurrence at 6 to 12 months is only about 46% [232–235] and patients often discontinue therapy due to side effects [236–238]. Despite recent advancements in AF management, current pharmacological therapies still present limitations in terms of efficacy and side effects and there is an unmet need for safe and effective ADT for AF [239].

Class III antiarrhythmic drugs that block potassium channels can prolong the APD and ERP in both the atria and the ventricles. They can be beneficial in treating AF by preventing reentry and restoring normal SR. However, they can also have harmful effects on the ventricles. One of the main concerns is their potential to cause torsades de pointes, a type of polymorphic ventricular tachycardia that can degenerate into ventricular fibrillation and cause sudden cardiac death. Prolonged ventricular repolarization can lead to EAD, which can trigger torsades de pointes in susceptible individuals. To minimize potentially harmful side effects on the ventricles, potassium channels primarily expressed in the atria are being considered as targets for AF therapy and new targets are continuously sought.

PVI has become a common treatment for AF patients over the decades [203]. However, the long-term efficacy of catheter ablation reported in AF single-procedures does not exceed 70% [240]. Adding GP ablation to PVI has shown some degree of improvement in AF recurrence outcomes. Po et al [26] showed that the combination of GP ablation with PV isolation was effective in more than 80% of patients at a long-term follow-up. However, the validity of existing methods for the selective location of GP clusters is in question. The significant heterogeneity of such location can be inferred from the complex anatomy of the ANS, which is why various attempts have been made in the literature to simplify the location of cardiac GPs. Many authors have adopted a selective approach characterized by RF applications in atrial areas where vagal reaction could be elicited during high-frequency stimulation (HFS). An alternative method is the anatomic approach, which is characterized by an extended RF ablation of the GPs based on anatomic knowledge of cardiac ganglia topography. This method, mainly performed in the LA and in patients with pxAF, resulted in higher effectiveness than the selective approach in some investigations [27]. The same approach was not beneficial when applied to ablate longstanding psAF.

1.4 Objectives and outline of the thesis

The research in this thesis aims, on the one hand, to shed light on the role of the ANS in the onset and maintenance of AF, and on the other hand, to evaluate therapies for AF treatment acting on autonomic neural components, either individually or in combination with other therapies targeting ion channels of atrial cells.

To achieve these objectives, realistic computational models of human atria have been developed, which incorporate descriptions of sympathetic and parasympathetic modulation of atrial electrical activity. These models have been used to elucidate the role of neural stimuli in the onset and maintenance of AF. In addition, descriptions of the effects of antiarrhythmic drugs that act on ion channels have been included. The efficacy of autonomic modulation, both with and without the action of these drugs, to stop AF in humans has been analyzed.

1.4.1 Chapter 2

In this chapter, general methods used in the following chapters are described. In particular, we present the computational models, from cellular to whole atrial level, employed to simulate human atrial electrophysiology in SR and AF.

1.4.2 Chapter 3

In this chapter, we used computational modeling and simulation to investigate cardiorespiratory interactions during AF. In particular, we evaluated the role of the spatiotemporal release pattern of ACh, considered to temporally vary in phase with inspiration and expiration, in the modulation of the f-wave frequency. The computational results were compared with results obtained from the analysis of clinical ECGs.

The following publications are based on the results described in this chapter:

- **C. Celotto**, C. Sánchez, K. A. Mountris, P. Laguna, E. Pueyo, Relationship between Atrial Oscillatory Acetylcholine Release Pattern and f-wave Frequency Modulation: a Computational and Experimental Study. *International Conference on Computing in Cardiology (CinC)*, 2020, article no. 303.
- **C. Celotto**, C. Sánchez, M. Abdollahpur, F. Sandberg, J.F. Rodríguez, P. Laguna, E. Pueyo, Effects of Acetylcholine Release Spatial Distribution on the Frequency of Atrial Reentrant Circuits: a Computational Study. *International Conference on Computing in Cardiology (CinC)*, 2022, article no. 396.
- **C. Celotto**, C. Sánchez, M. Abdollahpur, F. Sandberg, J.F. Rodríguez, P. Laguna, E. Pueyo, The Frequency of Atrial Fibrillatory Waves is Modulated by the Spatiotemporal Pattern of Acetylcholine Release: a 3D Computational Study, *Frontiers in Physiology*, *Under review*.

1.4.3 Chapter 4

In this chapter, we aimed to assess the relationship between changes in autonomic balance and in atrial fibrillatory rate (AFR) oscillations induced by head-up and head-down tilt test. We used computational modeling and simulation to investigate the effects of the combination of different levels of parasympathetic and sympathetic stimulation on AFR.

The following publications are based on the results described in this chapter:

- **C. Celotto**, C. Sánchez, M. Abdollahpur, F. Sandberg, P. Laguna, E. Pueyo, Dependence of Atrial Fibrillatory Rate Variations Induced by Head-Up/Down Tilt-Test on

Autonomic Action. *International Conference on Computing in Cardiology (CinC)*, 2023, *Submitted.*

- **C. Celotto***, M. Abdollahpur*, C. Sánchez, P. Laguna, E. Pueyo, F. Sandberg. Tilt Induced changes in f-wave characteristics during atrial fibrillation: an experimental and computational investigation. *In preparation*. * Joint first authorship.

1.4.4 Chapter 5

In this chapter, we used computational simulation to develop a method to locate sites of atrial parasympathetic innervation within atrial GPs, based on measurements from a EGM multielectrode grid. This approach, developed to aid cardioneuroablation procedures overcoming the limitations of the current techniques (HFS and anathomical), is expected to provide information not only on the approximate location but also on the dimensions of those sites.

The following publications are based on the research described in this chapter:

- **C. Celotto**, C. Sánchez, P. Laguna, E. Pueyo, Location of Parasympathetic Innervation Regions From Electrograms to Guide Atrial Fibrillation Ablation Therapy: An *in silico* Modeling Study. *Frontiers in Physiology*, 2021;12:674197.

1.4.5 Chapter 6

In this chapter, we assessed how the combination of β-adrenergic stimulation and SK channel block (SKb) could counteract alterations in atrial electrical activity caused by cholinergic stimulation. Our hypothesis was that by administering Iso and SKb at the same time, we could extend the APD shortening induced by ACh and return it to its original state. We conducted numerical simulations based on human atrial cellular models and 2D tissue models to analyze the effects of adrenergic and cholinergic stimulation and of SKb, both transiently and at steady-state.

The following publications are based on the research described in this chapter:

- **C. Celotto**, C. Sánchez, P. Laguna, E. Pueyo, Calcium-Activated Potassium Channel Inhibition in Autonomically Stimulated Human Atrial Myocytes. *International Conference on Computing in Cardiology (CinC)*, 2019, article no. 334.
- **C. Celotto**, C. Sánchez, K. A. Mountris, P. Laguna, E. Pueyo, SK Channel Block and Adrenergic Stimulation Counteract Acetylcholine-Induced Arrhythmogenic Effects in Human Atria. *Annual International Conference of the IEEE Engineering in Medicine and Biology Society (EMBC)*, 2020.
- **C. Celotto**, C. Sánchez, K. A. Mountris, P. Laguna, E. Pueyo, Rotor Termination in Cholinergic Paroxysmal Atrial Fibrillation by Small-Conductance Calcium-Activated K + Channels Inhibition and Isoproterenol: a Computational Study. *International Conference on Computing in Cardiology (CinC)*, 2021, article no. 166.
- **C. Celotto**, C. Sánchez, K. A. Mountris, P. Laguna, E. Pueyo, Steady-state and transient effects of SK channel block and adrenergic stimulation to counteract acetylcholine-induced arrhythmogenic effects in the human atria: A computational study. *Computers in Biology and Medicine*, 2023;157:106719.

1.4.6 Chapter 7

This chapter contains the main achievements, limitations, possible future work and the main conclusions of this PhD thesis.

Chapter 2

General methods

In this chapter, general methods used in following chapters are presented. The section includes the description of the computational electrophysiological models later employed to perform AF simulations. All the described models and simulation methods will be further discussed in each chapter with respect to the specific applications.

Computational models have become powerful tools to complement *in vivo* and *in vitro* research. They do not have ethical restrictions and can test almost unlimited hypotheses, including those that may not be feasible in traditional studies, in a time- and cost-effective manner. These models can be used to model physiological processes and diseases, to develop drugs, to study the mode of action and identify adverse cardiac effects and to enhance the understanding of AF mechanisms and discover potential pharmacological targets.

2.1 *In silico* models of cellular electrical excitability

In 1952, Alan L. Hodgkin and Andrew F. Huxley proposed the first computational model of an excitable cell, which described the electrical activity of the squid giant axon [241]. They formulated the equations of the temporal evolution of the transmembrane voltage and the ionic currents based on the selective permeability of the cellular membrane to ions in a voltage and time dependent manner. Particularly, the cell was described as an electrical circuit with the cell membrane acting as a capacitor and ion channels modeled by resistors and voltage sources. Figure 2.1 shows the equivalent circuit of the Hodgkin-Huxley model

(HH), which comprises four ionic currents: a sodium current, $\mathrm{I_{Na}}$, a potassium current, $\mathrm{I_K}$, a capacitive current and a leak current, $\mathrm{I_L}$. The leak current refers to the current generated by other ions.

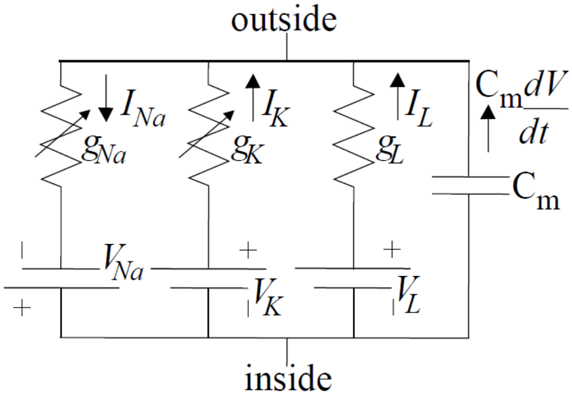

Figure 2.1: The equivalent circuit of the Hodgkin-Huxley model representing the cell, with voltage sources ($\mathrm{V_{Na}}$, $\mathrm{V_K}$, $\mathrm{V_L}$), membrane capacitance ($\mathrm{C_m}$) and three currents, namely sodium ($\mathrm{g_{Na}}$ conductance), potassium ($\mathrm{g_K}$ conductance) and leak ($\mathrm{g_L}$ conductance) currents. Adapted from [242].

Ionic movements across the cell membrane are governed by electrical and diffusion forces. Each ionic species is in equilibrium when these two forces are equal in magnitude but opposite in sign. The equilibrium potential of an ion k is known as the Nernst potential and is defined as follows:

$$\mathrm{E_k} = -\frac{\mathrm{R\,T}}{\mathrm{z_k F}} \log\left(\frac{[\mathrm{k}]_\mathrm{i}}{[\mathrm{k}]_\mathrm{o}}\right), \tag{2.1}$$

where $\mathrm{E_k}$ is the Nernst potential for ion k, T is the absolute temperature, R is the ideal gas constant, $\mathrm{z_k}$ is the valence of ion k, F is Faraday's constant and $[\mathrm{k}]_\mathrm{i}$ and $[\mathrm{k}]_\mathrm{o}$ are the intracellular and extracellular concentrations of ion k, respectively.

Using Ohm's law, the conductance per unit area, $\mathrm{g_k}$, for a specific ion k, can be computed as:

$$\mathrm{g_k} = \frac{\mathrm{I_k}}{\mathrm{V_m} - \mathrm{E_k}}, \tag{2.2}$$

where $\mathrm{I_k}$ is the electric current carried by ion k per unit area, $\mathrm{V_m}$ is the transmembrane potential and $\mathrm{E_k}$ is the Nernst potential for ion k.

Considering that the ion channels are selective for a particular type of ion and that the ions pass through the specific channel only when the channel is open, the conductance $\mathrm{g_k}$

is computed as:

$$\mathrm{g_k = G_{k,max} p_{k,o}} \tag{2.3}$$

where $\mathrm{G_{k,max}}$ is the maximum current when all channels are open and $\mathrm{p_{k,o}}$ is the proportion of k channels that are open, with this proportion being dependent on the transmembrane potential.

In the HH model, each of the gates can be in the open or the closed states and transitions between these two states along time, with the opening and closing transition rates being dependent on transmembrane voltage. For the $\mathrm{Na^+}$ channels, Hodgkin and Huxley defined three activation gates (named m gates), which became open when voltage increased and remained closed during the resting AP phase, and one inactivation gate (named h gate) that was open during the resting AP phase and became closed when transmembrane potential increased. In the HH model, $\mathrm{K^+}$ channels were composed of four activation gates (named n gates). Assuming that each of the gates open and close independently of the others, the proportion of open channels is equal to the product of the proportions of open gates for the different types of gates the channel is composed of [151]. For $\mathrm{Na^+}$ channels this can be written as:

$$\mathrm{p_{Na,o} = m^3 h}, \tag{2.4}$$

where m represents the probability that any of the three activation gating subunits of the channel is open, and h represents the probability that the inactivation gate is open. For $\mathrm{K^+}$ channels:

$$\mathrm{p_{K,o} = n^4}, \tag{2.5}$$

where n represents the probability that any of the four activation gating subunits of the channel is open.

Therefore, $\mathrm{I_{Na}}$ and $\mathrm{I_K}$ can be described by the following equations:

$$\mathrm{I_{Na} = g_{Na}(V_m - E_{Na}) = G_{Na_{max}} m^3 h (V_m - E_{Na})}, \tag{2.6}$$

$$\mathrm{I_K = g_K(V_m - E_k) = G_{K_{max}} n^4 (V_m - E_k)}, \tag{2.7}$$

where $\mathrm{G_{Na_{max}}}$ and $\mathrm{G_{K_{max}}}$ are the maximal conductances of sodium and potassium channels, respectively. The variables m, h and n are the gates of the ion channels. The ionic conductance is equal to the maximal ionic conductance when all the gates are in the open state for a specific ion channel.

The opening and closing of the gate variables m, h and n are regulated by the following ordinary differential equation (ODE):

$$\frac{\mathrm{dx}}{\mathrm{dt}} = \alpha_{\mathrm{x}}(1-\mathrm{x}) - \beta_{\mathrm{x}}\mathrm{x}, \tag{2.8}$$

where x refers to the m, h or n gates of ion channels and α_x and β_x are transition rates from closed to open state and from open to closed state, respectively.

Therefore, the total current across the cell membrane can be computed as the sum of all ionic currents and the capacitance current as follows:

$$\mathrm{I_{tot}} = \mathrm{C_m}\frac{\mathrm{dV_m}}{\mathrm{dt}} + \mathrm{I_{Na}} + \mathrm{I_K} + \mathrm{I_L}. \tag{2.9}$$

2.2 *In silico* models of human atrial cellular electrophysiology

Since the original HH model, the development of computational models has been driven by the increasing computational power available to researchers at decreasing costs [243]. Models for cardiac cellular electrophysiology and ion dynamics have been developed for over five decades. The first cellular models specific of the atria were published by Courtemanche et al. in 1998 [244] and Nygren et al. in 1998 [245]. These model lineages have been retroactively extended with novel features. Also, new models have been introduced, as shown in Figure 2.2.

Currently, there are three families of *in silico* human atrial cell models [246]: the Nygren-Maleckar-Koivumäki-Skibsbye [245, 247–249], the Courtemanche [244], and the Grandi [38] models. These models were built based on different sets of human and animal experimental data and rely on slightly different formulations of ionic currents, pumps and exchangers. There are substantial differences among these models in terms of AP and calcium transient morphologies and of their rate adaptation properties [246]. Furthermore, some of these models include ionic currents not incorporated in the other models [250]. An advantage of the diversity of existing cardiac computational models is the larger representation of data responses when modeling pharmacodynamics or other effects, as the outcome of *in silico* interventions varies between different models and could better represent the extensive variability found experimentally.

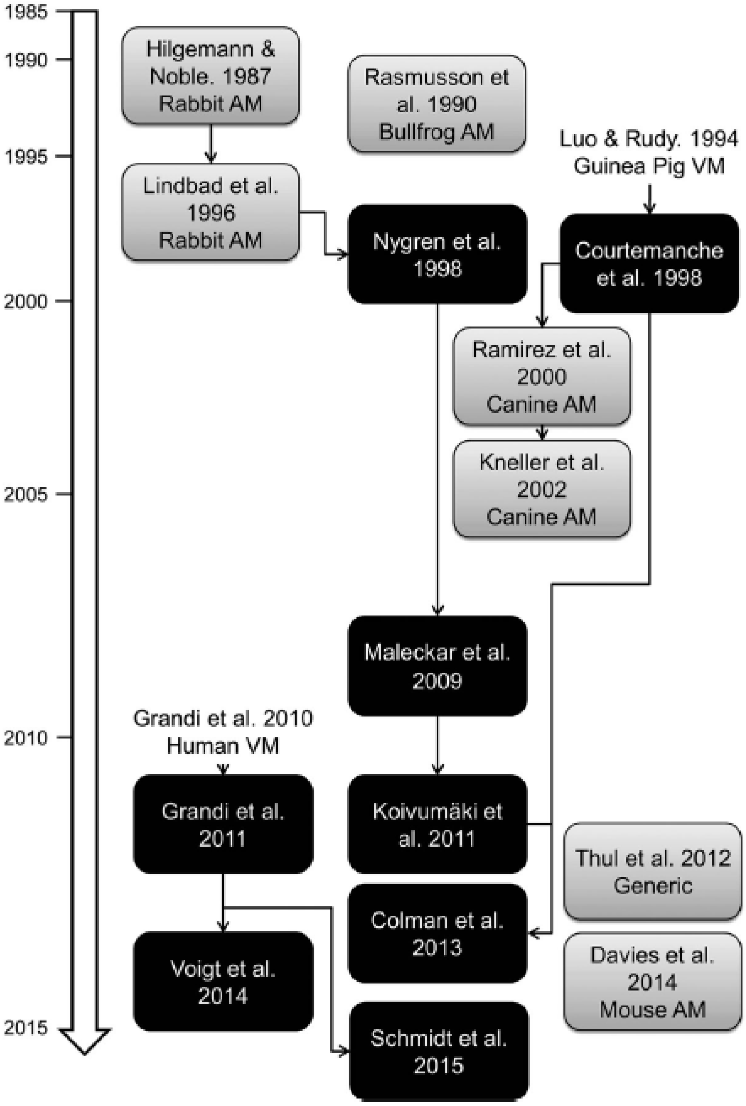

Figure 2.2: Evolution of the development of atrial cardiomyocyte models and their interdependencies. Extracted from [251].

As a basis for our research, we took three previously published computational models of human atrial cellular electrophysiology. Those models differ in AP morphology and rate adaptation properties, which may reflect the inherent diversity in cell phenotypes of the human atria. To test the model independence of our findings, we selected a model of each of the three main types of available atrial cellular models in the literature. Specifically, we used the Courtemanche ($\mathcal{C}$) [244], Skibsbye ($\mathcal{S}$) [249] and Grandi ($\mathcal{G}$) [38] human atrial AP models. For each of the three models, the effects of cholinergic stimulation by ACh, adrenergic stimulation by the non-specific β-adrenergic agonist isoproterenol (Iso) and the formulation of the $\mathrm{I_{SK}}$ current were incorporated, as described in the following sections and summarized in Table 2.1.

2.2.1 Courtemanche model

The Courtemanche, $\mathcal{C}$, model is based on the guinea pig ventricular model of Luo and Rudy [252]. It is a common-pool model, approximating the cytosol as a homogeneous compartment without considering local changes in intracellular ion concentrations. HH ion channel formulations are used. Human experimental data was used to model the fast $\mathrm{Na^+}$ current $\mathrm{I_{Na}}$, the transient outward potassium current $\mathrm{I_{to}}$, the ultrarapid delayed rectifier $\mathrm{K^+}$ current $\mathrm{I_{Kur}}$, the rapid and slow delayed rectifier $\mathrm{K^+}$ currents $\mathrm{I_{Kr}}$ and $\mathrm{I_{Ks}}$, the inward rectifier $\mathrm{K^+}$ current $\mathrm{I_{K1}}$ and the L-type $\mathrm{Ca^{2+}}$ current $\mathrm{I_{CaL}}$. The $\mathrm{Na^+}$ and $\mathrm{Ca^{2+}}$ background currents $\mathrm{I_{bNa}}$ and I_{bCa}, the $\mathrm{Na^+/Ca^{2+}}$ exchange current $\mathrm{I_{NaCa}}$, the $\mathrm{Na^+/K^+}$ pump current $\mathrm{I_{NaK}}$, the sarcolemmal $\mathrm{Ca^{2+}}$ pump current $\mathrm{I_{PMCA}}$ and the intracellular calcium handling were based on a previous (canine) model [253]. The sarcoplasmic reticulum is divided into two compartments, one for uptake and one for release of $\mathrm{Ca^{2+}}$. The $\mathrm{Ca^{2+}}$ uptake current $\mathrm{I_{up}}$ pumps $\mathrm{Ca^{2+}}$ into the sarcoplasmic reticulum and a leak current $\mathrm{I_{leak}}$ allows flow back into the intracellular space. The transfer current $\mathrm{I_{tr}}$ transports $\mathrm{Ca^{2+}}$ to the release compartment, where $\mathrm{Ca^{2+}}$ stores are emptied into the intracellular space by the $\mathrm{Ca^{2+}}$ release current $\mathrm{I_{rel}}$. Regarding intracellular $\mathrm{Ca^{2+}}$ buffers, there are formulations for troponin, calmodulin and calsequestrin. The AP shows a pronounced spike-and-dome morphology. The original application of the $\mathcal{C}$ model was the investigation of the rate dependence of the AP and its response to inhibition of $\mathrm{I_{CaL}}$ and $\mathrm{I_{NaCa}}$.

In this thesis, we introduced a new formulation for the $\mathrm{I_{SK}}$ current into the $\mathcal{C}$ model. The current formulation was as in Engel et al [254], with adjustments made to match the experimental $\mathrm{I_{SK}}$ characteristics found in the literature [121, 255]. The $\mathrm{I_{SK}}$ current was defined as:

$$\mathrm{I_{SK}(t) = g_{SK} f^2 \left(\left[Ca^{2+}\right]_i \right) \left(V_m(t) - E_k(t) \right)}, \tag{2.10}$$

where $\mathrm{g_{SK}}$ is the conductance of $\mathrm{I_{SK}}$, $\mathrm{E_k}$ is the Nernst potential for potassium and $\mathrm{f\left([Ca^{2+}]_i\right)}$ is a gating variable that depends on $\mathrm{[Ca^{2+}]_i}$. $\mathrm{f\left([Ca^{2+}]_i\right)}$ satisfies the equation:

$$\frac{\mathrm{df\left([Ca^{2+}]_i\right)}}{\mathrm{dt}} = \frac{\mathrm{f_\infty\left([Ca^{2+}]_i\right) - f\left([Ca^{2+}]_i\right)}}{\tau_\mathrm{f}} \tag{2.11}$$

where τ_f=3 ms is the time constant associated with the activation gate f. The steady-state value of gate f is:

$$\mathrm{f_\infty\left(\left[Ca^{2+}\right]_i\right) = \frac{\left([Ca^{2+}]_i/0.0025\right)^q}{K_{SK} + \left([Ca^{2+}]_i/0.0025\right)^q}} \tag{2.12}$$

where the constant $\mathrm{K_{SK}}$ is the half-activation calcium concentration and the Hill coefficient q account for the cooperativity effect. In the literature, a disparity of values for the $\mathrm{I_{SK}}$ current parameters exists. In the Engel model, $\mathrm{K_{SK}}$=1 μM and q=2 were used. Since the model by Engel et al. was built for neurons and not for cardiac cells, we adapted the conductance $\mathrm{g_{SK}}$ so that the contribution of the $\mathrm{I_{SK}}$ current was consistent with the results reported from experiments in isolated atrial myocytes and atrial trabeculae strips from patients in SR, where SK channel block increased $\mathrm{APD_{90}}$ by around 20% [121, 256].

After adding the $\mathrm{I_{SK}}$ current to the $\mathcal{C}$ model, we compared the ionic current traces in the original and modified model. The results are presented in Figure 2.3. We found that most of the currents were only slightly impacted by the addition of the SK current, with the exception of $\mathrm{I_{Kr}}$, which showed a reduction in peak value of 15%, and of $\mathrm{I_{Ks}}$, which showed a peak reduction of 35%. Nonetheless, the values of these two currents in the original and modified models were relatively close, especially compared to the wide range of physiological variability reported in experiments, up to 45% for $\mathrm{I_{Kr}}$ and 72% for $\mathrm{I_{Ks}}$ [257] (Figure 2.4). These percentages were computed referring to the 0 mV voltage, corresponding to the transmembrane voltage at the peak of the currents I_{Ks} and I_{Kr}. From Figure 2.4, the percentage value was obtained by dividing the standard deviation by the mean and multiplying the result by 100. The experimental variability would indeed be expected to be higher, as one standard deviation around the mean would only cover 68% of the observations if the data followed a Gaussian distribution. Based on these results, we concluded that the modified model was still within the physiological range of available experiments and, thus, it was not necessary to perform any reparametrization of the cellular model.

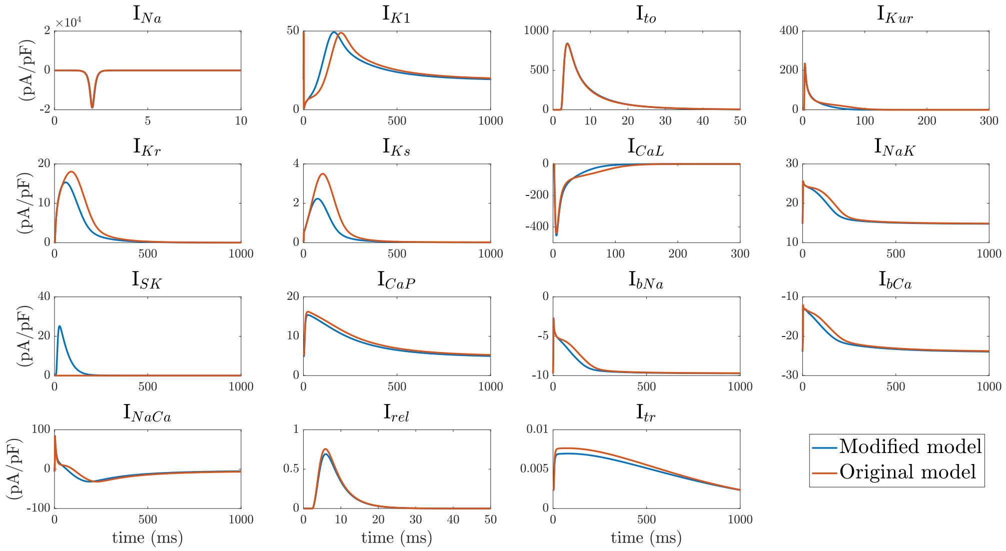

Figure 2.3: Representation of the individual currents in the $\mathcal{C}$ model before (red) and after (blue) the introduction of the I_{SK} current.

The parasympathetic stimulation effects were described by introducing the ACh-activated potassium current I_{KACh} in the models to account for the activation of G protein-activated inwardly rectifying potassium channels induced by ACh. The I_{KACh} formulation was based on the study by Kneller et al. [196] and subsquently updated as proposed by Bayer et al. [258]. The equation is reported below:

$$\mathrm{I_{KACh}(t)} = \left(\frac{10.0}{1+\frac{9.14}{(\mathrm{ACh(t)}10^{-1})^{0.478}}}\right)\left(0.05+\frac{5.0}{1+\mathrm{e}^{\frac{\mathrm{V_m(t)}+85.0}{5.0}}}\right)(\mathrm{V_m(t)}-\mathrm{E_K(t)}) \quad (2.13)$$

where $\mathrm{ACh(t)}$ is the ACh concentration at time “t” expressed in μM, $\mathrm{V_m(t)}$ is the mem-

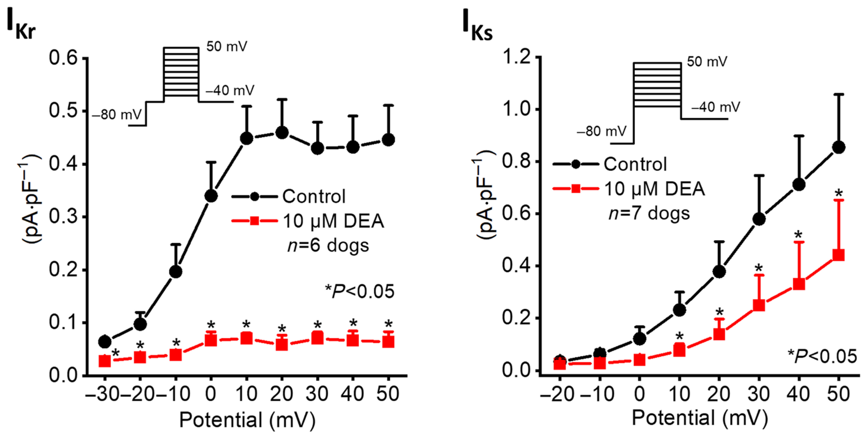

Figure 2.4: IV curves for $\mathrm{I_{Ks}}$ and $\mathrm{I_{Kr}}$ adapted from Kohajda et al. [257]. Data are expressed as mean ± SEM. Values obtained from dog myocytes. Here we are interested in the control black curves representing control conditions.

brane potential and $\mathrm{E_K(t)}$ is the Nernst potential for potassium.

Sympathetic stimulation affects atrial myocytes by activating the β-adrenergic signaling cascade, which triggers the phosphorylation of various cellular substrates by PKA. In the $\mathcal{C}$ model, the effects of β-adrenergic stimulation were modeled as proposed by González de la Fuente et al. [259]. This involved modeling the increases in the maximal conductances of $\mathrm{I_{CaL}}$ and $\mathrm{I_{Ks}}$ and the decrease in the maximal conductance of $\mathrm{I_{to}}$ following the experimentally reported concentration-dependent conductance modulation curves [259]. At an Iso concentration of 1 μM, the maximal conductances of $\mathrm{I_{CaL}}$ and $\mathrm{I_{Ks}}$ were increased by 160.6% and 65.7%, respectively, while the maximal conductance of $\mathrm{I_{to}}$ was reduced by 18.6%.

2.2.2 Grandi model

The Grandi, $\mathcal{G}$ model is based on a human ventricular model from the same research group [260], which in turn relies on the rabbit ventricular model of Shannon et al. [261]. The majority of the current formulations are similar to those found in the human ventricular model but with appropriate adaptation to human atrial data. It is a common-pool model of the atrial cardiomyocyte with detailed validation of rate-dependent $\mathrm{Ca^{2+}}$ handling based on experimental data obtained in isolated human atrial cardiomyocytes at physiological temperature [38].

In contrast to the $\mathcal{C}$ model, the concentration of $\mathrm{Cl^-}$, a background $\mathrm{Cl^-}$ current $\mathrm{I_{bCl}}$ and a $\mathrm{Ca^{2+}}$-activated $\mathrm{Cl^-}$ current $\mathrm{I_{Cl}(Ca)}$ are also taken into account. Furthermore, a plateau $\mathrm{K^+}$ channel $\mathrm{I_{Kp}}$ is included. For the $\mathrm{I_{to}}$ and $\mathrm{I_{Kur}}$ currents, slightly adapted formulations of the Malekar model were employed [247]. The intracellular $\mathrm{Ca^{2+}}$ handling is identical to the rabbit ventricular model of Shannon et al. [261] and includes a subsarcolemmal space and a junctional cleft between the $\mathrm{I_{CaL}}$ channels and the release unit. In this model, repolarization occurs in two distinct phases, resulting in a longer APD. This model was originally developed to analyze the differences between human atrial and ventricular electrophysiology with a focus on $\mathrm{Ca^{2+}}$ handling.

As we did for the $\mathcal{C}$ model, we introduced in the $\mathcal{G}$ model a new formulation of the $\mathrm{I_{SK}}$ current based on the formulations by Peñaranda et al. [262], which we chose based on experimental evidence [255]. The current was written as:

$$\mathrm{I_{SK}} = \mathrm{g_{SK}} \mathrm{f}\left(\left[\mathrm{Ca^{2+}}\right]_{\mathrm{i}}\right)\left(\mathrm{V_m(t)} - \mathrm{E_k(t)}\right), \tag{2.14}$$

where $\mathrm{g_{SK}}$ is the conductance of $\mathrm{I_{SK}}$, $\mathrm{E_k}$ is the Nernst potential for potassium and $\mathrm{f}\left([\mathrm{Ca^{2+}}]_{\mathrm{i}}\right)$ is a gating variable that satisfies the equation:

$$\frac{\mathrm{d}\mathrm{f}\left([\mathrm{Ca^{2+}}]_{\mathrm{i}}\right)}{\mathrm{dt}} = \frac{\mathrm{f}_{\infty}\left([\mathrm{Ca^{2+}}]_{\mathrm{i}}\right) - \mathrm{f}\left([\mathrm{Ca^{2+}}]_{\mathrm{i}}\right)}{\tau_{\mathrm{f}}} \tag{2.15}$$

where the steady-state value of gate f is:

$$\mathrm{f}_{\infty}\left(\left[\mathrm{Ca^{2+}}\right]_{\mathrm{i}}\right) = \frac{\left([\mathrm{Ca^{2+}}]_{\mathrm{i}}\right)^{\mathrm{q}}}{\mathrm{K_{SK}^{q}} + \left([\mathrm{Ca^{2+}}]_{\mathrm{i}}\right)^{\mathrm{q}}} \tag{2.16}$$

and $\mathrm{K_{SK}}$=700 nM is the half-activation calcium concentration, q=2 is the Hill coefficient and τ_{f}=5 ms is the activation time.

Comparing the ionic current traces in the original and modified $\mathcal{G}$ model (Figure 2.5) we found again that the most impacted currents were $\mathrm{I_{Kr}}$, which showed a reduction in peak value of 10%, and $\mathrm{I_{Ks}}$, which showed a peak reduction of 31%. Given those results we did not perform a reparametrization of the $\mathcal{G}$ cellular model on the basis of the same arguments described above for the $\mathcal{C}$ model.

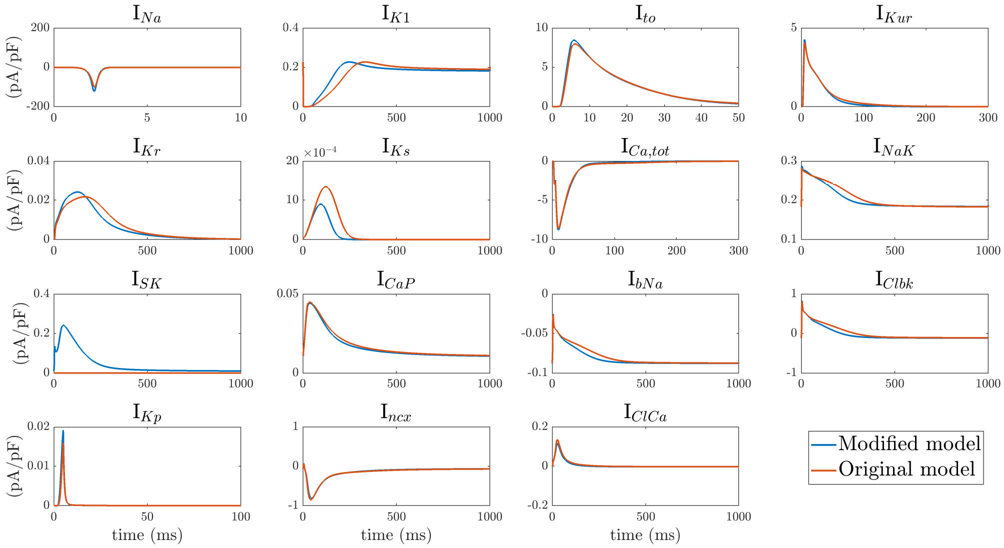

Figure 2.5: Representation of the individual currents in the $\mathcal{G}$ model before (red) and after (blue) the introduction of the $\mathrm{I_{SK}}$ current.

To simulate the effects on atrial electrophysiology of parasympathetic stimulation, the $\mathcal{G}$ model adopted the formulation by Voigt et al. [263], with further adjustments based on the experimental data from Koumi et al. [38, 264]:

$$\mathrm{I_{KACh}(t)} = \mathrm{g_{KACh}}\sqrt{\frac{\mathrm{[K^+]_o}}{5.4}}\,\frac{\mathrm{ACh(t)}}{\mathrm{ACh(t)}+0.125}\mathrm{R_{KACh}}\left(\mathrm{V_m(t)}-\mathrm{E_K(t)}\right) \tag{2.17}$$

$$\mathrm{g_{KACh}} = 0.1275\left(1+\frac{1.6863}{1+\left(\frac{10}{\mathrm{[Na^+]_i}}\right)^3}\right) \tag{2.18}$$

$$\mathrm{R_{KACh}(t)} = 0.055+\frac{0.40}{1+\exp\left(\frac{(\mathrm{V_m(t)}-\mathrm{E_K(t)}+9.53)}{17.18}\right)} \tag{2.19}$$

where $\mathrm{ACh(t)}$ is the ACh concentration at time "t" expressed in μM, $\mathrm{V_m(t)}$ is the membrane potential and $\mathrm{E_K(t)}$ is the Nernst potential for potassium.

In the $\mathcal{G}$ model, the effects of β-adrenergic stimulation were modeled based on the method described in [265]. This involved PKA regulation of various subcellular targets, such as a 3-fold increase in the maximal conductance of I_{Ks} and a 40 mV leftward shift in the IV relationship, a 3-fold increase in the maximal conductance of I_{Kur} and a 50% increase in the fraction of available channels for I_{CaL} with a 3 mV leftward shift in the channel availability. The sensitivity of the SERCA pump to Ca^{2+} was increased by reducing the forward mode, k_{mf}, by 50%. The sensitivity of RyR to Ca^{2+} was increased 2-fold, while the troponin affinity for Ca^{2+} (TnI) was decreased by increasing k_d by 50%. Finally, the affinity of the Na^+/K^+ pump for $[Na^+]_i$ was increased by 25% [38].

2.2.3 Skibsbye model

The starting point for the Skibsbye, $\mathcal{S}$, model was the *in silico* human atrial cell model of Koivumaki et al. [248, 266]. Skibsby et al. reformulated the I_{Na} current and adjusted the I_{to} and I_{CaL} currents to obtain a more spike and dome-like AP morphology in 1D tissue strand simulations. They also extended the model to include I_{SK} and they updated the psAF model variant [266] to include the disease-related remodeling reported after the publication of the original Koivumaki model. One of the main differences between the $\mathcal{C}$ and $\mathcal{G}$ models and the $\mathcal{S}$ model is that in the latter the cytosol and sarcoplasmic reticulum are divided into several transverse components with centripetal Ca^{2+} diffusion between them, thereby providing the first model with a partial spatial representation of the atrial cardiomyocyte [248].

In the $\mathcal{S}$ model, the description of the I_{SK} current was already included as per Skibsbye et al. [249]. SK channel opening is described as a two-state Markov model that shares the properties reported by Hirschberg et al. [267]. The opening of the channel simply depends on the subsarcolemmal calcium concentration (squared). Rectification of I_{SK} was adjusted based on the *in vitro* data by Tang et al. [268]. The equations defining the opening of the channel and the current are as follows:

$$I_{SK} = g_{SK} O \left(\frac{1}{1 + \exp\left(\frac{V_m(t) - E_K(t) + 120}{45}\right)} \right) (V_m(t) - E_K(t)), \tag{2.20}$$

where g_{SK}=3.6 is the conductance of I_{SK}, E_K is the Nernst potential for potassium and O

is a gating variable that satisfies the equation:

$$\frac{\mathrm{dO}}{\mathrm{dt}} = (1 - \mathrm{O})\,\mathrm{SK_{on}Ca_{ss}^2} - \mathrm{OSK_{off}} \tag{2.21}$$

To account for parasympathetic stimulation, the $\mathcal{S}$ model adopted the formulation by Voigt et al. [263] and the effects of β-adrenergic stimulation were described as proposed by González de la Fuente et al. [259], which are described above for the $\mathcal{C}$ model.

2.2.4 *In silico* cellular models of AF-related electrical remodeling

The human atrial cardiomyocyte models described in section 2.2 were considered to represent atrial cells in either SR or with early-onset AF. In this thesis, models of psAF were generated by incorporating AF-induced electrical remodeling as described in previous studies.

In the $\mathcal{C}$ model, electrical remodeling was simulated by reducing the maximal conductances of $\mathrm{I_{to}}$, $\mathrm{I_{CaL}}$ and $\mathrm{I_{Kur}}$ by 50%, 70% and 50%, respectively, and by increasing the maximal conductance of the inward rectifier potassium current, $\mathrm{I_{K1}}$, by 100% [269].

In the $\mathcal{G}$ model, electrical remodeling involved reductions in the conductances of $\mathrm{I_{to}}$, $\mathrm{I_{Kur}}$ and the fast sodium current, $\mathrm{I_{Na}}$, by 45%, 45% and 10%, respectively. Additionally, a late component was added to the $\mathrm{I_{Na}}$ current, as previously described [109]. The density of $\mathrm{I_{CaL}}$ was reduced by 50%, sensitivity of RyR to luminal $\mathrm{Ca^{2+}}$ was doubled and the rate of the SERCA pump was decreased [270]. The conductances of $\mathrm{I_{K1}}$, $\mathrm{I_{Ks}}$ and $\mathrm{I_{NaCa}}$ were increased by 100%, 100% and 40%, respectively. Finally, passive sarcoplasmic reticulum calcium leak was increased by 25% [38].

In the $\mathcal{S}$ model, under psAF-related electrical remodeling, $\mathrm{I_{CaL}}$, $\mathrm{I_{to}}$, $\mathrm{I_{Kur}}$, I_{Na} and the sarcolipin to SERCA ratio (SLN) were reduced by 55%, 62%, 38%, 18% and 40%, respectively, while $\mathrm{I_{K1}}$, $\mathrm{I_{Ks}}$, $\mathrm{I_{NaCa}}$ and the phospholamban to SERCA ratio (PLB) were increased by 68%, 145%, 50% and 18%, respectively [121]. Additionally, the expression of SERCA was decreased and the sensitivity of RyR to sarcoplasmic reticulum calcium was increased 2-fold. Cell dilation was also considered by increasing the cell length by 10% [121].

Regarding $\mathrm{I_{SK}}$, AF-induced remodeling was considered to reduce the magnitude of the

I_{SK} current by 50% in all models, in concurrence with experimental evidence [121]. Finally, the formulation of Iso effects on atrial electrophysiology from González et al. provided specific conductance modulation curves for the psAF case [259].

The above described representations of psAF-related electrical remodeling are summarized in Table 2.1 for each of the cellular models.

2.3 *In silico* models of cardiac electrical propagation

Two commonly used mathematical models for simulating electrical propagation in cardiac tissue are the bidomain and the monodomain models.

The bidomain equations consist of a system of two partial differential equations that describe the electrical potential in the intracellular and extracellular domains of the cardiac tissue. These equations are coupled with the system of nonlinear ordinary differential equations that represent the electrical activity of a cardiac cell, as can be seen from the equations of the HH model described in section 2.1. The cardiac tissue consists of both extra- and intracellular media that interact through the cellular membrane. In both the monodomain and bidomain models, every point in space is assumed to be in both domains and is therefore assigned both extra- and intracellular potentials. This assumption, although not reflective of actual cardiac tissue, has been surprisingly accurate in producing normal resolution by averaging over a large number of cardiomyocytes. Several alternatives to the bidomain and monodomain models have been published in the literature that explicitly represent all individual cells in the models [271–278].

The parabolic-elliptic form of the bidomain equations is as follows:

$$\chi\left(\mathrm{C_m}\frac{\partial \mathrm{V_m(t)}}{\partial \mathrm{t}} + \mathrm{I_{ion}}(\mathbf{u}, \mathrm{V_m(t)})\right) - \nabla\cdot(\mathbf{D}_i\nabla(\mathrm{V_m(t)} + \phi_\mathrm{e})) = 0, \tag{2.22}$$

$$\nabla\cdot((\mathbf{D}_i + \mathbf{D}_e)\nabla\phi_e + \mathbf{D}_i\nabla\mathrm{V_m(t)}) = 0, \tag{2.23}$$

where $\mathrm{V_m(t)}$ is the transmembrane potential, $\mathrm{C_m}$ is the membrane capacitance, χ is the membrane surface-to-volume ratio (the amount of membrane found in a given volume of tissue), $\mathrm{I_{ion}}(\mathbf{u}, \mathrm{V_m(t)})$ is the sum of all transmembrane ionic currents and of the applied

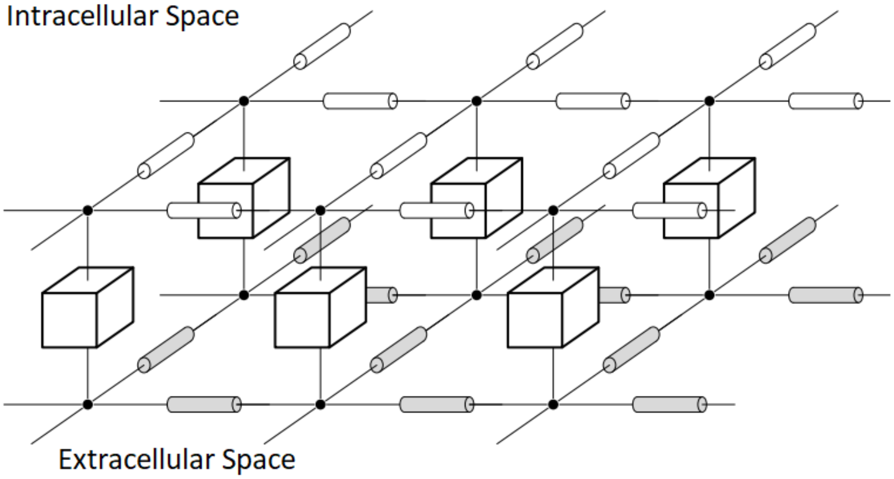

Figure 2.6: Tissue model used in electrical propagation models, in which the membranes of the cells (boxes) are connected to each other with resistances in both intracellular (white cylinders) and extracellular (grey cylinders) spaces. Adapted and modified from [279].

stimulation current, ϕ_e is the extracellular potential, $\mathbf{D}_i$ and $\mathbf{D}_e$ represent the intracellular and extracellular conductivity tensor fields, respectively.

The boundary conditions for equations (2.22) and (2.25) specify the current applied along the border:

$$\mathbf{n} \cdot ((\mathbf{D}_i + \mathbf{D}_e)\nabla(\mathrm{V_m(t)} + \phi_\mathrm{e})) = 0 \tag{2.24}$$

$$\mathbf{n} \cdot (\mathbf{D}_e \nabla\phi_e) = 0 \tag{2.25}$$

where **n** is the outward pointing unit normal vector to the tissue.

A scheme of a tissue model is illustrated in Figure 2.6.

The bidomain model, which is a system of partial differential equations, is challenging to solve and analyze. However, by assuming equal anisotropy ratios between the intracellular and extracellular conductivity tensors, the coupled system can be decoupled. This allows the extracellular potential to be calculated as a postprocessing step, once the transmembrane potential has been obtained. This simplification leads to the monodomain equations, which were used to simulate atrial electrical propagation in this thesis. Indeed, for the type of simulations run here, the accuracy of the monodomain model is similar to that of the bidomain model and its computational cost is lower, thus making it more suitable for our investigations[280].

The monodomain equations read as:

$$\chi(\mathrm{C_m}\frac{\partial \mathrm{V_m(t)}}{\partial \mathrm{t}} + \mathrm{I_{ion}}(\mathbf{u}, \mathrm{V_m(t)})) = \nabla \cdot (\mathbf{D}\nabla \mathrm{V_m(t)}), \tag{2.26}$$

$$(1+\lambda)\nabla \cdot (\mathbf{D}\nabla \phi_e) = -\nabla \cdot (\mathbf{D}\nabla \mathrm{V_m(t)}) \tag{2.27}$$

where $\mathbf{D}$ is a conductivity tensor as described by $\mathbf{D} = \mathbf{D}_i\ (\mathbf{D}_i + \mathbf{D}_e)^{-1}\mathbf{D}_e$ [281], while λ is the proportionality factor between the intracellular and extracellular conductivity tensor fields, being $\mathbf{D}_\mathrm{i} = \lambda \mathbf{D}_\mathrm{e}$.

And the boundary conditions become:

$$\mathbf{n} \cdot (\mathbf{D}\nabla \mathrm{V_m}) = 0 \tag{2.28}$$

$$\mathbf{n} \cdot (\mathbf{D}\nabla \phi_e) = 0 \tag{2.29}$$

2.4 *In silico* models of fibrosis

As reported in section 1.3.3, fibrotic remodeling is a multiscale process associated with GJs remodeling [87, 88], fibroblast proliferation [89, 90] and excess collagen deposition [89, 91]. Computational models of fibrotic atria have accounted for these remodeling characteristics, either separately or in combination. Nonetheless, due to the need for further experimental characterization from human tissue, additional work could help to shed light on how to best model atrial fibrosis in humans [282]. In our models, we did not consider the increase in collagen content, which is usually modeled as non-conductive obstacles in the tissue. However, we considered a combination of GJ remodeling and fibroblasts proliferation. GJ remodeling was simulated through tissue conductance reduction in fibrotic regions. The fibroblast-fibroblast GJ conductance was reduced 4-fold with respect to the myocyte-myocyte conductance. When myocytes were coupled to fibroblasts, the junctional conductance was linearly adjusted depending on the number of fibroblasts coupled to a myocyte.

Fibroblast proliferation was modeled by replacing myocytes with fibroblasts and using the MacCannell active fibroblast ionic model [283], as in previous studies [284]. This model comprises a time- and voltage-dependent potassium current I_{Kv}, an inward rectifying potassium current I_{K1}, a sodium-potassium pump current I_{NaK} and a background sodium current I_{bNa} [283].

2.5 *In silico* 2D and 3D atrial models

Human atrial electrical activity was simulated in 2D square sheets of tissue and in 3D biatrial anatomical models. The 2D models represented square pieces of tissue of 5x5 cm^2 or 7x7 cm^2, discretized in square elements of 200-µm side. A uniform bottom-to-top fiber direction was assigned to the tissues. For the 3D biatrial models, the anatomy was in all cases defined as in [285]. The 3D anatomical models were discretized in a multi-layer mesh with a homogeneous wall thickness between 600 and 900 µm, built with linear hexahedral elements with regular spatial resolution of 300 µm, resulting in a total of 754,893 nodes and 515,010 elements. The models included detailed regional description of fiber direction and functional heterogeneity.

In the 3D models, the $\mathcal{C}$ cellular model was adapted to represent different atrial regions by varying the ionic current conductances as in [285]. The eight regions with different electrophysiological characteristics were: LA, right atrium (RA), left atrial appendage (LAA), right atrial appendage (RAA), PVs, tricuspid valve ring (TVR), mitral valve ring (MVR), crista terminalis (CT) and Bachmann bundle (CTBB). In Figure 2.7, the APs corresponding to these regions are shown.

The myocyte-myocyte conductance was adapted to match experimental evidence in terms of CV and total activation time (TAT). In the 3D models, we used values of longitudinal conductivity (L_{CV}) and transverse-to-longitudinal conductivity ratio (T/L_{CR}) that were adapted from [285] for different atrial regions. Particularly, for definition of the conductivity values, we considered ten atrial regions: LA, RA, PV, SAN, coronary sinus (CS), isthmus (IST), fossa ovalis (FO), CT, limb of the fossa ovalis (LFO), Bachmann bundle and pectinate muscles (BBPMS). The defined conductivity values, reported in Table 2.2, led to a TAT of 180 ms, in line with data reported in the literature for psAF patients [286]. It is

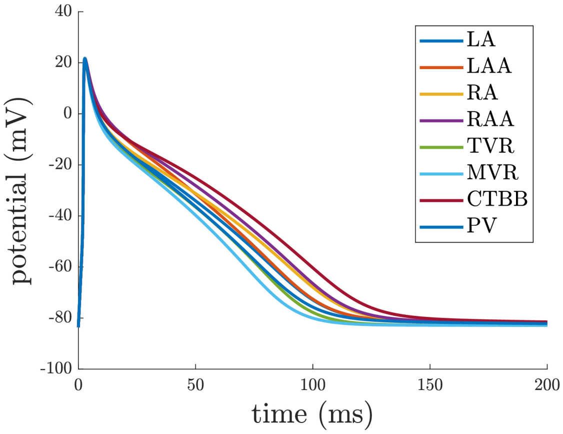

Figure 2.7: APs corresponding to the different electrophysiological regions in the 3D biatrial models.

worth noting that the heterogeneities in electrophysiological characteristics and in conductivities were defined by using eight and eleven atrial regions, respectively, so as to match experimental evidence [285]. In the 2D models, we used the same values of longitudinal conductivity and transverse-to-longitudinal conductivity ratio as in the LA region of the 3D model, which rendered a longitudinal CV of 50 cm/s for a planar wave, in agreement with values reported for AF patients in previous studies [258].

2.6 Stimulation protocols and numerical simulations

Single cells were subjected to pacing at a fixed cycle length (CL) until they reached steady state for each of the three employed models ($\mathcal{C}$, $\mathcal{G}$ and $\mathcal{S}$). Steady state was considered to be attained when changes in state variables between consecutive stimuli measured at the end of each cardiac cycle were below 3%. In particular, the $\mathcal{C}$ model was paced for 10 minutes, while the $\mathcal{G}$ and $\mathcal{S}$ models were paced for 5 minutes.

The $\mathcal{C}$ model was used for tissue simulations with its state variables initialized to the steady-state values obtained from single cell simulations. The temporal resolution use to solve the ODEs defining the $\mathcal{S}$ and $\mathcal{C}$ models was 0.005 ms, while the $\mathcal{G}$ model was run with a temporal resolution of 0.001 ms, in all cases ensuring numerical convergence of the results. In the tissue simulations, a spatial resolution of 0.02 cm was considered. To define the spatial resolution, a convergence analysis was conducted by running simulations with progressively reduced space step. When differences in longitudinal CV between consecutive step sizes were below 0.2%, no improvement was considered to be achieved by additionally refining the mesh and that space step was taken as the spatial resolution for all the simulations.

The cellular simulations were performed using MATLAB, while tissue simulations were performed using the software ELECTRA [287–289] and and the software ELVIRA [290]. ELECTRA is an in-house software that implements the Finite Element Method (FEM) and Meshfree Methods for the solution of the monodomain model. In this work, FEM was used. In some of the simulations, a dual adaptive explicit time integration (DAETI) method was used [291]. DAETI employs adaptive explicit integration for the solution of both the reaction and diffusion terms of the cardiac monodomain model, which allows obtaining accurate solutions while reducing the computational time. ELVIRA describes electrical propagation in the atria by the monodomain model and uses FEM in combination with the operator splitting numerical scheme to solve the propagation equations.

Table 2.1: Summary of formulations for descriptions of cholinergic (ACh) and β-adrenergic (1 μM Iso) stimulation effects, SK current (I_{SK}) and psAF-induced electrical remodeling.

Models	**ACh**	**Iso**	$\mathbf{I_{SK}}$	**psAF**
$\mathcal{C}$)	I_{KACh} as in *Kneller* [196] + *Bayer* [258]	I_{to}: -48.6% I_{CaL}: +160.6% I_{Ks}: +65.7% *González* [259]	I_{SK} as in *Engel* [254]	I_{to}: -50% I_{CaL}: -70% I_{Kur}: -50% I_{K1}: -70% *Courtemanche* [244] g_{SK}: -50%
$\mathcal{G}$)	I_{KACh} as in *Voigt* [263]	I_{Ks}: $+300\%$ and IV relationship leftward shift (-40 mV). g_{Kur}: $+300\%$. I_{CaL}: increased fraction of available channels ($+50\%$), channel availability shifted leftward (-3 mV). SERCA forward mode k_{mf}: -50%. RyR Sensitivity to Ca^{2+}: $+200\%$. TnI: decreased (k_d $+50\%$). I_{NaK} affinity for $[Na^+]_i$: $+25\%$. *Grandi* [38]	I_{SK} as in Peñaranda [262]	I_{Na}: -10% peak density. I_{NaL}: added. I_{Ks}: $+200\%$. I_{Kur}: -45%. I_{K1}: $+100\%$. I_{to}: -45%. I_{CaL}: -50%. I_{NaCa}: $+40\%$ in cAF. SERCA: reduced maximal pump rate. RyR: sensitivity for luminal Ca $+200\%$. sarcoplasmic reticulum Ca^{2+} leak: $+25\%$. *Grandi* [38] g_{SK}: -50%
$\mathcal{S}$)	I_{KACh} as in *Voigt* [263]	I_{to}: -48.6% I_{CaL}: $+160.6\%$ I_{Ks}: $+65.7\%$ González [259]	I_{SK} as in *Skibsbye* [121]	g_{Na}: -18% g_{CaL}: -55% g_{to}: -62% g_{Kur}: -38% g_{Ks}: $+145\%$ g_{K1}: $+68\%$ g_{NaCa}: $+50\%$ PLB: $+18\%$ SLN: -40% Cell length: $+10\%$ SERCA expression: -18% RyR: $+100\%$ g_{SK}: -50% *Skibsbye* [121]

Table 2.2: Longitudinal conductivity (L_{CV}) and transverse-to-longitudinal conductivity ratio (T/L_{CR}) values for the different atrial regions.

Region	**L_{CV} (S/cm)**	**T/L_{CR}**
RA	0.0030	0.35
CT	0.0085	0.15
PV	0.0017	0.50
BBPMS	0.0075	0.15
IST	0.0015	1.00
SAN	0.0008	1.00
FO	0.0000	1.00
CS	0.0060	0.5
LA	0.0030	0.25
LFO	0.0075	0.15

Chapter 3

Characterization of ANS modulation of atrial fibrillatory rate

3.1 Motivation

As described in section 1.3.3, ANS activity is closely related to the genesis and maintenance of atrial arrhythmias, including AF [292]. While sympathetic activation mainly acts as a trigger by facilitating the generation of ectopic beats, vagal hyperactivity facilitates the formation of reentries by shortening the WL, defined as the distance traveled by the depolarization wave during the ERP [169] and estimated as the product of CV and ERP.

During AF, the P-waves of the ECG, representative of atrial activation, are replaced with a series of waves known as fibrillatory waves (f-waves) [293]. Some f-wave features have been proposed to characterize atrial electrical activity during AF, including the amplitude, morphology, regularity, complexity and frequency [294–297]. Among those features, the f-wave frequency ($\mathrm{F_f}$), often referred to as the atrial fibrillatory rate (AFR), has received considerable clinical attention [74, 296, 298]. Different methods have been employed to compute $\mathrm{F_f}$. In some studies, $\mathrm{F_f}$ has been derived through spectral (frequency domain) analysis by identifying the frequency presenting the highest peak in the power spectral density [299]. In other works, $\mathrm{F_f}$ has been extracted from the analysis of the ECG in the time domain using a model-based approach [300, 301].

In SR, cardiorespiratory interactions regulated by the ANS have been widely studied

[302], with respiratory sinus arrhythmia (RSA) defined as the autonomically-mediated modulation of the SAN pacemaker frequency in synchrony with inspiration and expiration [302–305]. The contribution of RSA to heart rate variability (HRV) can be measured from the high-frequency components of HRV and can be used for noninvasive assessment of parasympathetic activity [303, 305–308]. At typical breathing frequencies (around 0.25 Hz), the shortening of the heart period during inspiration would be associated with the withdrawal of parasympathetic activity, while its lengthening during expiration would be associated with enhanced vagal activity [309]. There is currently a need for non-invasive methods to assess ANS activity during AF other than HRV, which cannot be used to measure ANS activity during AF since heartbeats do not originate in the SAN. This need arises because differences in ANS activity among AF patients could contribute to varied responses to treatment. Consequently, information on such differences could help in developing personalized treatment.

Observations of cyclic fluctuations exhibiting an in-phase relationship with respiration have been reported in f-wave frequency in patients with AF [310] and in flutter cycle length in patients with atrial flutter [311, 312]. Based on the above described observations, the hypothesis has been formulated that this phenomenon could be connected to respiratory-related oscillations of parasympathetic activity. Nonetheless, there is limited research on how respiration affects atrial rate during atrial tachyarrhytmias, particularly AF, primarily due to technical difficulties [310]. These difficulties include distinguishing noise from f-waves, the presence of modulation that is unrelated to the respiratory signal, the very small magnitude of the respiratory-induced f-wave frequency modulation that may be concealed by other variations and the unknown and variable respiration rate over time. The study by Holmqvist et al. [310] was, however, able to show that low-frequency, controlled respiration can induce cyclic fluctuations in $\mathrm{F_f}$, which might be linked to parasympathetic regulation of the AF refractory period given that the modulation was reduced in response to vagal blockade.

In this chapter, we used computational modeling and simulation to evaluate the role of the spatiotemporal release pattern of ACh, considered to temporally vary in phase with inspiration and expiration, in the modulation of the f-wave frequency. Both 2D tissues and

3D whole-atria models representative of psAF were built and distinct spatial distributions of ACh release sites were defined. Also, different stimulation protocols were simulated to evaluate the role of the spatiotemporal ACh release pattern combined with the reentry characteristics on the fibrillatory rate. To provide a more extensive characterization, $\mathrm{F_f}$ was analyzed in terms of mean ($\overline{\mathrm{F}}_\mathrm{f}$) and range of variation ($\Delta\mathrm{F_f}$), as studies on ECGs from patients have shown $\Delta\mathrm{F_f}$ to provide complementary information to $\overline{\mathrm{F}}_\mathrm{f}$ [301]. The computational results from the present work were compared with results obtained from the analysis of clinical data [301]. The final objective was to assess the impact of vagal stimulation on the AF fibrillatory frequency to potentially assess differences in autonomic modulation of atrial activity in psAF patients.

3.2 Methods

3.2.1 Clinical recordings

By modeling and simulation of human atrial electrophysiology, we aimed at reproducing variations in $\mathrm{F_f}$ like those described in previous clinical studies [301, 310]. A group of eight patients with psAF, atrioventricular block III and a permanent pacemaker was studied to investigate the modulation of $\mathrm{F_f}$ by respiration and its parasympathetic regulation. ECGs were recorded at rest during baseline (spontaneous respiration) ($\mathcal{B}$), during 0.125 Hz frequency-controlled respiration ($\mathcal{CR}$) and during controlled respiration post atropine injection ($\mathcal{PA}$) that led to full vagal blockade [310].

3.2.2 Atrial models

To perform the simulations, we used the 2D square tissue model and the 3D biatrial anatomical model presented in section 2.5. To simulate the electrophysiological activity of the cardiomyocytes, the $\mathcal{C}$ human atrial AP model was used [244]. In the 2D models, all the myocardial nodes were assigned with the same electrophysiological characteristics representative of left atrial tissue. In the 3D models, the $\mathcal{C}$ model was adapted to represent different atrial regions by varying the ionic current conductances following the work presented in [285], as explained in section 2.5.

In the $\mathcal{C}$ model, the effects of cholinergic and adrenergic stimulation and the formulation of the I_{SK} current were introduced as fully described in section 2.2.1. PsAF-induced electrical remodeling was represented as explained in section 2.2.4. PsAF-induced structural remodeling was modeled by including 20% diffuse fibrosis on the basis of histological studies reporting diffuse fibrosis percentages up to 40%, with a mean of approximately 20%, in psAF patients [78, 313]. Both in the 2D and 3D models, 20% of the nodes were uniformly randomly selected. These nodes were assigned with fibroblast properties and their electrical activity was defined by the MacCannell active fibroblast computational AP model [283].

The myocyte-myocyte, myocyte-fibroblast and fibroblast-fibroblast conductivities were defined as described in section 2.4.

3.2.3 Simulated ACh release patterns

We defined four different 3D models corresponding to distinct spatial ACh release configurations throughout the atria:

- $\mathcal{O}_{08}$: Octopus 8%. The heterogeneous ACh release in the atria was realistically represented by modeling the GPs location following the anatomical study by Armour et al. [52], as represented in Figure 3.1. This model included the anatomical locations of the GPs plus the nerves departing from the GPs. The heterogeneous transmural distribution of autonomic innervation was accounted for.

  Specifically, the five major GPs (SRA-GPs, SLA-GPs, PRA-GPs, PMLA-GPs and PLLA-GPs) were considered in this model. To additionally take into account the nerves communicating the GPs with the atrial tissue, we modeled the GPs following the octopus hypothesis [168]. Considering that the neural cell distribution is mainly epicardial [56], we concentrated the ACh release mostly in the two more external layers, as represented in Figure 3.3. In the $\mathcal{O}_{08}$ model, considering both the GPs bodies and the nerves departing from them, 8% of all the mesh nodes were considered to be ACh release nodes. The model is represented in panel A) of Figure 3.2.

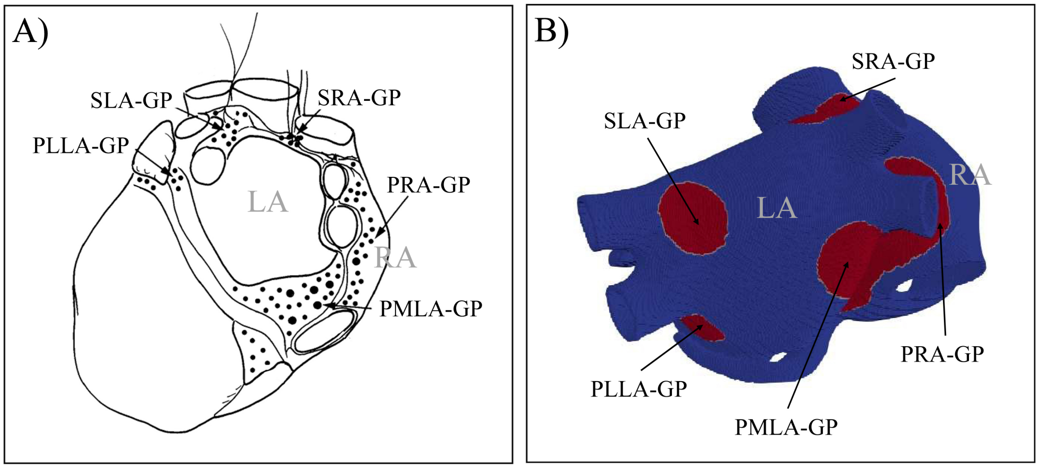

Figure 3.1: (A) anatomical description by Armour et al. [52]. (B) computational model used in this study, with GPs represented in red.

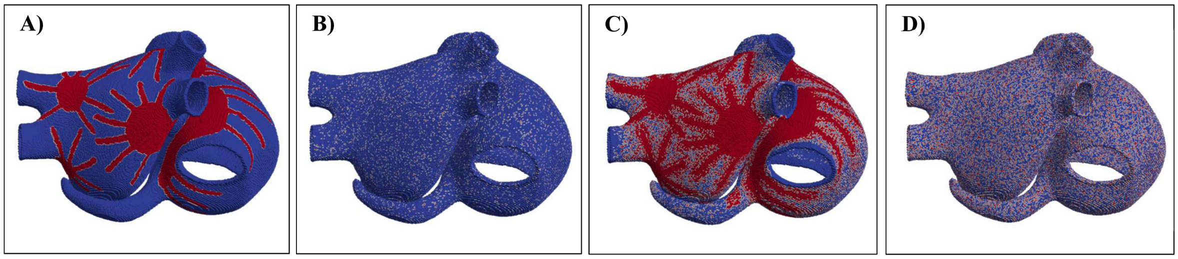

Figure 3.2: 3D biatrial anatomies, with ACh release nodes depicted in red. Representation of (A) $\mathcal{O}_{08}$ model, (B) $\mathcal{D}_{08}$ model, (C) $\mathcal{O}_{30}$ model and (D) $\mathcal{D}_{30}$ model.

- $\mathcal{D}_{08}$: Diffuse 8%. To assess the impact of the spatial distribution of ACh release, we built another 3D model in which 8% of the nodes were uniformly randomly selected all over the atria to be ACh release nodes. This model is represented in Figure 3.2, panel B), and referred to as $\mathcal{D}_{08}$.

- $\mathcal{O}_{30}$: Octopus 30%. We defined another 3D model containing 30% of ACh release nodes, which we denoted as $\mathcal{O}_{30}$. In this model, the GPs and nerves of the octopus configuration were identified as release nodes. Additional nodes all over the atria were identified as release nodes with a probability that decreased with the distance to the octopus, completing a total of 30% of ACh release nodes in the atria. The $\mathcal{O}_{30}$ model is represented in Figure 3.2, panel C).

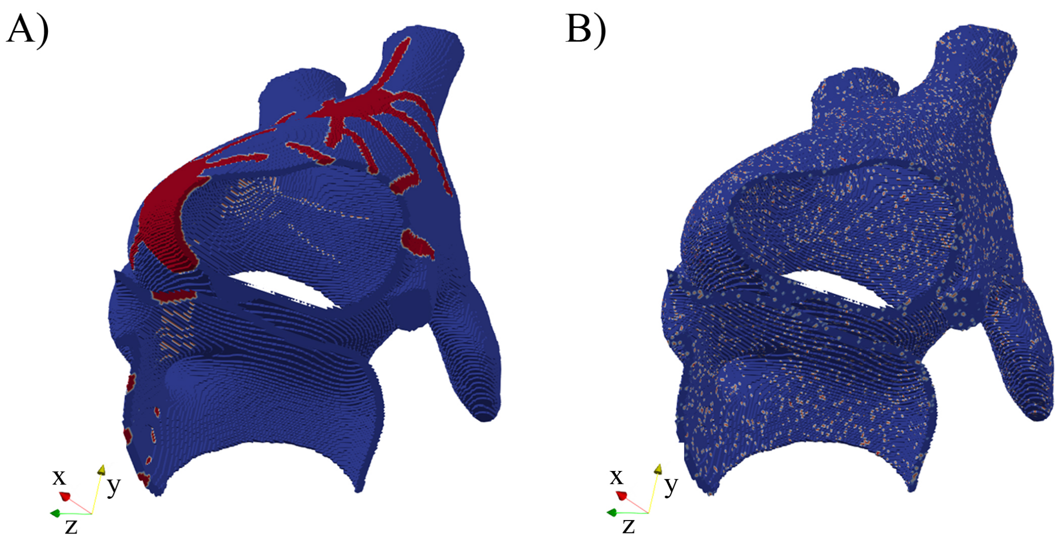

Figure 3.3: Sections of the left atrium for the $\mathcal{O}_{08}$ model (A) and $\mathcal{D}_{08}$ model (B). In the $\mathcal{O}_{08}$ the ACh release nodes (red) are concentrated in the 2 most external layers of the mesh, while in the $\mathcal{D}_{08}$ model they are uniform randomly distributed in all the three node layers.

- $\mathcal{D}_{30}$: Diffuse 30%. In this model, 30% of all nodes in the atria were uniformly randomly selected as ACh release nodes. The $\mathcal{D}_{30}$ model is represented in Figure 3.2, panel D).

In 2D models, we defined two spatial configurations of ACh release.

- $\mathcal{D}_{2D,08}$: 2D Diffuse 8%. In this model, we uniformly randomly selected 8% of the tissue nodes to be ACh release nodes, similarly to the ACh diffuse 3D models.

- $\mathcal{D}_{2D,30}$: 2D Diffuse 30%. In this model, the uniformly randomly selected nodes for ACh release represented 30% of the total number of nodes.

For both 2D and 3D models and for each of the identified release nodes, ACh was simulated to cyclically vary in time following a sinusoidal waveform of frequency equal to 0.125 Hz, which corresponds to the controlled respiratory frequency of the clinical recordings. We tested different mean concentrations of ACh ($\overline{\mathrm{ACh}}$), equal to 0.05 and 0.075 μM, and different peak-to-peak variations of ACh ($\Delta\mathrm{ACh}$), equal to 0, 0.05 and 0.1 μM. All simulated ACh values were within the physiological limits tested in preceding studies (0 - 0.1 μM) [258].

3.2.4 Numerical methods and simulations

Electrical propagation in the atria was described by the monodomain model and solved by means of the FEM in combination with the operator splitting numerical scheme using the software ELVIRA [290].

Single cells were paced at a fixed CL of 800 ms for 16 minutes to reach steady state. For 2D and 3D simulations, the state variables of the AP models were initialized to the steady-state values determined from single cell simulations.

Both the 2D and 3D models were pre-paced by delivering 14 stimuli at a CL of 800 ms. In the 2D tissues, the stimuli were applied onto the bottom edge of the tissue. In the 3D models, the stimuli were applied onto the region of the sinus node.

In the 2D tissue models, an S1-S2 cross-stimulation protocol was applied to initiate a rotor: the first stimulus (S1) was applied at the bottom edge of the tissue and the second stimulus (S2) was applied onto a 3.5 x 3.5 cm square at the bottom right corner.

In the 3D whole-atria models, two protocols were applied to initiate arrhythmias. The first one was an S1-S2 protocol similar to the one applied onto the 2D tissue, with the S1 stimulus delivered at a line joining the region between the superior and inferior left PVs and the region between the right PVs, and the S2 stimulus being subsequently applied parallel to the first one starting from the inferior left PV and covering only half of the S1 line length. The second protocol aimed to recreate a physiological setting and consisted in the application of an S1 stimulus followed by a train of premature stimuli delivered at a region surrounding the PVs, where ectopic beats are usually generated. In total, 10 stimuli were applied, with the first interval between stimuli being 200 ms and these intervals decreasing in 10-ms steps. Figure 3.4 displays the delivery locations for S1 and S2 stimuli (panel (A)) and the delivery location of the ectopic beats (panel (B)).

3.2.5 Dominant frequency characterization

From the ECGs of the patients, the f-wave signal was obtained by applying spatiotemporal QRST cancellation [314]. The $\mathrm{F_f}$ time series, denoted as $F_{\mathrm{f}}(t)$, was estimated using a model-based approach [300], as previously described [301]. $\overline{\mathrm{F}}_{\mathrm{f}}$ was computed as the aver-

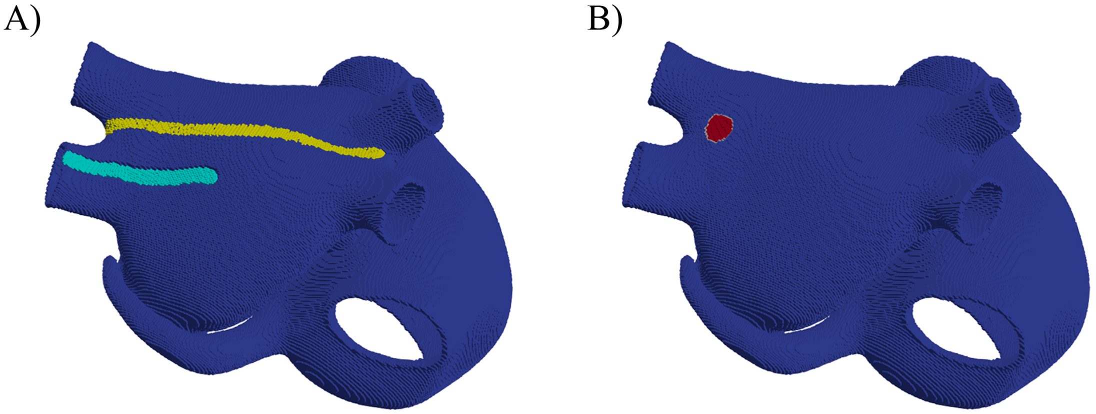

Figure 3.4: A) Location of the S1 stimulation (yellow region) and of the S2 stimulation (cyan region). B) Location of ectopic beats stimulation (red region)

age value over time of $F_{\mathrm{f}}(t)$ (Figure 3.5, panel (A)). The magnitude of f-wave frequency modulation, denoted as $\Delta \mathrm{F_f}$, was computed by first bandpass filtering the time series $F_{\mathrm{f}}(t)$ in a narrow frequency band (0.06 Hz) centered around the respiration rate, thus generating $\tilde{F}_{\mathrm{f}}(t)$, and subsequently computing its upper envelope $\tilde{F}_{\mathrm{f}}^{u}(t)$ from the magnitude of its analytic signal computed using the Hilbert transform. The median over time of $\tilde{F}_{\mathrm{f}}^{u}(t)$ was defined as $\Delta \mathrm{F_f}$ [301], as illustrated in Figure 3.5 panels (C) and (D).

From the simulations, voltage time series were extracted from 169 evenly sampled points in the 2D tissue models and 223 points manually selected to be approximately uniformly distributed in the 3D whole-atria models (white dots in Figure 3.6, panels (A) and (B)).

The AP trace for a point $\mathrm{j_0}$ in a 2D tissue is illustrated in Figure 3.7 (A). For each point j in each 2D tissue or 3D anatomy, the time instant $\mathrm{t_m(j,i)}$ corresponding to the maximum AP upstroke velocity of the i-th beat was determined (Figure 3.7 (B)). The instantaneous frequency was computed as $\mathrm{F_{f,j}(t_m(j,i)) = 1/(t_m(j,i) - t_m(j,i-1))}$ and linearly interpolated at 20 Hz to obtain $\mathrm{F_{f,j}(t)}$, which is depicted in Figure 3.7 (C) for point $j = j_0$. Next, averaging (in space) was performed to compute the tissue dominant frequency $\mathrm{F_f(t)}$ along time, as follows. First, each $\mathrm{F_{f,j}(t)}$ was subjected to power spectral analysis to obtain $\mathrm{S_j(f)}$. Spectral “peak-conditioned” selection was performed following the method described in [315] and the time series whose spectra were not sufficiently peaked were discarded (Fig-

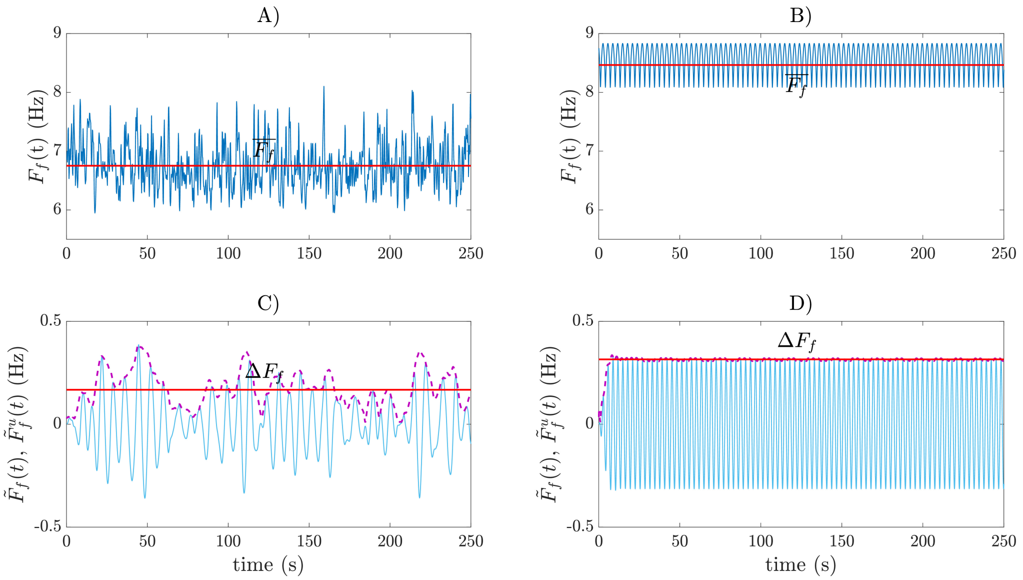

Figure 3.5: Examples of $\overline{\mathrm{F}}_{\mathrm{f}}$ and $\Delta\mathrm{F}_{\mathrm{f}}$ computation for clinical (A) and simulated (B) time series $F_{\mathrm{f}}(t)$. The time series in (B) was obtained by time replication of an 8-second simulated signal. The corresponding bandpass-filtered time series $\tilde{F}_{\mathrm{f}}(t)$ and their upper envelopes $\tilde{F}_{\mathrm{f}}^{u}(t)$, from which $\Delta\mathrm{F}_{\mathrm{f}}$ was computed, are displayed in panels (C) and (D).

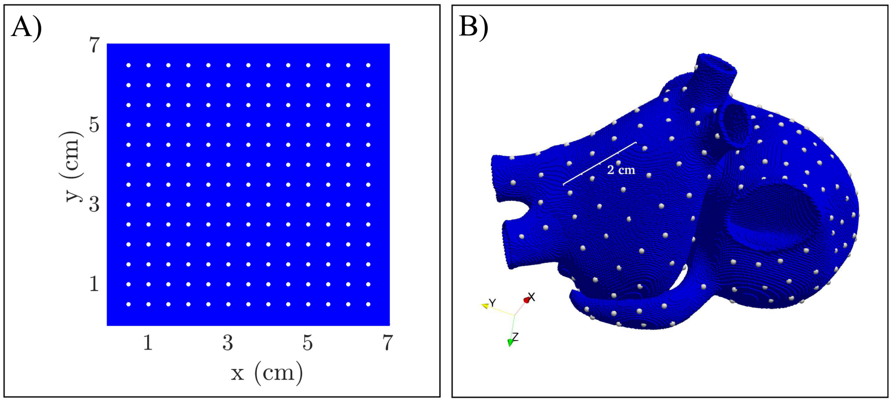

Figure 3.6: 2D tissue (A) and 3D biatrial (B) models, with white dots representing the points used for the computation of F_{f}.

ure 3.7 (D) and (E)). $\mathrm{F}_{\mathrm{f}}(\mathrm{t})$ was eventually computed as the spatial mean of the remaining time series (Figure 3.7 (F)). Finally, $\overline{\mathrm{F}}_{\mathrm{f}}$ and $\Delta\mathrm{F}_{\mathrm{f}}$ were obtained from the estimated $\mathrm{F}_{\mathrm{f}}(\mathrm{t})$ time series as described at the beginning of this section for the clinical signals.

In tables 1, 2 and 3, $\overline{\mathrm{F}}_{\mathrm{f}}$ and $\Delta\mathrm{F}_{\mathrm{f}}$ will be reported for all the different simulations. To evaluate the correlation between the variation in ACh concentration over time $(\mathrm{ACh}(\mathrm{t}))$

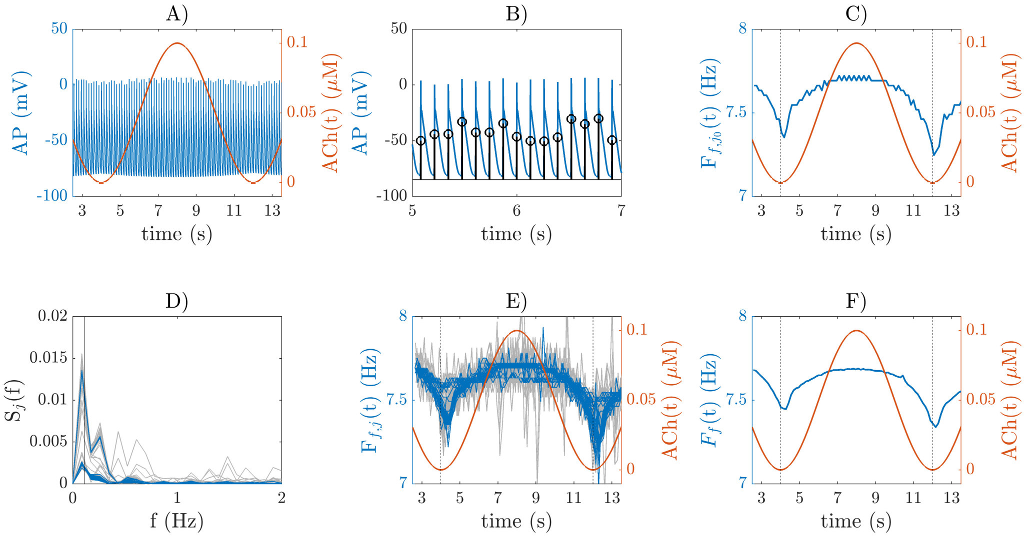

Figure 3.7: A) AP trace for a point $\mathrm{j_0}$ in a 2D tissue (blue line) and ACh temporal variation, $\mathrm{ACh(t)}$ (red line). B) Identification of the time instants for each beat i, denoted as $\mathrm{t_m(j_0, i)}$, corresponding to the maximum AP upstroke velocity for the point $\mathrm{j_0}$. C) Instantaneous frequency $\mathrm{F_{f,j_0}(t)}$ (blue line) and $\mathrm{ACh(t)}$ (red line). D) "Peak-conditioned" selection of spectra computed for all spatial points j in the tissue. The discarded and accepted spectra are shown in grey and blue, respectively. E) Instantaneous frequencies $\mathrm{F_{f,j}(t)}$ for all spatial points j (blue and grey lines) and $\mathrm{ACh(t)}$ (red line). F) Time series of the dominant frequency for the tissue, $\mathrm{F_f(t)}$, obtained by spatial trimmed averaging (blue line) plotted on top of $\mathrm{ACh(t)}$ (red line).

and the corresponding fibrillatory frequency signal $\mathrm{F_f(t)}$, we adopted Pearson's correlation coefficient (r), whose values are shown in the tables.

It should be noted that the range of ACh is considered from peak to peak, while in the case of $\Delta\mathrm{F_f}$, only half of the signal's variability amplitude range was considered. This choice was made to be consistent with the clinical results presented in [301].

3.3 Results

3.3.1 Clinical results

In all patients, the ECGs showed an f-wave frequency modulation in the $\mathcal{B}$, $\mathcal{CR}$ and $\mathcal{PA}$ phases. In the $\mathcal{CR}$ phase, the magnitude of the frequency modulation was 0.18 ± 0.02 Hz. The magnitude of these variations was significantly reduced ($\mathrm{p} < 0.05$, computed with a Kruskal-Wallis test with Dunn-Sidak correction) in 4 out of 8 patients after atropine-induced parasympathetic inhibition, while in the other four patients no changes were observed in the $\mathcal{PA}$ phase [301]. Complete results including $\mathcal{B}$, $\mathcal{CR}$ and $\mathcal{PA}$ phases for all the patients, as well as their mean values ($\overline{\overline{\mathrm{F}}}_{\mathrm{f}}$, $\overline{\Delta\mathrm{F}}_{\mathrm{f}}$), are reported in Table 3.1. Additionally, the mean over patients of the mean dominant frequency for the $\mathcal{CR}$ phase, denoted as $\overline{\overline{\mathrm{F}}}_{\mathrm{f}}{}^{\mathcal{CR}}$, the mean of the modulation magnitude for the $\mathcal{CR}$ phase, denoted as $\overline{\Delta\mathrm{F}}_{\mathrm{f}}{}^{\mathcal{CR}}$, and the standard deviation over patients of those two measures, denoted as $\sigma_{\overline{F}_{\mathrm{f}}{}^{\mathcal{CR}}}$ and $\sigma_{\Delta F_{\mathrm{f}}{}^{\mathcal{CR}}}$, respectively, are reported in the right panel of Tables 3.2, 3.3 and 3.4 [301].

Values of $\overline{\overline{\mathrm{F}}}_{\mathrm{f}}{}^{\mathcal{CR}}$, $\overline{\Delta\mathrm{F}}_{\mathrm{f}}{}^{\mathcal{CR}}$,$\sigma_{\overline{F}_{\mathrm{f}}{}^{\mathcal{CR}}}$ and $\sigma_{\Delta F_{\mathrm{f}}{}^{\mathcal{CR}}}$ are reported in Table 2.2 and repeated for convenience on the the right panels of Tables 3.2, 3.3 and 3.4 for the $\mathcal{CR}$ phase [301]. Complete results including $\mathcal{B}$, $\mathcal{CR}$ and $\mathcal{PA}$ phases for all the patients are reported in Table 2.2.

Table 3.1: Results from clinical data ($\mathcal{B}$: baseline, $\mathcal{CR}$: Controlled Respiration, $\mathcal{PA}$: Post Atropine). Table adapted from [301]. The quality of the baseline signal of patient f was too low to evaluate $\Delta\mathrm{F}_{\mathrm{f}}{}^{\mathcal{B}}$ and $\overline{\mathrm{F}}_{\mathrm{f}}{}^{\mathcal{B}}$.

Patient	$\Delta\mathrm{F}_{\mathrm{f}}{}^{\mathcal{B}}$ (Hz)	$\Delta\mathrm{F}_{\mathrm{f}}{}^{\mathcal{CR}}$ (Hz)	$\Delta\mathrm{F}_{\mathrm{f}}{}^{\mathcal{PA}}$ (Hz)	$\overline{\mathrm{F}}_{\mathrm{f}}{}^{\mathcal{B}}$ (Hz)	$\overline{\mathrm{F}}_{\mathrm{f}}{}^{\mathcal{CR}}$ (Hz)	$\overline{\mathrm{F}}_{\mathrm{f}}{}^{\mathcal{PA}}$ (Hz)
a	0.16 ± 0.06	0.17 ± 0.09	0.16 ± 0.08	6.84 ± 0.43	6.67 ± 0.45	6.71 ± 0.41
b	0.13 ± 0.06	0.16 ± 0.08	0.13 ± 0.07	6.17 ± 0.35	6.31 ± 0.37	6.46 ± 0.36
c	0.16 ± 0.08	0.17 ± 0.08	0.14 ± 0.07	6.57 ± 0.43	6.75 ± 0.39	6.36 ± 0.43
d	0.16 ± 0.08	0.19 ± 0.10	0.19 ± 0.10	7.68 ± 0.51	7.39 ± 0.54	7.57 ± 0.54
e	0.14 ± 0.07	0.21 ± 0.10	0.21 ± 0.12	7.46 ± 0.46	7.29 ± 0.49	7.14 ± 0.48
f	-	0.17 ± 0.08	0.16 ± 0.08	-	5.91 ± 0.41	5.96 ± 0.42
g	0.15 ± 0.08	0.17 ± 0.07	0.17 ± 0.07	7.73 ± 0.43	8.11 ± 0.44	7.98 ± 0.43

	$\overline{\Delta\mathrm{F}}_{\mathrm{f}}{}^{\mathcal{B}}$ (Hz)	$\overline{\Delta\mathrm{F}}_{\mathrm{f}}{}^{\mathcal{CR}}$ (Hz)	$\overline{\Delta\mathrm{F}}_{\mathrm{f}}{}^{\mathcal{PA}}$ (Hz)	$\overline{\overline{\mathrm{F}}}_{\mathrm{f}}{}^{\mathcal{B}}$ (Hz)	$\overline{\overline{\mathrm{F}}}_{\mathrm{f}}{}^{\mathcal{CR}}$ (Hz)	$\overline{\overline{\mathrm{F}}}_{\mathrm{f}}{}^{\mathcal{PA}}$ (Hz)
Average	0.15 ± 0.01	0.18 ± 0.02	0.17 ± 0.03	7.07 ± 0.64	6.93 ± 0.73	6.88 ± 0.71

3.3.2 2D simulation results

In the 2D tissue models, a stable rotor was initiated after application of the S1-S2 protocol in both the $\mathcal{D}_{2D,08}$ and $\mathcal{D}_{2D,30}$ spatial configurations of ACh release. Simulation results in the 2D tissues confirmed that the rotor frequency variations followed the induced ACh patterns (Figure 3.8), with Pearson correlation coefficient r between $\mathrm{ACh}(\mathrm{t})$ and $\mathrm{F}_{\mathrm{f}}(\mathrm{t})$

Table 3.2: $\overline{\mathrm{F}}_{\mathrm{f}}$ and $\Delta\mathrm{F}_{\mathrm{f}}$ (Hz) computed from 2D tissue simulations and from patients' ECGs.

2D SIMULATIONS										**REAL DATA**	
ACh release 0.125 Hz		$\mathcal{D}_{2D,08}$ ΔACh [μM]			$\mathcal{D}_{2D,30}$ ΔACh [μM]			**Mean values in simulation**		**Mean values in patients**	
$\overline{\mathrm{ACh}}$ [μM]		**0.0**	**0.05**	**0.1**	**0.0**	**0.05**	**0.1**				
0.05	$\overline{\mathrm{F}}_{\mathrm{f}}$	8.23	8.57	8.38	8.22	9.04	8.56	$\overline{\overline{\mathrm{F}}}_{\mathrm{f}}$ $\sigma_{\overline{\mathrm{F}}_{\mathrm{f}}}$	8.62 0.34	$\overline{\overline{\mathrm{F}}}_{\mathrm{f}}^{\mathrm{CR}}$ $\sigma_{\overline{\mathrm{F}}_{\mathrm{f}}^{\mathrm{CR}}}$	6.93 0.73
	$\Delta\mathrm{F}_{\mathrm{f}}$	0.00	0.05	0.10	0.00	0.13	0.30				
	r		0.86	0.90		0.91	0.91				
0.075	$\overline{F}_{\mathrm{f}}$	8.49	8.57	N. T.: out of p. range	9.18	9.05	N. T.: out of p. range	$\overline{\Delta\mathrm{F}_{\mathrm{f}}}$ $\sigma_{\Delta F_{\mathrm{f}}}$	0.13 0.09	$\overline{\Delta F_{\mathrm{f}}}^{CR}$ $\sigma_{\Delta F_{\mathrm{f}}^{CR}}$	0.18 0.02
	$\Delta\mathrm{F}_{\mathrm{f}}$	0.00	0.04		0.00	0.15					
	r		0.88			0.93					

being above 0.86 in all cases, as reported in Table 3.2. Furthermore, r increased with $\overline{\mathrm{ACh}}$ and $\Delta\mathrm{ACh}$. The mean dominant frequency $\overline{\mathrm{F}}_{\mathrm{f}}$ was found to be dependent on the $\overline{\mathrm{ACh}}$ level, while its magnitude of modulation $\Delta\mathrm{F}_{\mathrm{f}}$ was dependent on $\Delta\mathrm{ACh}$, with increases in $\overline{\mathrm{ACh}}$ and $\Delta\mathrm{ACh}$ leading to increases in $\overline{\mathrm{F}}_{\mathrm{f}}$ and $\Delta\mathrm{F}_{\mathrm{f}}$, respectively.

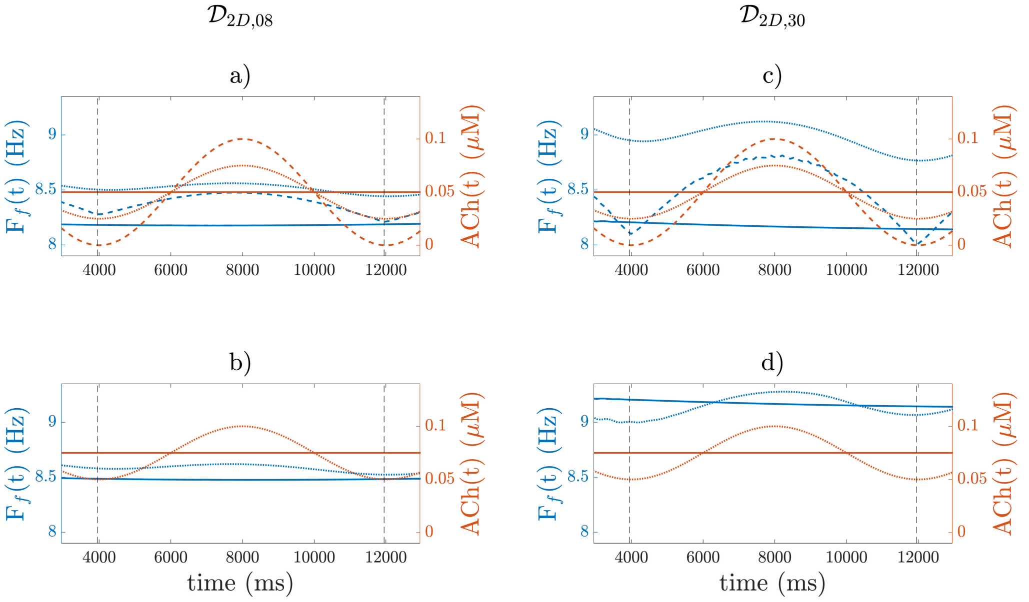

Figure 3.8: Results from 2D tissue simulations with $\mathcal{D}_{2D,08}$ (panels a and b) and $\mathcal{D}_{2D,30}$ (panels c and d) spatial configurations of ACh release. $\mathrm{F}_{\mathrm{f}}(\mathrm{t})$ (blue) and $\mathrm{ACh}(\mathrm{t})$ (red) are plotted in all panels for $\overline{\mathrm{ACh}}$ of 0.05 μM (a, c) and 0.075 μM (b, d) represented as red horizontal lines. Solid/dotted/dashed lines represent $\Delta\mathrm{ACh}$ values of 0.0/0.05/0.1 μM. In panels b and d, $\Delta\mathrm{ACh}$=0.1 μM was not included, as $\mathrm{ACh}(\mathrm{t})$ contained non-physiological ACh values.

3.3.3 3D simulation results under S1-S2 stimulation

In the 3D biatrial models, S1-S2 stimulation was able to generate multiple stable rotors. The induced fibrillatory patterns were different for the distinct spatial configurations of ACh release, with the generation of 2 to 5 stable rotors, as represented in Figure 3.9.

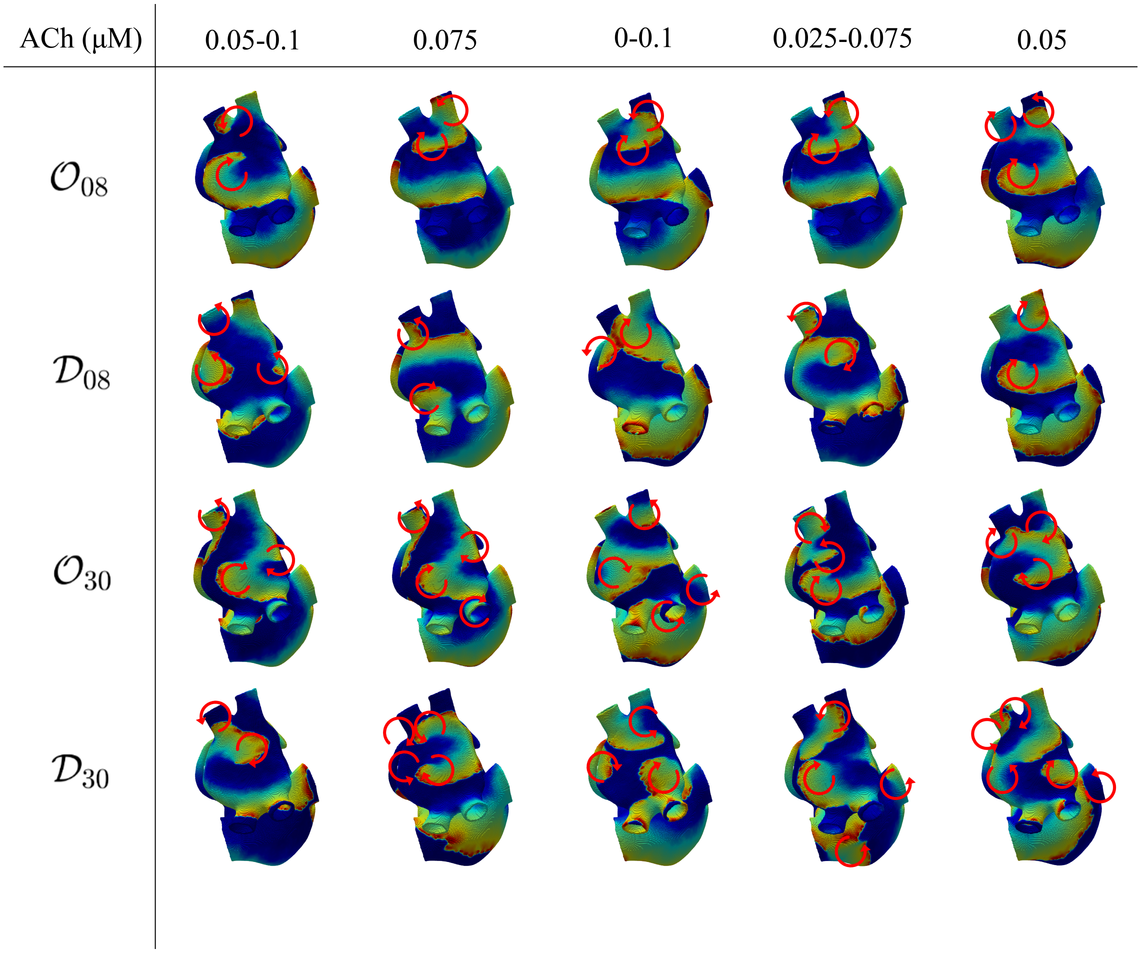

Figure 3.9: Voltage maps representative of the induced fibrillatory pattern after application of S1-S2 stimulation. Each circular arrow represents the location of a rotor with its direction of rotation. The ACh values indicate a constant ACh release when only a number is reported, corresponding to $\overline{\mathrm{ACh}}$, and to a range of variation when two numbers are given, corresponding to $\overline{\mathrm{ACh}} \pm \Delta\mathrm{ACh}$.

We observed a general increase in the number of stable rotors with the highest percentage of ACh release nodes ($\mathcal{O}_{30}$ and $\mathcal{D}_{30}$). In all cases, the rotors stabilized in the LA, with only three exceptions: $\mathcal{O}_{30}$ model with ACh varying from 0.0 to 0.1 μM, $\mathcal{D}_{30}$ model with ACh varying from 0.025 to 0.075 μM and $\mathcal{D}_{30}$ model with ACh equal to 0.05 μM, for which 2 to 4 stable rotors in the LA and 1 to 2 stable rotors in the RA were observed.

Figure 3.10, bottom row, illustrates voltage maps at different time instants for the case of multiple reentries generated by S1-S2 stimulation in the $\mathcal{D}_{30}$ model, with $\mathrm{ACh(t)}$ varying from 0 to 0.1 μM (ΔACh=0.1 μM).

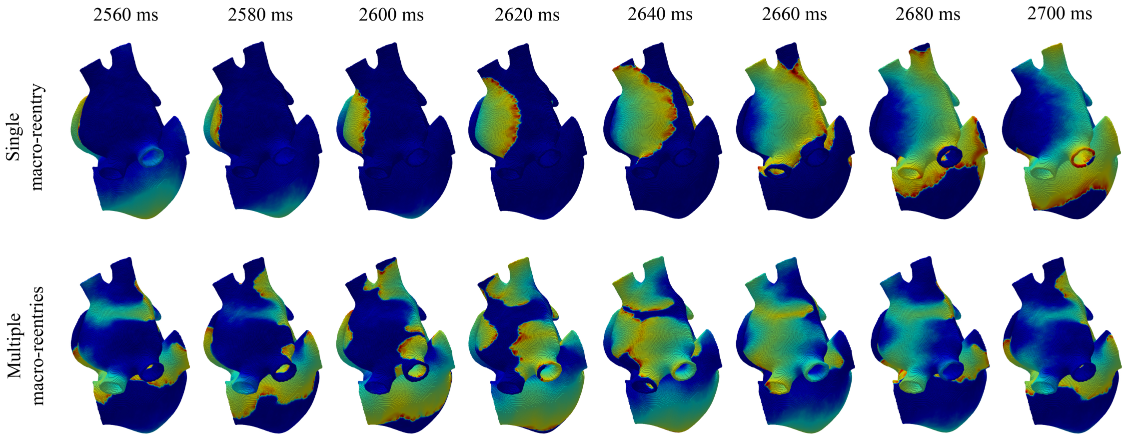

Figure 3.10: Voltage maps in a simulation where, after ectopic beat stimulation, a single macro-reentry was initiated (top panel) and in a simulation where, after S1-S2 stimulation, multiple macro-reentries were initiated (bottom panel).

For the four spatial ACh release models, i.e. $\mathcal{O}_{08}$, $\mathcal{D}_{08}$, $\mathcal{O}_{30}$ and $\mathcal{D}_{30}$, the atrial dominant frequency followed the induced $\mathrm{ACh(t)}$ patterns (Figure 3.11 and Figure 3.12), similarly to the observations in the 2D tissues. For $\mathcal{O}_{08}$ and $\mathcal{D}_{08}$, the Pearson correlation coefficient values r were above 0.72 and 0.45 for $\Delta\mathrm{ACh} = 0.1$ and $\Delta\mathrm{ACh} = 0.05$ μM, respectively, while for $\mathcal{O}_{30}$ and $\mathcal{D}_{30}$, the r values were above 0.54 and 0.80.

Table 3.3 shows $\overline{\mathrm{F}}_\mathrm{f}$ and $\Delta\mathrm{F}_\mathrm{f}$ for each of the simulated cases. $\Delta\mathrm{F}_\mathrm{f}$ was found to be highly dependent on ΔACh. Furthermore, for 30% ACh release nodes, $\Delta\mathrm{F}_\mathrm{f}$ was higher in the diffuse than in the octopus configuration. For 8%, the spatial distribution of ACh release did not have significant effects on $\Delta\mathrm{F}_\mathrm{f}$ when all other factors were kept constant. We observed that when the fibrillatory patterns in the 3D models were similar to one another, as occurs for the $\mathcal{O}_{08}$ and $\mathcal{D}_{08}$ models with $\Delta\mathrm{ACh} = 0.05$ μM, or for the $\mathcal{D}_{08}$ model with $\Delta\mathrm{ACh} = 0.0$ μM, our results were in accordance with those in 2D tissues, with $\overline{\mathrm{F}}_\mathrm{f}$ increasing with $\overline{\mathrm{ACh}}$. As expected, we also observed an increase in the dominant f-wave frequency with the number of stable rotors in the atria regardless the $\overline{\mathrm{ACh}}$ level. The octopus $\mathcal{O}$ and diffuse $\mathcal{D}$ configurations did not seem to correlate to the induced fibrillatory pattern and did not cause significant variations in terms of $\overline{\mathrm{F}}_\mathrm{f}$, at least for 8% ACh release

Table 3.3: $\overline{\mathrm{F}}_\mathrm{f}$ and $\Delta\mathrm{F}_\mathrm{f}$ (Hz) computed from 3D biatrial simulations in response to S1-S2 stimulation and from patients' ECGs.

3D S1-S2 SIMULATIONS										**REAL DATA**	
ACh release 0.125 Hz		$\mathcal{O}_{08}$			$\mathcal{D}_{08}$			**Mean values in simulation**		**Mean values in patients**	
		ΔACh [μM]			ΔACh [μM]						
ACh [μM]		**0.0**	**0.05**	**0.1**	**0.0**	**0.05**	**0.1**				
0.05	$\overline{F_f}$	7.69	7.66	7.66	7.43	7.42	7.63	$\overline{\overline{\mathrm{F}}}_\mathrm{f}$	7.59		
	$\Delta\mathrm{F}_\mathrm{f}$	0.00	0.01	0.11	0.00	0.01	0.08	$\sigma_{\overline{\mathrm{F}}_\mathrm{f}}$	0.13		
	r		0.45	0.80		0.46	0.72				
0.075	$\overline{F_f}$	7.43	7.73	N. T.: out of p. range	7.51	7.76	N. T.: out of p. range			$\overline{\overline{\mathrm{F}}}_\mathrm{f}^{CR}$	6.93
	$\Delta\mathrm{F}_\mathrm{f}$	0.01	0.02		0.00	0.01		$\overline{\Delta\mathrm{F}_\mathrm{f}}$	0.04	$\sigma_{\overline{\mathrm{F}}_\mathrm{f}^{\mathrm{CR}}}$	0.73
	r		0.47			0.59		$\sigma_{\Delta F_f}$	0.04		
		$\mathcal{O}_{30}$			$\mathcal{D}_{30}$						
0.05	$\overline{F_f}$	8.86	8.92	8.04	8.87	8.33	8.30	$\overline{\overline{\mathrm{F}}}_\mathrm{f}$	8.47		
	$\Delta\mathrm{F}_\mathrm{f}$	0.00	0.04	0.19	0.00	0.12	0.35	$\sigma_{\overline{\mathrm{F}}_\mathrm{f}}$	0.49		
	r		0.95	0.59		0.80	0.54			$\overline{\Delta\mathrm{F}_\mathrm{f}}^{CR}$	0.18
0.075	$\overline{F_f}$	8.96	8.89	N. T.: out of p. range	7.84	7.70	N. T.: out of p. range			$\sigma_{\Delta F_f^{CR}}$	0.02
	$\Delta\mathrm{F}_\mathrm{f}$	0.00	0.03		0.00	0.03		$\overline{\Delta\mathrm{F}_\mathrm{f}}$	0.13		
	r		0.89			0.96		$\sigma_{\Delta F_f}$	0.12		

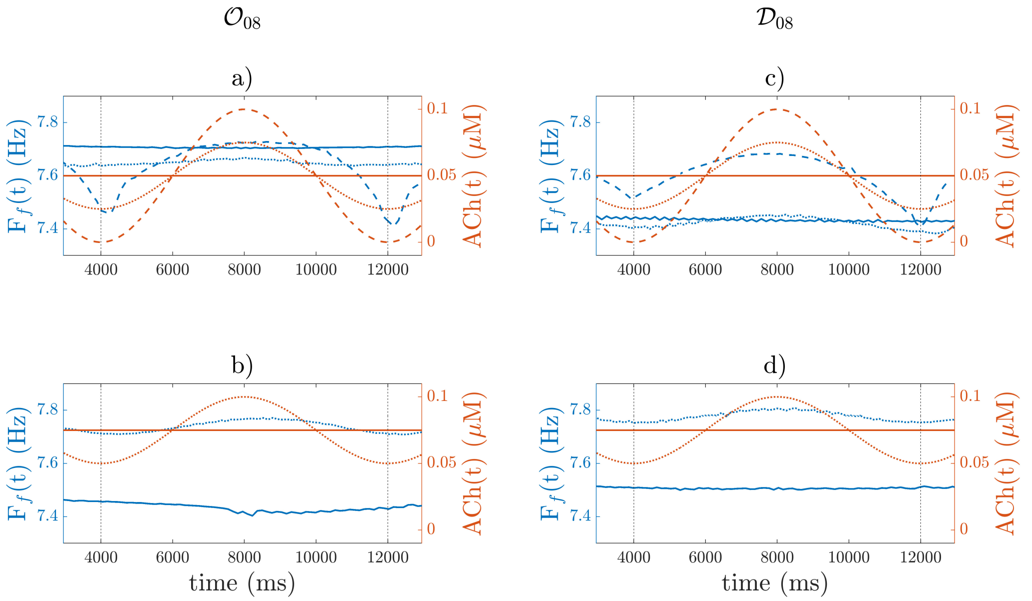

Figure 3.11: Results from 3D biatrial simulations with $\mathcal{O}_{08}$ (panels a and b) and $\mathcal{D}_{08}$ (panels c and d) spatial configurations of ACh release and application of S1-S2 stimulation. $\mathrm{F}_\mathrm{f}(\mathrm{t})$ (blue) and $\mathrm{ACh}(\mathrm{t})$ (red) are plotted in all panels for $\overline{\mathrm{ACh}} = 0.05$ μM (a, c) and $\overline{\mathrm{ACh}} = 0.075$ μM (b, d). Solid/dotted/dashed lines represent ΔACh values of 0.0/0.05/0.1 μM . In panels (b, d), ΔACh=0.1 μM was not included, as $\mathrm{ACh}(\mathrm{t})$ contained non-physiological ACh values.

nodes. For 30% ACh release nodes, significant differences in $\overline{\mathrm{F}}_\mathrm{f}$ could be observed in several cases (up to -12.5% when comparing $\mathcal{O}_{30}$ with respect to $\mathcal{D}_{30}$ under $\overline{\mathrm{ACh}}$=0.075 μM and ΔACh=0 μM) while little or no differences could be observed in other cases.

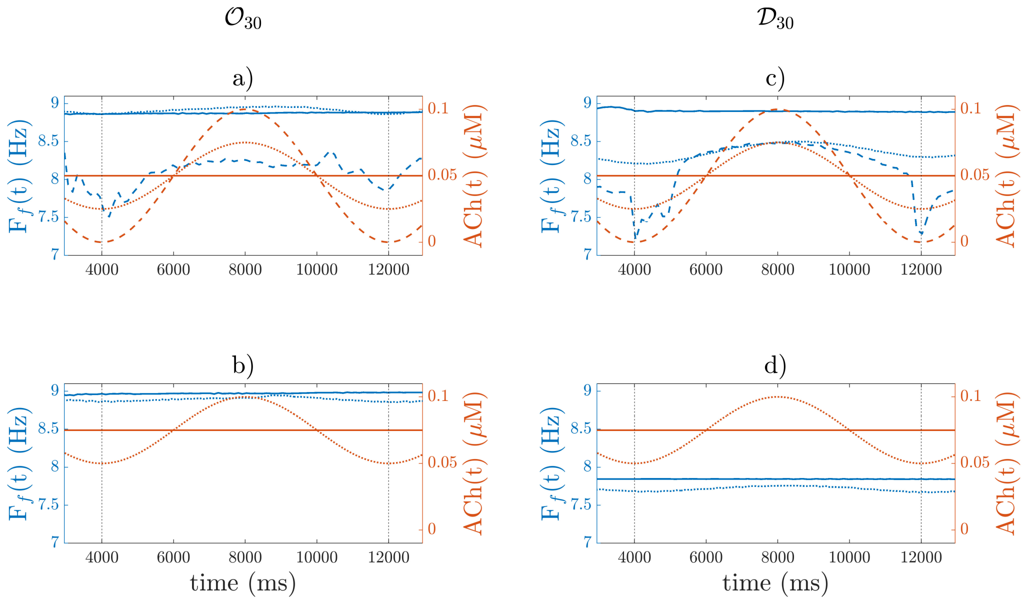

Figure 3.12: Results from 3D biatrial simulations with $\mathcal{O}_{30}$ (panels a and b) and $\mathcal{D}_{30}$ (panels c and d) spatial configurations of ACh release and application of S1-S2 stimulation. The figure is structured as Figure 3.11

3.3.4 3D simulation results under stimulation with a train of ectopic beats

When the 3D biatrial models were stimulated with a train of ectopic beats, a macro-reentry through the coronary sinus was generated in all cases. Figure 3.10, top row, illustrates voltage maps at different time instants in the case of a single macro-reentry in the $\mathcal{D}_{30}$ model, with ACh(t) varying from 0 to 0.1 μM (ΔACh=0.1 μM). In this case, the rotor frequency variations $F_{\mathrm{f}}(t)$ were in opposite phase to the induced ACh(t) patterns (Figure 3.13 and Figure 3.14).

Table 3.4 reports $\overline{\mathrm{F}}_{\mathrm{f}}$ and $\Delta\mathrm{F}_{\mathrm{f}}$ for each of the simulated cases. $\Delta\mathrm{F}_{\mathrm{f}}$ was greatly influenced by both ΔACh and the number of ACh release nodes. Moreover, $\overline{\mathrm{F}}_{\mathrm{f}}$ was observed to increase along with ΔACh. However, the relationship between $\overline{\mathrm{F}}_{\mathrm{f}}$ and $\overline{\mathrm{ACh}}$ was not consistent across all cases. In some instances, there was a decrease, in others an increase, and in yet others, no change was observed. For both 8% and 30% ACh release nodes, $\Delta\mathrm{F}_{\mathrm{f}}$ was higher in the diffuse than in the octopus configurations. Again, the different spatial distributions of ACh release, i.e. $\mathcal{O}$ and $\mathcal{D}$ configurations, did not cause significant variations in

Table 3.4: $\overline{\mathrm{F}}_\mathrm{f}$ and $\Delta\mathrm{F}_\mathrm{f}$ (Hz) computed from 3D biatrial simulations in response to a train of ectopic beats and from patients' ECGs.

SIMULATIONS 3D ECTOPIC										**REAL DATA**	
ACh release 0.125 Hz		$\mathcal{O}_{08}$			$\mathcal{D}_{08}$			**Mean values in simulation**		**Mean values in patients**	
		ΔACh [μM]			ΔACh [μM]						
$\overline{\mathrm{ACh}}$ [μM]		**0.0**	**0.05**	**0.1**	**0.0**	**0.05**	**0.1**				
0.05	$\overline{F}_\mathrm{f}$	5.18	5.19	5.21	5.03	5.11	5.18	$\overline{\overline{\mathrm{F}}}_\mathrm{f}$	5.12		
	$\Delta\mathrm{F}_\mathrm{f}$	0.000	0.005	0.011	0.000	0.015	0.050	$\sigma_{\overline{\mathrm{F}}_\mathrm{f}}$	0.09		
	r		-0.58	-0.63		-0.96	-0.94				
0.075	$\overline{F}_\mathrm{f}$	5.18	5.18	N. T.: out of p.range	4.97	4.97	N. T.: out of p.range	$\overline{\Delta\mathrm{F}_\mathrm{f}}$	0.02	$\overline{\overline{\mathrm{F}}}_\mathrm{f}{}^{CR}$	6.93
	$\Delta\mathrm{F}_\mathrm{f}$	0.000	0.001		0.000	0.022		$\sigma_{\Delta F_\mathrm{f}}$	0.02	$\sigma_{\overline{\mathrm{F}}_\mathrm{f}{}^{\mathrm{CR}}}$	0.73
	r		-0.39			-0.91					
		$\mathcal{O}_{30}$			$\mathcal{D}_{30}$						
0.05	$\overline{F}_\mathrm{f}$	4.52	4.76	4.99	4.60	4.74	4.94	$\overline{\overline{\mathrm{F}}}_\mathrm{f}$	4.77		
	$\Delta\mathrm{F}_\mathrm{f}$	0.000	0.055	0.150	0.000	0.066	0.156	$\sigma_{\overline{\mathrm{F}}_\mathrm{f}}$	0.15		
	r		-0.94	-0.94		-0.96	-0.91			$\overline{\Delta\mathrm{F}_\mathrm{f}}{}^{CR}$	0.18
0.075	$\overline{F}_\mathrm{f}$	4.62	4.66	N. T.: out of p.range	4.63	4.65	N. T.: out of p.range			$\sigma_{\Delta F_\mathrm{f}{}^{CR}}$	0.02
	$\Delta\mathrm{F}_\mathrm{f}$	0.000	0.062		0.000	0.047		$\overline{\Delta\mathrm{F}_\mathrm{f}}$	0.08		
	r		-0.87			-0.96		$\sigma_{\Delta F_\mathrm{f}}$	0.04		

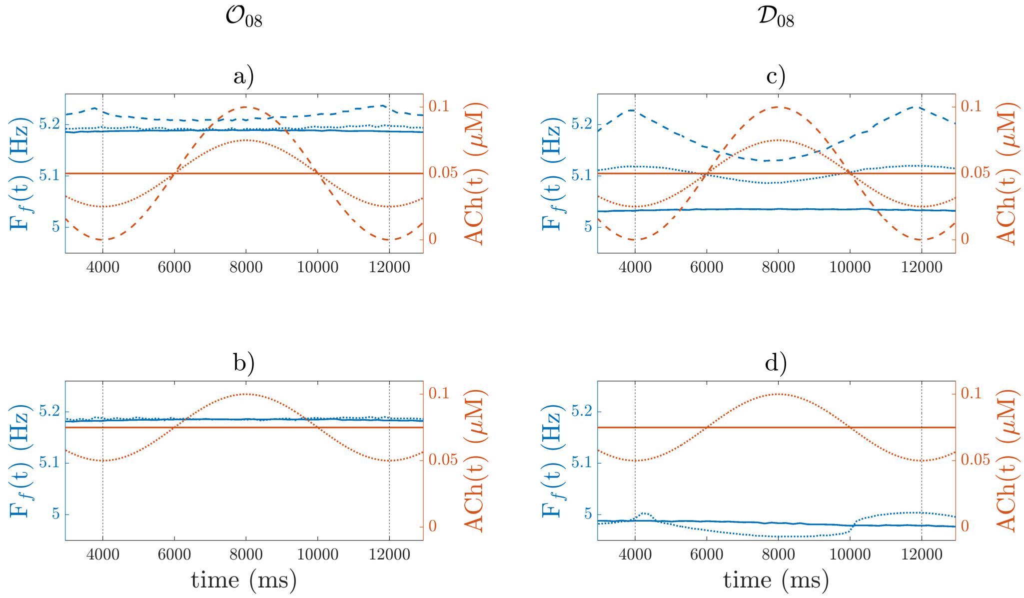

Figure 3.13: Results from 3D biatrial simulations with $\mathcal{O}_{08}$ (panels a and b) and $\mathcal{D}_{08}$ (panels c and d) spatial configurations of ACh release and application of a train of ectopic beats. The figure is structured as Figure 3.11

$\overline{\mathrm{F}}_\mathrm{f}$. The absolute values of the Pearson correlation coefficient r were above 0.87 for $\mathcal{O}_{30}$ and $\mathcal{D}_{30}$ and above 0.91 for $\mathcal{D}_{08}$. For $\mathcal{O}_{08}$, the r values were above 0.58 for $\overline{\mathrm{ACh}}$=0.05 μM and equal to 0.39 for $\overline{\mathrm{ACh}}$=0.075 μM.

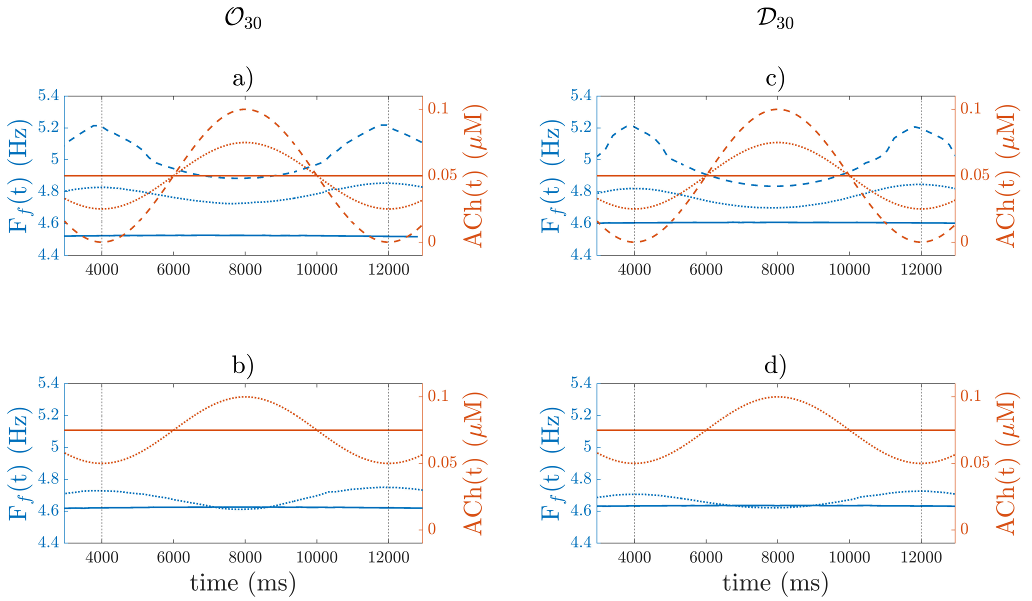

Figure 3.14: Results from 3D biatrial simulations with $\mathcal{O}_{30}$ (panels a and b) and $\mathcal{D}_{30}$ (panels c and d) spatial configurations of ACh release and application of a train of ectopic beats. The figure is structured as Figure 3.11

It can be noted that, when comparing simulated and clinical results, mean $\overline{\mathrm{F}}_{\mathrm{f}}$ was approximately 1 to 2 Hz higher in both the simulations of 2D tissue models and of 3D biatrial models stimulated with the S1-S2 protocol than in the patients, while, in the 3D biatrial models stimulated with a train of ectopic beats, it was approximately 1 to 2 Hz lower. In the 3D models, the mean of $\Delta\mathrm{F}_{\mathrm{f}}$ values were lower than in the patients for models with 8% of ACh release nodes and close to the patients' values for models with 30% of ACh release nodes.

3.4 Discussion

3.4.1 Characterization of f-wave frequency variations in response to cholinergic stimulation

We used computational modeling and simulation to assess the role of the ANS in the modulation of f-wave frequency. We built 2D tissue and 3D biatrial models in which we included different spatial distributions of ACh release. By additional modeling of the temporal evolution of cholinergic stimulation, we computed its impact on the atrial fibrillatory rate. We compared our simulation results with those from the analysis of patients' ECGs, which showed that, in as much as 50% of the patients, the f-wave frequency modulation was strongly reduced after injection of the anticholinergic agent atropine. After confirmation of the agreement between simulation and clinical outcomes, we used our *in silico* approach to dissect the influence of spatiotemporal ACh release characteristics on f-wave frequency modulation independently of other factors.

For a comprehensive characterization of cholinergic effects on f-wave frequency modulation, we conducted simulations with different spatial configurations of ACh release, using a sinusoidal waveform with varying mean concentrations and peak-to-peak variation ranges of ACh. We also used two stimulation protocols: the S1-S2 protocol and a train of ectopic beats near the pulmonary veins in the 3D models.

We discovered that the f-wave frequency responded to changes in ACh levels in both 2D tissue and 3D biatrial models. The average f-wave frequency was mainly influenced by the fibrillatory pattern, which was determined by the number and location of stable reentrant circuits. Additionally, the percentage of ACh release nodes and the mean ACh concentration also contributed to the mean f-wave frequency. The peak-to-peak variation in the f-wave frequency was primarily affected by the percentage of ACh release nodes and the temporal changes in ACh concentration. The distribution of ACh release sites, whether dispersed or in an octopus-like arrangement, had a minor impact.

More in detail, application of an S1-S2 protocol generated a single stable rotor in all 2D simulations while, in the 3D simulations, multiple stable reentries (2 to 5) were generated. In almost all the simulated cases, the generated rotors stabilized in the LA. Only in three cases, we observed stable rotors also in the RA. Rotor stabilization in the LA was expected, considering that we delivered the S1 and S2 stimuli in the region between the 4 pulmonary veins in the LA. The delivery of the stimuli in other atrial regions would be expected to lead to different fibrillatory patterns, with rotors stabilizing in other regions. Since we were interested in analyzing the ACh effects on the modulation of the atrial dominant frequency, our goal was to induce similar atrial activations in the different simulated cases to establish a comparison while reducing the influence of other factors. Nevertheless, we would not expect qualitatively different results when stimulating other atrial regions. When a train of ectopic beats was used to stimulate the atria, we observed a single macro-reentry in all cases. During both S1-S2 and ectopic stimulation, we did not include stimuli coming from the sinus node to avoid more complex electrical activation patterns due to wavefront collision. The more stable patterns of atrial activation in our study allowed improved characterization of ACh effects over a period of eight seconds.

The f-wave frequency trend $\mathrm{F_f(t)}$ was computed and characterized with two variables: its temporal mean $\mathrm{\overline{F}_f}$; and the range of its modulation $\mathrm{\Delta F_f}$. We found a clear correlation between the induced $\mathrm{ACh(t)}$ pattern and the computed $\mathrm{F_f(t)}$ trend, with variations in $\mathrm{F_f(t)}$ following the variations of $\mathrm{ACh(t)}$ throughout the atria, both for 8% and 30% of ACh release nodes. In the 2D tissues, where the fibrillatory activity consisted of a single stable rotor, we found that $\mathrm{F_f(t)}$ varied in phase with $\mathrm{ACh(t)}$. In 3D biatrial anatomies, we found that $\mathrm{F_f(t)}$ was in phase with $\mathrm{ACh(t)}$ when multiple reentries (AF pattern) were generated and was out of phase when a single macro-reentry (more similar to atrial flutter) was generated. A possible explanation could lie on the different relative contribution of CV and APD to the fibrillatory phenomena. For cases with a single macro-reentry, the main factor determining $\mathrm{F_f(t)}$ modulation induced by ACh was CV. When ACh increased,, the mean CV throughout the atria decreased and this led to a decrease in the rotation frequency of the macro-reentry. For cases with multiple stable rotors, $\mathrm{F_f(t)}$ modulation was mainly determined by the shortening of the APD and ERP. For the highest ACh value, the APD and ERP were at its minimum and the rotor spun at an increased frequency due to the tissue being available earlier to be depolarized.

3.4.2 Contributors to mean f-wave frequency

$\mathrm{\overline{F}_f}$ was found to strongly depend on the fibrillatory pattern, generally increasing for a larger number of rotors. This finding was expected, considering that the larger the number of rotors, the smaller their size and the faster their spin. There were two exceptions to our findings, corresponding to the $\mathcal{O}_{30}$ configuration with $\mathrm{\Delta ACh}$ of 0.0 and 0.05 μM. Those cases showed a higher number of rotors under 0.075 μM $\mathrm{\overline{ACh}}$, but $\mathrm{\overline{F}_f}$ was equal or higher under lower $\overline{\mathrm{ACh}}$. A possible explanation could be based on the fact that, for the lower $\overline{\mathrm{ACh}}$, the rotors were closer in space, which led to smaller and faster spinning rotors. Conversely, in the other cases, while the number of rotors was higher, they were further apart from one another, resulting in larger and slower rotors.

The percentage of ACh release nodes in the atria emphasized the dependence of $\overline{\mathrm{F}}_{\mathrm{f}}$ on the fibrillatory pattern. A larger proportion of ACh release nodes led to higher $\overline{\mathrm{F}}_{\mathrm{f}}$ in the case of multiple reentries and lower $\overline{\mathrm{F}}_{\mathrm{f}}$ in the case of one single macro-reentry.

A third factor influencing $\overline{\mathrm{F}}_{\mathrm{f}}$ was $\overline{\mathrm{ACh}}$, which increased or decreased $\overline{\mathrm{F}}_{\mathrm{f}}$ in the same way as the percentage of $\overline{\mathrm{ACh}}$ release.

The spatial distribution of ACh release nodes (diffuse or octopus) did not seem to be directly correlated to $\overline{\mathrm{F}}_{\mathrm{f}}$. In most cases, no significant differences were observed between diffuse and octopus configurations, with only noticeable differences (up to 12%) found in specific cases, which could, however, be attributed to the fibrillatory pattern. Actually, for single macro-reentries, the differences in $\overline{\mathrm{F}}_{\mathrm{f}}$ between octopus and diffuse distributions were negligible. The higher differences were observed for the most chaotic AF patterns generated after S1-S2 stimulation in models with 30% ACh release nodes, where the fibrillatory pattern could have a larger impact.

Comparing simulation and clinical results in terms of $\overline{\mathrm{F}}_{\mathrm{f}}$, we found higher $\overline{\mathrm{F}}_{\mathrm{f}}$ values for the models stimulated with an S1-S2 protocols and lower values for the models stimulated with a train of ectopic beats with respect to the clinical $\overline{\mathrm{F}}_{\mathrm{f}}$ values. In the simulations, the main factor determining $\overline{\mathrm{F}}_{\mathrm{f}}$ is the excitation pattern. For similar fibrillatory patterns, the differences in $\overline{\mathrm{F}}_{\mathrm{f}}$ could be attributed to $\overline{\mathrm{ACh}}$. The differences between simulation and clinical outcomes could be explained by the contribution of CV and the amount of fibrosis, on top of the values of $\overline{\mathrm{ACh}}$. Furthermore, the overestimation of $\overline{\mathrm{F}}_{\mathrm{f}}$ under S1-S2 stimulation may also depend on the APD of the cellular electrophysiological model. Indeed, the Courtemanche model used in this study has a steady-state APD that is at the lower end of the experimentally reported APD range.

3.4.3 Contributors to magnitude of f-wave frequency modulation

$\Delta\mathrm{F_f}$ was found to be directly dependent on the percentage of ACh release nodes and on $\Delta\mathrm{ACh}$. The spatial configuration of ACh release sites showed mild impact only for the highest (30%) percentage of ACh release nodes.

Comparing simulated and clinical values of $\Delta\mathrm{F_f}$, better agreement was overall observed when considering 30% of ACh release nodes, either in a diffuse or octopus configuration. Higher values of $\Delta\mathrm{ACh}$ and larger percentages of ACh release sites along the atria could lead to simulated $\Delta\mathrm{F_f}$ being closer to the values measured from clinical data.

3.4.4 Comparison between simulations and clinical data

The inclusion of real data in our study was useful in determining a comprehensive range for the mean f-wave frequency and the magnitude of respiratory modulation. While not all our findings lie within this established range, there is some degree of overlap. The observed discrepancies could be attributed to various factors and can arise from limitations of either clinical data or simulations.

First, it is important to highlight the limited number of patients in the clinical database. Furthermore, while in simulations the modulation of the fibrillatory rate is determined only by ACh, in clinical signals variations in the respiratory frequency band can be influenced by other factors other than respiration. Mechanical stretch, mechano-electrical feedback or the endocrine system have been reported as possible modulators for the fibrillatory frequency [316]. These other mechanisms may interfere in a possibly nonlinear manner with the effects of ACh. Additionally, in the simulation setting, the use of a single anatomical model and a single model describing cellular electrophysiology may not have fully captured the inter-patient variability observed in the clinical scenario.

3.5 Study limitations and future work

Some limitations of this study should be acknowledged to provide direction for further work.

The clinical results are based on the method proposed in [301], where all variations in the respiratory frequency interval are considered in the estimation of the respiratory modulation. Hence, variations in such frequency band that are unrelated to respiration may influence the result. In a more recent study, a subspace projection approach that only considers variations linearly related to respiration was proposed to quantify respiratory f-wave frequency modulation [317]. However, the subspace projection approach could not be applied to the present dataset, since it requires a respiratory signal. In [317], a respiratory signal was derived from the ECG, but the presence of pacemaker spikes in the present dataset makes that approach unfeasible.

Another aspect that needs to be addressed is the inter-patient variability observed in the clinical cases reported in Abdollahpur et al. [301], in which atropine reduced atrial frequency variability in just half of the patients. This phenomenon can possibly be attributed to factors beyond the effects mediated by the ANS. One such factor could be the influence of mechanical stretch and mechano-electrical feedback on respiratory-related atrial rate variability. Different studies have shown that atrial tissue stretch affects atrial conduction and refractoriness in humans [311, 318]. The changes in electrical behavior resulting from stretch can be explained by the concept of mechanoelectrical feedback, which involves the activation of stretch-activated ion channels [319, 320]. Additionally, stretch can also modulate the concentration of calcium inside the cells, either by increasing the sensitivity of myofilaments to calcium or by triggering the entry of calcium ions [321]. Indeed, the mechanical regulation of heart rate has been proposed as a factor influencing RSA in heart transplant recipients [322, 323]. It also plays a significant role in conditions associated with reduced vagal tone, such as mild HF [324], and in healthy individuals during exercise [323, 325]. However, in normal physiological conditions, mechanical mechanisms are secondary to the effects of the ANS in modulating SAN pacemaker activity and, consequently, determining RSA [309]. Extensive analysis has been conducted to understand the mechanical modulation, including cardiorespiratory modulation, of atrial activity, specifically in the case of atrial flutter [309, 311, 312, 326]. Waxman et al. [326] observed that certain interventions, such as passive upright tilting, the strain phase of the Valsalva maneuver and expiration, all of which reduce cardiac size, independently increased the rate of atrial flutter regardless of autonomic tone. Similarly, Ravelli et al. [311] found that acute atrial stretch caused by ventricular contractions and respiratory movements led to a shortening of the atrial flutter cycle length in humans. They attributed this phenomenon to the stretch-induced shortening of atrial ERP. Importantly, they also discovered that both ventricular and respiratory oscillations in atrial flutter cycle length persisted even after autonomic blockade, suggesting that these oscillations are independent of autonomic tone. Focusing on AF, the modeling studies of Kuijpers and coworkers [327, 328] provided a detailed understanding of mechanoelectrical currents at the ionic level and their impact on AF. In their investigations, Kuijpers focused on the role of the stretch-activated current I_{sac} in conduction slowing and block, particularly in acutely dilated atria. They discovered that the magnitude of I_{sac} was associated with the local stretch ratio. Local heterogeneity in the activation of I_{sac}, leading to dispersion of refractoriness and variation in conduction properties, increased susceptibility to AF.

Due to a lack of comprehensive understanding of the spatial distribution of parasympathetic innervation in the atria, we followed two approaches to represent ACh release nodes. One of such approaches is based on the octopus configuration reported in previous anatomical studies [52], which includes the spatial location of GPs and nerves departing from them. In the GPs, despite the predominance of parasympathetic fibers, sympathetic fibers can be found too [56]. Here, we only considered cholinergic stimulation but future work could include additional modeling of the adrenergic stimulation.

We used the Courtemanche model to describe human atrial electrophysiology. Further investigations using other computational AP models with longer steady-state APD values could be conducted to assess the impact on f-wave frequency characterizations. Also, additional values of the longitudinal conductivity and the transverse-to-longitudinal conductivity ratio in the atrial tissue could be tested to identify the values leading to closer agreement between simulated and clinical f-wave frequency variables.

The computational models presented here were representative of psAF patients. As reported in section 1.3.3, structural changes in the atria due to AF may present as various alterations such as an enlarged atrial chamber, hypertrophy of cardiomyocytes, increased mismatch between epicardial and endocardial myofibers' orientations, changes in atrial wall thickness and, notably, an increased amount of fibrotic or connective tissue. [81–83]. As illustrated in 2.4, we represented psAF-related structural remodeling by a combination of GJs remodeling, modeled through tissue conductance reduction in fibrotic regions, and fibroblast proliferation. The latter was modeled by assigning some of the mesh nodes with fibroblast rather than myocyte properties and by using a fibroblast ionic model [283].

3.6 Conclusions

We assessed the impact of the spatiotemporal release pattern of ACh on f-wave frequency modulation. In agreement with clinical data, we found that the f-wave frequency varied in response to the temporal variation of ACh in both 2D tissue and 3D biatrial models. The mean f-wave frequency was found to be primarily dependent on the fibrillatory pattern, being largely determined by the number and spatial location of stable reentrant circuits. Other factors contributing to the mean f-wave frequency were the percentage of ACh release nodes throughout the atria and the mean ACh concentration. The magnitude of the f-wave frequency modulation was found to be dependent on the percentage of ACh release nodes and the variation over time in the ACh concentration. The spatial distribution of ACh release sites, either diffuse or following an octopus configuration, showed only mild impact.

Chapter 4

Analysis of variations in atrial fibrillatory rate induced by autonomic maneuvers

4.1 Motivation

Assessing autonomic activity in AF patients could be highly relevant, as inter-patient variability in ANS activity might contribute to explain the large differences in the effectiveness of anti-AF therapies between patients. RSA, as introduced in Chapter 3, accounts for parasympathetic modulation of the SAN activity in synchrony with the respiratory cycle and can be quantified from the high-frequency components of HRV [329]. This approach is suitable to assess autonomic regulation in SR but not in AF, since the cardiac rhythm is not dictated by the SAN.

During AF, the mean frequency of the f-waves in the ECG, often referred to as AFR and characterized by $\mathrm{F_f}$, has been employed as a surrogate marker for local refractoriness. Observations from different studies have suggested that changes in autonomic balance can result in $\mathrm{F_f}$ oscillations ($\mathrm{F_f(t)}$). In particular, it has been reported that the dominant AF frequency follows a circadian pattern, with an increase during the daytime and a decrease at night [330]. Controlled respiration has also been shown to cause short-term modulation of

$\mathrm{F_f}$, leading to cyclic fluctuations that can be later suppressed by vagal blockade [301]. Other studies [301, 317, 331], already described in Chapter 3, have indicated that, in addition to $\mathrm{F_f}$, the magnitude of the respiratory f-wave frequency modulation, ΔF_{f}, could provide additional insights into the parasympathetic modulation of the f-wave frequency, similarly to the observations made for RSA in SR.

In this chapter, we investigated the relationship between autonomic influences and changes in $\overline{\mathrm{F}}_{\mathrm{f}}$ and in ΔF_{f} during head-up tilt test (HUT) and head-down tilt test (HDT). We used computational modeling and simulation to evaluate $\mathrm{F_f(t)}$ under different combinations of β-adrenergic stimulation, as a means to represent enhanced sympathetic stimulation (SS) in the patients, and cholinergic stimulation, as a means to represent enhanced parasympathetic stimulation (PSS) in the patients. Cholinergic stimulation in the computational models was described as a function of the spatiotemporal release pattern of the parasympathetic neutrotransmitter ACh. Simulation results were compared to the findings from clinical ECG analysis obtained from the psAF patients who underwent a tilt test protocol.

4.2 Methods

4.2.1 Clinical recordings

The research population comprised 29 psAF patients, with a mean age of 64 ± 12 years, who underwent a tilt table test. During the tilt table examination, 12-lead ECGs were recorded in three distinct phases: five minutes in the baseline (BL) supine position, five minutes in the HDT position ($-30°$) and five minutes in the HUT position ($+60°$). Additional details are provided in[298].

From the ECGs, the trend of the f-wave frequency time series, denoted as $\mathrm{F_f(t)}$, was estimated using a model-based approach [300], as previously described [301]. Unlike in the database used in Chapter 3, the respiratory signal was not available for the recordings here analyzed. An orthogonal subspace projection technique was used to extract respiration-related fluctuations in the f-wave frequency trend. [317]. $\overline{\mathrm{F}}_{\mathrm{f}}$ and $\Delta\mathrm{F_f}$ were computed using a method similar to the one presented in section 3.2.5. In brief, $\overline{\mathrm{F}}_{\mathrm{f}}$ was computed as the average value over time of $\mathrm{F}_{\mathrm{f}}(\mathrm{t})$. To compute $\Delta\mathrm{F}_{\mathrm{f}}$, the time series $\mathrm{F}_{\mathrm{f}}(\mathrm{t})$ was first subjected to a bandpass filtering in a narrow frequency band (0.06 Hz) centered around the respiration rate and subsequently computing its upper envelope ($\tilde{\mathrm{F}}^{\mathrm{u}}_{\mathrm{f}}(\mathrm{t})$) from the magnitude of its analytic signal computed using the Hilbert transform. The median over time of $\tilde{\mathrm{F}}^{\mathrm{u}}_{\mathrm{f}}(\mathrm{t})$ was defined as $\Delta\mathrm{F}_{\mathrm{f}}$ [301].

4.2.2 Human atrial tissue models

We used the 2D square tissue model presented in section 2.5. The electrophysiological activity of human atrial cardiomyocytes was described by the $\mathcal{C}$ AP model [244]. All the myocardial nodes in the tissue mesh were assigned with the same electrophysiological characteristics representative of LA tissue. A longitudinal conductivity of 0.003 S/cm and a transverse-to-longitudinal conductivity ratio of 0.5 were considered. This corresponds to a longitudinal conduction velocity of 40.0 cm/s for a planar wave, in agreement with values reported for AF patients in previous studies [258].

The effects of cholinergic and β-adrenergic stimulation and the description of the I_{SK} current were introduced as defined in section 2.2.1. The electrical remodeling associated with psAF was represented as described in section 2.2.4.

To incorporate psAF-induced structural remodeling in the 2D tissue model, we introduced 20% diffuse fibrosis based on the ranges reported experimentally [78]. Specifically, we randomly selected 20% of the nodes based on a uniform distribution and we assigned them the MacCannell fibroblast computational model [283] described in section 2.4. The myocyte-myocyte, myocyte-fibroblast and fibroblast-fibroblast conductivities were defined as described in section 2.4.

4.2.3 Simulated ACh and Iso release patterns

To model the respiratory modulation of ACh concentration, the temporal pattern of ACh release was simulated as cyclically varying following a sinusoidal waveform of frequency equal to 0.125 Hz, as done in Chapter 3. Different mean levels (0.0125, 0.05 μM) and peak-to-peak variation ranges (0.1, 0.025 μM) of ACh (ΔACh) were tested, all of them within the ACh ranges tested in previous studies (0.0 - 0.1 μM) [258].

The effects of β-adrenergic stimulation were simulated by administration of Iso at spatially and temporally fixed concentrations of 0.0, 0.01 and 1 μM.

4.2.4 Numerical methods and simulations

Electrical propagation in the atria was described by the monodomain model and solved by FEM in combination with the operator splitting numerical scheme using the software ELVIRA [290].

To establish steady-state conditions, single cells were paced at a fixed CL of 800 ms for a duration of 16 minutes. The steady-state values of the state variables in the cellular models were used to initialize the multi-cellular models.

Four stimuli at a CL of 800 ms were applied at the bottom edge of the 2D tissue to pre-excite the model. Subsequently, an S1-S2 cross-stimulation protocol was employed to induce a rotor. The first stimulus (S1) was applied at the bottom edge of the tissue, while the second stimulus (S2) was applied onto a 3.5 by 3.5 cm square at the bottom right corner. Following the delivery of the S1 stimulus, the simulations were run for a duration of 12.5 seconds.

4.2.5 F-wave frequency characterization

The frequency of f-waves was computed as described in section 3.2.5 and summarized below. From the simulations, voltage time series were extracted from 169 points uniformly distributed across the tissue. For each of the extracted points, the time instant $\mathrm{t_{m,i}}$ correspondent to the maximum upstroke velocity of i-th beat was determined and the instantaneous frequency was computed as $1/(\mathrm{t_{m,i+1}} - \mathrm{t_{m,i}})$, for all beat indices i in the recording. The time series of instantaneous frequencies calculated for each tissue point were subjected to power spectral analysis. Spectral "peak-conditioned" selection was performed as in [315] so that the series whose spectrum was not sufficiently peaked were discarded. $\mathrm{F_f(t)}$ was eventually computed as the mean of the remaining time series. Finally, $\overline{\mathrm{F}}_\mathrm{f}$ was computed as the average value of $\mathrm{F_f(t)}$, while $\Delta\mathrm{F_f}$ was computed as the median of the upper envelope of the bandpass-filtered $\mathrm{F_f(t)}$ signal [301].

4.3 Results

4.3.1 F-wave frequency analysis from ECGs of psAF patients

Respiration signals for estimating respiratory f-wave variation could be obtained from 22 patients. In the BL phase, the mean over patients of $\overline{\mathrm{F}}_\mathrm{f}$ was 6.66 Hz and the range over patients was 5.74 - 8,73 Hz. HDT resulted in a decrease in $\overline{\mathrm{F}}_\mathrm{f}$, with the mean over patients of $\mathrm{F_f}$ being 6.48 Hz and the range being 5.50 - 8,52 Hz. Contrarily, HUT led to an increase in $\overline{\mathrm{F}}_\mathrm{f}$, with the mean over patients being 6.74 Hz and the range being 5.50 - 8.83 Hz.

Examining the relative changes in $\overline{\mathrm{F}}_\mathrm{f}$ with respect to the relative changes in $\Delta\mathrm{F_f}$ between the three phases (BL, HDT and HUT), significant positive correlation was found between $\Delta\mathrm{F}_{\mathrm{f}_{\mathrm{HDT-BL}}}$ and $\overline{\mathrm{F}}_{\mathrm{f}_{\mathrm{HDT-BL}}}$ (Pearson correlation coefficient $r = 0.51, \mathrm{p} < 0.05$) and between $\Delta\mathrm{F}_{\mathrm{f}_{\mathrm{HUT-HDT}}}$ and $\overline{\mathrm{F}}_{\mathrm{f}_{\mathrm{HUT-HDT}}}$ ($r = 0.50, \mathrm{p} < 0.05$). This is depicted in Figure 4.1, panels a) and c).

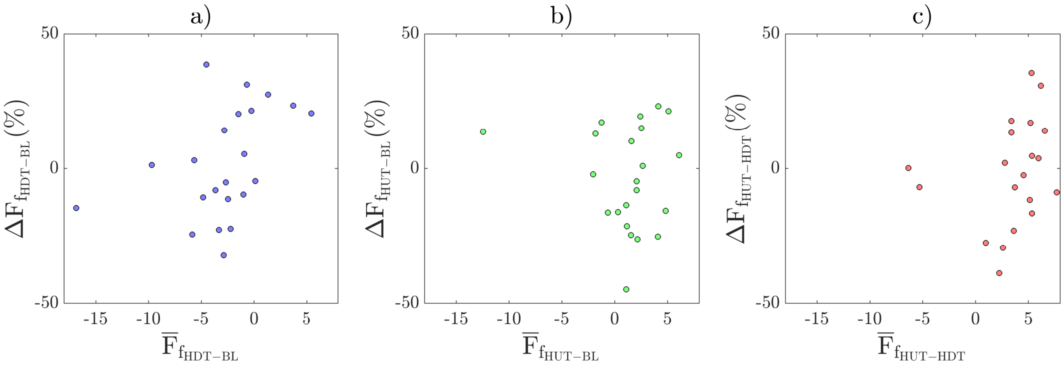

Figure 4.1: Relative changes in $\overline{\mathrm{F}}_\mathrm{f}$ vs $\Delta F_\mathrm{f}(t)$ for the three tilt test phases (HDT with respect to BL, HUT with respect to BL, HUT with respect to HDT) measured from patients' ECGs.

4.3.2 F-wave frequency analysis from simulations of psAF tissues

From the simulations, it could be observed that an increase in the mean or minimum ACh levels resulted in higher $\mathrm{F_f}$ values. Specifically, when the mean ACh value remained the same but the minimum value was increased (indicating reduced modulation magnitude as measured by ΔACh), the resulting $\mathrm{F_f}$ was higher.

β-adrenergic stimulation by Iso to simulate enhanced SS clearly increased the mean frequency in the case of ΔACh=0.1 μM. The tested Iso concentrations of 0.01 and 1 μM rendered approximately the same results, with an increase in $\mathrm{F_f}$ of approximately 0.2 Hz with respect to the case without Iso (Figure 4.2, panel a)). In the case of the smallest tested ACh variation range (ΔACh=0.025 μM), the addition of Iso did not have significant effects on frequency variations (Figure 4.2, panels b) and c)). For the case of 0 - 0.025 μM ACh and 1 μM Iso no stable rotational activity could be initiated and chaotic activity was observed.

Regarding the variations in $\Delta\mathrm{F_f}$ with ACh and Iso, we found that $\Delta\mathrm{F_f}$ was dependent on the range of ACh concentration, with its magnitude augmenting as the range increased. For the minimum tested ACh variation range of 0.025 μM, the maximum frequency variation was 0.05 Hz while for the maximimum tested ACh variation range of 0.1 μM, the maximum frequency variation was 0.65 Hz.

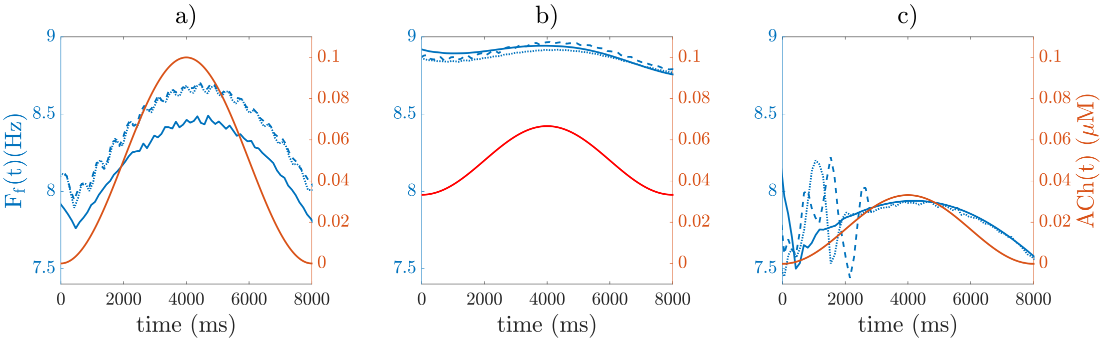

Figure 4.2: $\mathrm{F_f(t)}$ (blue) and ACh(t) (red) from simulations. Solid/dotted/dashed lines represent 0.0/0.01/1 μM Iso.

4.4 Discussion

A large number of studies have postulated an increase in SS during HUT in subjects in SR [332–334]. In our study, this observation is further reinforced in the context of AF. Specifically, the increase in $\mathrm{F_f}$ that we observed in response to the HUT maneuver in AF patients is consistent with the increase in in $\mathrm{F_f}$ that we measured for increased Iso in our simulations, particularly under high ACh. The concurrent variation in $\Delta\mathrm{F_f}$ also aligns with these findings, as it shows a larger increase in $\mathrm{F_f}$ coupled with larger increases in $\Delta\mathrm{F_f}$ in the patients (Figure 4.1, panel c)), which is also reproduced when simulating increasingly higher Iso concentrations even if to a lower extent in the simulations and only when Iso is varied from 0 to 0.01 or 1 μM.

Although there is scarce research on the autonomic effects during HDT, in SR there is a tendency to associate the slowing of HR during HDT with both an increase in PSS and a decrease in SS [334, 335]. Only one study reported a decrease in both PSS and SS [336]. In the case of AF or atrial flutter, some studies have linked the observed outcomes to an increase in PSS [298, 309]. Based on the findings of this work, similar results may not hold true since PSS, causing a shortening of the effective refractory period, actually leads to an increase in $\mathrm{F_f}$, as reported in the literature and confirmed by our simulations [337]. Considering the results of our study, the reduction in $\mathrm{F_f}$ observed in the psAF patients in response to HDT could be better explained by a reduction in SS, possibly mediated by the cardiopulmonary baroreflex, as indicated by lower $\mathrm{F_f}$ in simulated psAF tissues when the Iso concentration was diminished. Regarding the modulation magnitude, measured by $\Delta\mathrm{F_f}$, previous studies have related it to respiratory modulation and parasympathetic activity [301]. In the transitions from BL to HDT and from HDT to HUT, we observed an increase and a decrease in $\Delta\mathrm{F_f}$ in mean over the psAF population, suggesting an increase and a decrease in PSS, respectively. Taking into account these two transitions and the relationship between relative changes in $\Delta\mathrm{F_f}$ and $\overline{\mathrm{F}}_\mathrm{f}$, it appears that greater respiratory modulation (higher increase in $\Delta\mathrm{F_f}$) corresponds to a lesser decline in SS (lower decrease in $\overline{\mathrm{F}}_\mathrm{f}$) when going from BL to HDT, and a greater elevation in SS (higher decrease in $\overline{\mathrm{F}}_\mathrm{f}$) when going from HDT to HUT). These findings could suggest a potential dependence of SS effects on the underlying level of PSS, as supported by our simulations. Our observations on the changes in f-wave frequency characteristics in response to HDT and HUT should possibly be attributed to additional factors beyond the ANS modulation. Among such factors, mechanical stretch and mechano-electrical feedback should be considered, as they have been reported to exert significant contribution to atrial electrical activity in patients with atrial flutter [311, 312, 326]. As reported in Chapter 3, a study conducted by Waxman et al. [326] examined various interventions, including passive upright tilting, the strain phase of the Valsalva maneuver and expiration, and all of them were found to reduce cardiac size. Interestingly, regardless of autonomic activity, these interventions were found to independently increase the rate of atrial flutter. Similarly, Ravelli et al. [311] discovered that acute atrial stretch caused by ventricular contractions and respiratory movements resulted in a shortening of the atrial flutter CL in humans. Importantly, even after blocking autonomic influences, oscillations in the atrial flutter CL were still present, further supporting the idea that factors beyond autonomic activity contribute to these oscillations.

4.4.1 Conclusions

The findings of this study suggest that the increase in $\overline{\mathrm{F}}_{\mathrm{f}}$ following HUT and the decrease in $\overline{\mathrm{F}}_{\mathrm{f}}$ following HDT could be attributed to heightened and diminished sympathetic activity, respectively, on top of other factors not accounted for in our study like mechanical effects. Parasympathetic activity, assessed by the magnitude of $\Delta\mathrm{F}_{\mathrm{f}}$, appears to exert a modulating role on the effects of sympathetic activity rather than being an independent force driving the observed changes in f-wave frequency.

Chapter 5

Identification of parasympathetic innervation in the atria to guide ablation of ganglionated plexi

5.1 Motivation

As already introduced in section 1.3.4, RF catheter ablation is one of the most common procedures for AF treatment when ADT is not effective. Targets for successful AF ablation are continuously being sought [338]. GP ablation has been associated with a decreased risk of AF recurrence [23, 25, 220–225], either in addition to PVI [23, 24, 26, 227–230] or as a stand-alone procedure [26, 231]. The percentage of success in eliminating AF seems to be similar for PVI and GP ablation individually, but it is significantly higher when the two are combined [26, 47, 227].

One potentially contributing factor to the effectiveness of GP ablation is accurate GP location. During ablation procedures, GPs are normally located by the induction of vagal reflexes through rapid, short stimulation at their expected anatomical sites until a positive response is found (AV block, hypotension or more than 50% increase in R-R interval during AF) [26, 55, 339, 340]. As an alternative to this functional approach, the anatomical approach consists in the ablation of the four main GPs based on their presumed anatomical locations [227]. An important limitation of these methods is that once the GPs have been located, there is still no information on the actual area occupied by each of them [341].

The aim of this study was to develop a method to locate regions of atrial parasympathetic innervation sites within atrial GPs based on measurements from a multielectrode grid of EGMs. This approach is expected to provide information not only on the approximate location but also on the dimensions of those sites. Our hypothesis is that the EGM atrial repolarization wave amplitude could be representative of the presence of ACh release sites [342], as I_{KACh} activation is expected to accelerate phase 3 of the AP, leading to higher EGM repolarization amplitudes. Even if the effectiveness of GP ablation has shown to be higher in pxAF [25, 343], here both pxAF and psAF were simulated, with psAF models including electrical and structural AF-related remodeling.

5.2 Methods

5.2.1 Human atrial tissue models

2D human atrial tissue models of 5×5 cm^2, with and without fibrosis, were built as described in section 2.5. A square grid of 251 by 251 nodes was used, where each node in the grid took the properties of a cardiomyocyte or a fibroblast. The $\mathcal{C}$ model [244] was used to describe atrial myocyte electrophysiology while fibroblasts were described with the MacCannell model [283]. Parasympathetic effects were incorporated into the $\mathcal{C}$ model as defined in section 2.2.1 [196, 258].

An additional simulation considering cell-to-cell variability was performed. In this study, we only considered variability in the conductances of the currents having the largest effects on the last stage of repolarization (i.e. APD_{90}), which corresponds to the repolarization wave we are interested in analyzing. According to the work by Sánchez et al. [344], I_{K1} and I_{CaL} were the two currents having the largest influence on APD_{90} in the $\mathcal{C}$ model, while other currents like I_{NaK}, I_{to}, I_{Kur} and I_{NaCa} had notably lower effects on APD_{90}. For the conductances of I_{K1} and I_{CaL}, a variation range between -30% and +30% in 15% steps was considered, thus leading to 25 ionic combinations used to simulate cells with distinct characteristics.

Non-AF, pxAF and psAF tissue models were developed. AF is usually a progressive disease, starting from short and infrequent episodes to longer and more frequent ones. In general, the progression from pxAF to psAF forms is accompanied by alteration of the myocardial substrate. In our models, psAF was characterized by both structural and electrical remodeling, whereas pxAF included only modest structural remodeling. One aspect of structural remodeling included in pxAF and psAF tissue models was an increase in the amount of fibrosis with respect to the non-AF case, which was characterized by the absence of fibrosis [78, 84]. Fibrosis distribution in pxAF and psAF tissues was modeled as either uniform diffuse ($\mathcal{F}_u$) or non-uniform diffuse ($\mathcal{F}_{nu}$) [345]. To generate a uniform fibrosis distribution $\mathcal{F}_u$, each node in the tissue was assigned a probability 0.2 (for 20% fibrosis) or 0.4 (for 40% fibrosis) of being a fibroblast, otherwise being an atrial cardiomyocyte. A non-uniform diffuse fibrosis distribution $\mathcal{F}_{nu}$ was defined by setting circular patches in the tissue and generating diffuse fibrosis within them in degrees of 20% or 40%. Two different geometries of the fibrotic patches were considered, denoted as $\mathcal{F}^1_{nu}$ and $\mathcal{F}^2_{nu}$, which are illustrated in Figure 5.1 (E)-(F).

Another aspect of structural remodeling in the psAF tissue models was a reduction in the longitudinal diffusion coefficient ($\mathcal{D}$) between myocytes to simulate the effects of gap junction remodeling [87, 88]. $\mathcal{D}$ was varied to obtain longitudinal conduction velocities in line with values reported in the literature [258]. Values for $\mathcal{D}$ of 0.003 cm^2/ms and 0.002 cm^2/ms were considered for non-AF/pxAF and psAF tissues, respectively. In all types of tissues, a transverse-to-longitudinal conductivity ratio of 0.5 was adopted. Fiber orientation was considered parallel to the y-axis. Furthermore, a four-fold reduction in the diffusion coefficient was considered for myocyte-fibroblast and fibroblast-fibroblast coupling, both in pxAF and psAF tissues [346], as illustrated in 2.4. Electrical remodeling was associated with psAF only and was accounted for by reducing the maximal conductances of $\mathrm{I_{to}}$, $\mathrm{I_{CaL}}$ and $\mathrm{I_{Kur}}$ by 50%, 70% and 50%, respectively, as in [269]. In this study, we did not consider the 100% increase in $\mathrm{I_{K1}}$ illustrated in 2.2.4, as we solely relied on the original paper by Courtemanche et al. [269]. See Table 5.1 for a summary of simulation parameters.

Parasympathetic effects were modeled by randomly increasing the concentration of

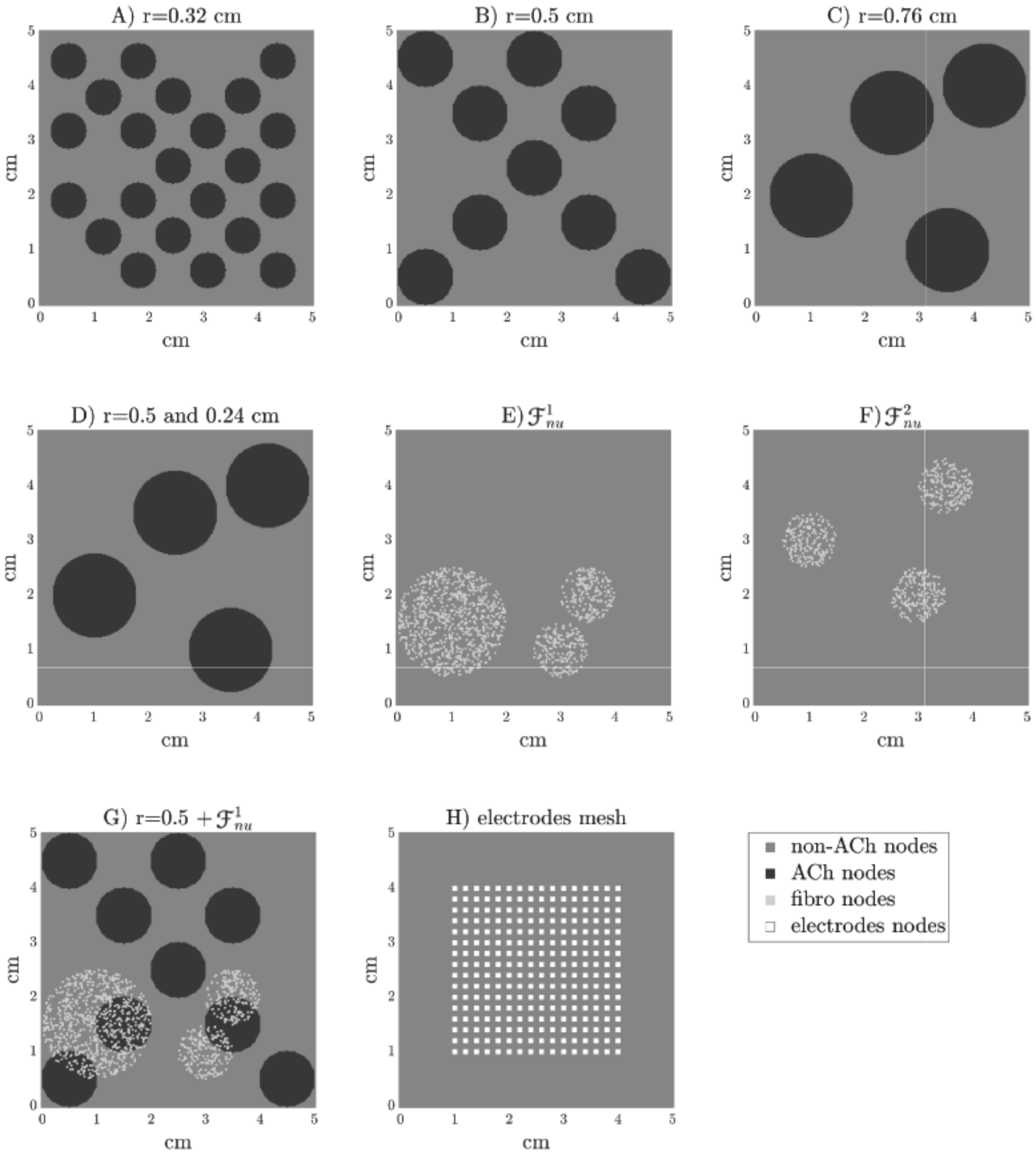

Figure 5.1: 2D tissue models with different distributions of ACh release sites in A), B), C), D) and with different fibrosis distributions in E) and F). In G), an example of a tissue model with ACh release sites and non-uniform diffuse fibrosis. In H), the mesh of electrodes is represented. Electrode size is adapted for clarity.

the ACh neurotransmitter in circles distributed across the tissue, which activated the I_{KACh} current in those areas. We simulated an ACh concentration of 0.1 μM, following a previous work in which ACh concentrations varying from 0 to 0.1 μM were used [258]. Cases of parasympathetically innervated circles all of the same radius, this being 0.32, 0.5 or 0.76

Table 5.1: Characteristics of electrical and structural remodeling in non-AF, PxAF and PsAF tissues, and simulated ACh concentrations.

		non-AF	**PxAF**	**PsAF**
Structural remodeling	Fibrosis ($\mathcal{F}_u$ or $\mathcal{F}_{nu}$)	0%	20%	40%
	$\mathcal{D}$ (cm^2/ms) at myocyte-myocyte	0.003	0.003	0.002
	$\mathcal{D}$ reduction factor at myocyte-fibroblast		$\propto 0.25$	$\propto 0.25$
	Transverse-to-longitudinal conductivity ratio	0.5	0.5	0.5
Electrical remodeling	I_{to}	$\propto 1$	$\propto 1$	$\propto 0.5$
	I_{CaL}	$\propto 1$	$\propto 1$	$\propto 0.3$
	I_{Kur}	$\propto 1$	$\propto 1$	$\propto 0.5$
Parasympathetic effects		**non-ACh sites**	**ACh sites**	
	ACh (μM)	0	0.1	

cm, as well as a case with parasympathetically innervated circles of different radii (0.24 and 0.5 cm) were considered. All these ACh geometries are illustrated in Figure 5.1 (A)-(D).

The interaction between vagal stimulation and fibrosis was investigated by considering models with all different combinations of ACh patches, 20% - 40% $\mathcal{F}_u$ or $\mathcal{F}_{nu}$. One of these possible combinations is represented in Figure 5.1 (G). In the GPs, despite the predominance of parasympathetic fibers, sympathetic ones can be found too [56]. To account for it, an additional simulation considering small islands of β-adrenergic stimulation inside the ACh patches was performed (radius of Iso patches = 0.1 cm). β-adrenergic stimulation was simulated as in the study by González de la Fuente et al. [259], where the effects of Iso were modeled by modulation of the maximum conductances of the I_{CaL}, I_{to} and I_{Ks} currents following the reported concentration-dependent. A 1μM Iso concentration was considered.

5.2.2 Simulation protocols

Tissue simulations were performed using the FEM implementation of the software ELECTRA [347, 348] for the solution of the cardiac monodomain model. Simulations were performed using DAETI with an adaptive time step ranging from 0.005 to 0.01 ms.

The single cells were simulated in MATLAB while being paced at a fixed CL of 1000 ms for one minute. The values of the state variables of the models at steady-state were used for initialization in the tissue simulations. Tissue stimuli were applied at its bottom edge, with a CL of 1000 ms. Results for the last simulated beat were analyzed. It should be noted that, in contrast to the description in Chapter 2, the prepacing duration for the $\mathcal{C}$ model in this study was limited to one minute. This was based on the results presented in the original paper where the $\mathcal{C}$ model was proposed in 1998, in which the authors conducted simulations with a one-minute pacing duration. Even if further analysis revealed that steady-state was actually reached after longer pacing time, it is possible to identify a first rapid adaptation followed by a second slower adaptation, with larger AP changes occurring within the first minute [349].

5.2.3 EGM feature extraction

Unipolar EGMs were computed in a 16×16 electrode mesh at the center of the tissue, with an inter-electrode spacing of 2 mm in both the ‘x’ and ‘y’ directions, as represented in Figure 5.1 (H). Electrode positioning at different distances from the tissue in the orthogonal direction, namely 0.5, 1 and 2 mm, was tested. To compute the EGMs $\phi_e(\mathrm{r}', \mathrm{t})$ for an electrode located at r', the following formula was used [350–352]:

$$\phi_e(\mathrm{r}', \mathrm{t}) = \int\int \left[-\nabla_{\mathrm{r}} \mathrm{V}_{\mathrm{m}}(\mathrm{r}, \mathrm{t}) \cdot \nabla_{\mathrm{r}} \left(\frac{1}{\mathrm{d}(\mathrm{r}, \mathrm{r}')} \right) \right] \mathrm{dx}\, \mathrm{dy} \tag{5.1}$$

where the distance function d is defined as:

$$d(\mathrm{r}, \mathrm{r}') = ||\mathrm{r} - \mathrm{r}'||_2 \tag{5.2}$$

and $\mathrm{r} = \begin{bmatrix} \mathrm{x} & \mathrm{y} & \mathrm{z} \end{bmatrix}$ and $\mathrm{r}' = \begin{bmatrix} \mathrm{x}' & \mathrm{y}' & \mathrm{z}' \end{bmatrix}$ are the coordinate vectors for a 2D tissue point and for the electrode, respectively.

The discretized form of this formula is reported below:

$$\phi_e(\mathrm{r}', \mathrm{t}) = \sum_{\mathrm{i}=1}^{\mathrm{N}-1} \sum_{\mathrm{j}=1}^{\mathrm{N}-1} \left[-\left(\frac{\Delta_{\mathrm{x}} \mathrm{V}_{\mathrm{m}}(\mathrm{r}_{\mathrm{i,j}}, \mathrm{t})}{\Delta \mathrm{x}}, \frac{\Delta_{\mathrm{y}} \mathrm{V}_{\mathrm{m}}(\mathrm{r}_{\mathrm{i,j}}, \mathrm{t})}{\Delta \mathrm{y}} \right) \cdot \left(\frac{\Delta_{\mathrm{x}} \frac{1}{\mathrm{d}(\mathrm{r}_{\mathrm{i,j}}, \mathrm{r}')}}{\Delta \mathrm{x}}, \frac{\Delta_{\mathrm{y}} \frac{1}{\mathrm{d}(\mathrm{r}_{\mathrm{i,j}}, \mathrm{r}')}}{\Delta \mathrm{y}} \right) \right] \Delta \mathrm{x} \Delta \mathrm{y} \tag{5.3}$$

where $\mathbf{r}_{\mathrm{i,j}} = \begin{bmatrix} \mathrm{x}_{\mathrm{i}} & \mathrm{y}_{\mathrm{j}} & \mathrm{z} \end{bmatrix}$, $\mathrm{r}_{\mathrm{i+1,j}} = \begin{bmatrix} \mathrm{x}_{\mathrm{i+1}} & \mathrm{y}_{\mathrm{j}} & \mathrm{z} \end{bmatrix}$ and $\mathbf{r}_{\mathrm{i,j+1}} = \begin{bmatrix} \mathrm{x}_{\mathrm{i}} & \mathrm{y}_{\mathrm{j+1}} & \mathrm{z} \end{bmatrix}$ are the coordinate vectors, in the Cartesian system, of points in the 2D tissue. N is the number of nodes in the x and y directions, both equal to $\mathrm{N} = 251$, and $\Delta\mathrm{x} = \Delta\mathrm{y} = 0.02$ cm. Finally, $\Delta_{\mathrm{x}}\mathrm{V}_{\mathrm{m}}(\mathrm{r}_{\mathrm{i,j}}, \mathrm{t}) = (\mathrm{V}_{\mathrm{m}}(\mathrm{r}_{\mathrm{i+1,j}}, \mathrm{t}) - \mathrm{V}_{\mathrm{m}}(\mathrm{r}_{\mathrm{i,j}}, \mathrm{t}))$, $\Delta_{\mathrm{y}}\mathrm{V}_{\mathrm{m}}(\mathrm{r}_{\mathrm{i,j}}, \mathrm{t}) = (\mathrm{V}_{\mathrm{m}}(\mathrm{r}_{\mathrm{i,j+1}}, \mathrm{t}) - \mathrm{V}_{\mathrm{m}}(\mathrm{r}_{\mathrm{i,j}}, \mathrm{t}))$, $\Delta_{\mathrm{x}}\frac{1}{d(\mathrm{r}_{i,j},\mathrm{r}')} = (\frac{1}{d(\mathrm{r}_{i+1,j},\mathrm{r}')} - \frac{1}{d(\mathrm{r}_{i,j},\mathrm{r}')})$ and $\Delta_{\mathrm{y}}\frac{1}{d(\mathrm{r}_{i,j},\mathrm{r}')} = (\frac{1}{d(\mathrm{r}_{i,j+1},\mathrm{r}')} - \frac{1}{d(\mathrm{r}_{i,j},\mathrm{r}')})$.

$\phi_e(\mathrm{r}', \mathrm{t})$ represents the unipolar electrogram for a "punctual" electrode (pEGM) located at r'. Additionally, to more realistically model the electrode size, electrodes of 0.8×0.8 mm [353–355] were considered. For "dimensional" electrodes, the EGM correspondent to that electrode was obtained by performing the average of the pEGMs computed in all the points covered by the electrode's surface, namely 25 nodes [354]. The EGMs were then normalized by a factor dependent on the electrode-tissue distance (350 for z=0.5 mm, 250 for z=1 mm and 150 for z=2 mm) to obtain an amplitude of the depolarization wave in line with the amplitude of clinical EGMs (6/7 mV). Subsequently, the EGMs were filtered with a 2 Hz high-pass filter, mimicking the implementation in most commercial systems, to remove the DC level due to the differences in the resting membrane potentials between distinct cells in the tissue.

To assess the performance of our proposed algorithms (see section 5.2.3) under noisy conditions, noisy EGM signals were obtained as follows. Noise segments were extracted from 180 EGM recordings from patients. The power of each noise segment was normalized. Subsequently, the different noise segments were individually added to the EGMs with different multiplying factors to test signal-to-noise ratios (SNR) from 0 to 20 dB. For repolarization analysis, a 2 to 30 Hz band-pass filter was applied to the noisy EGMs to remove the DC level and the high frequency noise without altering the features of the repolarization waves. For depolarization analysis, a 2 to 250 Hz band-pass filter was applied.

The atrial repolarization wave of the $\phi_{\mathrm{e}}(\mathrm{r}', \mathrm{t})$ signal, at electrode (i, j), $\mathrm{i}, \mathrm{j} \in \{1, \cdots, 16\}$, was denoted as $\mathrm{R}_{\mathrm{i,j}}(\mathrm{t})$. Since the time window (TW) in which the $\mathrm{R}_{\mathrm{i,j}}(\mathrm{t})$ waves were located did not show a fixed distance from the depolarization wave, an automatic delineation method was developed. For each simulated case, the time location, t_{R}, of the absolute maximum repolarization peak (either positive or negative), $\mathrm{R}_{\mathrm{i}_{\mathrm{m}},\mathrm{j}_{\mathrm{m}}}(\mathrm{t}_{\mathrm{R}})$, identified at electrode $(\mathrm{i}_{\mathrm{m}}, \mathrm{j}_{\mathrm{m}})$ among all the (i, j) EGMs of a single case, was searched for in a window starting 100 ms after the depolarization-based reference time corresponding to the maximum slope of the depolarization wave, taken here as $\mathrm{t} = 0$. The onset and ending points of the

TW were set to 30 ms before and 150 ms after the t_R, respectively. For each EGM, the local minima ($R_{i,j}^{min}$) and maxima ($R_{i,j}^{max}$) within the TW were identified. The amplitude $R_{i,j}^{A}$ was selected as either $R_{i,j}^{min}$ or $R_{i,j}^{max}$, choosing the one with the largest absolute value (but maintaining its sign):

$$R_{i,j}^{A} = \arg\max_{x}\{|x|\}, \quad x \in \{R_{i,j}^{min}, R_{i,j}^{max}\} \tag{5.4}$$

One example of two EGMs recorded inside and outside a GPs, respectively, is represented in Figure 5.2.

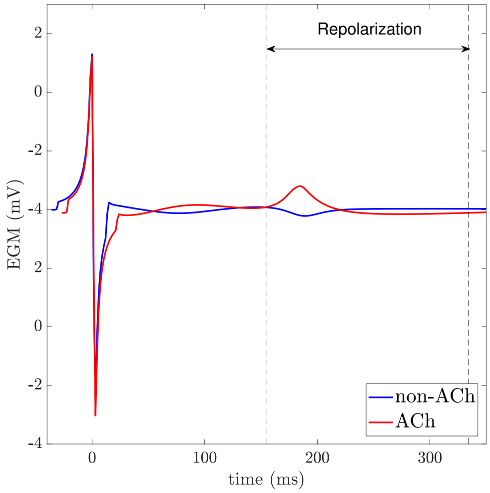

Figure 5.2: EGMs recorded in non-ACh (blue) and ACh (red) release sites. Dashed vertical lines indicate the repolarization window for analysis.

The relationship between the repolarization waves $R_{i,j}(t)$ and the corresponding APs are illustrated in Figure 5.3 for a simulated case with no fibrosis and with ACh distributed in patches of radius r=0.5 cm.

As it can be observed from the figure, ACh not only shortens the AP, but also accelerates phase 3 of AP repolarization, which leads to $R_{i,j}(t)$ waves of higher amplitude $R_{i,j}^{A}$. A sensitivity (Se) - specificity (Sp) analysis was performed by calculating a ROC curve to identify the optimal repolarization amplitude threshold R^{th} that allowed identification of EGM signals of ACh-release and non-ACh-release areas. Specifically, ACh and non-ACh areas were associated with EGMs presenting amplitudes $R_{i,j}^{A}$ above and below the threshold

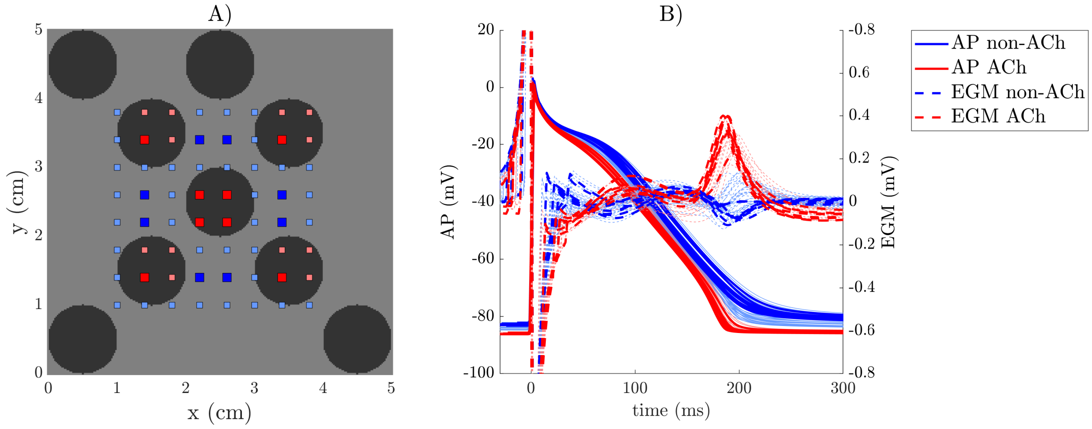

Figure 5.3: A) 2D model of a non-AF tissue with ACh release sites shown in black and EGM electrodes in red and blue. B) APs and EGMs recorded in the (i,j) points represented in the left panel. The thicker lines correspond to the points represented with big squares in the tissue.

R^{th}, respectively.

When simulating cases with non-uniform diffuse fibrosis $\mathcal{F}_{nu}$, we observed that the amplitude $\mathrm{R}^{\mathrm{A}}_{\mathrm{i,j}}$ of EGMs in ACh and non-ACh areas presented different behavior depending on the presence or absence of fibrosis. This is illustrated in Figure 5.4 together with the different APs that underlie this difference.

On this basis, an additional step in the EGM processing was applied to distinguish fibrotic from non-fibrotic areas before using the $\mathrm{R}^{\mathrm{A}}_{\mathrm{i,j}}$ amplitude to identify ACh areas. Identification of fibrotic areas was performed based on the amplitude of the EGM depolarization wave, $\mathrm{D}_{\mathrm{i,j}}(\mathrm{t})$, taken from EGM onset to TW window onset, which is a common method in clinical practice [356–358]. The amplitude $\mathrm{D}^{\mathrm{A}}_{\mathrm{i,j}}$ was computed as the difference between the maximum positive, $D^{\mathrm{max}}_{i,j}$, and minimum negative, $D^{\mathrm{min}}_{i,j}$, peaks of the depolarization wave $\mathrm{D}_{\mathrm{i,j}}(\mathrm{t})$:

$$D^{A}_{i,j} = D^{\mathrm{max}}_{i,j} - D^{\mathrm{min}}_{i,j} \tag{5.5}$$

Fibrotic areas were associated with lower $\mathrm{D}^{\mathrm{A}}_{\mathrm{i,j}}$ amplitudes. Considering the dependence of the depolarization amplitude on the amount of fibrosis, a ROC curve was again used to determine the optimal threshold D^{th} to distinguish fibrosis vs non-fibrotic areas.

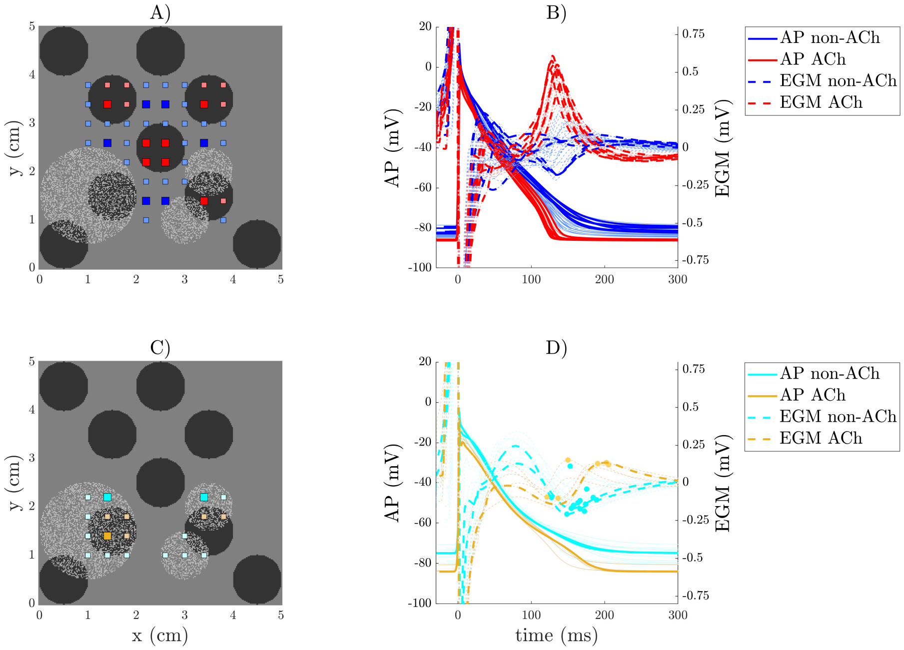

Figure 5.4: A) and C) 2D model of a psAF tissue with ACh release sites shown in black, fibrosis in light grey and EGM electrodes in red and blue in the non-fibrotic regions and in orange and cyan in the fibrotic regions. B) and D) APs and EGMs recorded in the points represented in the left panels. The thicker lines correspond to the points represented with the big squares in the tissue. In D) the peaks of the $\mathrm{R}_{\mathrm{i,j}}(\mathrm{t})$ waves are highlighted with a dot.

5.3 Results

5.3.1 EGM repolarization analysis for GP identification

EGM repolarization analysis in non-AF, pxAF and psAF tissues. In this section, the values of $\mathrm{R}^{\mathrm{A}}_{\mathrm{i,j}}$ for ACh-release and non-ACh-release areas are presented. To illustrate the results, figures are presented for some of the simulated cases with ACh patches of radius r=0.5 and ACh patches of radii r=0.5 and 0.24 cm.

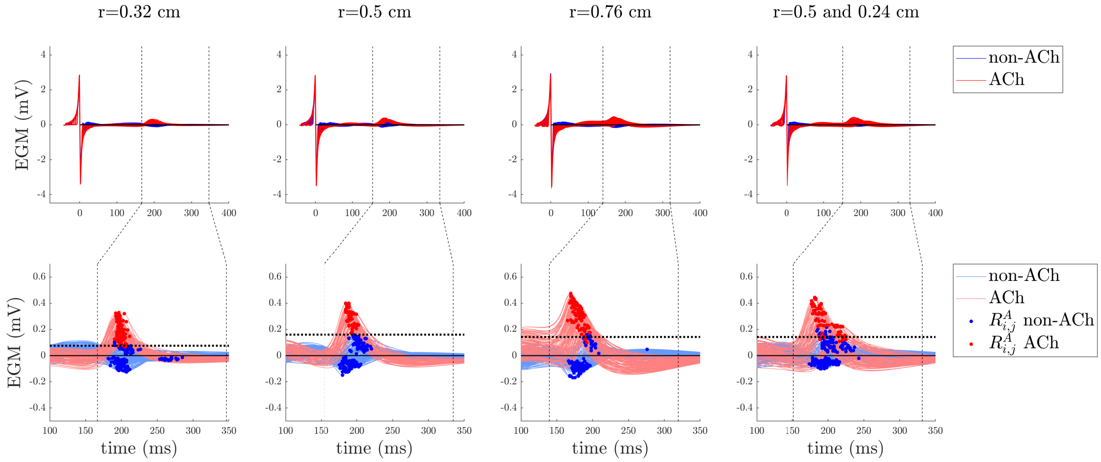

Figure 5.5: EGM analysis for a non-AF tissue. Top row: EGMs aligned with respect to the time correspondent to the maximum slope of the depolarization wave (marked as 0 in the x-axis). The vertical dashed lines delimit the time window TW for the $\mathrm{R}_{\mathrm{i,j}}(\mathrm{t})$ repolarization signals. Bottom row: atrial repolarization waves, $\mathrm{R}_{\mathrm{i,j}}(\mathrm{t})$, with dots indicating the maximum absolute value $\mathrm{R}^{\mathrm{A}}_{\mathrm{i,j}}$ of the waves within TW. The horizontal dotted lines represent the optimal threshold R^{th} found by Se/Sp analysis.

In non-AF tissues, and for all the tested ACh geometries, the optimal value of the threshold R^{th} to distinguish between ACh and non-ACh regions, and computed as later described, was found to lie in a range between 23% and 41% of $\mathrm{R}^{\mathrm{A,max}}$, the maximum $\mathrm{R}^{\mathrm{A}}_{\mathrm{i,j}}$ value in the grid,

$$R^{A,\mathrm{max}} = \max_{i,j}\{R^A_{i,j}\} = R_{i_m,j_m}(t_{\mathrm{R}}). \tag{5.6}$$

In pxAF tissues with 20% $\mathcal{F}_u$ fibrosis, similar behavior as in non-AF tissues was found. Results are illustrated in Figure 5.12.

In pxAF tissues with 20% $\mathcal{F}_{nu}$ fibrosis, the areas with fibrosis were analyzed separately

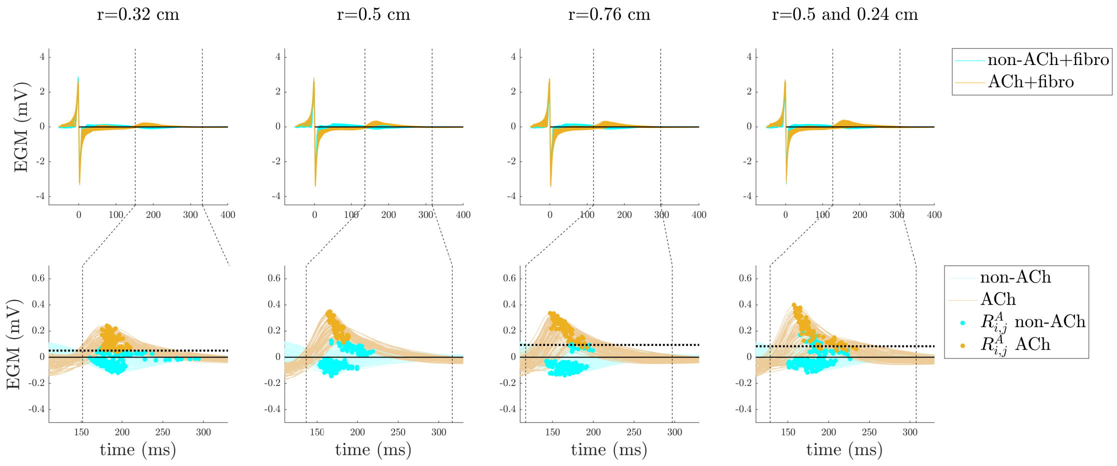

Figure 5.6: EGM analysis for the uniform diffusive fibrosis pxAF tissue ($\mathcal{F}_u$ 20%). The figure is structured as Figure 5.5.

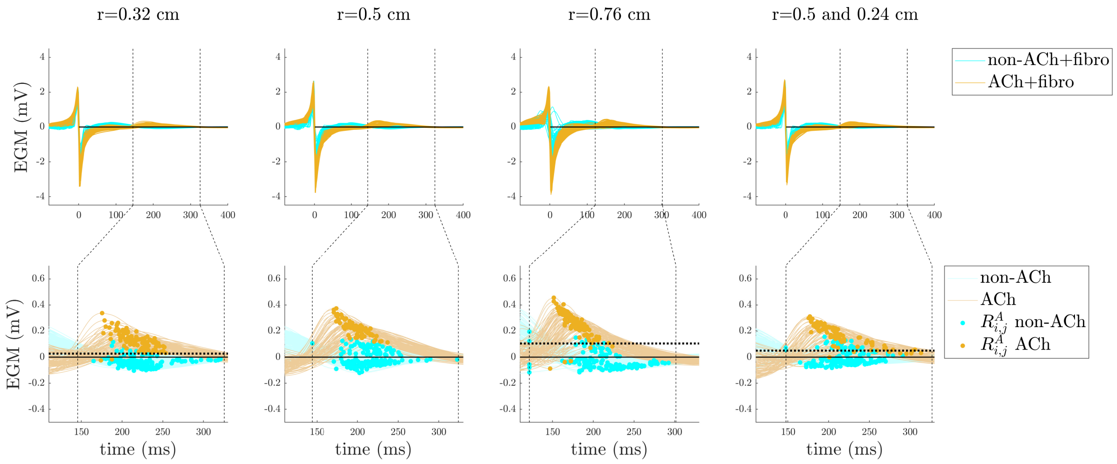

Figure 5.7: EGM analysis for the uniform diffusive fibrosis psAF cases ($\mathcal{F}_u$ 40%). The figure is structured as Figure 5.5.

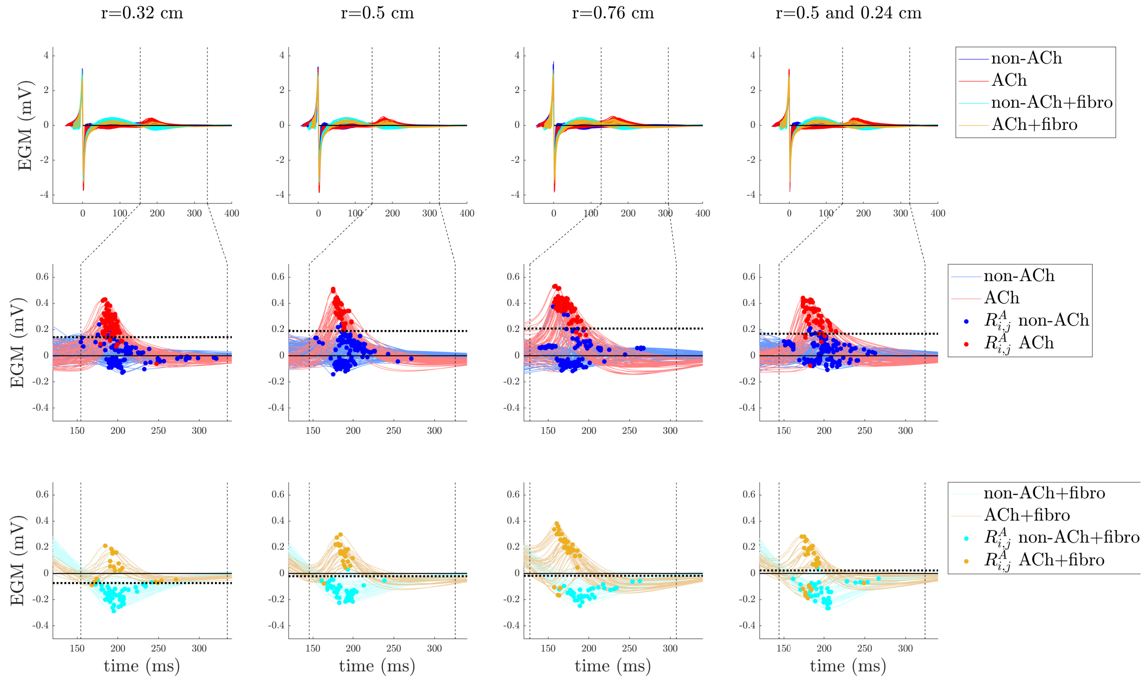

Figure 5.8: EGM analysis for a pxAF tissue with 20% patchy type 1 fibrosis (type 1 patchy fibrosis is represented in Figure 1E)) ($\mathcal{F}^1_{nu}$ 20%). Top row: EGMs aligned with respect to the time correspondent to the maximum slope of the depolarization wave (marked as 0 in the x-axis). The vertical dashed lines delimit the time window TW for the $\mathrm{R_{i,j}(t)}$ repolarization signals. Bottom row: atrial repolarization waves, $\mathrm{R_{i,j}(t)}$, with dots indicating the maximum absolute value $\mathrm{R^A_{i,j}}$ of the waves within TW. The horizontal dotted lines represent the optimal threshold $\mathrm{R^{th}}$ found by Se/Sp analysis.

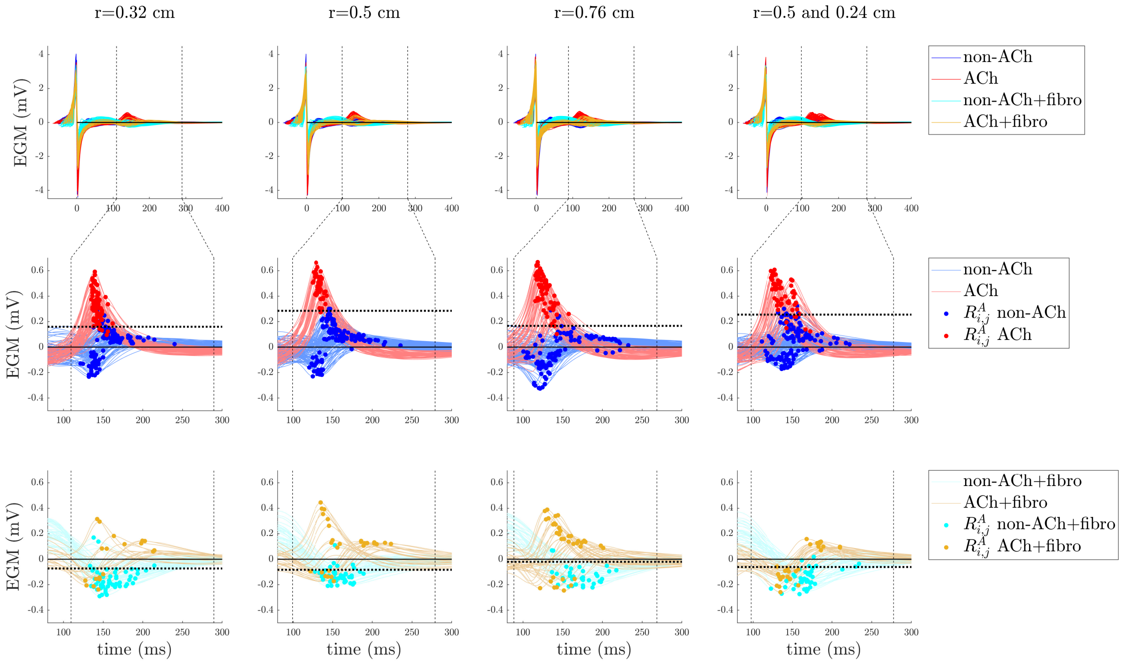

Figure 5.9: EGM analysis for a pxAF tissue with 20% patchy type 2 fibrosis (fibrosis geometry reported in Figure 5.1 F)) ($\mathcal{F}^2_{nu}$, 20%). The figure is structured as Figure 5.8.

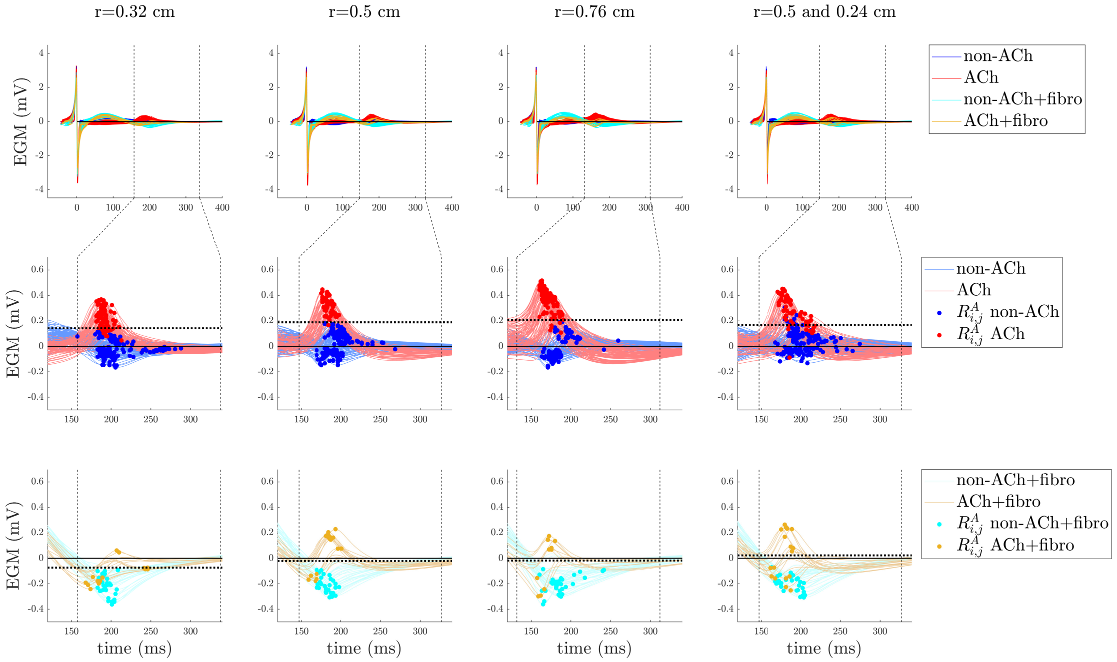

Figure 5.10: EGM analysis for a psAF tissue with 40% patchy type 1 fibrosis (fibrosis geometry reported in Figure 5.1 E)) ($\mathcal{F}^1_{nu}$, 40%). The figure is structured as Figure 5.8.

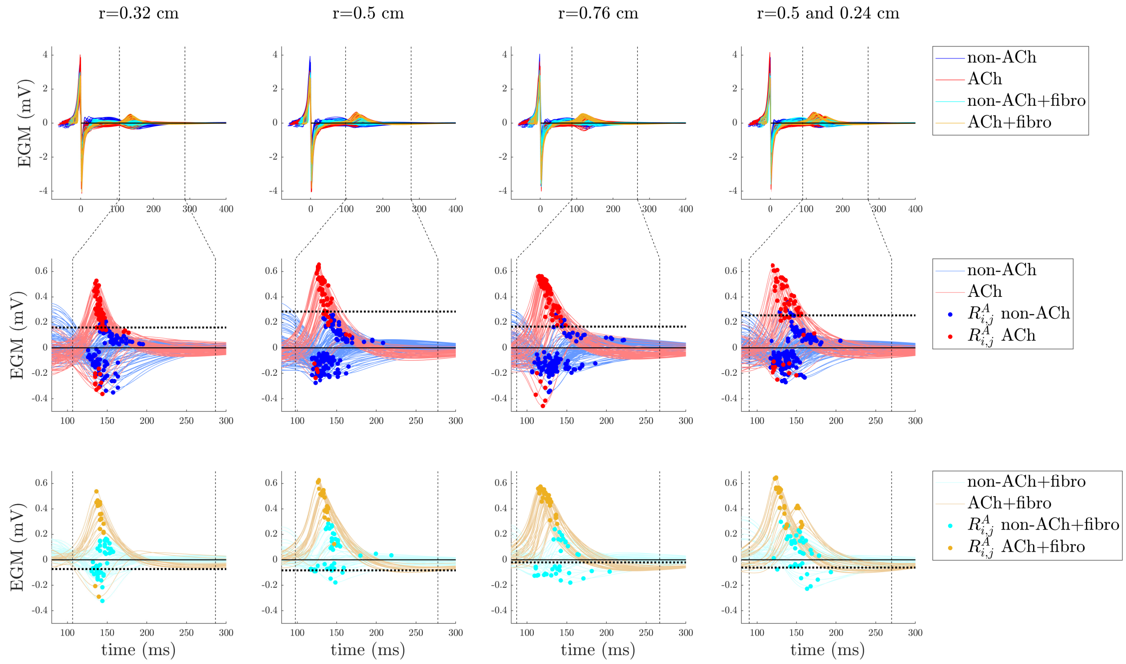

Figure 5.11: EGM analysis for a psAF tissue with 40% patchy type 2 fibrosis (fibrosis geometry reported in Figure 5.1 F)) $(\mathcal{F}^2_{nu}, 40\%)$. The figure is structured as Figure 5.8.

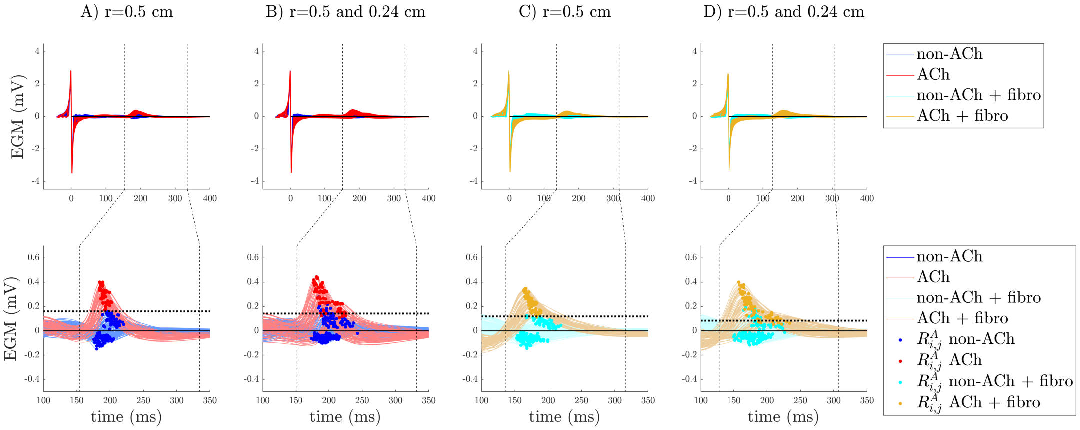

Figure 5.12: EGM analysis for a non-AF tissue in A), B) and a pxAF tissue with 20% uniform diffuse fibrosis in C) and D). Top row: EGMs aligned with respect to the time correspondent to the maximum slope of the depolarization wave (marked as $t = 0$ in the x-axis). The vertical dashed lines delimit the time window TW for the $\mathrm{R_{i,j}(t)}$ repolarization signals. Bottom row: atrial repolarization waves, $\mathrm{R_{i,j}(t)}$, with dots indicating the maximum absolute value, $\mathrm{R^A_{i,j}}$, of the waves within TW. The horizontal dotted lines represent the optimal threshold $\mathrm{R^{th}}$ found by Se/Sp analysis.

from the areas without fibrosis. In the non-fibrotic regions, the threshold was found to lie in the range between 30% and 46% of $\mathrm{R}^{\mathrm{A,max}}$ value. In the fibrotic regions, the peaks were generally organized in two clusters above and below zero, with the positive peaks corresponding to ACh regions. The results of the analysis for 20% $\mathcal{F}_{nu}$ fibrosis with the simulated fibrotic geometry $\mathcal{F}^{1}_{nu}$ are illustrated in Figure 5.13 for ACh patches of radius r=0.5 cm and for ACh patches of radii r=0.5 and 0.24 cm.

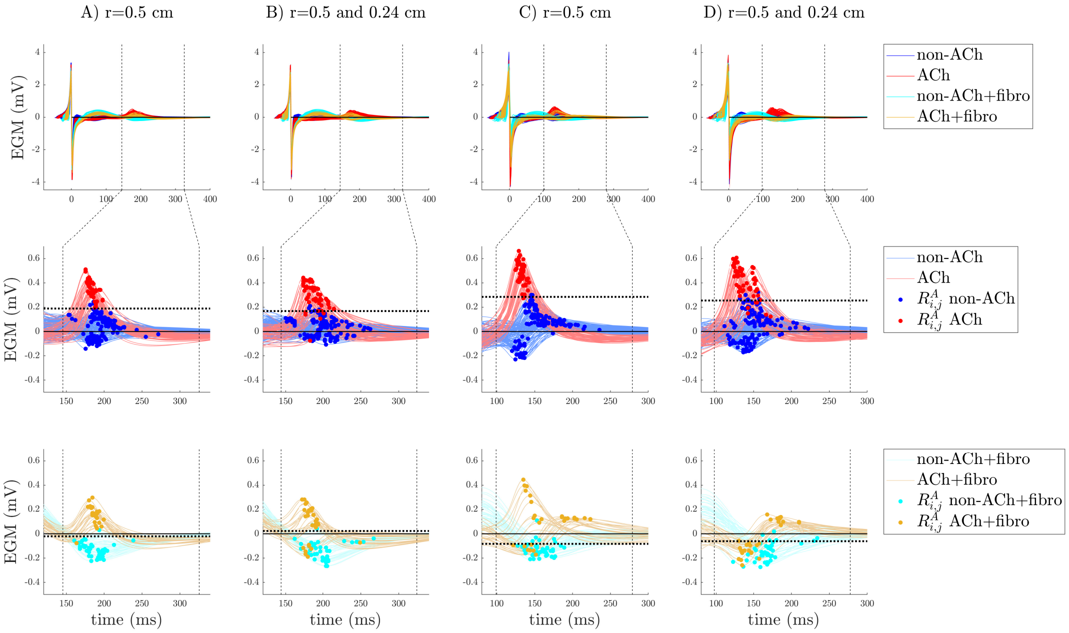

Figure 5.13: EGM analysis for a pxAF tissue with 20% non-uniform diffuse type 1 fibrosis in A), B) and a psAF tissue with 40% type 1 non-uniform diffuse fibrosis in C), D) (type 1 non-uniform diffuse fibrosis is represented in Figure 5.1(E)) cases. Top row: EGMs aligned with respect to the time correspondent to the maximum slope of the depolarization wave (marked as $t = 0$ in the x-axis). The vertical dashed lines delimit the time window TW for the $\mathrm{R}_{\mathrm{i,j}}(\mathrm{t})$ repolarization signals. Bottom rows: atrial repolarization waves, $\mathrm{R}_{\mathrm{i,j}}(\mathrm{t})$, with dots indicating the maximum absolute value $\mathrm{R}^{\mathrm{A}}_{\mathrm{i,j}}$ of the waves within TW. The horizontal dotted lines represent the optimal threshold R^{th} found by Se/Sp analysis.

In psAF tissues with 40% $\mathcal{F}_{u}$ fibrosis, similarly to previous cases, the threshold was found to lie in the range between 14% and 32% of $\mathrm{R}^{\mathrm{A,max}}$. For psAF tissues with 40% $\mathcal{F}_{nu}$ fibrosis, the behavior was the same as for 20% $\mathcal{F}_{nu}$ fibrosis reported above, with the only difference being the onset of the TW. Figure 5.13 shows the results for 40% $\mathcal{F}_{nu}$ fibrosis with the simulated fibrotic geometry $\mathcal{F}^{1}_{nu}$.

EGM depolarization analysis in pxAF and psAF tissues. Given the different morphology of the $\mathrm{R_{i,j}(t)}$ waves in fibrotic vs non-fibrotic areas when non-uniform diffuse fibrosis is simulated, prior identification of fibrotic areas was required to set up thresholds on repolarization amplitude that allow identification of ACh areas. The distribution of the depolarization amplitude $\mathrm{D^A_{i,j}}$ in fibrotic areas, non-fibrotic areas and the whole tissue are shown in Figure 5.14, top line.

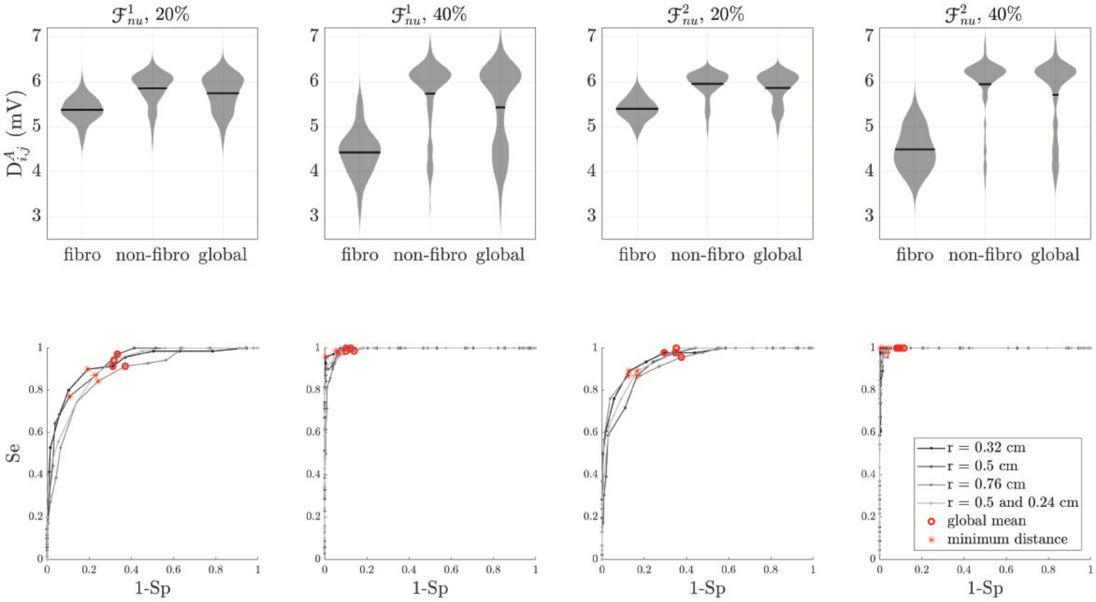

Figure 5.14: Depolarization wave, $\mathrm{D_{i,j}(t)}$ analysis. Top row: statistical distribution of depolarization wave amplitude $\mathrm{D^A_{i,j}}$ in fibrotic areas, non-fibrotic areas and the whole tissue for simulated cases with non-uniform diffuse type 1 and type 2 fibrosis at 20% and 40%. Black lines represent the mean of the distribution. Bottom line: ROC curves for the same simulated cases as in the top row. Optimal thresholds minimizing the Euclidean distance to the top-left corner of the graph are shown with asterisks. Red circles correspond to the mean of the depolarization wave amplitudes. In all cases, the optimal threshold $\mathrm{D^{th}}$ is lower than the global mean.

The results presented in Figure 5.14 for the ACh patches of radius 0.5 cm are representative of all other simulated cases, as ACh distribution does not have an observable effect on the amplitude of the depolarization waves. As it can be observed from the figure, although there is some overlap of the violin plots, particularly for 20% $\mathcal{F}_{nu}$ fibrosis, it is still possible to some extent to distinguish fibrotic vs non-fibrotic areas based on the $\mathrm{D}^{\mathrm{A}}_{\mathrm{i,j}}$ only.

5.3.2 Optimal thresholds for identification of fibrotic and ACh-release areas

The optimal value for the threshold D^{th} on the depolarization amplitude to identify fibrotic areas was found by calculating a ROC curve. Starting from the global mean value of $\mathrm{D}^{\mathrm{A}}_{\mathrm{i,j}}$, 40 different threshold values were analyzed by decreasing and increasing it in voltage steps of 0.1 mV. The optimal value for D^{th} was determined as the point of the curve that was closer, in terms of the Euclidean distance, to the top left corner corresponding to 100% sensitivity and 100% specificity. ROC curves for different fibrosis distributions are illustrated in Figure 5.14, bottom line. Overall, the optimal threshold value was lower than the global mean of $\mathrm{D}^{\mathrm{A}}_{\mathrm{i,j}}$. From the ROC curves, it is also evident that the separability is higher for 40% $\mathcal{F}_{nu}$ than for 20% $\mathcal{F}_{nu}$ fibrosis distributions. The values of the threshold D^{th} on the depolarization amplitude are presented in Table 5.2, as % of the maximum $\mathrm{D}^{\mathrm{A}}_{\mathrm{i,j}}$ value in the grid,

$$\mathrm{D}^{\mathrm{A,max}} = \max_{\mathrm{i,j}}\{\mathrm{D}^{\mathrm{A}}_{\mathrm{i,j}}\}. \tag{5.7}$$

The optimal value for the threshold R^{th} on the repolarization amplitude to identify ACh-release areas was analogously found by a statistical ROC curve analysis. 160 different thresholds expressed in terms of percentage of $\mathrm{R}^{\mathrm{A,max}}$, in voltage steps of 1% of $\mathrm{R}^{\mathrm{A,max}}$, were studied. For simulated cases with non-uniform diffuse fibrosis $\mathcal{F}_{nu}$ distributions, the analysis was separately performed for fibrotic and non-fibrotic areas previously identified according to the optimal threshold D^{th} described above. The ROC curves for ACh identification are illustrated in Figure 5.15.

In the $\mathcal{F}_{nu}$ cases, ROC curves for both fibrotic and non-fibrotic areas are represented. As can be observed from the figure, the detection of ACh areas was more challenging in the fibrotic regions, especially when simulating 40% $\mathcal{F}_{nu}$ fibrosis. Furthermore, for both 20% and 40% $\mathcal{F}_{nu}$ fibrosis, the mixed case containing ACh patches of radii 0.5 and 0.24 cm has the worst measure of separability. The optimal values for the threshold R^{th} are displayed as

Table 5.2: Values of the threshold $\mathrm{D^{th}}$ expressed as percentage of $\mathrm{D^{A,max}}$.

r (cm)	$\mathcal{F}_{nu}^{1}$ **20%**	$\mathcal{F}_{nu}^{2}$ **20%**	$\mathcal{F}_{nu}^{1}$ **40%**	$\mathcal{F}_{nu}^{2}$ **40%**	**mean**
0.32	88	86	75	75	81
0.5	86	88	77	78	82
0.76	88	84	77	81	83
0.5; 0.24	87	87	80	78	83
mean	87	86	77	78	82

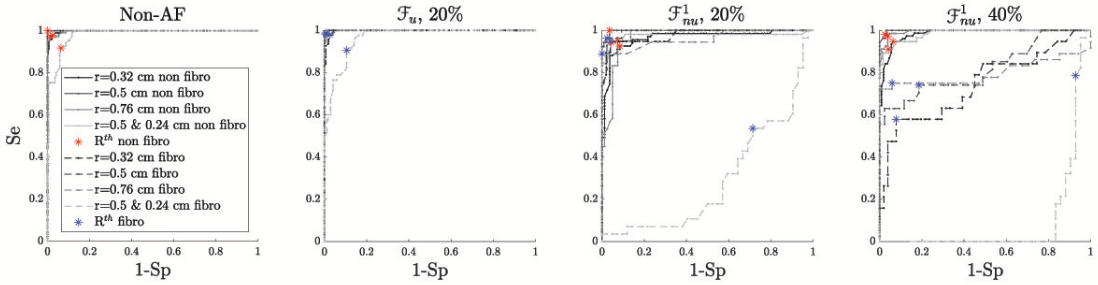

Figure 5.15: Repolarization wave analysis. ROC curves for non-AF tissues and pxAF and psAF tissues with 20% uniform diffuse or type 1 fibrosis and 40% type 1 fibrosis. Results for different sizes of ACh sites are presented. Optimal thresholds $\mathrm{R^{th}}$ thresholds are shown in red and blue. For non-uniform diffuse fibrosis ($\mathcal{F}_{nu}$) cases, the curves for both the fibrotic (dashed lines) and non-fibrotic (continuous lines) regions are represented in the same plot.

dotted lines in Figure 5.12 and Figure 5.13. The values of $\mathrm{R^{th}}$ for all simulated cases are represented in Table 5.3.

Table 5.3: Value of the threshold $\mathrm{R^{th}}$ expressed as percentage of $\mathrm{R^{A,max}}$.

				Non-fibrotic (fibrotic) regions				
r (cm)	**non-AF**	$\mathcal{F}_u$ **20%**	$\mathcal{F}_u$ **40%**	$\mathcal{F}_{nu}^1$ **20%**	$\mathcal{F}_{nu}^2$ **20%**	$\mathcal{F}_{nu}^1$ **40%**	$\mathcal{F}_{nu}^2$ **40%**	**mean**
0.32	23	20	14	33 (-24)	33 (-67)	27 (-24)	30 (-28)	26 (-45)
0.5	41	34	32	36 (-16)	46 (-54)	43 (-23)	44 (+27)	39 (-35)
0.76	32	28	25	39 (-13)	33 (-50)	25 (-12)	44 (-11)	32 (-16)
0.5; 0.24	32	19	17	37 (+17)	30 (-59)	42 (-2)	42 (-16)	31 (-21)
mean	32	25	22	36 (-9)	35 (-57)	34 (-19)	40 (-7)	32 (-33)

5.3.3 Joint analysis for identification of fibrotic and ACh-release areas

Identification of ACh-release areas from EGM signals. Results on the identification of ACh-release areas are presented from Figure 5.16 to Figure 5.19 for the simulated cases shown in Figure 5.12 and Figure 5.13.

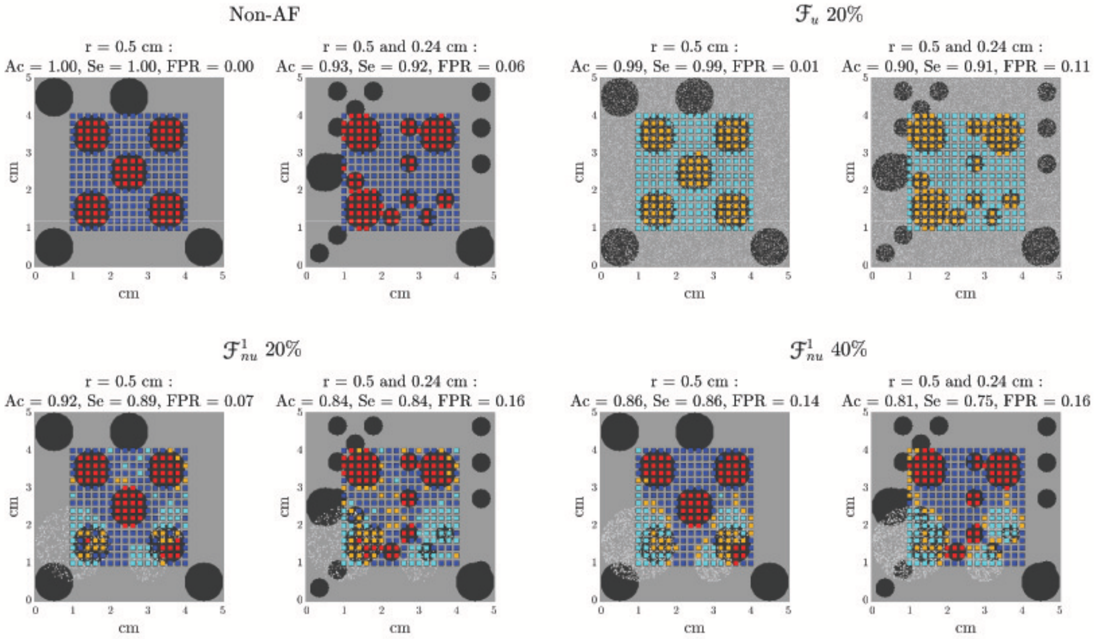

Figure 5.16: Results of the algorithm for detection of ACh release sites. Each electrode is assigned with non-ACh, ACh, non-ACh + fibro or ACh + fibro on the basis of EGM analysis. The color code is the same as in Figure 5.12 and Figure 5.13.

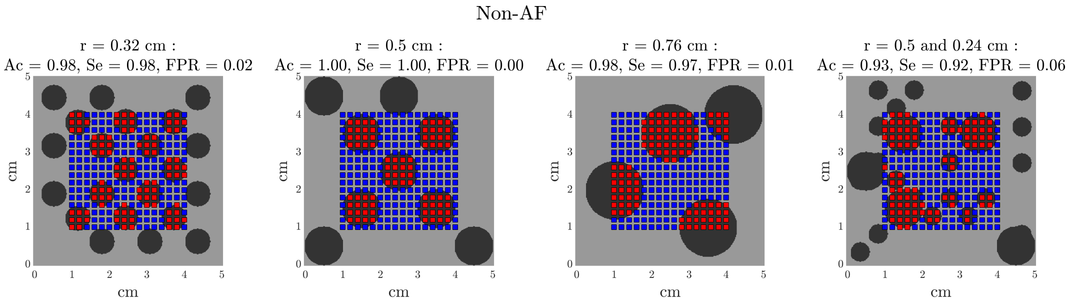

Figure 5.17: Results of the algorithm for detection of ACh release sites. Each electrode is assigned with non-ACh, ACh, non-ACh + fibro or ACh + fibro on the basis of EGM analysis. The color code is the same as in Figure 5.1.

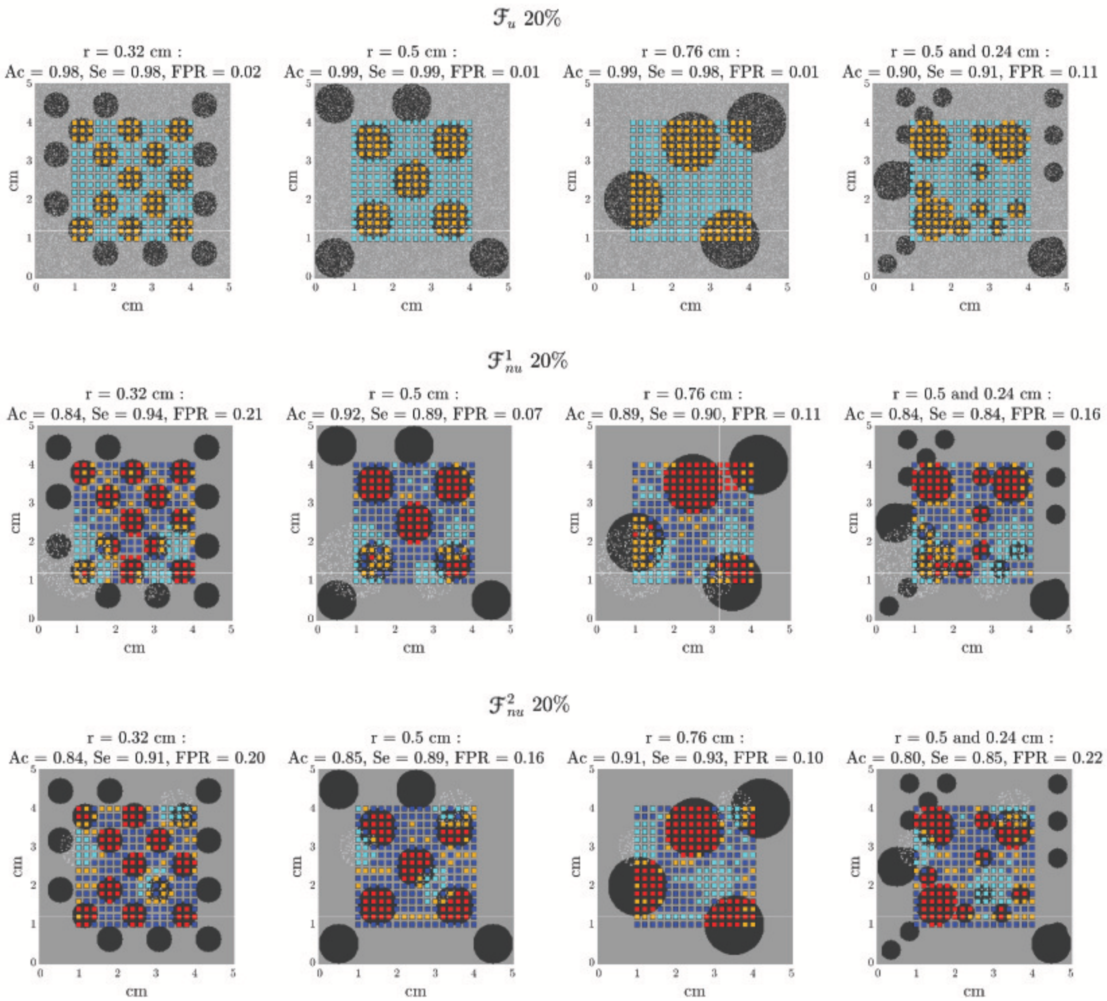

Figure 5.18: Results of the algorithm for detection of all the pxAF cases. Each electrode is assigned with non-ACh, ACh, non-ACh + fibro or ACh + fibro on the basis of EGM analysis. The color code is the same as in Figure 5.3 to Figure 5.16.

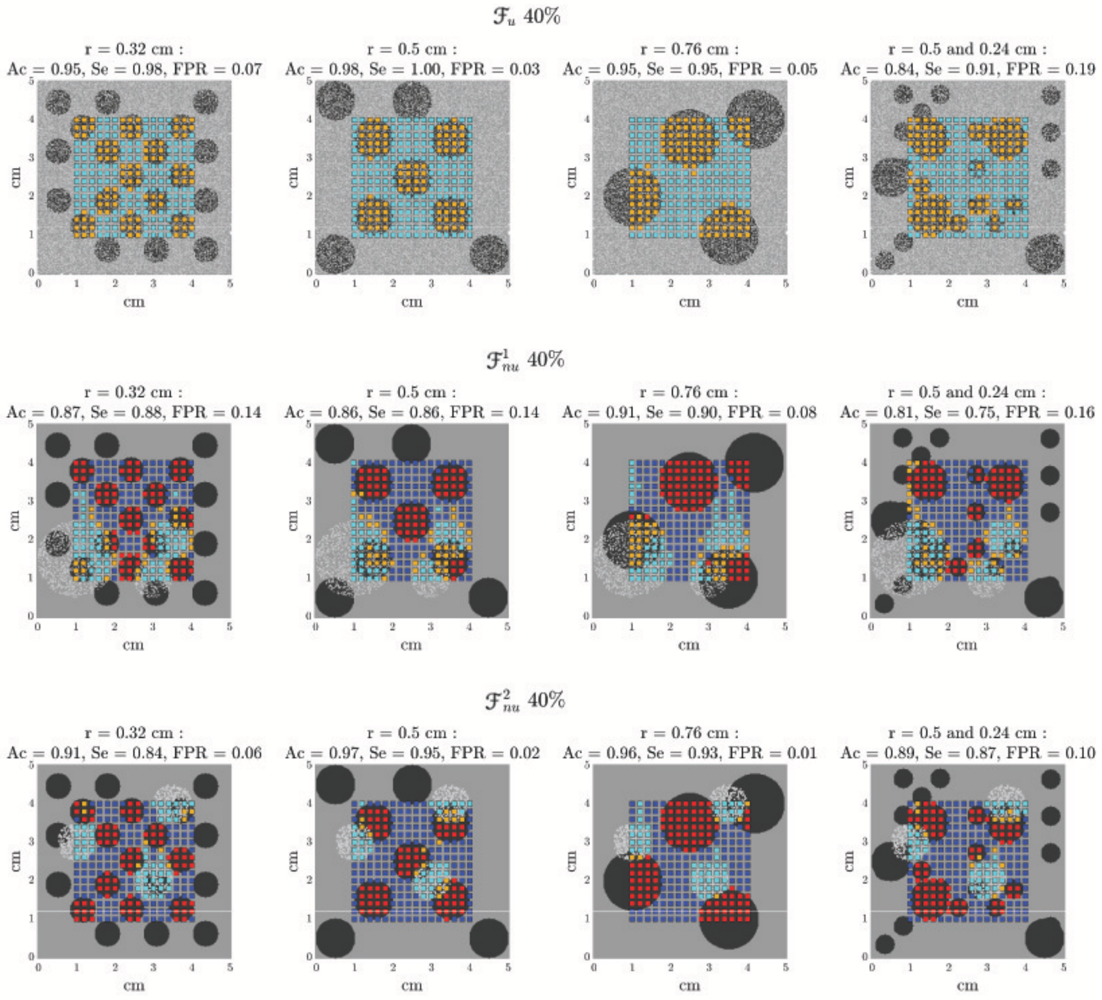

Figure 5.19: Results of the algorithm for detection of all the psAF cases. Each electrode is assigned with non-ACh, ACh, non-ACh + fibro or ACh + fibro on the basis of EGM analysis. The color code is the same as in Figure 5.3 to Figure 5.16.

The values of accuracy (Ac), sensitivity (Se) and false positive rate (FPR), equivalent to (1-Specificity), are reported above the maps presented in Figure 5.16. All results were obtained with the optimal values for the thresholds D^{th} and R^{th} described in section 5.3.2, except for the results presented in section 5.3.3 where the impact of the selected threshold is evaluated.

Non-AF tissues. In non-fibrotic tissues, our algorithm was able to identify all the ACh-release patches, with similar performance measures for the different simulated cases. The mean Ac and Se were both equal to 0.97 while mean FPR was equal to 0.03. The minimum Ac (0.93) and Se (0.92) and the maximum FPR (0.06) were obtained for ACh patches of different radii (r=0.5 and r=0.24).

pxAF tissues. In pxAF tissues with 20% uniform diffuse fibrosis $\mathcal{F}_u$, our algorithm was able to identify all the ACh patches, but, in the mixed case with ACh patches of different sizes, the isolated smaller areas were not completely identified. In pxAF tissues with non-uniform diffuse fibrosis $\mathcal{F}_{nu}^1$ and $\mathcal{F}_{nu}^2$, the algorithm showed very good performance (Mean Ac=0.83 , Mean FPR=0.19), although some of the ACh patches in the fibrotic areas were not detected correctly in its whole extent. Furthermore, some of the sites wrongly detected as fibrotic were subsequently erroneously classified as ACh points.

Nevertheless, in all cases, Ac and Se were above 0.80 and 0.83, respectively, and the maximum FPR rate was 0.22. non-uniform diffuse fibrosis $\mathcal{F}_{nu}$ cases presented worse performance than uniform diffuse fibrosis $\mathcal{F}_u$ cases, as can be observed in the representative cases presented in Figure 5.16.

psAF tissues. In psAF tissues with 40% uniform diffuse fibrosis $\mathcal{F}_u$, our algorithm was able to identify all the ACh patches. In psAF tissues with non-uniform diffuse fibrosis $\mathcal{F}_{nu}^1$ and $\mathcal{F}_{nu}^2$, most of the ACh patches were successfully detected, but those that were of small size and fell completely inside a fibrotic area could not be detected. As in pxAF tissues, the mixed case with ACh patches of different sizes were the one presenting the worst performance.

In all cases, Ac and Se were above 0.84 and 0.82, respectively, The maximum FPR rate was 0.18. ACh identification in psAF tissues with non-uniform diffuse fibrosis $\mathcal{F}_{nu}$ achieved superior performance than in pxAF tissues, mainly because the fibrotic regions were detected better. This can be appreciated from Figure 5.16, which shows the results for a psAF tissue with $\mathcal{F}_{nu}^{1}$ fibrosis.

Threshold selection. To evaluate the impact of using the optimal thresholds D^{th} and R^{th} for each configuration, Ac, Se and FPR were computed again using the mean optimal thresholds value for all situations, reported in Table 5.2 and Table 5.3. Results varied only minimally. The global mean Ac decreased from 0.91 to 0.88, the global mean Se from 0.92 to 0.91 and the global mean FPR from 0.09 to 0.01.

Effects of noise and tissue-electrode distance. The performance of the algorithm for identification of ACh-release areas was tested on noisy signals with different SNR values of 0, 5, 10, 15 and 20 dB, corresponding to σ values of 279.2, 149.6, 89.7, 47.8, 26.9 μV, respectively. The results are displayed in Figure 5.20.

For non-AF tissues and for pxAF and psAF tissues with uniform diffuse fibrosis $\mathcal{F}_{u}$, Ac and FPR highly decreased and increased, respectively, with the level of noise, even if still showing Ac values above 0.76 and FPR values below 0.29 when the SNR was 0 dB. On the other hand, Se was less dependent on noise and had values above 0.7 even for an SNR value of 0 dB. For pxAF and psAF tissues with non-uniform diffuse fibrosis F_{p}, the algorithm's performance was remarkably less dependent on the noise level. In the worst scenarios of SNR being 0 dB, the minimum Ac and Se values over all simulated cases with non-uniform diffuse fibrosis were 0.7 and of 0.63, respectively, while the maximum FPR

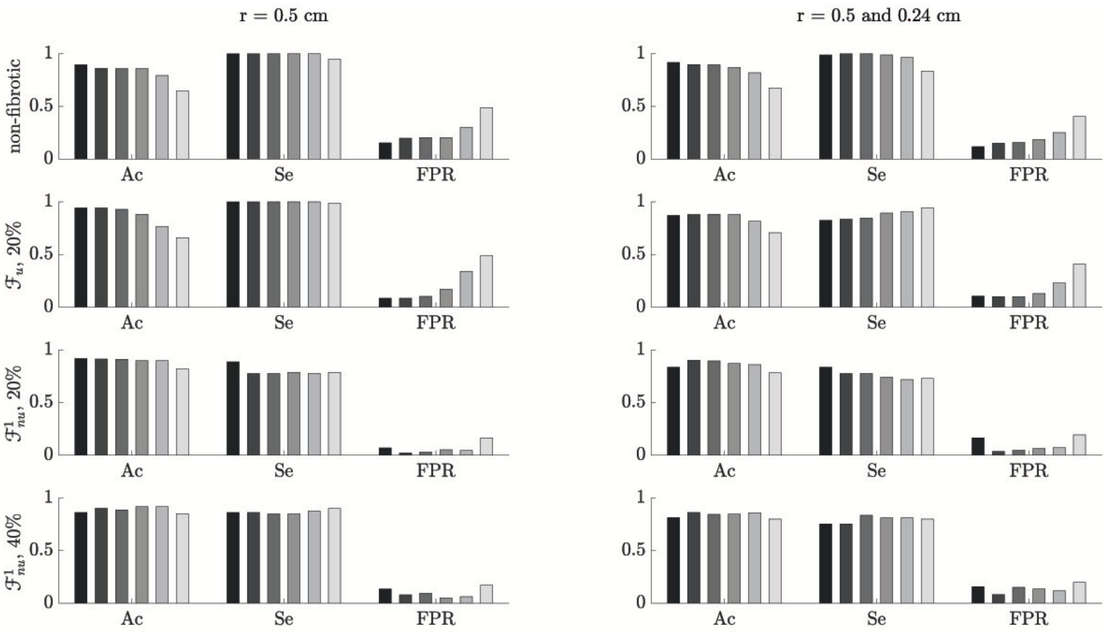

Figure 5.20: Accuracy (Ac), Sensitivity (Se) and false positive rate (FPR) for different noise levels. The color code from dark to light gray is representative of no noise and noise with SNR values of 20 dB, 15 dB, 10 dB, 5 dB and 0 dB.

value was 0.55.

To test the effect of electrode-tissue distance, 3 different distances in the orthogonal direction z, namely 0.5, 1 and 2 mm, were used for EGM calculation in all the simulated cases. The performance of the algorithm as a function of the electrode-tissue distance is reported in Figure 5.21. Ac and Se modestly increased when the electrode became closer to the tissue, while FPR rate slightly increased or decreased with the electrode-tissue distance depending on the characteristics of the tissue.

Assessment of model dependence, cell-to-cell variability and concomitant β-adrenergic stimulation. When using the $\mathcal{G}$ model, although the time windows for repolarization analysis were different with respect to the ones obtained with the $\mathcal{C}$ model, delineation could be successfully applied to the EGM waveforms. As in the $\mathcal{C}$ cases, positive $\mathrm{R_{i,j}(t)}$ waves were found in the ACh patches. A figure showing the corresponding results for the $\mathcal{G}$ and $\mathcal{C}$ model is presented in Figure 5.22.

Including cell-to-cell variability in the $\mathcal{C}$ model, as explained in the Methods section,

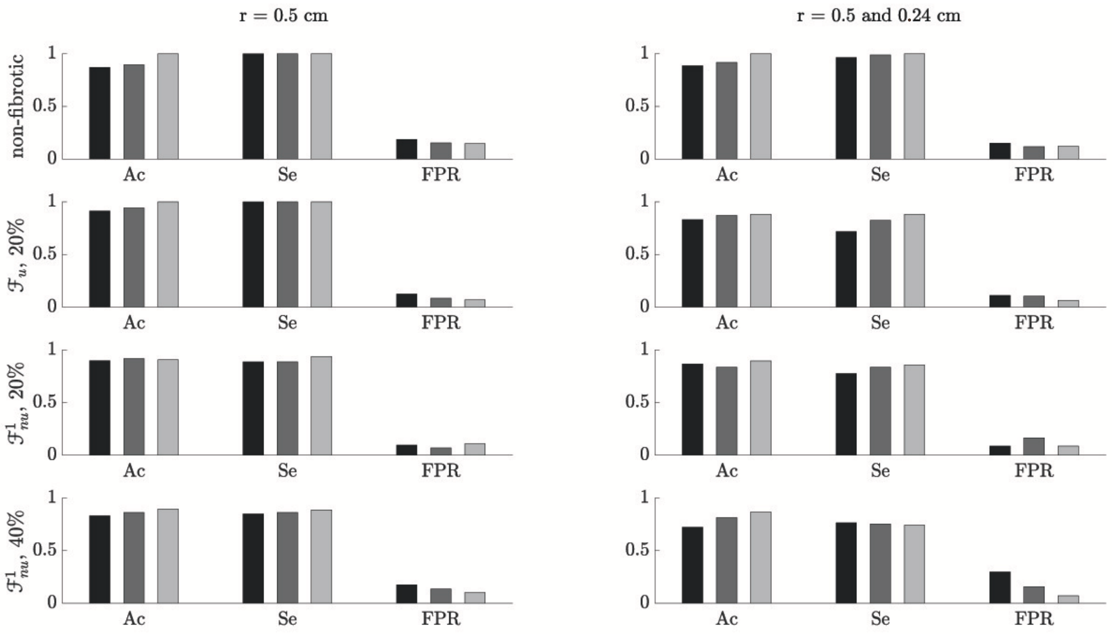

Figure 5.21: Accuracy (Ac), Sensitivity (Se) and false positive rate (FPR) for different electrode-to-tissue distances. The color code from dark to light grey is representative of 2, 1 and 0.5 mm distances.

led to similar results from a qualitative point of view, even if some quantitative differences could be observed. A comparison of the same case considering and not considering cell-to-cell variability can be found in Figure 5.23.

Incorporating β-adrenergic stimulation into some atrial sites led to Iso regions being detected as non-ACh regions on the basis of the amplitude of the $\mathrm{R_{i,j}(t)}$ waves. Based on these results, our method seems to be specifically meant to locate parasympathetic stimulated areas. A figure showing these results can be found in the Figure 5.24.

5.4 Discussion

We developed a novel method to identify ACh release sites in the atrial myocardium based on the characteristics of EGM signals on a grid of electrodes. The method is based on eval-

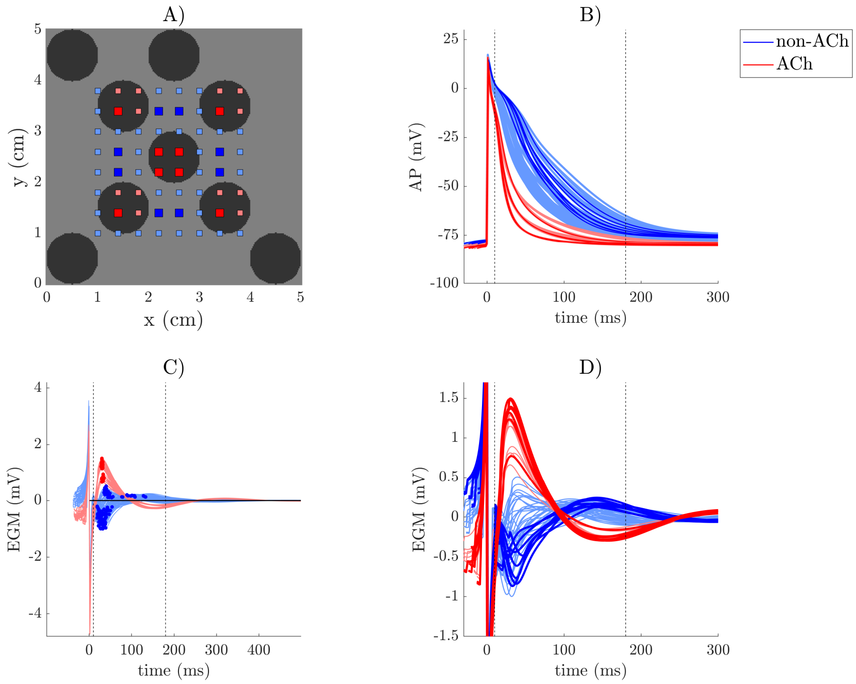

Figure 5.22: A) 2D model of a non-AF tissue with ACh release sites shown in black and EGM electrodes in red and blue. Cell electrophysiology is simulated using the $\mathcal{G}$ model. B)/D) APs/EGMs recorded in the (i,j) points represented in panel A). The thicker lines correspond to the points represented with big squares in the tissue. Panel C) represents the EGMs aligned with respect to the time correspondent to the maximum slope of the depolarization wave (marked as $t = 0$ in the x-axis). The vertical dashed lines delimit the time window TW for the $\mathrm{R}_{\mathrm{i,j}}(\mathrm{t})$ repolarization signals. The dots indicate the maximum absolute value, $\mathrm{R}^{\mathrm{A}}_{\mathrm{i,j}}$, of the waves within TW.

uating the amplitude of the EGM repolarization wave and compare it with a threshold that is dependent on the presence or absence of fibrosis in the tissue portion beneath the EGM electrode position. An accompanying method for fibrosis detection is considered based on the amplitude of the EGM depolarization wave. The performance of our proposed method for identification of ACh release sites in atrial myocardium was tested in simulated tissues representative of control (non-AF), pxAF and psAF. The simulated patterns of propagation resulted from pacing an entire edge of the tissue model at a fixed cycle length for all the cases, with no other AF patterns being simulated. We found that, in all cases, the algorithm was successful in identifying most of the simulated ACh release sites, both when there was no fibrosis in the tissue and when fibrosis was present in uniform diffuse or non-uniform diffuse forms at various degrees. In mean, accuracy and sensitivity values above 90% were achieved.

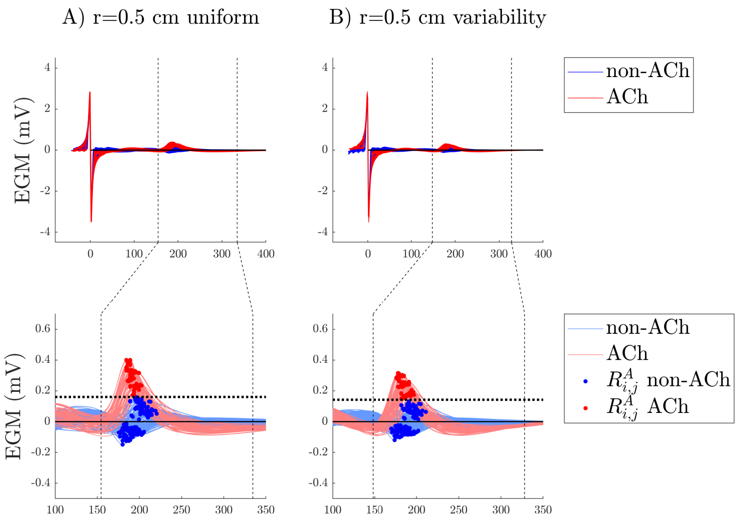

Figure 5.23: EGM analysis for a non-AF tissue. A) represents the uniform cells case while B) represents the case which considers cell to cell variabilty . Top row: EGMs aligned with respect to the time correspondent to the maximum slope of the depolarization wave (marked as 0 in the x-axis). The vertical dashed lines delimit the time window TW for the $\mathrm{R_{i,j}(t)}$ repolarization signals. Bottom row: atrial repolarization waves, $\mathrm{R_{i,j}(t)}$, with dots indicating the maximum absolute value, $\mathrm{R^A_{i,j}}$, of the waves within TW. The horizontal dotted lines represent the optimal threshold $\mathrm{R^{th}}$ found by $\mathrm{Se/Sp}$ analysis.

The role of the ECANS and ICANS in modulating cardiac electrical behavior is well evidenced in the literature. Alterations in autonomic activity are documented to contribute to both initiation and maintenance of AF [163, 359–364]. Decreasing ANS innervation is shown to reduce the incidence of atrial arrhythmias [21, 23, 220, 365]. Specifically regarding the ICANS, stimulation of GPs is reported to make them hyperactive and secrete excessive amounts of neurotranmsitters, which facilitates not only the initiation of AF but also its perpetuation. A study evaluating the intensity of vagal responses induced by endocardial HFS of left atrial GPs highlights an increase in such responses in AF patients compared to non-AF patients, suggesting an abnormally increased GPs activity in AF substrates [161]. Some studies have suggested that the extrinsic autonomic input to the heart exerts inhibitory control over GPs and, consequently, attenuation of this control allows GPs to become hyperactive [341]. On top of elevated neurotransmitter release, other possible explanations for GPs hyperactivity have been reported [161]. One explanation is through its link to oxidative stress, which is strongly related to AF and can cause nerve injury [366]. This injury, in fact, can trigger the expression of nerve growth factors and

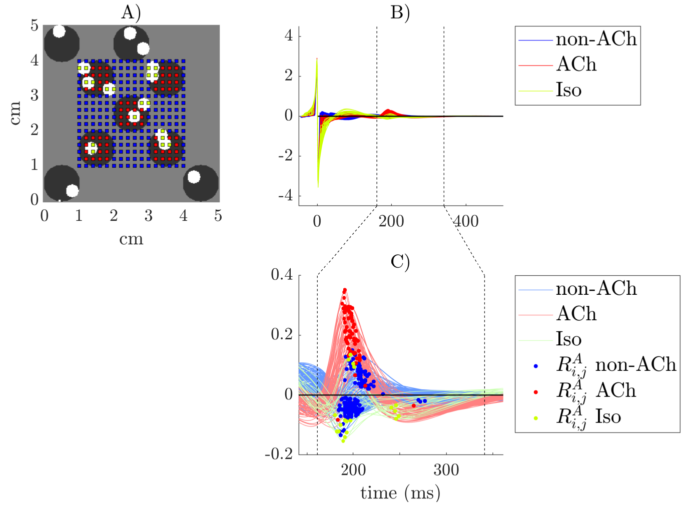

Figure 5.24: A) 2D model of a non-AF tissue with ACh release sites shown in black, β-adrenergically stimulated sites in white and EGM electrodes in red, blue and green. B) EGMs aligned with respect to the time correspondent to the maximum slope of the depolarization wave (marked as 0 in the x-axis). The vertical dashed lines delimit the time window TW for the $\mathrm{R_{i,j}(t)}$ repolarization signals. C) Atrial repolarization waves, $\mathrm{R_{i,j}(t)}$, with dots indicating the maximum absolute value, $\mathrm{R^A_{i,j}}$, of the waves within TW.

neurotrophic factors in non-neuronal cells near the site of the lesion [367], which can lead to nerve sprouting. Another possible explanation is the increase in the density of the neural network, with an increased number of sympathetic and parasympathetic neurons, in association with GPs-induced AF [368].

All the above effects related to GPs stimulation involve both the sympathetic and parasympathetic divisions of the ANS. Cholinergic stimulation shortens the APD and leads to membrane hyperpolarization, while β-adrenergic stimulation can induce early afterdepolarizations, leading to rapid, triggered firing [161, 170, 369, 370]. Of the two, a predominant role of the parasympathetic division has been reported [371, 372]. Here, we modeled the electrophysiology of 2D atrial tissues for non-AF, pxAF and psAF conditions, in which we incorporated circles of ACh release with different locations and/or sizes. Our simulations confirmed that cholinergic stimulation of atrial myocardium varies as a function of the atrial substrate, particularly depending on the fibrosis amount and distribution.

GP ablation as an adjunct to PV isolation has been shown to improve the outcomes of ablation procedures in pxAF and psAF patients [26, 227]. In a canine study where GPs are surgically removed, this technique is reported to acutely reduce the effects of vagosympathetic trunk stimulation on the atrial myocardium in an extensive way [373]. In situations in which GP activity facilitates the initiation and maintenance of AF, GP ablation could result in more beneficial than detrimental effects [371]. However, there are still a number of aspects related to GP ablation that deserve further investigation, including whether reinnervation occurs in the long-term after GP ablation and whether this could contribute to AF recurrence. In any case, if clinical trials with large number of patients and long follow-up establish the efficacy of GP ablation, accurate location of GPs should be key and our proposed approach could find a place in the identification of GPs location and extension. The methods currently available to locate GPs are the so called functional approach, based on HFS [22, 26], and the so called anatomical approach, which uses anatomical mapping to identify the presumed GPs locations [25]. Both methods, however, show limitations. On the one hand, the anatomical targeting of GPs sites leaves the question open regarding the extent of GPs area to be ablated, which could vary from one to another patient. On the other hand, GPs sites identified by functional HFS may require several cardioversions following AF induction before testing for additional sites. Also, the equipment to perform HFS is not commonly available in all hospital facilities where ablation is performed and, importantly, studies have shown that GP ablation based on the functional approach may lead to higher AF recurrence than that based on the anatomical approach in pxAF patients [25, 371, 374].

Considering that atrial EGM mapping is normally performed during ablation procedures, the aim of this work was to find EGM features that serve to locate ACh release sites in atrial myocardium. From our simulated atrial tissues, we computed EGMs on a high density mesh of 16×16 electrodes. We started by characterizing changes in the amplitude of the EGM atrial repolarization wave under the presence of cholinergic stimulation, showing an increased amplitude in myocardial sites stimulated by ACh. This can be explained by a faster phase 3 of action potentials in cholinergically stimulated cells. When setting a threshold on the repolarization amplitude to identify ACh release sites, that threshold was found to be different according to the amount of fibrosis in the myocardium beneath the EGM electrode. Considering that there are regions in the atria, like the posterior wall of the LA, that are preferential locations for GPs and fibrosis [375, 376], we used a method to distinguish fibrotic vs non-fibrotic areas before applying our algorithm for identification of ACh sites. There are only a few previous studies in the literature characterizing ACh effects on atrial EGMs. In [377], EGM patterns from pxAF patients are compared with *in silico* simulated EGMs. ACh release sites are associated with fractionated EGMs, being the number of deflections the first predictor of cholinergic response. In [342, 378], high density electrical recordings were acquired from dogs under vagal stimulation and computational simulations are performed. An increased amplitude of the atrial repolarization wave was found in and around ACh islands. In that study, however, the interaction between ACh release sites and different amounts and distributions of fibrosis was not investigated. Our work confirms the findings from that study regarding ACh effects in non-AF tissues and further extends the results to pxAF and psAF substrates in the presence of electrical and/or structural remodeling, highlighting the need to first identify fibrotic areas. To identify those areas, we used the amplitude of the EGM depolarization wave, as commonly performed in clinical practice [356–358]. When the amount of fibrosis was high (40%), the detection of fibrotic areas was successful. This performance was, however, reduced under lower levels of fibrosis (20%) if this was distributed in patches, making the error subsequently propagate to identification of ACh sites. Other strategies for fibrosis detection based on bipolar EGM amplitude or using shape-based methods [379] could improve the performance in those specific cases.

To identify ACh areas based on the amplitude of the repolarization waves, we preprocessed the EGM signals by application of a 2 Hz highpass filter, which is a possibility with NavX system (Endocardial Solutions, St. Jude Medical, Inc., St. Paul, MN, USA), but not with others like Carto® system (Biosense Webster, Baldwin Park, CA, USA), in which the lowest cutoff frequency is around 5 Hz and highpass filtering the signal using that cutoff frequency could lead to $\mathrm{R_{i,j}(t)}$ wave cancellation. Our method should, thus, be adjusted depending on the characteristics of the system. Regarding performance, we can conclude that our algorithm successfully identifies the ACh release sites, particularly in tissues with no fibrosis or with diffusive fibrosis and uniform dimensions of the ACh patches. In the case of tissues with non-uniform diffuse fibrosis, the smaller ACh release sites can only be partially identified, or in some cases not identified, if they lie in fibrotic regions. Since in the clinical setting it is likely that only the major GPs are of interest for ablation procedures, our strategy is expected to work fine. Indeed, our method generally produces very good results for the largest ACh release sites, providing information not only on their location but also on their extension. It should be noted that the method was tested on both pxAF and psAF substrates. Some studies show that the improvement in the outcome of ablation procedures is mainly observed in pxAF [25, 343]. When ablation includes GPs, this could be explained according to the hypothesis that autonomic hyperactivity plays a more predominant role in the early stages of AF development and that its relevance decreases with the progression of the disease and the consequent structural remodeling [341]. Independently of the amount of GPs hyperactivity, the method here proposed is able to locate ACh release sites with high performance, with mean Ac and Se over all simulated cases being above 0.91.

5.5 Limitations

Some limitations of this study should be acknowledged to provide direction for further work. We investigated 2D atrial tissue sheets with different fibrosis distributions and ACh-release areas. Although we did not include regional electrophysiological heterogeneities in the tissues, we confirmed that introducing cell-to-cell variability in electrical properties led to the same qualitative conclusions. Further studies could implement 3D atrial geometries with more realistic GPs distributions, accounting for its structural complexity and incorporating many of the regional electrical heterogeneities present in the intact organ. Also, different stimulation sites and protocols could be tested to assess the impact of other activation patterns on the performance of our proposed methods.

The differentiation between pxAF and psAF is challenging. Current clinical AF classification (paroxysmal, persistent, long-term persistent, permanent) is based on the duration of AF episodes and form of termination [76]. AF is considered to be a progressive disease, starting from short and infrequent episodes to longer and more frequent ones. This progression is overall shown to be accompanied by alterations in myocardial substrate. As introduced in section 1.3.3, increased fibrosis with the progression of the pathology is common in AF [78]. However, studies have shown that there are cases of pxAF patients having extensive fibrosis and psAF patients having only minor fibrosis [78, 84–86]. Our models reflect a simplified categorization of AF, with fibrotic load increasing with AF progression. As such, they should mainly serve as a proof of concept of the feasibility of our proposed method for different AF substrates.

To model atrial structural remodeling associated with the psAF substrate, we considered a combination of GJ remodeling, modeled through tissue conductance reduction in fibrotic regions, as well as fibroblast proliferation. We did not consider the increase in collagen content, which is usually modeled as non-conductive obstacles in the tissue. Nevertheless, considering that increased collagen content in the interstitial spaces between fibers has been found not to generally affect longitudinal conduction [88, 284, 380], and since we simulated a planar wavefront, this would not be expected to alter our results.

When simulating electrical remodeling in psAF, we also considered the possibility to add $\mathrm{I_{K1}}$ current remodeling, as several studies have reported an increase in this current in psAF by a factor of two or more [35, 107]. Simulation of such an $\mathrm{I_{K1}}$ increase in the $\mathcal{C}$ model required reducing the ACh concentration to 0.01 μM for an AP to be elicited. Therefore, we considered a 50% $\mathrm{I_{K1}}$ increase as in Shim et al. [381], which allowed considering an ACh concentration of 0.05 μM. The APs obtained from single cell simulations are reported in Figure 5.25. The results in terms of $\mathrm{R_{i,j}(t)}$ after including $\mathrm{I_{K1}}$ remodeling are qualitatively similar to the ones presented without including $\mathrm{I_{K1}}$ remodeling in psAF. It should be noted that, since ACh concentration was reduced, this led to a reduction in the repolarization waves' amplitude, which occurs with and without $\mathrm{I_{K1}}$ remodeling, the latter both for psAF and pxAF cases. Simulation results showing these effects are reported in the Figure 5.26.

To find the optimal values of depolarization and repolarization amplitude thresholds for identification of fibrotic and ACh regions, we used a statistical ROC curve analysis. For this method to be applicable in clinical practice, another set of data would be required to build the ROC curves, as in the set of data under analysis the Se and Sp values would not be available *a priori*. To evaluate the impact of the thresholds on the method performance, we alternatively computed Ac, Se and FPR using the mean values of depolarization and repolarization amplitudes in the tissue being analyzed. We found only minimal differences,

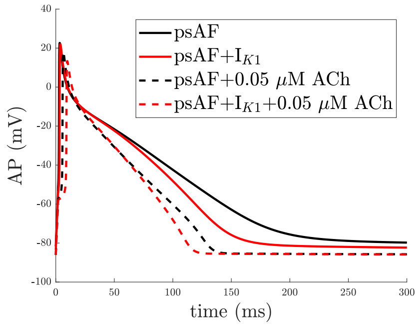

Figure 5.25: Action potentials obtained from single cell simulations pacing the cell at 1 Hz for 60 seconds. The continuous lines represent AP when ACh is not added, while the dashed lines represent the same cases with the addition of 0.05 μM ACh. The black lines represent the formulation of psAF adopted in the manuscript, while the red lines represent the results after including 50% increase in $\mathrm{I_{K1}}$.

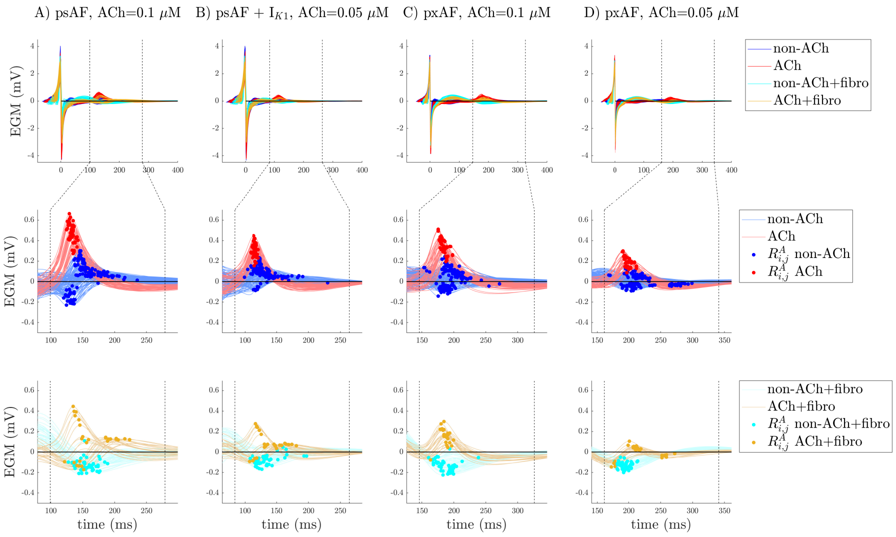

Figure 5.26: EGM analysis for the case with 0.5 cm ACh patches and 20% or 40% $\mathcal{F}^1_{nu}$. Panel A) represents psAF tissues without $\mathrm{I_{K1}}$ remodeling and ACh=0.1 μM. Panel B) represents psAF tissues with $\mathrm{I_{K1}}$ remodeling and ACh=0.05 μM. Panel C) shows the pxAF case with ACh=0.1 μM. Panel D) corresponds to the pxAF case with ACh=0.05 μM. Top row: EGMs aligned with respect to the time correspondent to the maximum slope of the depolarization wave (marked as $t = 0$ in the x-axis). The vertical dashed lines delimit the time window TW for the $\mathrm{R_{i,j}(t)}$ repolarization signals. Bottom row: atrial repolarization waves, $\mathrm{R_{i,j}(t)}$, with dots indicating the maximum absolute value, $\mathrm{R^A_{i,j}}$, of the waves within TW. The horizontal dotted lines represent the optimal threshold $\mathrm{R^{th}}$ found by Se/Sp analysis.

thus confirming that the performance was not degraded. This proves the robustness of our method using mean thresholds even if only in the simulation framework. In the clinical setting, one possibility to retrieve data to build ROC curves for the analysis of EGMs from patients would be to collect those EGMs while performing HFS location of GPs. This data could be analyzed offline to identify the optimal thresholds and compare the performance of the method using mean amplitude thresholds against the one using optimal thresholds. Upon confirmation of the suitability of using mean thresholds, these could be later used in real time.

Finally, detection of the atrial repolarization wave in EGMs could be difficult due to contamination related to ventricular depolarization activity. However, some works have already investigated the feasibility of unipolar EGMs' atrial repolarization waves identification and analysis. Jousset et al. investigated principal component analysis of intracardiac unipolar EGMs to subtract ventricular activity [382]. Other studies by the same group [383, 384] characterized atrial repolarization in sheep. Jousset et al. considered two sets of animals: one with AV block to prevent far-field ventricular depolarization impinging on the preceding atrial repolarization, and the other one without AV block. A method for ventricular activity cancellation was used in the non AV block group. In any case, atrial repolarization alternans were detected from unipolar EGMs in all sheep. The apex of the atrial repolarization wave was evaluated, which could serve as a basis to support the feasibility of measuring atrial repolarization amplitude, as proposed in our study. In another work, atrial repolarization waves were characterized using high resolution atrial bipolar EGMs and the effects of vagal nerve stimulation on repolarization duration were assessed [385].

5.5.1 Conclusions

Our study develops a method to locate atrial ACh release sites based on the analysis of the repolarization phase amplitude of EGM signals from a grid of electrodes. The method is tested in simulated non-AF, pxAF and psAF tissues with different sizes and locations of ACh and fibrosis areas, in which propagation patterns were simulated by pacing an entire edge of the tissue model at a constant cycle length. In all simulated cases, the method is able to identify ACh sites with an accuracy above 0.8, being the mean larger than 0.91.

The method is robust against noise and works well with various EGM electrode distances. Despite simplification in the *in silico* modeling of non-AF, pxAF and psAF tissues, our results could serve as a proof of concept for the feasibility of unveiling ACh sites from atrial electroanatomical mapping during ablation interventions.

Chapter 6

Characterization of the effects of pharmacological AF therapies targeting ion channels and sympathetic modulation

6.1 Motivation

Despite recent advancements in AF management, current pharmacological therapies still present limitations in terms of efficacy and side effects. Class III antiarrhythmic drugs target potassium channels driving AP repolarization, leading to an increase in APD and WL. To minimize potentially harmful side effects on the ventricles, potassium channels primarily expressed in the atria are being considered as targets for AF therapy.

SK channels have emerged as potential atrial-selective targets [121, 153, 386]. *In vivo* and *ex vivo* studies have postulated SK channel inhibition as a potential therapeutic strategy for AF treatment. By prolonging APD and ERP, SK channel inhibition may counteract the effects of parasympathetic stimulation in the atria [121, 387].

In another line of research and based on the crucial role of the ANS in modulating atrial electrical activity, therapies targeting the ANS have been investigated and shown, applied individually or in combination with other treatments, to reduce the incidence of atrial arrhythmias [153]. In particular, some studies have explored the interaction between adrenergic and cholinergic stimulation effects in the atria. In [388], low concentrations of Iso were found to significantly counteract cholinergic effects by limiting the shortening of APD caused by ACh. This modulation of atrial repolarization is due to the effects of Iso on the sarcoplasmic reticulum, I_{Ks} and I_{Kur} and I_{CaL}, among others [259, 389–391].

This study aims to evaluate the effectiveness of combining β-adrenergic stimulation and SK channel blockers (SKb) in countering cholinergic-induced abnormalities in atrial electrical activity. Our hypothesis is that the simultaneous application of Iso and SKb can prolong the APD shortened by ACh and restore it to its baseline state. To test this hypothesis, numerical simulations are conducted using human atrial cell and 2D tissue models that consider adrenergic, cholinergic and SKb effects. The steady-state effects of Iso and/or SKb on AP shape and APD_{90} are evaluated. The efficacy of Iso and SKb, both individually and in combination, in terminating rotational activity in a cholinergically stimulated 2D tissue model of AF is also investigated. A range of SKb and Iso application kinetics, representative of different drug binding rates, are considered to assess the role of pharmacokinetics in rotor termination under varying levels of cholinergic activation.

6.2 Methods

6.2.1 Human atrial cell models

As reported in section 2.2, to test the model independence of our findings, we selected a model of each of the three main types of available atrial cellular models in the literature: Courtemanche, Nygren-Maleckar-Koivumäki-Skibsbye and Grandi [246]. Specifically, we used $\mathcal{C}$ [244], $\mathcal{S}$ [121], and $\mathcal{G}$ [38] human atrial AP models. For each of the three models, the effects of cholinergic and adrenergic stimulation and the formulation of the I_{SK} current were incorporated, as described in section 2.2 and summarized in Table 2.1.

The cardiomyocyte models described in section 2.2 were considered to represent atrial cells in either SR or with early-onset AF. Models of psAF were generated by incorporating

AF-induced electrical remodeling as described in section 2.2.4 and summarized in Table 2.1.

6.2.2 Human atrial tissue models

The effects of cholinergic and β-adrenergic stimulation and SKb were investigated by modeling 2D human atrial tissues of 5x5 cm^2. The models considered a longitudinal diffusion coefficient of 0.003 cm^2/ms and a transverse-to-longitudinal diffusion coefficient ratio of 0.5. The longitudinal conduction velocity was found to be 94.12 cm/s, which is in line with experimental data reported in the literature [258]. The analysis of steady-state electrophysiological properties considered both a homogeneous spatial distribution of ACh and a heterogeneous distribution with circular patches of 0.5-cm radius. For the analysis of transient electrophysiological properties, only a uniformly distributed ACh was considered. After verifying that the combination of SKb and Iso produced comparable results in all three analyzed AP models, tissue analysis was performed using only the $\mathcal{C}$ model.

6.2.3 Numerical simulations

Single cells were subjected to pacing with a fixed CL until they reached steady state in each of the three employed models, as described in section 2.2.

The $\mathcal{C}$ model was used for tissue simulations with its state variables initialized to the steady-state values obtained from single cell simulations. The temporal resolution for the $\mathcal{S}$ and $\mathcal{C}$ models was 0.005 ms, while the $\mathcal{G}$ model was run with a temporal resolution of 0.001 ms, ensuring numerical convergence of the results. In the tissue simulations, a spatial resolution of 0.02 cm was considered. The electrical propagation in the tissue was described using the monodomain reaction-diffusion equation.

The cellular simulations were performed using MATLAB, while tissue simulations were performed using ELECTRA [287–289].

6.2.4 Analysis of steady-state and transient electrophysiological behavior

Steady-state behavior. At the cellular level, the impact of cholinergic stimulation on APs was studied at ACh concentrations of 0.001, 0.01, 0.1 and 1 μM. These ACh concentrations were within the ranges tested in previous studies [258]. In the tissue, the effects of ACh concentrations of 0.01 and 0.1 μM were investigated. The individual and combined effects of SKb and β-adrenergic stimulation were studied in conjunction with the various ACh levels. The impact of β-adrenergic stimulation was simulated by adding a saturating concentration of Iso of 1 μM, while the effect of complete SKb was simulated by reducing the conductance, g_{SK}, of the I_{SK} current to zero. SKb and Iso were applied uniformly throughout the tissue, regardless of whether ACh was distributed homogeneously or heterogeneously. To study the frequency-dependent effects, the models were paced at fixed CLs of 300, 500 and 1000 ms and AP properties were evaluated at steady state for each of those CL values.

Transient behavior. The tissue was subjected to a cross-stimulation protocol to induce reentrant activity, consisting of two stimuli, S1 and S2. S1 was delivered to the bottom edge of the tissue, while S2 was applied to a 2.5 x 2.5 cm^2 square at the bottom right corner. The timing of S2 was determined based on the concentration of ACh, as it altered the APD and conduction velocity. For ACh concentrations of 0.01 and 0.1 μM, the timing of S2 was equal to 155 and 105 ms, respectively. A rotor was considered stable if it did not end spontaneously during the 12-second simulation time. Once stability was confirmed, the simulation was restarted with the same initial conditions. After the first two seconds of simulation, 1 μM Iso and total SKb were progressively introduced following the load curves illustrated in Figure 6.1 [392] to assess their ability to halt the initiated rotor. The load curves were defined to depict different drug association rates to evaluate whether rotor termination was affected by the application kinetics. The time intervals Δt_a to go from 0 to maximum (either Iso concentration or SKb) were equal to 0.1, 1, 5, and 8 seconds. The simulation was run for a total of 12 seconds. After a rotor was stopped, different

S1-S2 intervals were applied again to the tissue to test for rotor re-inducibility, with the application time of the S1-S2 stimuli varying from 100 to 1000 ms after the rotor stopped.

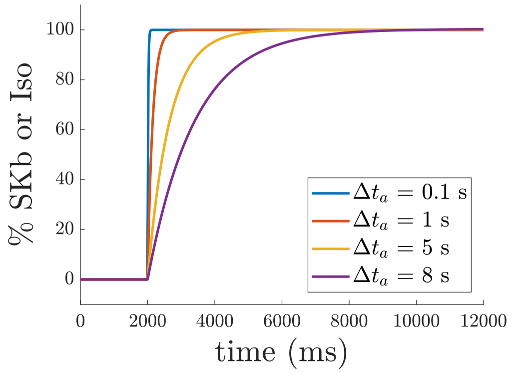

Figure 6.1: Load curves for Iso and SKb expressed as percentage of SKb and Iso concentration with respect to 1 μM Iso and complete SKb, respectively.

6.3 Results

6.3.1 Human atrial cell

Individual cholinergic, β-adrenergic and SKb effects. Cholinergic stimulation with ACh had a concentration-dependent effect on RMP hyperpolarization and APD_{90} shortening in all three analyzed AP models, which aligns with previous experimental findings [256, 388]. The shape of the AP was not significantly altered. The top row of Figure 6.2 and Figure 6.7 show the steady-state AP and APD_{90} at different ACh concentrations, with a CL of 1000 ms. Results for CLs of 500 and 300 ms can be found in Figure 6.3 and Figure 6.4, respectively.

ACh had a stronger effect on the $\mathcal{G}$ model compared to the $\mathcal{C}$ and $\mathcal{S}$ models. At the highest tested concentration of 0.1 μM, ACh reduced APD_{90} by 84.12% in the $\mathcal{G}$ model, 51.85% in the $\mathcal{C}$ model and 41.3% in the $\mathcal{S}$ model. Additionally, ACh decreased RMP by 6.32 mV in the $\mathcal{G}$ model, 5.50 mV in the $\mathcal{C}$ model and 2.37 mV in the $\mathcal{S}$ model. These results are presented in the first row of Figure 6.2.

Iso stimulation with 1 μM had different effects on APD_{90} depending on the baseline AP morphology, as seen in the middle row of Figure 6.2. In the $\mathcal{C}$ model, Iso shortened APD_{90}

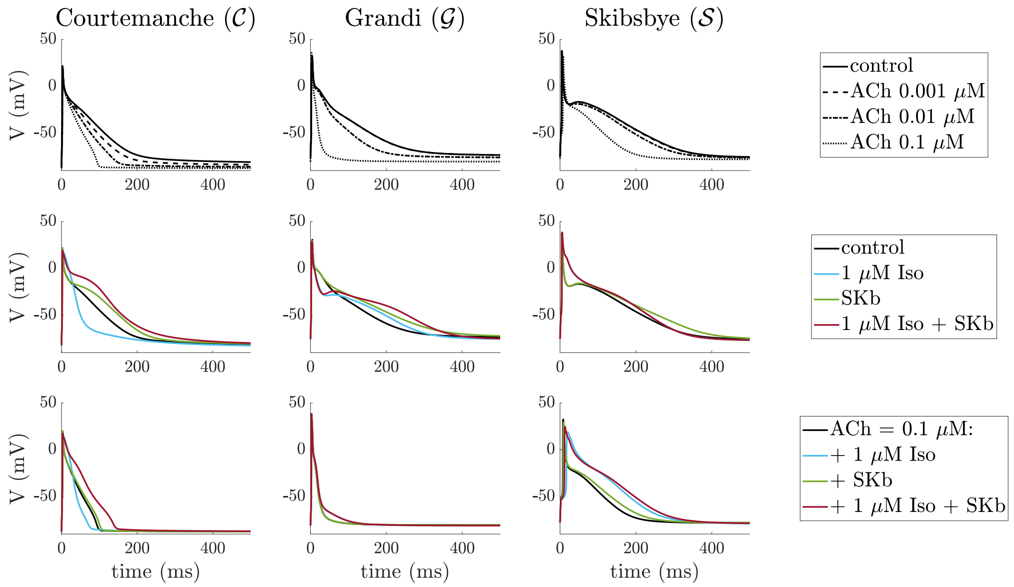

Figure 6.2: APs of human atrial cardiomyocytes models paced at a CL of 1000 ms. First row: simulated effects of ACh (at concentrations of 0.001, 0.01 and 0.1 μM). Second row: Iso (at 1 μM concentration) and SKb. Third row: Iso (at 1 μM concentration) and SKb on top of 0.1 μM ACh.

by 19.11%, whereas in the $\mathcal{G}$ and $\mathcal{S}$ models, Iso slightly prolonged APD_{90}. In the $\mathcal{C}$ model, Iso caused a strong plateau elevation and changed the AP from a triangular to a rectangular shape. This variation in AP response to Iso is consistent with previous research, with some studies observing APD_{90} shortening [388, 393] and others observing APD_{90} prolongation [196, 259, 394].

The application of SKb led to a longer phase 3 of the AP due to a reduction in the outward potassium current. As a result, the APD_{90} was increased. The AP morphology was particularly affected in the $\mathcal{C}$ model, with a notable prolongation of the plateau phase, as shown in the middle row of Figure 6.2.

When a concentration of 1 μM Iso and SKb were applied together, they acted synergistically to prolong the APD_{90} to values higher than those induced by SKb alone. The more pronounced effects of the combination of Iso and SKb were observed in the $\mathcal{C}$ model, with strong plateau elevation and prolongation, as seen in the middle row of Figure 6.2.

The individual effects of ACh, Iso and SKb were compared with experimental results published in the literature, both qualitatively (Figure 6.6) and quantitatively (Figure 6.2). Figure 6.6 presents a qualitative comparison between the computed APs and experimental APs from various studies. It is worth noting that these experimental results were obtained

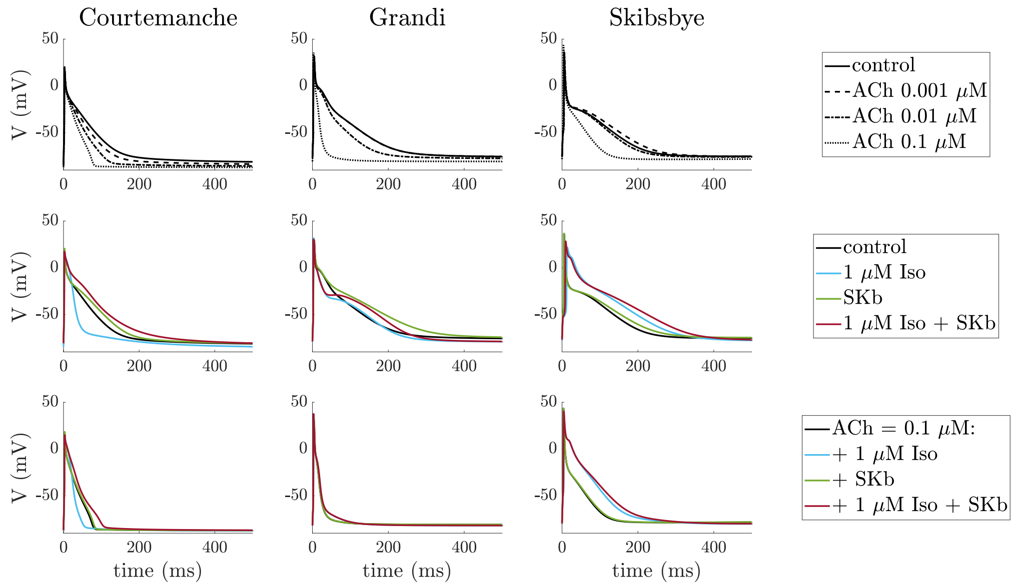

Figure 6.3: APs of human atrial cardiomyocytes models paced at a CL of 500 ms. The figure is strucured as figure 6.2.

from different animal species due to the scarcity of experimental data from humans.

Combined cholinergic, β-adrenergic and SKb effects. APs under cholinergic stimulation by 0.1 μM ACh, applied individually and in combination with β-adrenergic stimulation and/or I_{SK} block, are depicted in the bottom row of Figure 6.2 for a constant CL of 1000 ms. A summary of the results in terms of APD_{90} is shown in Figure 6.7. Results for CLs of 500 and 300 ms can be found in Figure 6.7.

SKb effectively neutralized the effects of cholinergic stimulation for ACh concentrations up to 0.001 μM in the $\mathcal{C}$ and $\mathcal{G}$ models and up to 0.01 μM in the $\mathcal{S}$ model. For the highest concentration of ACh (0.1 μM), SKb prolonged APD_{90} by 7.9% and 24.3% of the APD decrease caused by ACh in the $\mathcal{C}$ and $\mathcal{G}$ models, respectively, while its effects were negligible in the $\mathcal{S}$ model.

The effects of β-adrenergic stimulation applied on top of ACh were highly dependent on the baseline AP shape. A concentration of 1 μM Iso reduced the cholinergic-induced changes in the $\mathcal{G}$ and $\mathcal{S}$ models, but further shortened APD_{90} in the $\mathcal{C}$ model. In the $\mathcal{G}$ model, β-adrenergic effects weakened with increasing ACh concentrations, while in the $\mathcal{S}$ model, Iso effects grew proportionally with the increase in ACh concentration, recovering 71.6%

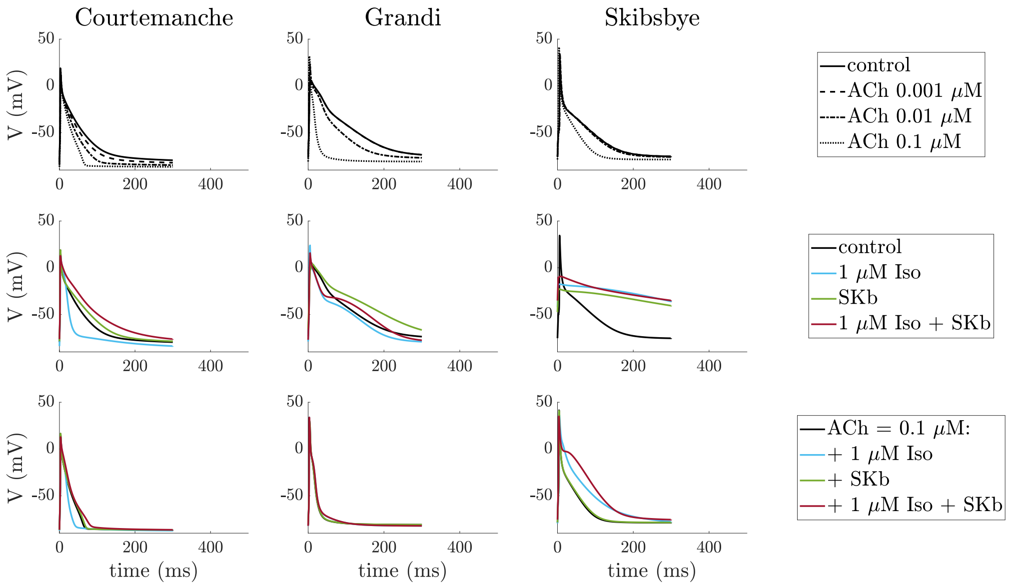

Figure 6.4: APs of human atrial cardiomyocytes models paced at a CL of 300 ms. The figure is strucured as figure 6.2. When pacing the $\mathcal{S}$ model at a CL of 300 ms, the AP was not able to fully repolarize under ACh combined with Iso and/or SKb.

of the APD$_{90}$ change for the highest tested ACh concentration.

The combination of SK block and 1 μM Iso counteracted ACh effects in all cases, with the exception of the $\mathcal{G}$ model with the highest concentration of ACh (0.1 μM), in which the combination did not enhance the effect caused by Iso alone. For the $\mathcal{C}$ and $\mathcal{S}$ models, the combined action led to the recovery of baseline APD$_{90}$, with the prolongation being 45.23% and 83.5% of the APD$_{90}$ shortening caused by 0.1 μM ACh, respectively. The above-described effects on APD$_{90}$ were accompanied by changes in AP morphology for the $\mathcal{C}$ and $\mathcal{S}$ models, as evident from the bottom row of Figure 6.2, where β-adrenergic stimulation and/or SKb applied on top of 1 μM ACh caused a significant elevation of the AP plateau.

Frequency-dependent effects. The dependence of APD$_{90}$ shortening on pacing frequency, as a result of ACh, β-adrenergic and SKb effects, was analyzed by comparing the relative changes in the AP waveform and APD$_{90}$ values at pacing CLs of 300, 500 and 1000 ms. The results for CL=1000 ms are shown in Figure 6.8, expressed as a percentage of the APD$_{90}$ change relative to the control case. The results for CLs of 500 and 300 ms can be

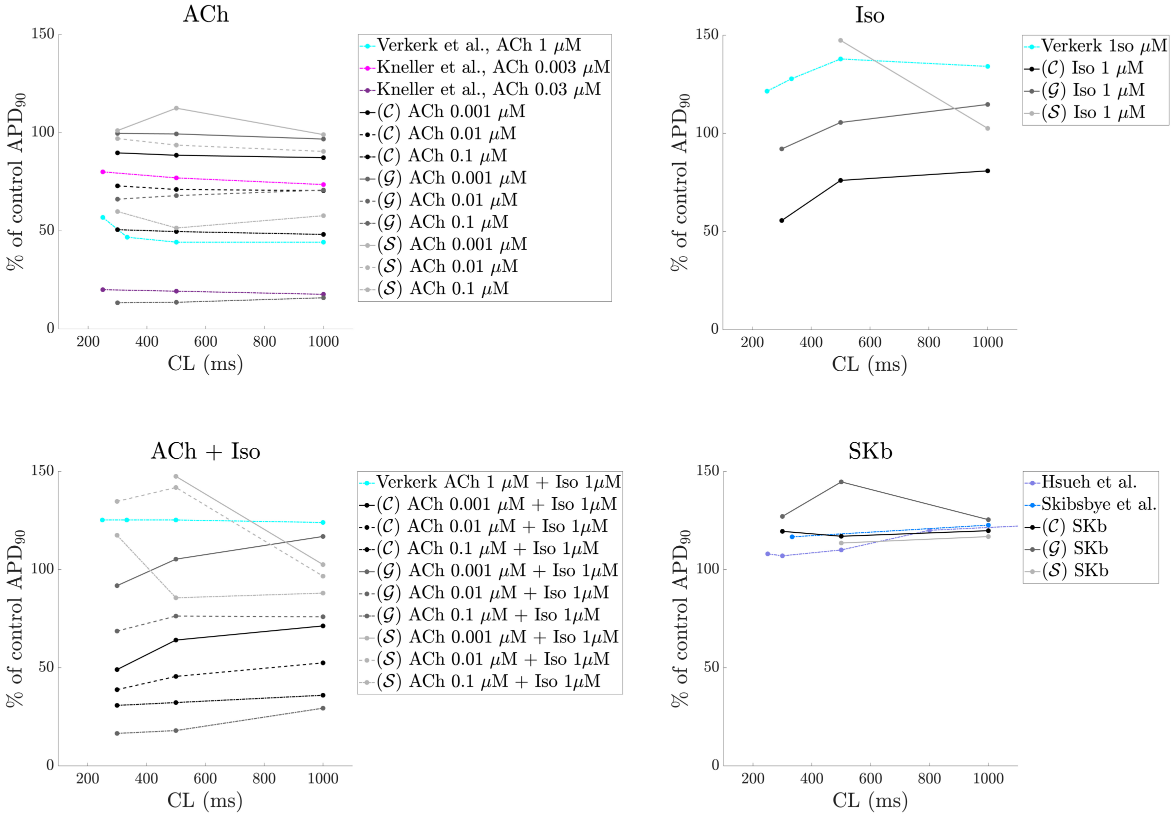

Figure 6.5: Percentages of change in APD$_{90}$ with respect to the APD$_{90}$ value in control when pacing at different CLs. Simulation results were compared with data published in the literature. Top-left panel) ACh-induced effects. The APD$_{90}$ obtained after adding different ACh concentrations in the $\mathcal{C}$, $\mathcal{G}$ and $\mathcal{S}$ models at different pacing CLs were compared with experimental results from Verkerk et al. [394]. Top-right panel) Iso-induced effects. Simulation results were compared with experimental results by Verkerk et al. [394]. Bottom-left panel) ACh + Iso-induced effects. Simulation results were compared with experimental results by Verkerk et al. Bottom-right panel) SKb-induced effects. Simulation results were compared with experimental results by Hsueh et al. [255] and by Skibsbye et al. [121]

found in Figures 6.9 and 6.10.

The relative ACh-induced APD$_{90}$ shortening was largely independent of the CL in all models, with differences up to 3%, except when ACh was applied at 0.001 μM in the $\mathcal{S}$ model, where differences between the CLs of 1000 and 500 ms were of 13.45%.

The frequency dependence of APD$_{90}$ changes induced by the application of 1 μM Iso on top of ACh was more pronounced, but it was reduced with increasing ACh concentration in the $\mathcal{C}$ and $\mathcal{G}$ models. In the $\mathcal{C}$ model, when Iso was applied on top of 0.001 μM ACh, it caused further shortening that increased, in relative terms, with reducing the CL. In the $\mathcal{G}$ model, Iso generally prolonged APD$_{90}$ that was shortened by ACh, except when CL=300 ms and ACh concentration = 0.001 μM ACh, where Iso further shortened it. In the $\mathcal{S}$ model, Iso strongly prolonged APD$_{90}$ in all cases, except when pacing at 1000 ms and using 0.001 and 0.1 μM ACh, where APD$_{90}$ was only slightly prolonged.

In the $\mathcal{S}$ and $\mathcal{C}$ models, SKb showed little frequency dependence, while in the $\mathcal{G}$ model, SKb showed mild frequency dependence that decreased with increasing ACh concentration and was stronger for lower pacing frequencies.

The combination of Iso and SKb applied on top of ACh showed weak frequency dependence in the $\mathcal{C}$ model, while in the $\mathcal{G}$ model, it presented stronger effects for lower pacing frequencies, particularly for ACh concentrations of 0.001 and 0.01 μM. In the $\mathcal{S}$ model, the combination of Iso and SKb showed strong frequency-dependent effects that decreased with increasing ACh concentration.

Finally, the effects of Iso and SKb on RMP were analyzed and presented in Figure 6.11.

In the $\mathcal{G}$ model, Iso led to a more hyperpolarized RMP, with greater effects observed at shorter cycle lengths, reaching a maximum extra hyperpolarization of 5 mV in control when pacing at a CL of 300 ms. The combination of Iso and SKb produced similar results to those seen with Iso alone, while SKb caused a less negative RMP only for ACh concentrations less than 0.001 μM. The same was true for the $\mathcal{S}$ model, but with weaker effects compared to the $\mathcal{G}$ model. In the $\mathcal{C}$ model, the effects of Iso and SKb on RMP were comparable to those in the $\mathcal{S}$ model, while the combination of Iso and SKb led to a less negative RMP, with the maximum effect observed for a CL of 300 ms.

Effects in electrically remodeled cells. The electrical remodeling caused by psAF resulted in shorter APs compared to non-remodeled myocytes, with APD$_{90}$ being 42.04%, 25.06% and 26.70% shorter in the $\mathcal{C}$, $\mathcal{G}$ and $\mathcal{S}$ models, respectively. The application of ACh further shortened APD$_{90}$ in psAF myocytes by a similar magnitude to that seen in non-remodeled myocytes, as shown in Figure 6.12.

SKb had no significant effect on APD$_{90}$ in cholinergically-stimulated myocytes under all tested ACh concentrations and across the three psAF models. This can be attributed to the lower conductance of I_{SK} in psAF cells.

β-adrenergic stimulation by Iso, applied in addition to ACh, prolonged APD_{90} in the $\mathcal{C}$ and $\mathcal{S}$ models of psAF cells to a greater extent than in non-remodeled myocytes. However, in the $\mathcal{G}$ model of psAF cells, Iso had no significant effect under all tested ACh concentrations, similar to the results observed in non-remodeled cells.

The combination of Iso and SKb increased the individual effects and resulted in a greater prolongation of APD_{90} in cholinergically-stimulated psAF cells, similar to what was observed in non-remodeled cells. This prolongation brought APD_{90} values near or above baseline for the $\mathcal{C}$ and $\mathcal{S}$ models of psAF cells. However, in the $\mathcal{G}$ model, the APD_{90} prolongation only partially recovered the shortening induced by ACh concentrations of 0.01 and 0.1 μM.

Variations in the RMP in remodeled myocytes were similar to those in non-remodeled myocytes (not displayed).

6.3.2 Human atrial tissues

Counteraction of ACh-induced changes in activation and repolarization. In non-remodeled tissue, electrical propagation was modestly slowed by 0.1 μM of ACh, resulting in a total activation time increase of 4.5 ms for homogeneous ACh distribution and 2 ms for heterogeneous ACh distribution. The longitudinal CV dropped from 94.56 cm/s at baseline to 86.5 cm/s under homogeneous ACh, which aligns with previous experimental findings [258]. The application of Iso, SKb or a combination of both restored the total activation time to baseline values in both homogeneous and heterogeneous ACh distribution scenarios.

The results of the study indicate that all interventions had a significant impact on APD_{90} in atrial tissues. The homogeneous addition of ACh resulted in a decrease of mean APD_{90} to 87.87 ms and 136.34 ms for 0.1 μM and 0.01 μM ACh respectively, compared to 206.42 ms at baseline. The addition of SKb on top of ACh lengthened mean APD_{90} by 6.13 ms for 0.1 μM ACh and 16.09 ms for 0.01 μM ACh. Conversely, 1 μM Iso had a shortening effect on mean APD_{90} by 23.28 ms and 32.87 ms, respectively. The combination of Iso and

SKb counterbalanced the effects of ACh, leading to mean APD_{90} values of 128.96 ms and 206.66 ms for 0.1 μM and 0.01 μM ACh, respectively.

For heterogeneous ACh distribution, Figure 6.13 shows that the heterogeneous addition of ACh resulted in a decrease in mean APD_{90} by 50.19 ms for 0.1 μM ACh and by 22.59 ms for 0.01 μM ACh. The addition of SKb caused an increase in mean APD_{90} by 22.3 ms and 29.96 ms, respectively. Conversely, 1 μM Iso reduced mean APD_{90} by 31.54 ms and 32.59 ms. The combination of SKb and Iso restored mean APD_{90} to values even greater than at baseline, with values of 224.52 ms and 263.35 ms for 0.1 μM and 0.01 μM ACh, respectively.

Termination of ACh-initiated rotors and prevention of re-induction. β-adrenergic stimulation with 1 μM Iso was able to terminate rotors in cholinergically-stimulated tissues, whether applied alone or in combination with SKb. This was true for all tested application kinetics (Δt_a=0.1, 1, 5 and 8 s, as shown in Figure 6.1) and ACh concentrations (0.01 and 0.1 μM). There was only one exception, which occurred when Iso was applied individually with the highest ACh concentration and slowest application kinetics. SKb alone only terminated the rotor under the lowest ACh concentration and with a Δt_a of 8 s. These results are summarized in Figure 6.14.

When the application kinetics of Iso and/or SKb was set to Δt_a = 0.1 s, Iso alone and in combination with SKb terminated the rotors in 0.2 s for both ACh concentrations. SKb alone did not terminate the rotor for either ACh concentration. The voltage maps over time for ACh = 0.01 μM are shown in Figure 6.15.

The same results were obtained for Δt_a equal to 1, 5 and 8 s, with longer times required to stop the rotors as Δt_a increased.

Two mechanisms were identified to explain rotor termination. After application of Iso or Iso combined with SKb, the rotor extinguished due to collision of the rotor tip with the rotor tail, which was likely facilitated by the increased amount of depolarized tissue resulting from prolongation of APD_{90}. In cases where SKb was applied individually, the rotor tip became less stable and started to span larger areas of tissue. In the one case where SKb led to rotor termination, the rotor drifted through the tissue border until it eventually extinguished at the tissue boundaries. To further study these mechanisms, a phase singularity (PS) analysis was performed for Δt_a=8 s and Δt_a=5 s using the method described in [397]. Figure 6.16 shows two cases: (a) ACh = 0.1 µM and Δt_a=8 s, where only Iso combined with SKb was able to stop the rotor, and (b) ACh = 0.01 µM and Δt_a=8 s, where the rotor was also stopped by Iso. In all cases, the rotor tip followed a five-pointed star-like trajectory with three long sides and two short sides. The time evolution of this trajectory over 350 ms intervals is shown in Figure 6.17. In the first milliseconds after administration of Iso and/or SKb, the rotor tip followed the same trajectory in all studied cases. However, in the Iso and Iso + SKb cases, it soon began to wander and deviate from control. In the SKb cases, deviation from control became apparent later, usually after 8 and 5.5 s from application under 0.1 and 0.01 µM ACh, respectively.

The results of the PS analysis are presented in Figures 6.18 to 6.25.

This analysis evaluates the movement of rotor tips in terms of the surface covered (A), distance covered (L), and mean velocity ($\overline{\mathrm{V}}$), which is defined as the average of the velocities between subsequent PS points. The analysis was conducted over a 10-second period, starting from 2 seconds after drug application and ending at 12 seconds. Under control conditions, a lower concentration of 0.01 μM ACh resulted in a larger surface area covered (3.56 cm^2) compared to a higher concentration of 0.1 μM ACh (1.70 cm^2). Adding SKb resulted in an increase in the surface area covered, which was negligible under 0.1 μM ACh, but significant under 0.01 μM ACh. In the latter case, when Δt_a=5 s, the surface area increased from 3.56 cm^2 to 4.83 cm^2. When Δt_a=8 s, the surface area increased to 4.95 cm^2. The analysis for the Iso and Iso + SKb cases was more challenging due to early rotor instability. To compare the different therapies, rotor characteristics were analyzed at the same time instant, which was the one preceding instability in the case where it occurred earlier. All cases showed a noticeable increase in the surface area spanned by the rotor tip, with increased rotor meandering potentially due to a larger effective refractory period. The biggest increase in percentage terms was observed for ACh=0.1 μM and Δt_a=5 s, where, after 0.85 s from Iso + SKb application, the surface area increased by 109%.

SKb increased the mean velocity under 0.01 μM ACh by 0.79 cm/s and 0.73 cm/s when Δt_a=5 and 8 s, respectively. Under 0.1 μM ACh, SKb increased the mean velocity by 0.79

cm/s and 0.94 cm/s. Iso and Iso in combination with SKb showed a stronger increase in mean velocity, especially under 0.1 μM ACh. Iso alone increased the mean velocity by 4.39 cm/s and 1.12 cm/s when Δt_a=5 and 8 s, respectively. When combined with SKb, the mean velocity increased by 3.15 cm/s and 3.52 cm/s.

The re-inducibility of rotors was also tested and the results are summarized in Table 6.1 for rotors initiated under ACh=0.01 μM and ACh=0.1 μM, with Iso or SKb application kinetics defined by Δt_a=5 s. For Iso and Iso combined with SKb, a narrow range of S1-S2 intervals led to rotor re-initiation, with rotors lasting from 260 ms to 840 ms.

Table 6.1: Summary of rotor re-inducibility tests, with Δt_a=5 s. **I-E**: rotor re-initiated but extinguishing.

ACh=0.01 μM			ACh=0.1 μM		
S1 (ms)	**S1-S2** (ms)	Inducibility	**S1 (ms)**	**S1-S2** (ms)	Inducibility
Iso			Iso		
100	190	**I-E**	100	150	**I-E**
500	190	**I-E**	500	160	**I-E**
1000	180	**I-E**	1000	150	**I-E**
SKb			SKb		
Rotor never stopped. No reinduction			Rotor never stopped. No reinduction		
Iso+SKb			Iso+SKb		
100	200	**I-E**	100	160	**I-E**
500	215	**I-E**	500	200	**I-E**
1000	215	**I-E**	1000	210	**I-E**

6.4 Discussion

The impact of inhibiting SK channels and of β-adrenergic stimulation on human atrial myocytes and tissues that have been stimulated by ACh was investigated. To do this, we used existing computational models of atrial cells and added the I_{SK} current and information about the cholinergic and adrenergic modulation of atrial electrical activity, if it was missing.

We found that SKb, especially in combination with Iso, was able to prolong the APD after ACh had shortened it at both cellular and tissue levels. Iso was also able to reverse arrhythmogenic behaviors induced by ACh, both alone and when combined with SKb. The results presented in this study were calculated using a transverse-to-longitudinal ratio value of 0.5. Different conclusions could be drawn for different anisotropy ratios, as the characteristics of the rotor tip trajectory (area covered, distance traveled, and mean velocity) vary with the ratio. This is demonstrated in Figure 6.26.

We first evaluated the effectiveness of SKb and/or Iso in countering the effects of cholinergic stimulation in single cells. SKb partially countered these effects, with the best results observed for low to moderate cholinergic stimulation corresponding to physiological ACh concentrations up to 0.01 μM. The effects of individual Iso application on the AP were highly dependent on the baseline AP shape, which aligns with previous research findings [398]. The literature contains conflicting results about the effects of Iso on APD. Some studies have reported that Iso leads to shortening of APD [388, 393], while others have reported that Iso leads to prolongation of APD [259, 394, 395]. The literature also contains conflicting results regarding the combination of Iso and ACh, with some studies showing that β-adrenergic stimulation can facilitate AF induction [362] while others have described β-adrenergic stimulation as a brake to reduce the extent of cholinergic-induced APD shortening [388]. These conflicting results could potentially be explained by patient characteristics, with age being identified as a differential factor in animal studies [388].

In our study, Iso-induced APD shortening, which was observed for the $\mathcal{C}$ model, could be attributed to an increase in intracellular calcium concentration due to enhanced release of calcium from the sarcoplasmic reticulum. This increased intracellular calcium concentration would activate calcium-activated potassium channels, contributing to APD shortening. Thus, blocking SK channels in addition to Iso was expected to reduce this effect and counteract APD shortening. Indeed, we found that the combination of SK block and Iso was able to reverse ACh effects, prolonging APD to near baseline levels. These results were generally consistent across the three tested models, although the magnitude of Iso and SKb effects was less pronounced for the $\mathcal{G}$ model compared to the $\mathcal{C}$ and $\mathcal{S}$ models.

Next, we tested for frequency-dependent behavior in Iso and SKb, and compared our observations between psAF-remodeled and non-remodeled myocytes. The relative changes in the AP induced by Iso and SKb applied on top of ACh showed minimal frequency dependence, especially for ACh concentrations of 0.01 and 0.1 μM. When comparing the results between psAF-remodeled and non-remodeled cells, we found that the observations were qualitatively similar, with only minor differences in the magnitude of relative changes induced by ACh, Iso and SKb. These changes were of lower amplitude in psAF-remodeled cells than in non-remodeled cells. It is worth mentioning that the effects of SKb were practically negligible in psAF-remodeled cells, which could be due to the lower conductance of SK channels in psAF electrical remodeling.

We then studied the actions of SKb and Iso in tissues with homogeneous and heterogeneous ACh distributions. Our results, in agreement with results at cellular level using the $\mathcal{C}$ model, showed that individual Iso application further shortened the APD, but the combination of Iso and SKb was able to bring APD back to its baseline value for both homogeneous and heterogeneous ACh distributions and all tested ACh concentrations. For the modeled heterogeneous ACh distribution, spatial APD dispersion was high, but administering Iso combined with SKb remarkably reduced it. We tested the efficacy of various therapies to stop stable rotors in cholinergically-stimulated tissues. The results showed that both Iso and the combination of Iso and SKb were effective in stopping rotors for all tested ACh concentrations and application kinetics, with only one exception for individual Iso. However, individual SKb was only able to stop the rotor in one case, causing it to drift towards the tissue border. The mechanism of rotor termination involved collision between the rotor tail and tip in the cases of individual Iso and combined Iso with SKb. Figure 6.27 displays APs recorded in the simulated tissue at a specific point between seconds 2 and 3 for four tested Iso and/or SKb application kinetics. Iso, whether applied individually or in combination with SKb, quickly led to strong prolongation of APD and elevation of AP plateau within the first three seconds of simulation for all tested application kinetics. On the other hand, SK block had slower effects. The transient Iso-induced APD prolongation observed during the first moments after its application is in contrast to the steady-state APD shortening. This transient APD prolongation upon Iso administration is consistent with previous experimental findings [399, 400] and has been attributed to differences in the phosphorylation kinetics of I_{Ks} and I_{CaL}, which are two cellular substrates that are altered by sudden, abrupt β-adrenergic stimulation. Both experimental and computational studies have shown that I_{CaL} responds to Iso very quickly, which explains the immediate APD prolongation after Iso administration, while I_{Ks} has a slower response that eventually counteracts the changes in I_{CaL} and leads to APD shortening [399–401]. This kinetic mismatch between I_{CaL} and I_{Ks} has also been observed in response to a gradual increase in Iso concentration [401, 402]. Our simulations showed similar observations regarding Iso effects, with even more prominent AP plateau elevation and APD prolongation at the time corresponding to maximum concentration for faster application kinetics (Figure 6.27).

The efficacy of Iso and Iso combined with SKb in stopping stable rotors under cholinergic stimulation was further evaluated by examining their ability to prevent re-induction of rotors. Our findings revealed that after the rotor was terminated by Iso alone or in combination with SKb, it could not be re-initiated within the next minute. When re-induced later, the rotor persisted for a maximum of 840 ms.

Based on these results, we can conclude that the combination of Iso and SKb may serve as an effective therapy to mitigate the harmful effects of ACh in the human atria. This conclusion is supported by the ability of combined Iso and SKb to prolong APD at steady state and to aid in cardioversion and maintenance of the restored sinus rhythm.

6.5 Study limitations

Our investigation aimed to evaluate the effectiveness of Iso and SKb in counteracting the cholinergic effects on human atrial cells and tissues. The simulations were performed at the cellular level and on 2D tissue sheets, but did not include the regional electrophysiological heterogeneities and cell-to-cell variability that exist in real human atria. This study highlights the importance of biological variability in drug evaluation and future research could include populations of cell models to account for this variability [403]. Another avenue for future investigation would be to use 3D whole-atrial models to better understand complex rotor behavior and rotor termination mechanisms.

The results of this study emphasize the non-steady-state kinetics of Iso as a factor in its impact on rotor termination. Further research using biophysically-detailed β-adrenergic signaling models could examine the effects of different Iso concentrations and help to understand its potential as an anti-arrhythmic therapy, particularly when combined with SK channel inhibition delivered with possibly different administration kinetics as those for Iso.

It is important to note that cellular models have limitations due to the scarce experimental human data and the large variability displayed by human atrial cells and tissues. Additionally, the Courtemanche model has a limitation in its simplified modeling of sarcoplasmic reticulum Ca^{2+} handling due to limited data on Ca^{2+} storage and release kinetics from the sarcoplasmic reticulum at the time the model was developed.

6.6 Conclusions

First, the impact of Iso and SKb on human atrial cardiomyocytes was evaluated. The ability of individual SKb to restore the APD shortening induced by ACh was observed, with the change ranging from 5% to 170% depending on the ACh concentration. The effects of SKb were, however, reduced in electrically remodeled cells. Additionally, when SKb was used to stop sustained rotors initiated under cholinergic stimulation, its effects were insufficient. On the other hand, Iso was successful in terminating rotors, but its impact on APD varied depending on the baseline AP morphology. The combination of Iso and SKb resulted in stronger APD prolongation at steady state, which effectively countered the shortening induced by ACh, restoring from 67% to 250% of the APD shortening. The combination of Iso and SKb was also successful in stopping stable rotors and preventing their reinducibility. Previous studies have explored the interactions between parasympathetic and sympathetic actions, as well as between parasympathetic activity and SKb, but this study is the first to consider the complex interactions between ACh, Iso and SKb. The results support the possibility of using a combination of SK channel block and β-adrenergic stimulation as a therapy to counteract the potential arrhythmogenic effects of cholinergic stimulation in human atria.

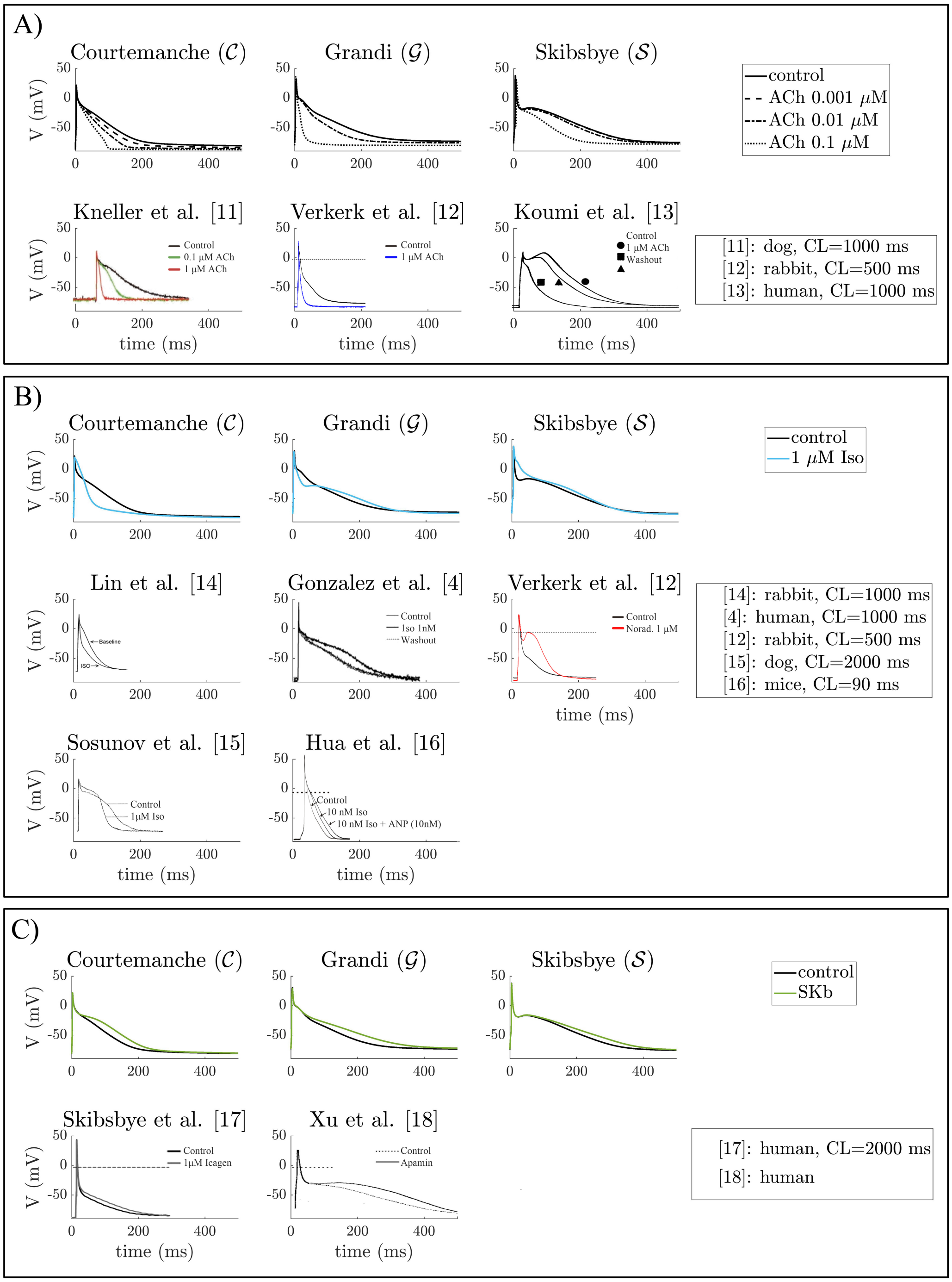

Figure 6.6: Comparison of AP traces simulated in this study with experimental AP traces published in the literature. Panel A) ACh-induced effects. The APs obtained after adding different ACh concentrations to the $\mathcal{C}$, $\mathcal{G}$ and $\mathcal{S}$ models were compared with experimental results from Koumi et al. [264], Kneller et al. [196] and Verkerk et al. [394]. Panel B) Iso-induced effects. The APs obtained adding 1 μM Iso to the $\mathcal{C}$, $\mathcal{G}$ and $\mathcal{S}$ models were compared with experimental results from González et al. [259], Hua et al. [395] and Verkerk et al. [394], reporting APD_{90} prolongation, and from Sosunov et al. [388] and Lin et al. [393], reporting APD_{90} shortening. Panel C) SK block induced effects. The APs obtained after complete SK block in the $\mathcal{C}$, $\mathcal{G}$ and $\mathcal{S}$ models are compared with experimental results from Skibsbye et al. [121] and Xu et al. [396]

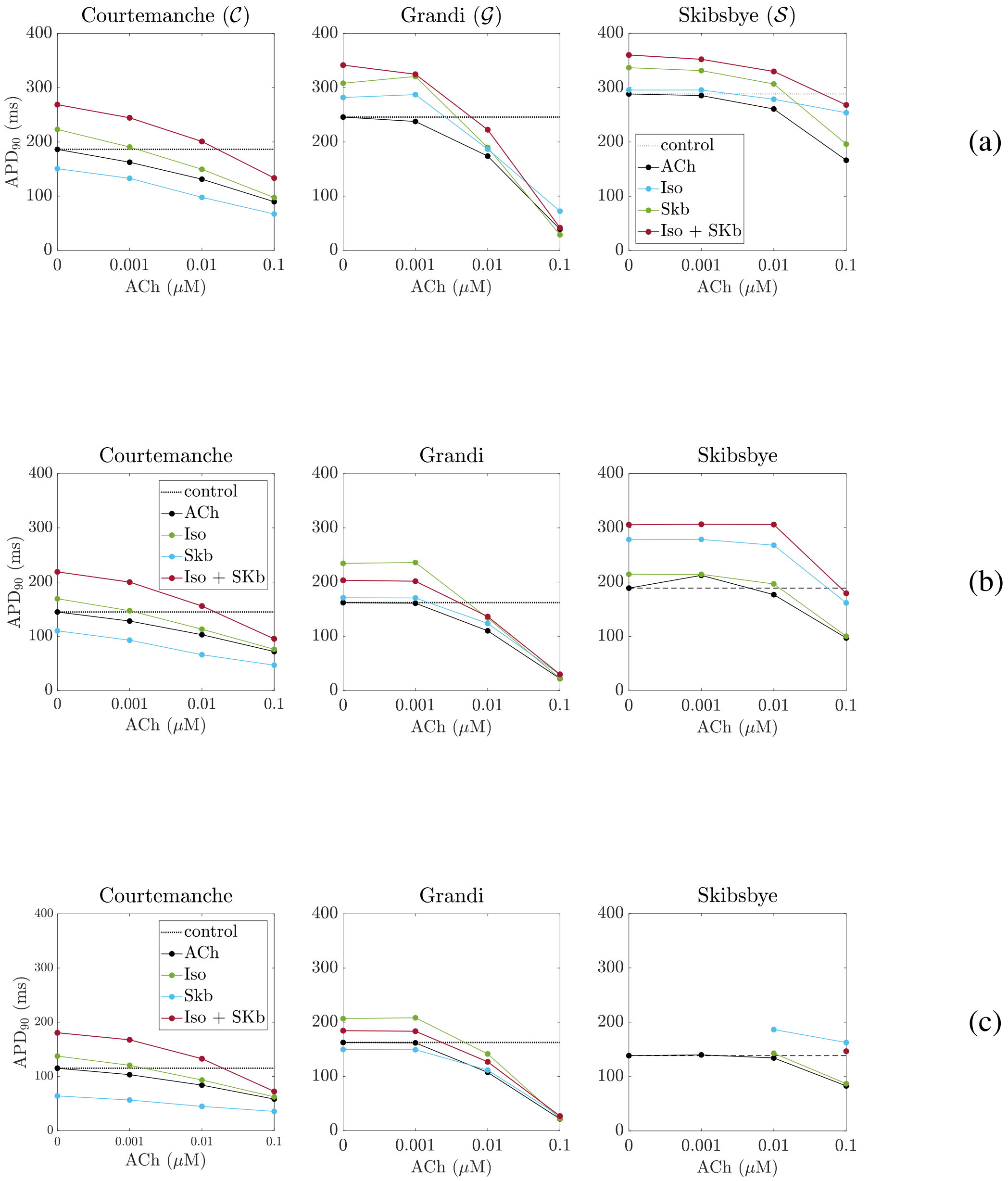

Figure 6.7: APD$_{90}$ vs ACh concentration for human atrial myocytes models paced a CL of 1000 ms (a), 500 ms (b) and 300 ms (c) at four different tested scenarios comprising cholinergic stimulation individually and in combination with β-adrenergic stimulation and/or SKb.

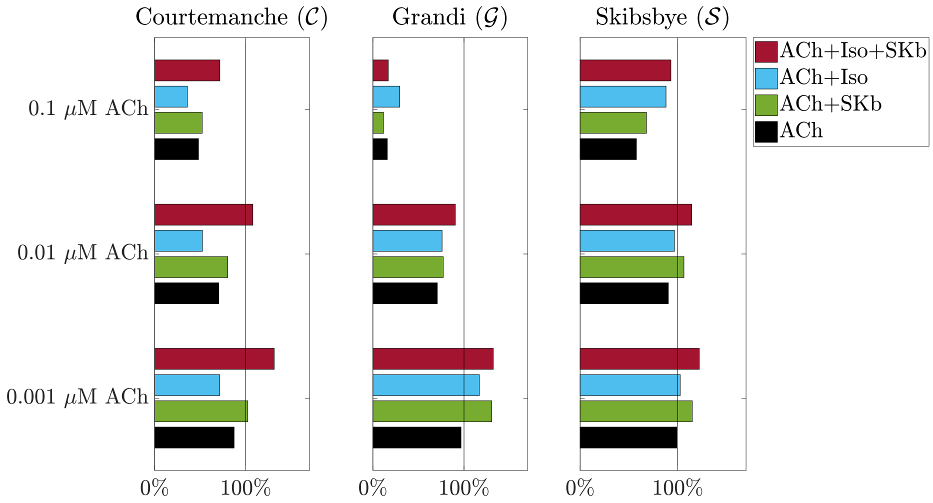

Figure 6.8: Percentage of APD_{90} prolongation calculated with respect to the control case (100%) for the different simulated scenarios when pacing at 1000 ms.

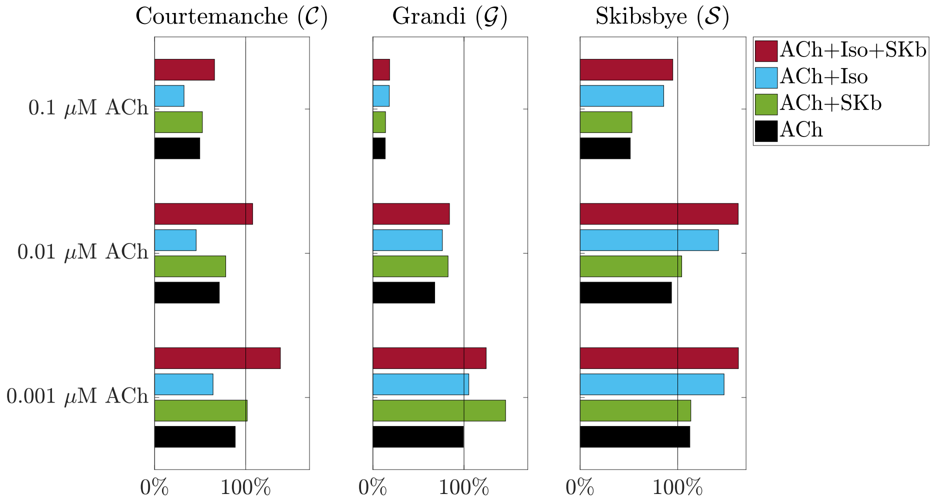

Figure 6.9: Percentage of APD_{90} prolongation calculated with respect to the control case (100%) for the different simulated scenarios when pacing at 500 ms.

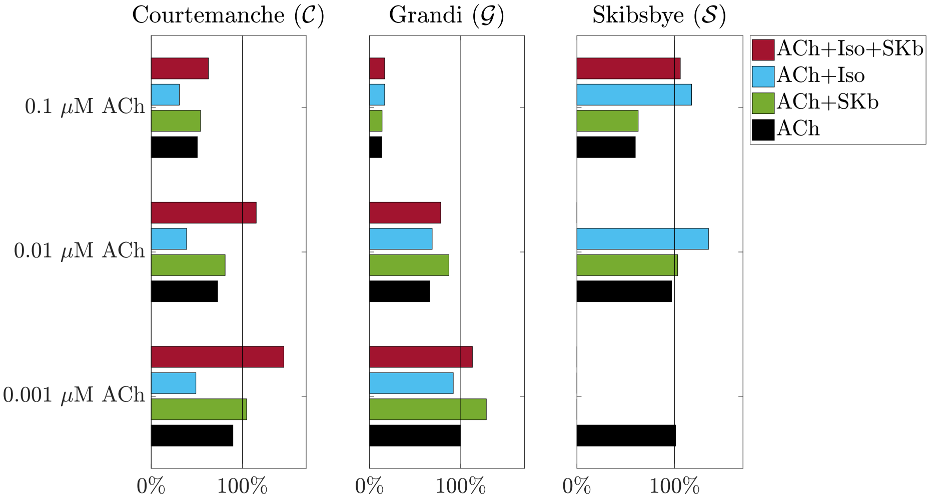

Figure 6.10: Percentage of APD_{90} prolongation calculated with respect to the control case (100%) for the different simulated scenarios when pacing at 300 ms. The AP was not able to fully repolarize under ACh combined with Iso and/or SKb and the corresponding bars are not represented in the figure.

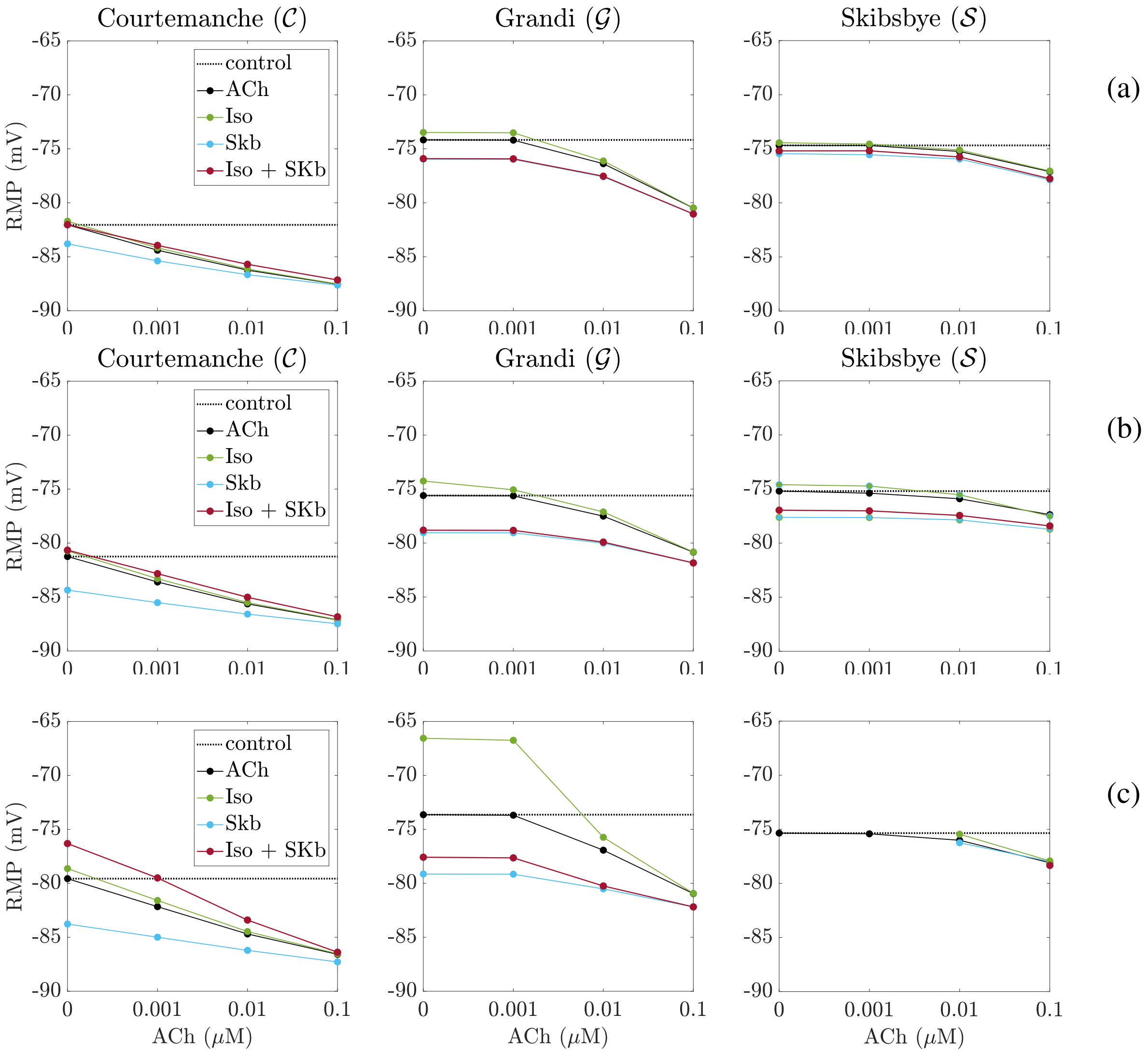

Figure 6.11: RMP vs ACh concentration for human atrial cardiomyocytes models paced at a CL of 1000 ms (a), 500 ms (b) and 300 ms (c), at four different tested scenarios comprising cholinergic stimulation individually and in combination with β-adrenergic stimulation and/or SKb.

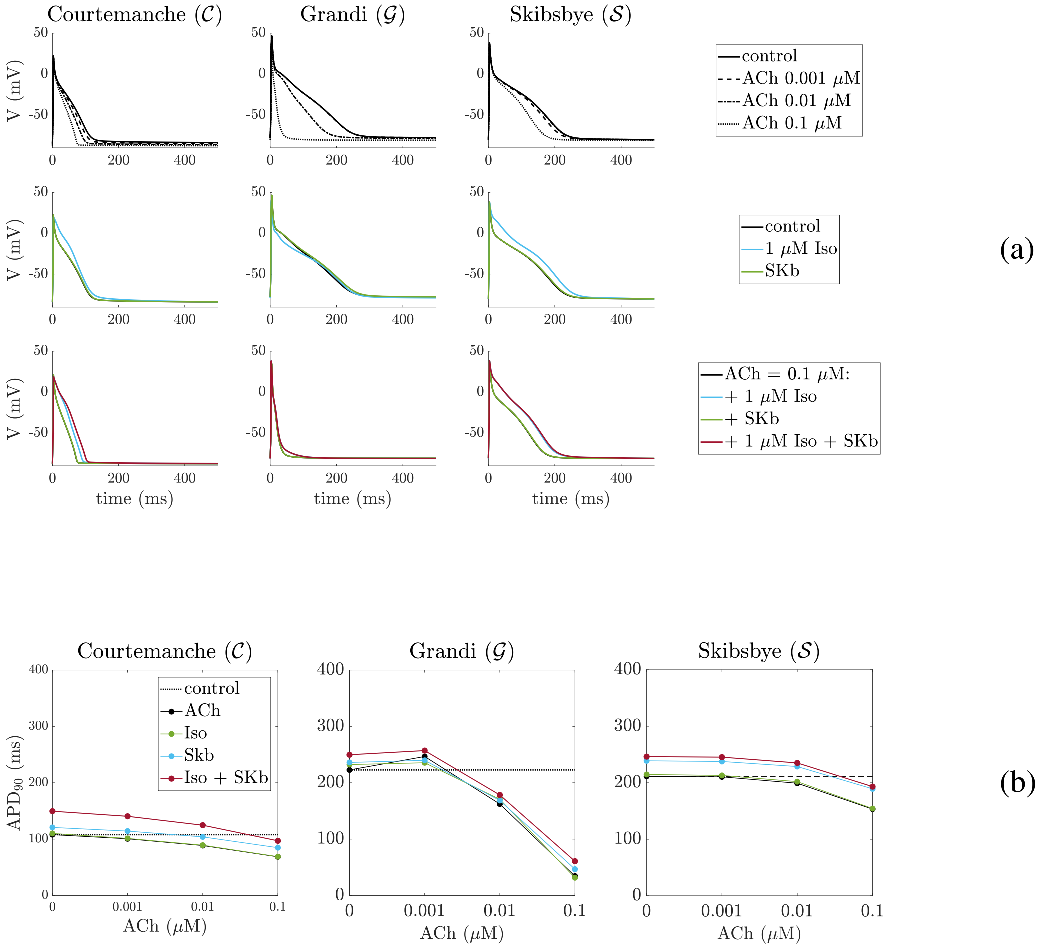

Figure 6.12: APs of psAF electrically remodeled human atrial cardiomyocytes paced at a CL of 1000 ms. First row: simulated effects of ACh (concentrations of 0.001, 0.01 and 0.1 μM). Second row: Iso (1 μM concentration) and SKb. Third row: Iso (1 μM concentration) and SKb on top of 0.1 μM ACh (a); APD$_{90}$ vs ACh concentration for psAF electrically remodeled human atrial myocytes paced at a CL of 1000 ms at four different tested scenarios comprising cholinergic stimulation individually and in combination with β-adrenergic stimulation and/or SKb (b).

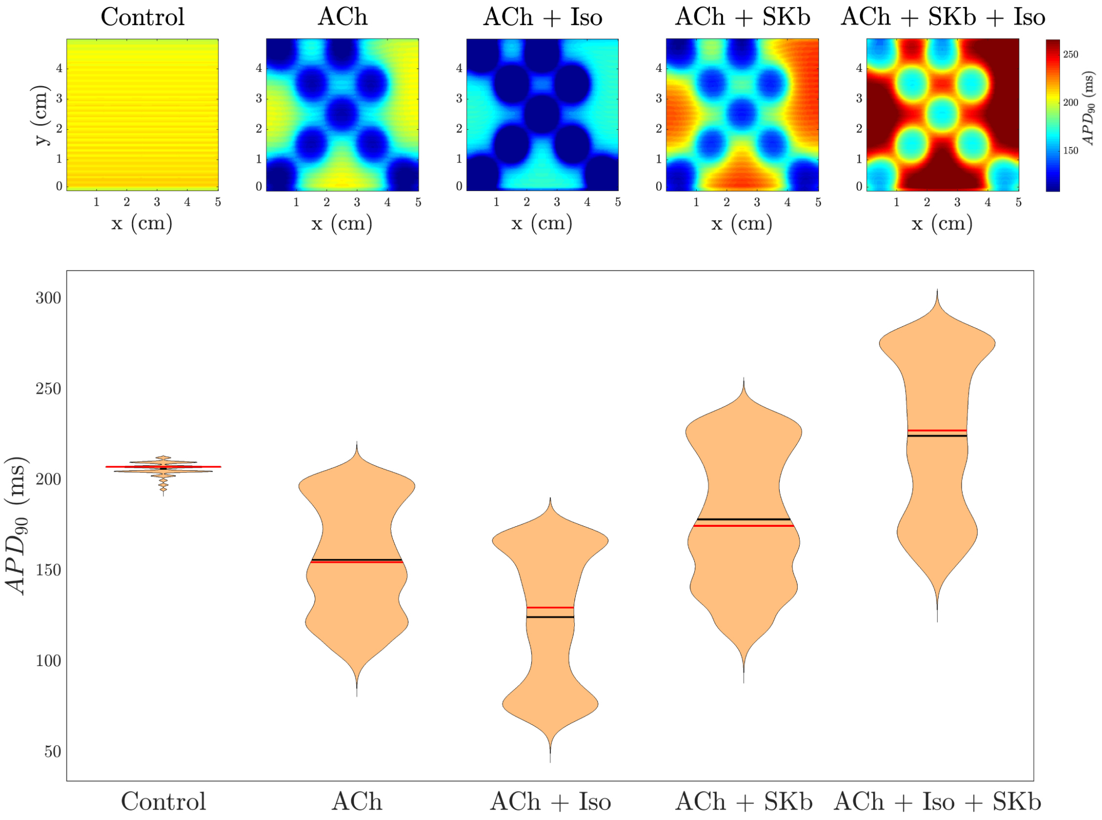

Figure 6.13: APD$_{90}$ maps (a) and violin plots (b) at baseline and under 0.1 μM ACh, individually and in combination with 1 μM Iso and/or SKb, for APs defined by the $\mathcal{C}$ model. The APD maps were built from the APD$_{90}$ values computed for the fourth beat at a CL of 1000 ms with the stimulus applied to the bottom edge of the tissue. The violin plots represent the APD$_{90}$ distribution all over the tissue for the different simulated cases. In the violin plots, black lines represent the mean APD$_{90}$ and red lines represent the median APD$_{90}$.

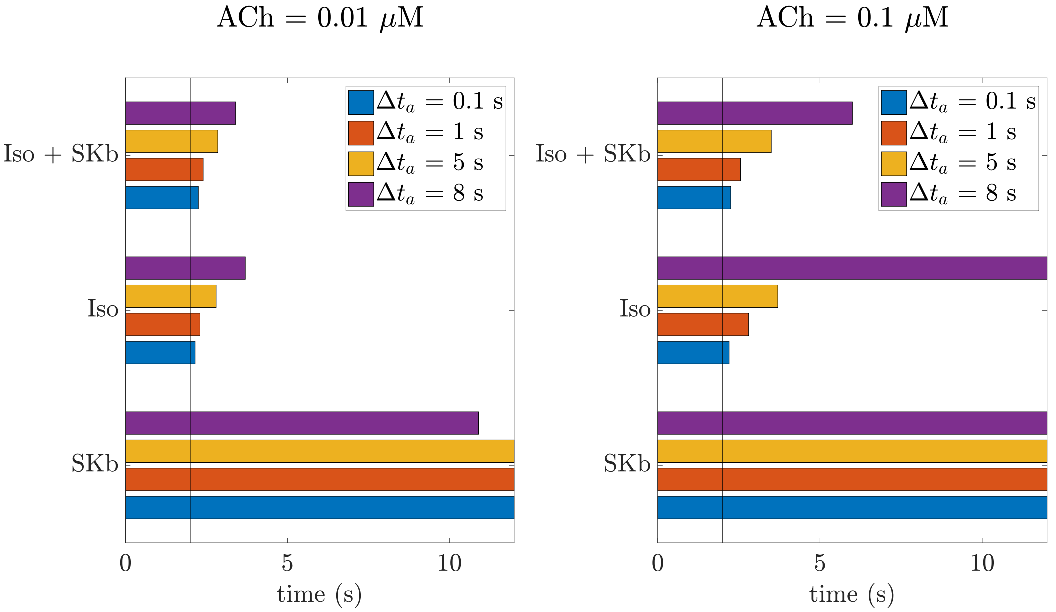

Figure 6.14: Time for rotor termination in the different simulated cases. The vertical black line represents the start time of Iso and SKb application. When Iso and SKb act concurrently, the timing is the same for both. Bars arriving to the end of the time scale denote no rotor termination.

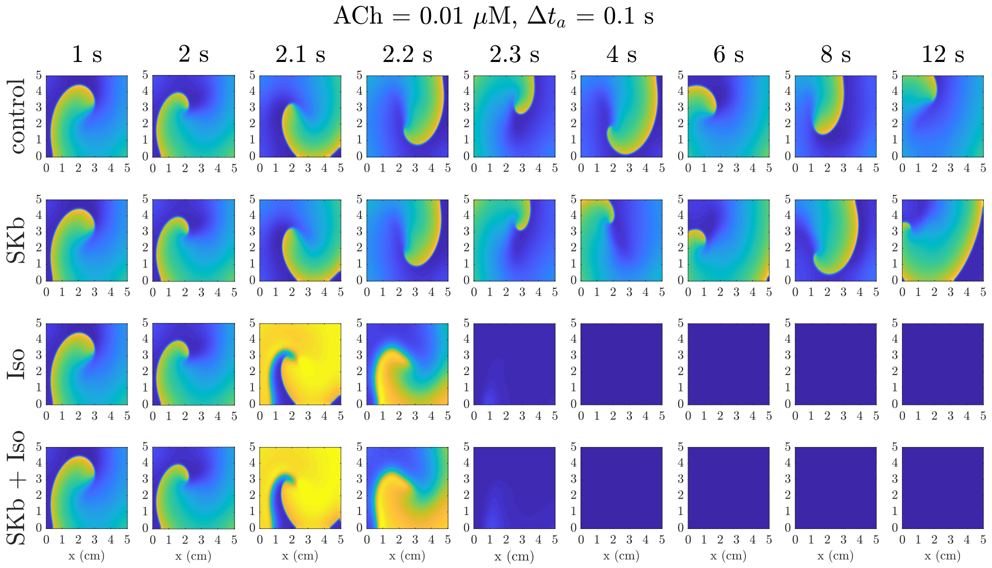

Figure 6.15: Voltage maps along time showing rotors in 2D human atrial tissues under 0.01 μM ACh. First row: control, second row: + SKb, third row: + 1 μM Iso, fourth row: + SKb + 1 μM Iso. Iso and/or SKb were applied progressively with Δt_a=0.1 s starting at time = 2 s.

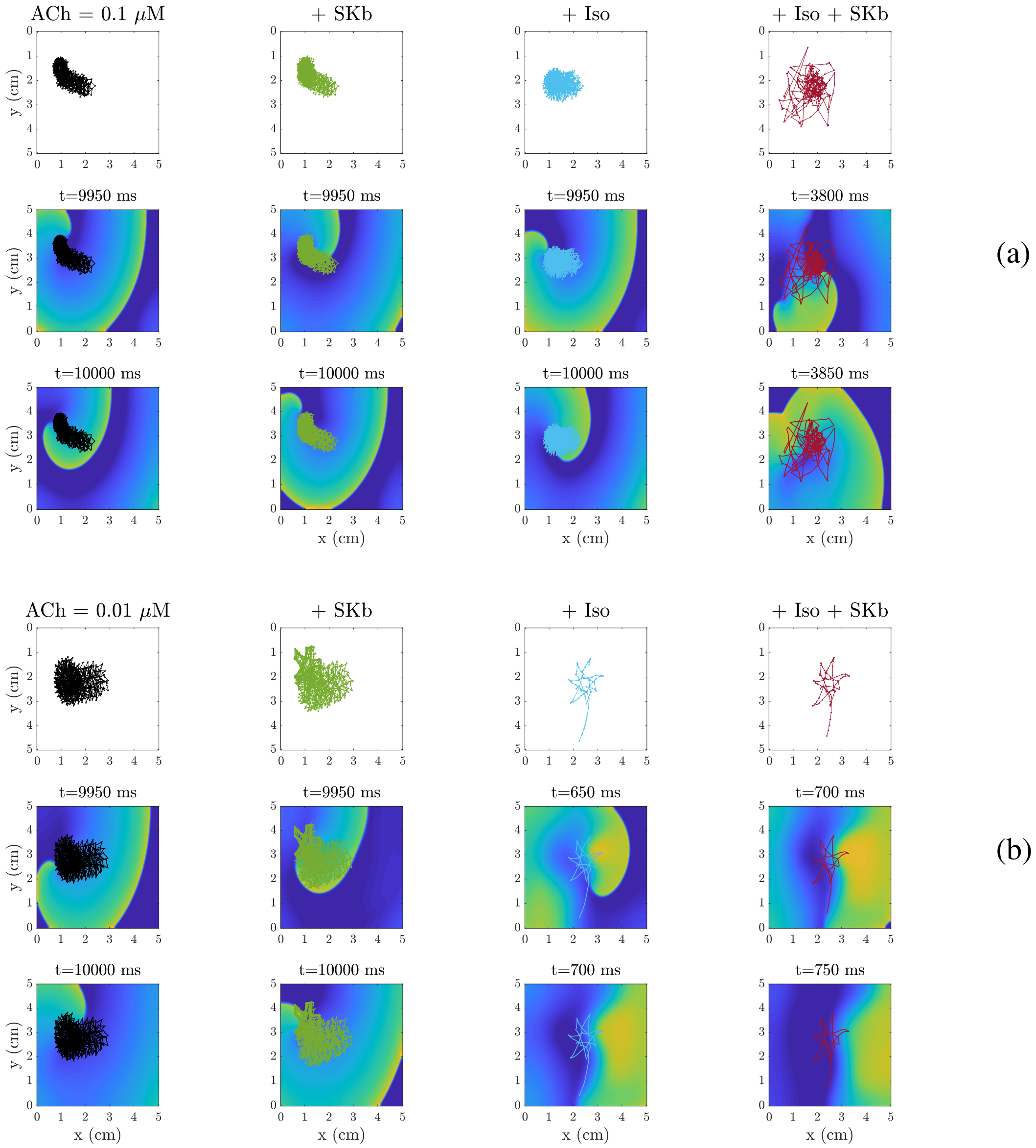

Figure 6.16: Phase singularity analysis for 0.1 μM ACh and Δt_a=8 s (a) and 0.01 μM ACh and Δt_a=8 s (b). First row: phase singularities in the different tested cases, traced starting from t=2000 ms. Second and third rows: voltage maps of the rotor at 50 ms before rotor termination or at the end of the simulation if the rotor was not stopped (t=10000 ms). The color code is the same as in previous figures, with black, green, blue and red representing the effects of ACh, ACh + SKb, ACh + Iso and ACh + Iso + SKb, respectively.

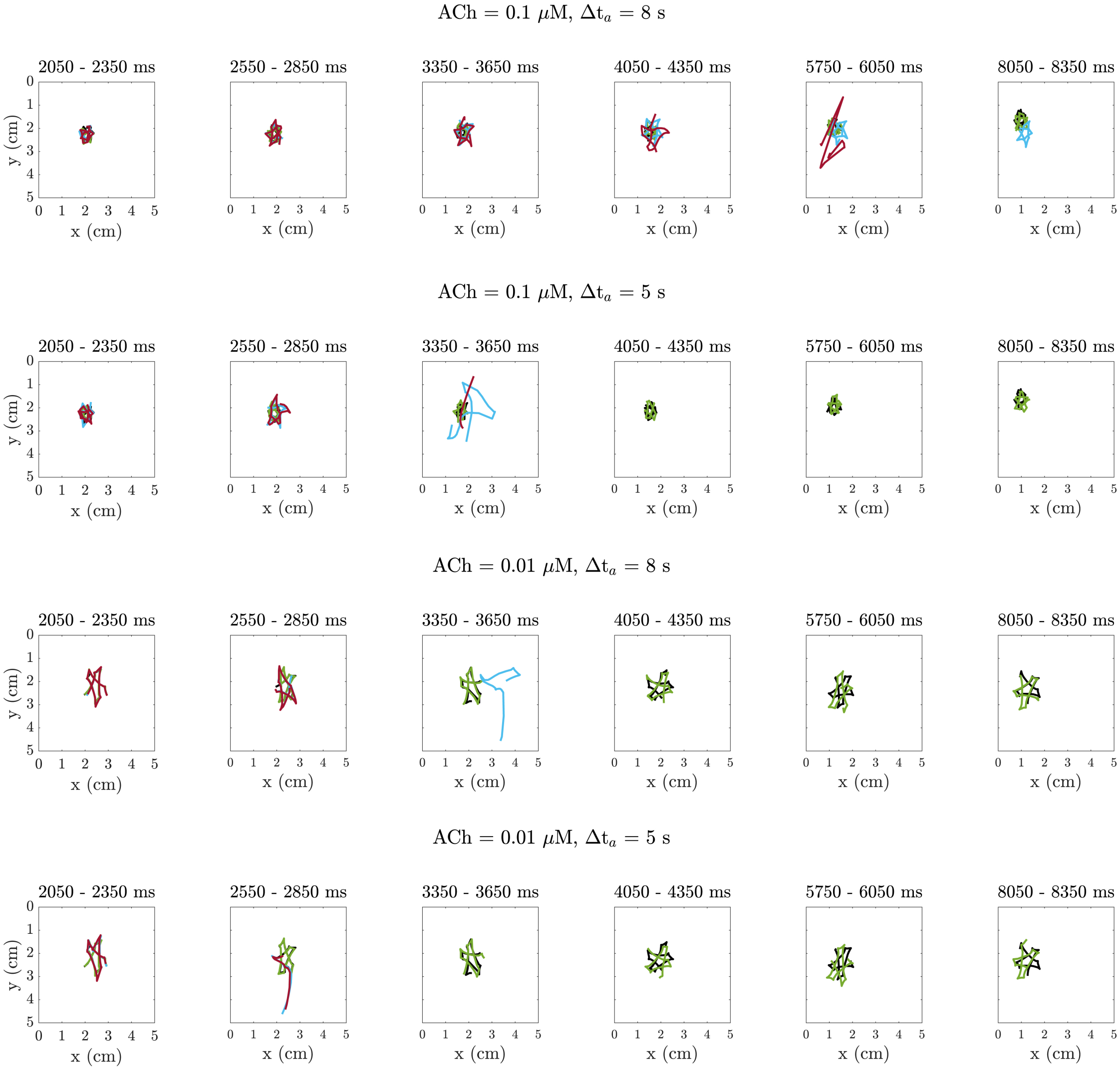

Figure 6.17: PS trajectories over time intervals covering 350 ms each, under 0.1 and 0.01 μM ACh applied with kinetics defined by Δt_a of 5 and 8 s. The color code is the same as in the previous figures, with black, green, light blue and red representing individual ACh effect, ACh + SKb, ACh + Iso and ACh + Iso + SKb, respectively.

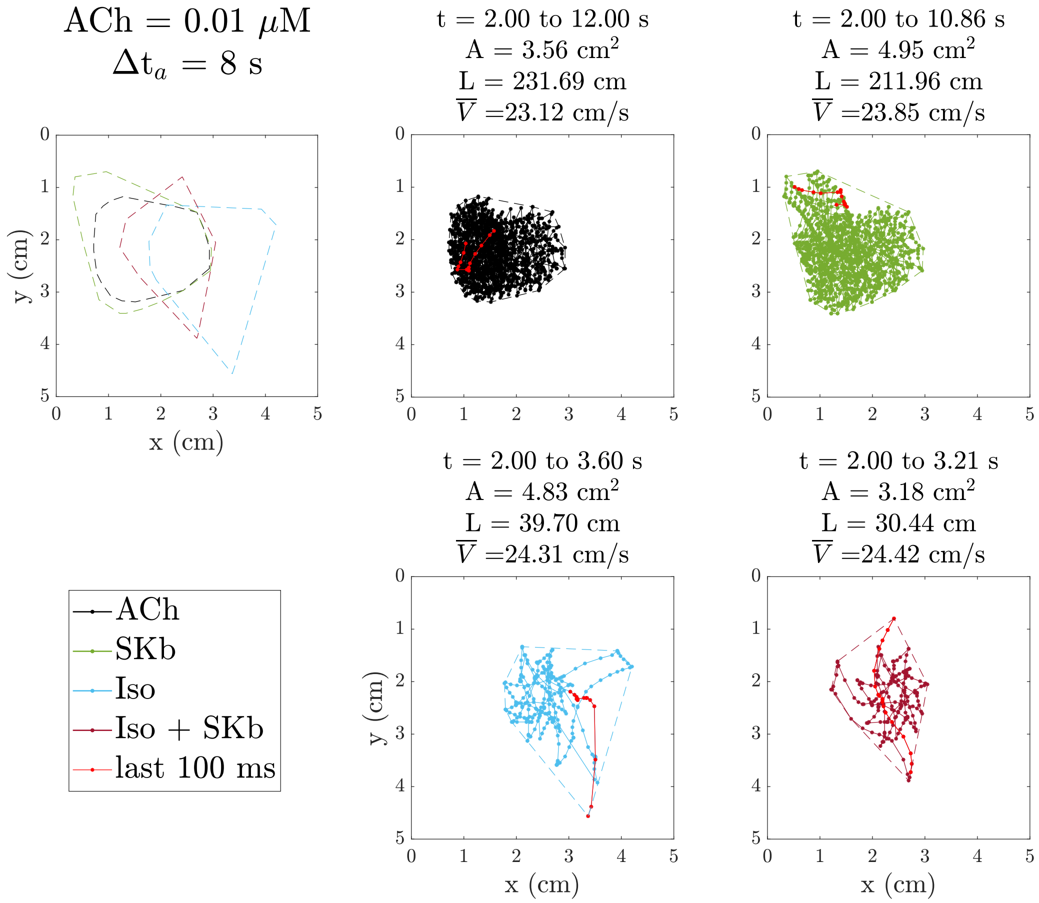

Figure 6.18: Rotor tip trajectory characteristics in terms of surface covered by the rotor tip (A), distance covered (L) and mean velocity ($\overline{V}$) when ACh=0.01 μM and Δt_a=8 s. In red the final segment of PSs, corresponding to the last 100 ms, is highlighted to point out the rotor tail. The top left panel represents the comparison between the area covered by the rotors in the different cases. The trajectory is analyzed for the entire lifespan of the rotor.

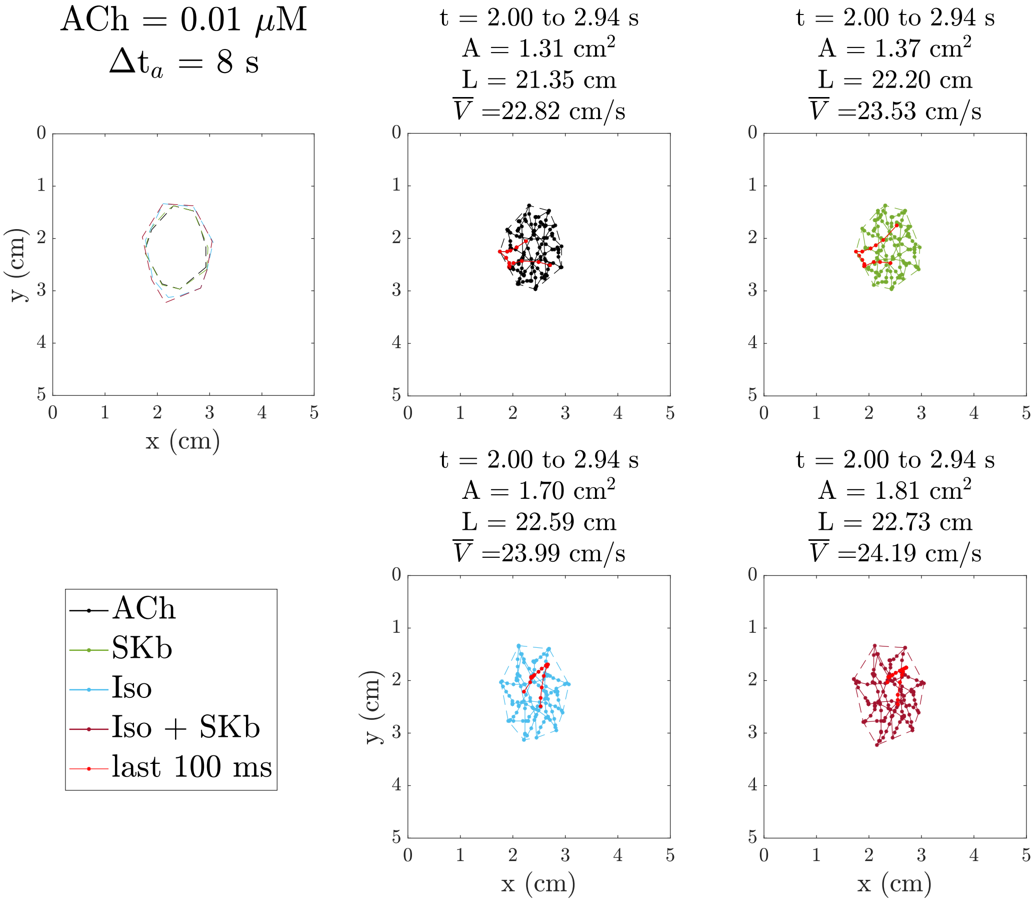

Figure 6.19: Rotor tip trajectory characteristics in terms of surface covered by the rotor tip (A), distance covered (L) and mean velocity ($\overline{\mathrm{V}}$) when ACh=0.01 μM and Δt_a=8 s. The figure is structured as Figure 6.18. The trajectory is analyzed in the time span before the onset of instability in the case when it manifested itself earlier.

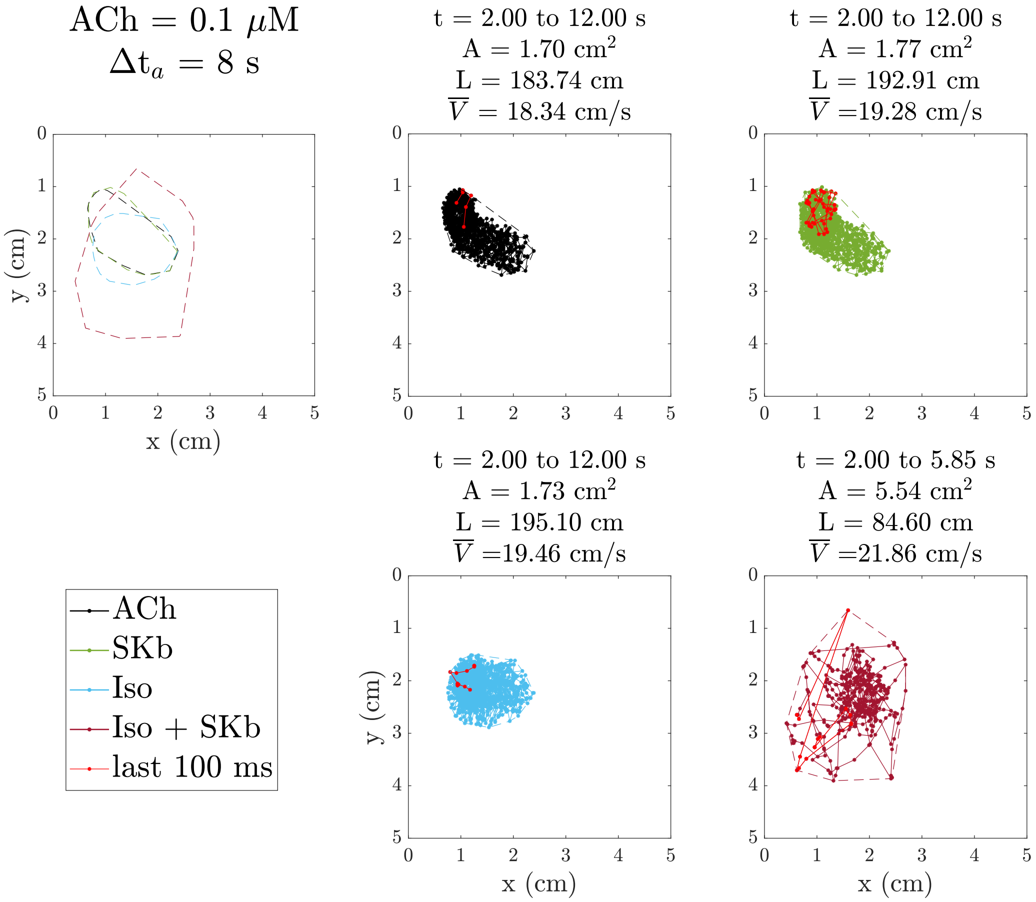

Figure 6.20: Rotor tip trajectory characteristics in terms of surface covered by the rotor tip (A), distance covered (L) and velocity ($\overline{\text{V}}$) when ACh=0.1 μM and Δt_a=8s. The figure is structured as Figure 6.18. The trajectory is analyzed for the entire lifespan of the rotor.

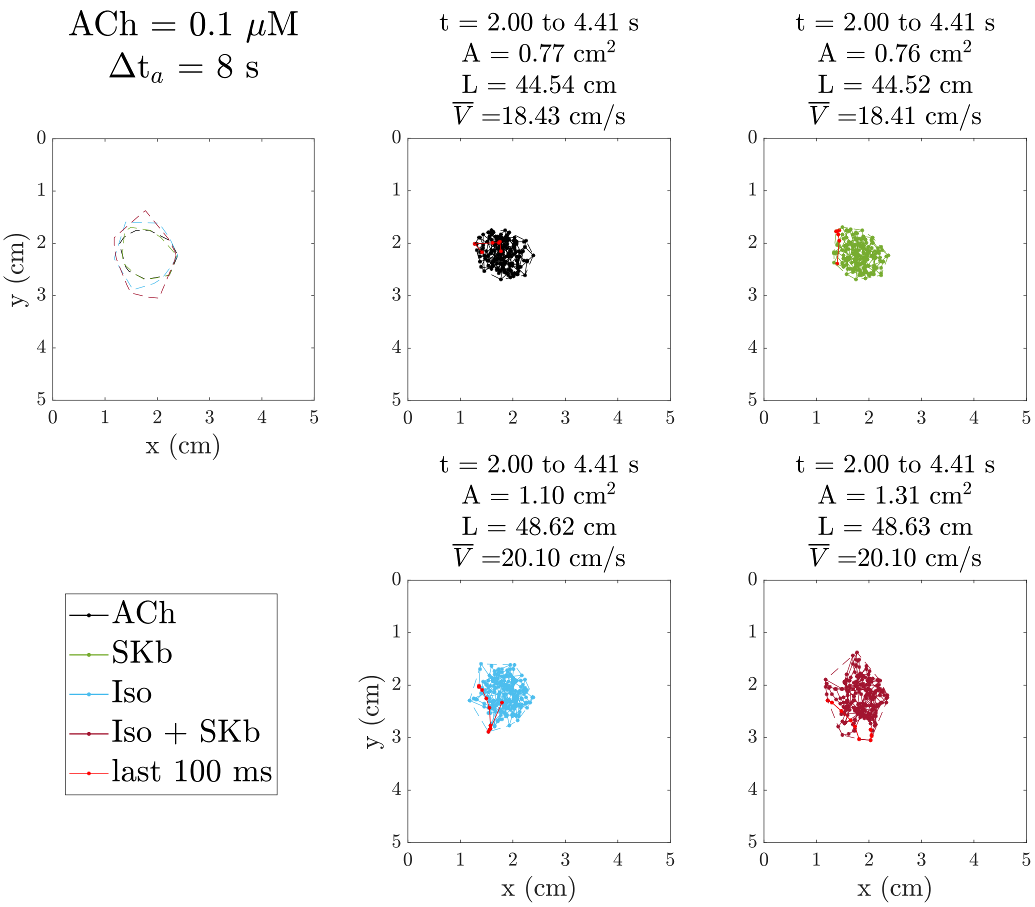

Figure 6.21: Rotor tip trajectory characteristics in terms of surface covered by the rotor tip (A), distance covered (L) and mean velocity ($\overline{\mathrm{V}}$) when ACh=0.1 μM and Δt_a=8 s. The figure is structured as Figure 6.18. The trajectory is analyzed in the time span before the onset of instability in the case when it manifested itself earlier.

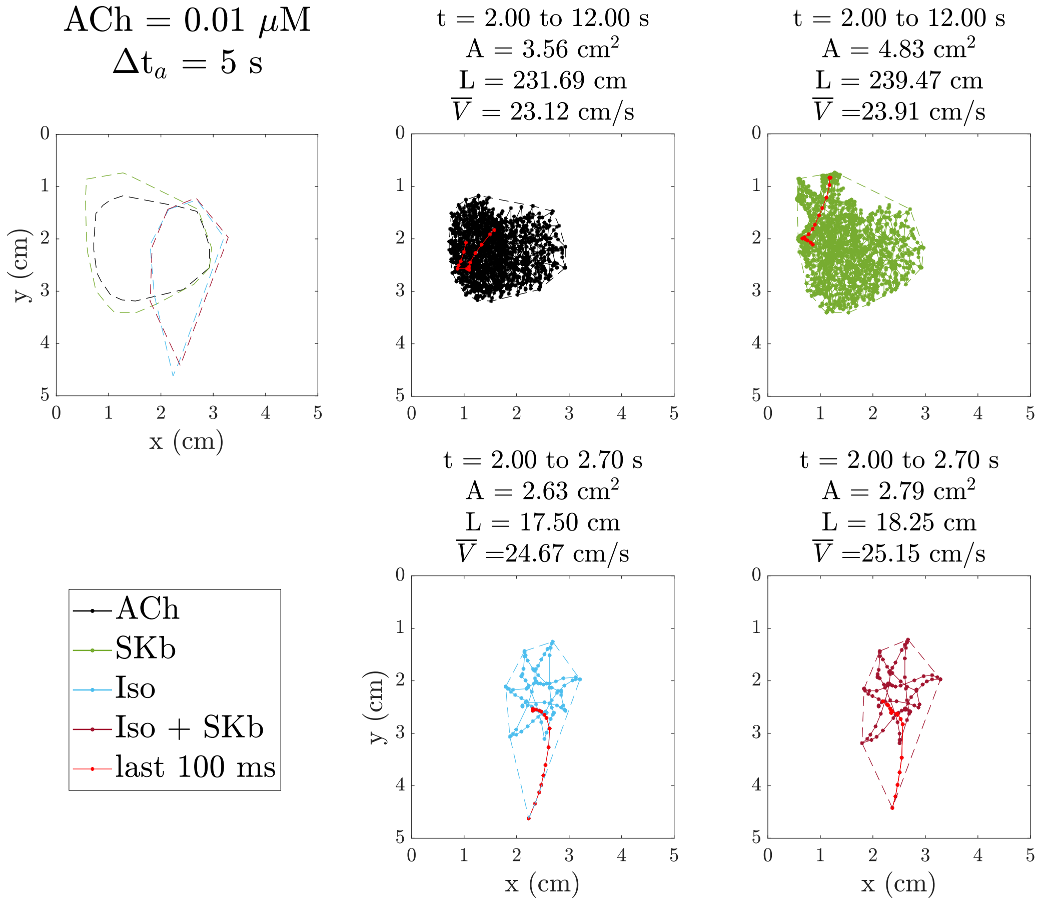

Figure 6.22: Rotor tip trajectory characteristics in terms of surface covered by the rotor tip (A), distance covered (L) and mean velocity ($\overline{\mathrm{V}}$) when ACh=0.01 μM and Δt_a=5 s. The figure is structured as Figure 6.18. The trajectory is analyzed for the entire lifespan of the rotor.

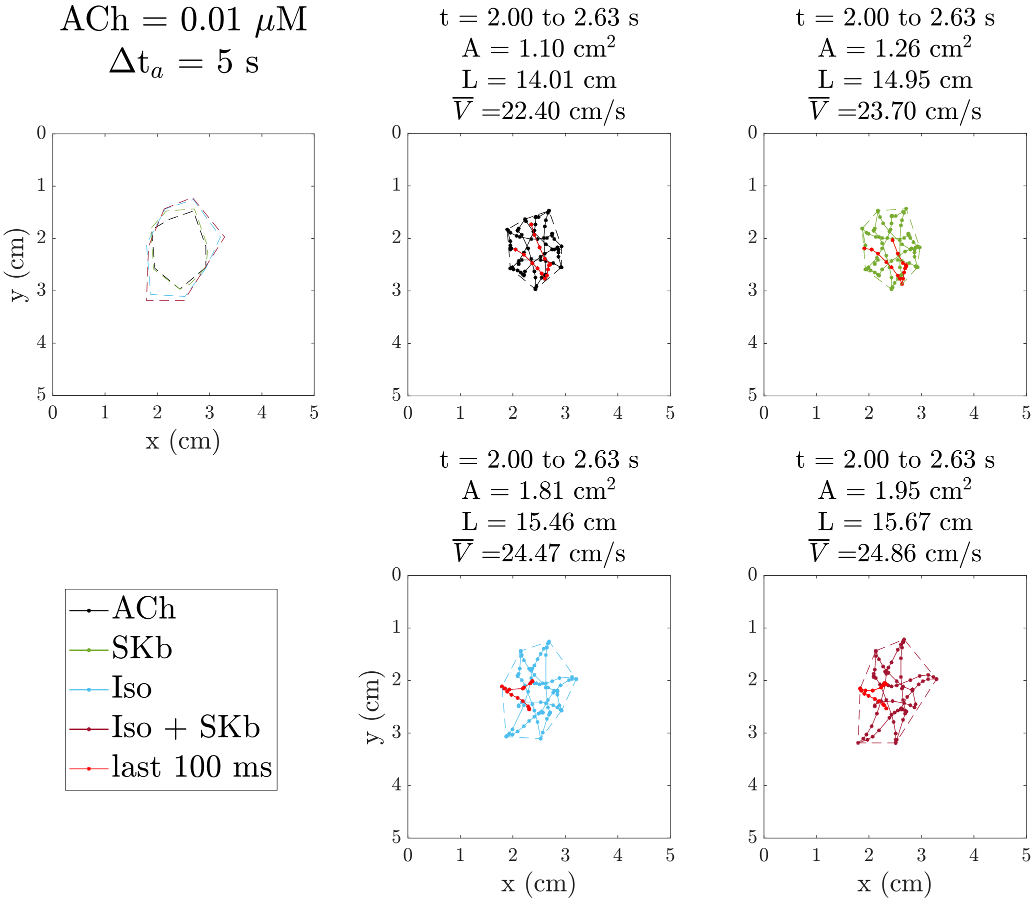

Figure 6.23: Rotor tip trajectory characteristics in terms of surface covered by the rotor tip (A), distance covered (L) and mean velocity ($\overline{\text{V}}$) when ACh=0.01 μM and Δt_a=5 s. The figure is structured as Figure 6.18. The trajectory is analyzed in the time span before the onset of instability in the case when it manifested itself earlier.

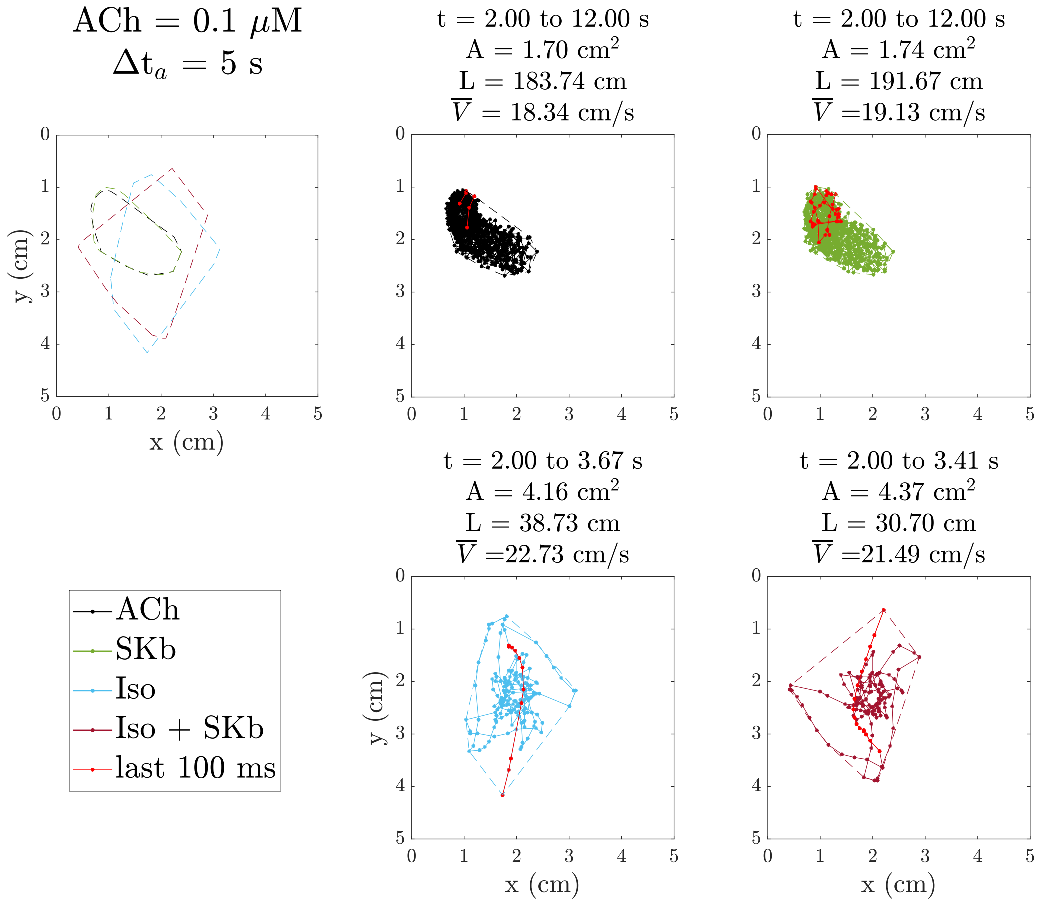

Figure 6.24: Rotor tip trajectory characteristics in terms of surface covered by the rotor tip (A), distance covered (L) and mean velocity ($\overline{\mathrm{V}}$) when ACh=0.1 μM and Δt_a=5 s. The figure is structured as Figure 6.18. The trajectory is analyzed for the entire lifespan of the rotor.

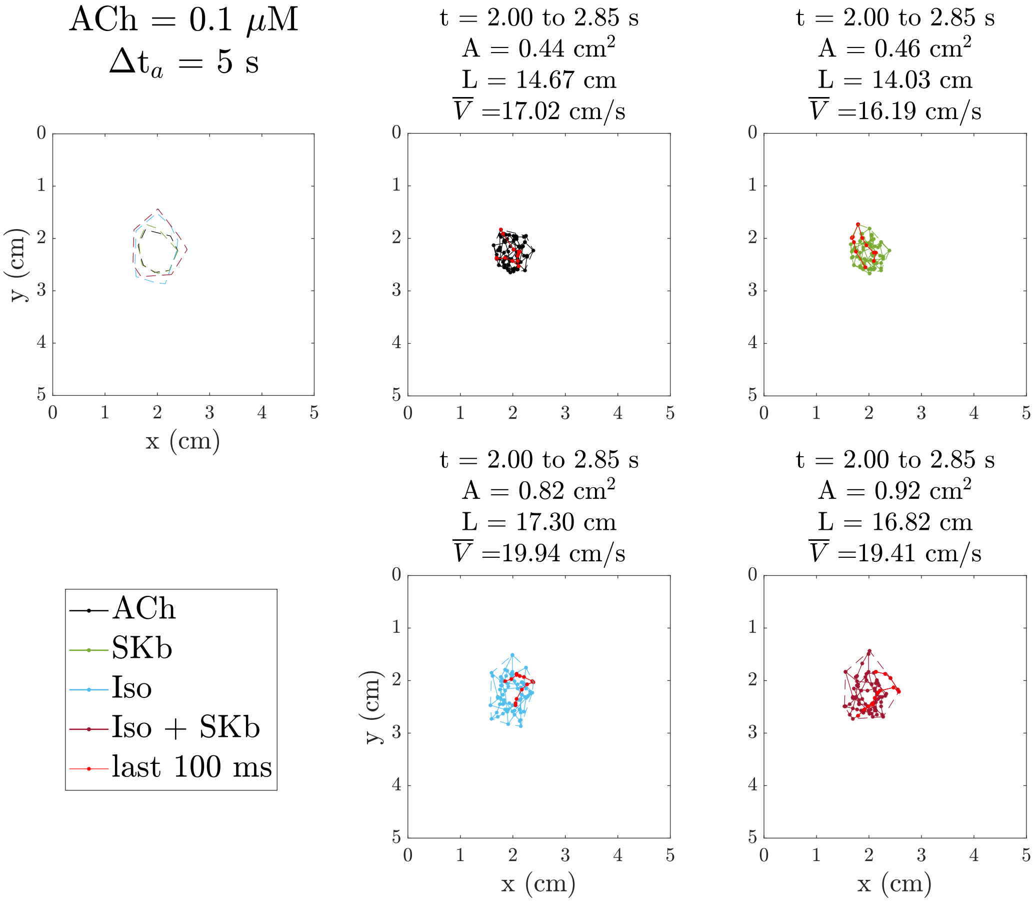

Figure 6.25: Rotor tip trajectory characteristics in terms of surface covered by the rotor tip (A), distance covered (L) and mean velocity ($\overline{\mathrm{V}}$) when ACh=0.1 μM and Δt_a=5 s. The figure is structured as Figure 6.18. The trajectory is analyzed in the time span before the onset of instability in the case when it manifested itself earlier.

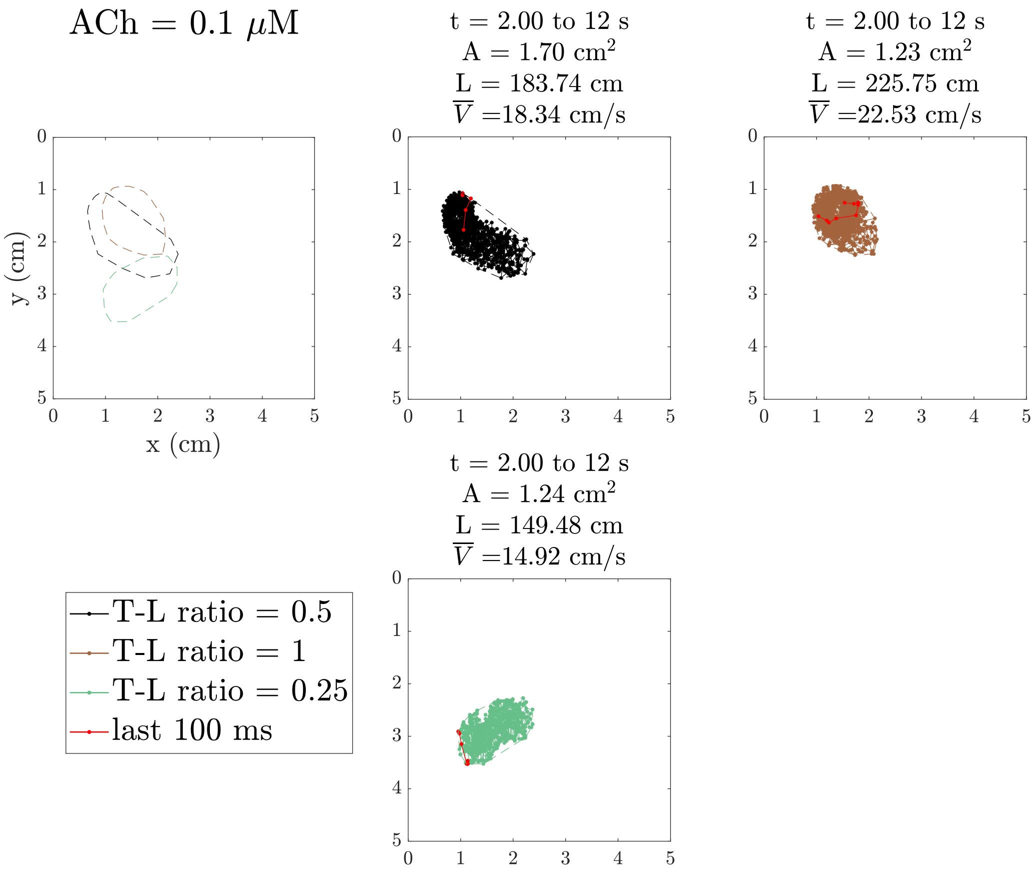

Figure 6.26: Effect of different transverse-to-longitudinal ratios (0.25, 0.5, 1) on the following rotor tip trajectory characteristics (ACh = 0.1 μM): surface (A) and distance (L) covered by the rotor tip and mean velocity ($\overline{\mathrm{V}}$).

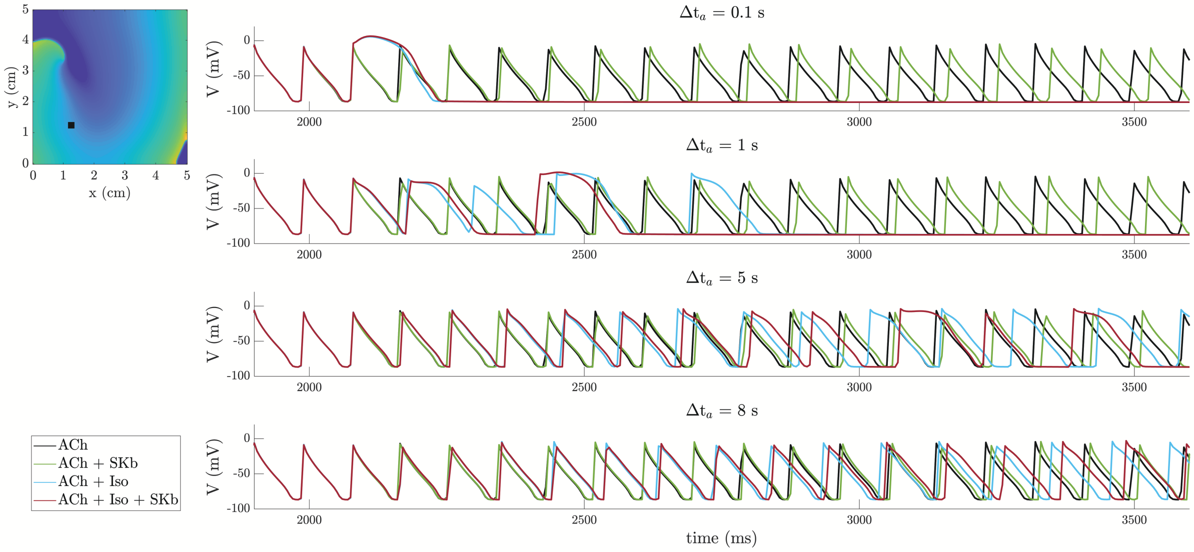

Figure 6.27: APs recorded at one point in the tissue (represented with the black square in the top left panel) when applying Iso and/or SKb with kinetics defined by Δt_a of 0.1, 1, 5 and 8 s.

Chapter 7

Conclusions and future extensions

7.1 Summary and main conclusions

7.1.1 Relevance of research contributions

The objective of this thesis was to develop novel computational modeling and simulation methods to provide a more detailed understanding of the interplay between the ANS and AF and to assess the potential of targeted interventions for managing this condition.

Numerous studies have established a relation between the ANS and the onset and perpetuation of AF [152–154]. Research has demonstrated that fluctuations in both the sympathetic and parasympathetic branches of the ANS play a role in atrial tachyarrhythmias [155–159]. Nevertheless, the mechanisms underlying the interplay between ANS and AF are not fully known yet.

In silico modeling and simulation is a potent tool that offers reproducible control over experimental conditions, enables virtual interventions that are not feasible in clinical or laboratory settings and facilitates in-depth mechanistic research. Therefore, considering the complex and incompletely understood role of the ANS in AF, computational simulations can prove highly valuable in addressing a range of issues, encompassing characterization as well as the development of novel treatments.

The variability in ANS activity among patients can play a significant role in explaining the variations in the effectiveness of anti-AF therapies. Therefore, the evaluation of the autonomic activity in AF patients could become crucial. In this thesis, investigations have been carried out to shed light on the role of autonomic-mediated modulation of fibrillatory frequency through the analysis of data involving controlled respiration and the performance of autonomic maneuvers.

The main AF treatments are ADT and catheter ablation. However, the clinical efficacy of these treatments, both in the short and long term, remains controversial.

PVI has become a common treatment approach for AF patients [203]. However, the reported long-term efficacy of catheter ablation in single-procedure AF cases does not exceed 70% [240]. Combining GP ablation with PVI has shown some improvement in AF recurrence outcomes [26]. Given the complex anatomy of the ANS, various attempts have been made in the literature to simplify the localization of cardiac GPs. Nonetheless, the reliability of existing methods for selectively locating GP clusters is sub-optimal. In this thesis, we introduced a novel method for accurately determining the location of the GPs by using information obtained from the repolarization waves of an EGM grid.

Class III antiarrhythmic drugs, blocking potassium channels, can prolong the APD and the refractory period in both the atria and ventricles. While they can be beneficial in treating AF by preventing reentry and restoring normal SR, they can also have detrimental effects on the ventricles. Of particular concern is their potential to cause torsades de pointes, a polymorphic ventricular tachycardia that can degenerate into ventricular fibrillation and lead to sudden cardiac death. Therefore, there is a need for the development of new and safe antiarrhythmic drugs acting on ion channels mainly expressed in the atria. In this work, we proposed the combination of SK channels blockers and β-adrenergic agonists as a possible therapy to counteract detrimental cholinergic-induced effects in the atria.

7.1.2 Assessment of autonomic modulation of the atrial fibrillatory rate

By integrating clinical data with computational simulations, our objective was to assess the feasibility of a non-invasive evaluation of ANS activity in psAF patients. This information has the potential to guide the development of personalized treatment strategies, specifically designed to address individual ANS dysregulation patterns. This could result in enhanced outcomes and more effective management of AF.

There are different evidences that support the fact that changes in autonomic balance can result in AFR oscillations ($\mathrm{F_f(t)}$). For instance, it has been observed that AF follows a circadian pattern, with an increase during the daytime and a decrease at night [330]. Controlled respiration has also been shown to cause short-term modulation of AFR, leading to cyclic fluctuations that were later suppressed by vagal blockade [301]. Additionally, AFR increases in response to HUT but decreases during HDT [298].

Observations of cyclic fluctuations exhibiting an in-phase relationship with respiration have been reported in AFR during AF [310] and in flutter CL in atrial flutter [311, 312]. Drawing an analogy to the phenomenon of RSA, where heart rate oscillations synchronous with respiration are modulated by the parasympathetic nervous system, we aimed to explore the hypothesis that this phenomenon during atrial arrhythmias may also be linked to parasympathetic modulation.

Through computational simulation, we investigated the influence of the spatiotemporal release pattern of ACh on the modulation of f-wave frequency. Our simulations encompassed various geometries and innervation patterns. Additionally, we examined different mean levels and ranges of variation of ACh to explore their effects on the modulation process.

Consistent with clinical observations, our findings showed that the f-wave frequency responded to temporal variations in ACh levels both in 2D tissue models and in 3D biatrial models. The mean f-wave frequency primarily relied on the fibrillatory pattern, which was predominantly determined by the number and spatial arrangement of stable reentrant circuits. Additionally, the average ACh concentration and the proportion of ACh release nodes throughout the atria contributed to the mean f-wave frequency. The extent of modulation in the f-wave frequency was influenced by the percentage of ACh release nodes and the temporal variation in ACh concentration. The spatial distribution of ACh release sites exhibited only a minor impact on the modulation effect.

Furthermore, we investigated the modulation of the fibrillatory frequency during HUT and HDT. Computational modeling and simulation was used to evaluate the fibrillatory rate variations in terms of mean fibrillatory rate and magnitude of respiratory modulation. We explored different combinations of sympathetic stimulation (SS) and parasympathetic stimulation (PSS), with PSS being influenced by the spatiotemporal release pattern of the parasympathetic neurotransmitter ACh. To validate our simulations, we compared the results with clinical ECG analyses obtained from psAF patients who underwent a tilt test protocol.

Our study findings collectively indicated that the increase in AFR observed during the HUT maneuver and the decrease in AFR during the HDT maneuver could primarily be attributed to heightened and diminished sympathetic activity, respectively. Furthermore, it appears that PSS plays a modulatory role of SS effects rather than being the primary driving force behind the observed trends in the AFR.

7.1.3 An algorithm to aid cardioneuroablation procedures for AF patients

RF catheter ablation is a common procedure for AF treatment when ADT is ineffective. GP ablation has been associated with a decreased risk of AF recurrence, either in addition to PVI or as a stand-alone procedure.

The effectiveness of GP ablation may be influenced by accurate GP location. Current methods for locating GPs during ablation procedures rely on functional or anatomical approaches but provide limited information about the actual area occupied by each GP. This study aimed to develop a method to locate atrial parasympathetic innervation sites within GPs using a multielectrode grid of EGM measurements.

Our study hypothesized that the amplitude of the EGM atrial repolarization wave could indicate the presence of ACh release sites. The proposed method was tested in simulated non-AF, pxAF and psAF tissues with different sizes and locations of ACh relase sites and fibrosis areas. The method relies on assessing the amplitude of the repolarization wave in the EGM and comparing it to a threshold. This threshold is determined based on the presence or absence of fibrosis in the underlying tissue beneath the EGM electrode position. For this purpose, we considered a complementary method for detecting fibrosis, which relies on evaluating the amplitude of the depolarization wave in the EGM. The simulated tissue models were paced uniformly along an entire edge of the 2D tissue, maintaining a fixed CL. Other AF patterns were not simulated. As a result, this method can be readily applied to patients with pxAF who are not currently in AF.

Our results showed that the proposed algorithm successfully identified most of the simulated ACh release sites, irrespective of the presence or absence of fibrosis. The accuracy in the identification of ACh sites was above 0.8, with a mean accuracy larger than 0.91. The method demonstrated robustness against noise and worked well with various EGM electrode distances.

7.1.4 Antiarrhythmic drug therapies targeting ion channels and neural components

Fluctuations in the activities of the sympathetic and parasympathetic branches of the ANS play a role in atrial tachyarrhythmias [155]. Specifically, increased activity of the parasympathetic branch is associated with pxAF [161]. ACh shortens the APD and hyperpolarizes the RMP in a concentration-dependent manner. These effects reduce the WL, facilitating reentrant activity. The uneven distribution of parasympathetic nerve endings and the rapid breakdown of ACh by acetylcholinesterase result in heterogeneous effects on atrial refractoriness, further increasing the susceptibility to AF.

Despite significant progress in AF management, the effectiveness of current pharmacological therapies remains limited, with many of them associated with potentially severe side effects. Specifically, class III antiarrhythmic drugs may carry risks of adverse effects on the ventricles. By directing attention towards atrial-specific potassium channels as potential targets for treating AF, the aim is to minimize the potential for adverse side effects.

SK channels have emerged as potential atrial-selective targets [121, 153, 386]. Inhibition of those channels has been proposed as a therapeutic strategy for AF treatment. SKb, by prolonging APD and ERP, could counteract the effects of parasympathetic stimulation [121, 387].

Therapies targeting the ANS have also been investigated [153]. The interaction between adrenergic and cholinergic stimulation effects in the atria has been explored, with low concentrations of Iso found to counteract cholinergic effects by limiting APD shortening caused by ACh [388].

This study aimed to evaluate the effectiveness of combining SKb and β-adrenergic stimulation by Iso in countering cholinergic-induced abnormalities in atrial electrical activity.

Numerical simulations using human atrial cell and tissue models were conducted to assess the steady-state effects of Iso and/or SKb on AP shape and APD_{90}, and their efficacy in terminating rotational activity in a cholinergically-stimulated 2D tissue model of AF.

The study found that individual SKb could restore ACh-induced APD shortening in atrial cardiomyocytes, while Iso was successful in terminating rotors but had varying effects on APD. The combination of Iso and SKb resulted in stronger APD prolongation and effectively countered ACh-induced shortening. The combined therapy was also effective in stopping stable rotors and preventing their reinducibility.

7.1.5 General limitations

Computational modeling and simulation offers a powerful approach to investigate complex phenomena. While these models have been thoroughly validated and proven effective in replicating physiological behaviors, their reliance on experimental data, particularly human data, can pose challenges due to limited availability. Specifically, the Courtemanche model has a limitation in its simplified modeling of sarcoplasmic reticulum Ca^{2+} handling due to limited data on Ca^{2+} storage and release kinetics from the sarcoplasmic reticulum at the time the model was developed. Furthermore, the significant variability exhibited by human atrial cells and tissues has to be taken into account. Models are typically constructed based on averaged data obtained from specific preparations, thereby disregarding this inherent variability. Approaches based on the construction of populations of models have been proposed to overcome this limitation and to account for inter-cellular and inter-individual variability. Nevertheless, experimental data is required for calibration of these populations of models and for subsequent validation of computationally-generated data.

Our simulations have been performed at the cellular level, in 2D tissue sheets and at the whole atria level. In the 3D models, we included regional electrophysiological heterogeneities as reported in previous works [285]. Nonetheless, in our studies we did not include the cell-to-cell variability that exists in human atria. This would be of particular importance in drug evaluation studies considering the relevance of biological variability in drug evaluation.

In our different studies, we dealt with pxAF and psAF models. It should be stressed that the differentiation between pxAF and psAF is challenging. Current clinical AF classification (paroxysmal, persistent, long-term persistent, permanent) is based on the duration of AF episodes and the form of termination [3, 76]. AF is considered to be a progressive disease, starting from short and infrequent episodes that later evolve to longer and more frequent ones. This progression is overall shown to be accompanied by alterations in myocardial substrate. As introduced in section 1.3.3, an increase in fibrosis with the progression of AF is common [78]. However, studies have shown that there are cases of pxAF patients having extensive fibrosis and psAF patients having only minor fibrosis[78, 84–86]. Our models reflect a simplified categorization of AF, with fibrotic load increasing with AF progression. As such, their primary purpose is to serve as a proof of concept, validating the applicability of our findings across various AF substrates.

AF is associated with various structural changes in the heart, including atrial chamber enlargement, cardiomyocyte hypertrophy, altered orientation of heart muscle fibers between different layers of the heart, changes in atrial wall thickness and a significant increase in fibrotic or connective tissue deposition [81–83]. Among these changes, our main focus was on simulating fibrotic remodeling, which was represented by fibroblast proliferation using the MacCannell fibroblast ionic model [283] and by GJ remodeling through a reduction in the fibroblast-myocyte and fibroblast-fibroblast conductivity. Previous computational models of fibrotic atria have attempted to incorporate various aspects of remodeling, such as remodeling of the GJ between cells, fibroblast proliferation and excess collagen deposition, either individually or in combination [87–91]. Nevertheless, further experimental characterization using human tissue is necessary to better understand and model atrial fibrosis in humans [282].

Finally, our models did not take into account the effects of electro-mechanical coupling. This could be of particular relevance when studying atrial rate variability. Studies have shown that the stretch of atrial tissue affects atrial conduction and refractoriness, possibly through mechanoelectrical coupling involving stretch-activated ion channels. Stretch can also modulate intracellular calcium concentration, affecting myofilament sensitivity and calcium entry. Extensive analyses have been conducted to understand the mechanical modulation, including cardiorespiratory modulation, of atrial activity, specifically in the case of atrial flutter [309, 311, 312, 326]. Passive upright tilting, the strain phase of the Valsalva maneuver and expiration, which reduce cardiac size, have been found to independently increase the rate of atrial flutter regardless of autonomic tone [326]. Furthermore, acute atrial stretch caused by ventricular contractions and respiratory movements shortens the atrial flutter CL through stretch-induced shortening of the ERP [311]. Again, these oscillations persist even after autonomic blockade, suggesting their independence from autonomic activity.

7.2 Future Extensions

The following are potential areas of future research that can be derived from this work:

In Chapters 3 and 4, we investigated how the ANS modulates the AFR in response to respiration and postural changes. To enhance the accuracy of our results, it would be beneficial to incorporate other factors such as stretch-activated ion channels that contribute to mechanoelectrical coupling. Additionally, the use of different atrial cellular models and the incorporation of cell-to-cell variability into the computational models could help to better represent inter-patient variability, thereby improving the overall understanding of the observed results.

In Chapter 5, we developed a method to identify ACh release sites in the atria using unipolar EGMs derived from *in silico* simulations. Future studies can build upon this method and test it on EGM signals collected from AF patients. Moreover, investigating atrial repolarization measured not only from unipolar EGMs but also from bipolar EGMs to identify ACh release sites could be a promising extension of this research. While our simulations focused on the effects of a 0.1 µM ACh concentration applied uniformly to all

ACh release sites, future studies could consider different ACh concentrations, potentially in relation to the number of available cholinergic receptors.

In Chapter 6, we explored the potential of using SKb in combination with Iso as a treatment for parasympathetically-induced pxAF. Further investigation could involve employing 3D whole-atrial models to gain a deeper understanding of complex rotor behavior and the mechanisms for terminating such rotors. Additionally, future research could explore the effects of electro-mechanical coupling, which were not accounted for in our models.

References

[1] E. J. Benjamin et al. “Impact of atrial fibrillation on the risk of death: the Framingham Heart Study”. In: *Circulation* 98.10 (Sept. 1998), pp. 946–952. ISSN: 0009-7322.

[2] Eugene Braunwald. “Cardiovascular Medicine at the Turn of the Millennium: Triumphs, Concerns, and Opportunities”. In: *New England Journal of Medicine* 337.19 (Nov. 1997), pp. 1360–1369.

[3] Gerhard Hindricks et al. “2020 ESC Guidelines for the diagnosis and management of atrial fibrillation developed in collaboration with the European Association for Cardio-Thoracic Surgery (EACTS): The Task Force for the diagnosis and management of atrial fibrillation of the European Society of Cardiology (ESC) Developed with the special contribution of the European Heart Rhythm Association (EHRA) of the ESC”. In: *European Heart Journal* 42.5 (Feb. 2021), pp. 373–498. ISSN: 1522-9645.

[4] Jeanne E. Poole et al. “Recurrence of Atrial Fibrillation After Catheter Ablation or Antiarrhythmic Drug Therapy in the CABANA Trial”. In: *Journal of the American College of Cardiology* 75.25 (June 2020), pp. 3105–3118. ISSN: 1558-3597.

[5] Nassir F. Marrouche et al. “Catheter Ablation for Atrial Fibrillation with Heart Failure”. In: *The New England Journal of Medicine* 378.5 (Feb. 2018), pp. 417–427. ISSN: 1533-4406.

[6] Jeffrey L. Anderson et al. “ACC/AHA statement on cost/value methodology in clinical practice guidelines and performance measures: a report of the American College of Cardiology/American Heart Association Task Force on Performance

Measures and Task Force on Practice Guidelines". In: *Journal of the American College of Cardiology* 63.21 (June 2014), pp. 2304–2322. ISSN: 1558-3597.

[7] Douglas L. Packer et al. "Ablation Versus Drug Therapy for Atrial Fibrillation in Heart Failure: Results From the CABANA Trial". In: *Circulation* 143.14 (Apr. 2021), pp. 1377–1390. ISSN: 1524-4539.

[8] Paul Dorian et al. "Quality of life improves with treatment in the Canadian Trial of Atrial Fibrillation". In: *American Heart Journal* 143.6 (June 2002), pp. 984–990. ISSN: 00028703.

[9] Michael H. Kim et al. "Estimation of total incremental health care costs in patients with atrial fibrillation in the United States". In: *Circulation. Cardiovascular Quality and Outcomes* 4.3 (May 2011), pp. 313–320. ISSN: 1941-7705.

[10] Ashish Shukla and Anne B. Curtis. "Avoiding permanent atrial fibrillation: treatment approaches to prevent disease progression". In: *Vascular Health and Risk Management* 10 (2014), pp. 1–12. ISSN: 1178-2048.

[11] Jan Heeringa et al. "Prevalence, incidence and lifetime risk of atrial fibrillation: the Rotterdam study". In: *European Heart Journal* 27.8 (Apr. 2006), pp. 949–953. ISSN: 0195-668X.

[12] A. S. Go et al. "Prevalence of diagnosed atrial fibrillation in adults: national implications for rhythm management and stroke prevention: the AnTicoagulation and Risk Factors in Atrial Fibrillation (ATRIA) Study". In: *JAMA* 285.18 (May 2001), pp. 2370–2375. ISSN: 0098-7484.

[13] Donald M. Lloyd-Jones et al. "Lifetime risk for development of atrial fibrillation: the Framingham Heart Study". In: *Circulation* 110.9 (Aug. 2004), pp. 1042–1046. ISSN: 1524-4539.

[14] Yoko Miyasaka et al. "Secular trends in incidence of atrial fibrillation in Olmsted County, Minnesota, 1980 to 2000, and implications on the projections for future prevalence". In: *Circulation* 114.2 (July 2006), pp. 119–125. ISSN: 1524-4539.

[15] Carlos A. Morillo et al. “Atrial fibrillation: the current epidemic”. In: *Journal of geriatric cardiology: JGC* 14.3 (Mar. 2017), pp. 195–203. ISSN: 1671-5411.

[16] P. Coumel. “Autonomic influences in atrial tachyarrhythmias”. In: *Journal of Cardiovascular Electrophysiology* 7.10 (Oct. 1996), pp. 999–1007. ISSN: 1045-3873.

[17] P. Coumel. “Cardiac arrhythmias and the autonomic nervous system”. In: *Journal of Cardiovascular Electrophysiology* 4.3 (June 1993), pp. 338–355. ISSN: 1045-3873.

[18] Marco Bettoni and Marc Zimmermann. “Autonomic Tone Variations Before the Onset of Paroxysmal Atrial Fibrillation”. en. In: *Circulation* 105.23 (June 2002), pp. 2753–2759. ISSN: 0009-7322, 1524-4539.

[19] Alina Scridon, Răzvan Constantin Şerban, and Philippe Chevalier. “Atrial fibrillation: Neurogenic or myogenic?” In: *Archives of Cardiovascular Diseases* 111.1 (Jan. 2018), pp. 59–69. ISSN: 1875-2128.

[20] Christian Jons et al. “Autonomic dysfunction and new-onset atrial fibrillation in patients with left ventricular systolic dysfunction after acute myocardial infarction: a CARISMA substudy”. In: *Journal of Cardiovascular Electrophysiology* 21.9 (Sept. 2010), pp. 983–990. ISSN: 1540-8167.

[21] P. Schauerte et al. “Catheter Ablation of Cardiac Autonomic Nerves for Prevention of Vagal Atrial Fibrillation”. In: *Circulation* 102.22 (Nov. 2000), pp. 2774–2780. ISSN: 1524-4539.

[22] Robert Lemery et al. “Feasibility Study of Endocardial Mapping of Ganglionated Plexuses During Catheter Ablation of Atrial Fibrillation”. In: *Heart Rhythm* 3.4 (Apr. 2006), pp. 387–396. ISSN: 1547-5271.

[23] Mauricio Scanavacca et al. “Selective Atrial Vagal Denervation Guided by Evoked Vagal Reflex to Treat Patients With Paroxysmal Atrial Fibrillation”. In: *Circulation* 114.9 (Aug. 2006), pp. 876–885. ISSN: 0009-7322, 1524-4539.

[24] Kristina Lemola et al. “Pulmonary Vein Region Ablation in Experimental Vagal Atrial Fibrillation: Role of Pulmonary Veins Versus Autonomic Ganglia”. In: *Circulation* 117.4 (Jan. 2008), pp. 470–477. ISSN: 1524-4539.

[25] Evgeny Pokushalov et al. “Selective Ganglionated Plexi Ablation for Paroxysmal Atrial Fibrillation”. In: *Heart Rhythm* 6.9 (Sept. 2009), pp. 1257–1264. ISSN: 15475271.

[26] Sunny S. Po, Hiroshi Nakagawa, and Warren M. Jackman. “Localization of Left Atrial Ganglionated Plexi in Patients with Atrial Fibrillation”. en. In: *Journal of Cardiovascular Electrophysiology* 20.10 (Oct. 2009), pp. 1186–1189. ISSN: 10453873, 15408167.

[27] Evgeny Pokushalov et al. “Ganglionated Plexi Ablation for Longstanding Persistent Atrial Fibrillation”. In: *EP Europace* 12.3 (Mar. 2010), pp. 342–346. ISSN: 1099-5129.

[28] Robert K. Clark. *Anatomy And Physiology: Understanding The Human Body*. 1st ed. pp.288-297. Sudbury, MA: Jones and Bartlett, 2005. ISBN: 9780763748166.

[29] Charles Antzelevitch and Alexander Burashnikov. “Overview of Basic Mechanisms of Cardiac Arrhythmia”. In: *Cardiac Electrophysiology Clinics* 3.1 (Mar. 2011), pp. 23–45. ISSN: 18779182.

[30] Amit S. Dhamoon and José Jalife. “The inward rectifier current (IK1) controls cardiac excitability and is involved in arrhythmogenesis”. In: *Heart Rhythm* 2.3 (Mar. 2005), pp. 316–324. ISSN: 1547-5271.

[31] Zhe Lu. “Mechanism of Rectification in Inward-Rectifier K+ Channels”. In: *Annual Review of Physiology* 66.1 (Mar. 2004), pp. 103–129. ISSN: 0066-4278, 1545-1585.

[32] Esther Pueyo, Juan Pablo Martínez, and Pablo Laguna. “Cardiac repolarization analysis using the surface electrocardiogram”. In: *Philosophical Transactions of the Royal Society A: Mathematical, Physical and Engineering Sciences* 367.1887 (Jan. 2009), pp. 213–233. ISSN: 1364-503X, 1471-2962.

[33] Wolfgang Trautwein et al. “Electrophysiological Study of Human Heart Muscle”. In: *Circulation Research* 10.3 (Mar. 1962), pp. 306–312. ISSN: 0009-7330, 1524-4571.

[34] G. J. Amos et al. “Differences between outward currents of human atrial and subepicardial ventricular myocytes”. In: *The Journal of Physiology* 491 (Pt 1).Pt 1 (Feb. 1996), pp. 31–50. ISSN: 0022-3751.

[35] D. Dobrev et al. “Molecular basis of downregulation of G-protein-coupled inward rectifying K(+) current (I(K,ACh) in chronic human atrial fibrillation: decrease in GIRK4 mRNA correlates with reduced I(K,ACh) and muscarinic receptor-mediated shortening of action potentials”. In: *Circulation* 104.21 (Nov. 2001), pp. 2551–2557. ISSN: 1524-4539.

[36] Yanggan Wang et al. “Differences in transient outward current properties between neonatal and adult human atrial myocytes”. In: *Journal of Molecular and Cellular Cardiology* 35.9 (Sept. 2003), pp. 1083–1092. ISSN: 0022-2828.

[37] D. Escande et al. “Age-related changes of action potential plateau shape in isolated human atrial fibers”. In: *The American Journal of Physiology* 249.4 Pt 2 (Oct. 1985), H843–850. ISSN: 0002-9513.

[38] Eleonora Grandi et al. “Human Atrial Action Potential and Ca2+ Model: Sinus Rhythm and Chronic Atrial Fibrillation”. In: *Circulation Research* 109.9 (Oct. 2011), pp. 1055–1066. ISSN: 1524-4571.

[39] Mathis Korseberg Stokke et al. “From global to local: a new understanding of cardiac electromechanical coupling”. In: *Tidsskrift for Den Norske Laegeforening: Tidsskrift for Praktisk Medicin, Ny Raekke* 132.12-13 (June 2012), pp. 1457–1460. ISSN: 0807-7096.

[40] John E. Hall A. C. Guyton. *Textbook of Medical Physiology, 12th ed.* London: Elsevier, 2011.

[41] Jacques Mt de Bakker. “Electrogram recording and analyzing techniques to optimize selection of target sites for ablation of cardiac arrhythmias”. In: *Pacing and clinical electrophysiology: PACE* 42.12 (Dec. 2019), pp. 1503–1516. ISSN: 1540-8159.

[42] Andrea Buttu. “Novel ECG and Intracardiac Electrograms Signal Processing Schemes for Predicting the Outcome of Atrial Fibrillation Catheter Ablation”. PhD thesis. Lausanne: ÉCOLE POLYTECHNIQUE FÉDÉRALE DE LAUSANNE, 2015.

[43] L. Sörnmo and P. Laguna. *Bioelectrical Signal Processing in Cardiac and Neurological Applications*. Elsevier Science, 2005.

[44] J. Andrew Armour. “Functional anatomy of intrathoracic neurons innervating the atria and ventricles”. eng. In: *Heart Rhythm* 7.7 (July 2010), pp. 994–996. ISSN: 1556-3871.

[45] J. Andrew Armour. “The little brain on the heart”. eng. In: *Cleveland Clinic Journal of Medicine* 74 Suppl 1 (Feb. 2007), S48–51. ISSN: 0891-1150.

[46] Dainius H. Pauza et al. “Morphology, Distribution, and Variability of the Epicardiac Neural Ganglionated Subplexuses in the Human Heart”. In: *The Anatomical Record* 259.4 (Aug. 2000), pp. 353–382. ISSN: 0003-276X.

[47] Stavros Stavrakis et al. “Ganglionated Plexi Ablation: Physiology and Clinical Applications”. en. In: *Arrhythmia & Electrophysiology Review* 6.4 (2017), p. 186. ISSN: 2050-3369.

[48] Tomokazu Kawashima. “The autonomic nervous system of the human heart with special reference to its origin, course, and peripheral distribution”. In: *Anatomy and Embryology* 209.6 (July 2005), pp. 425–438. ISSN: 0340-2061.

[49] Mark J. Shen and Douglas P. Zipes. “Role of the autonomic nervous system in modulating cardiac arrhythmias”. In: *Circulation Research* 114.6 (Mar. 2014), pp. 1004–1021. ISSN: 1524-4571.

[50] C. W. Chiou, J. N. Eble, and D. P. Zipes. “Efferent vagal innervation of the canine atria and sinus and atrioventricular nodes. The third fat pad”. In: *Circulation* 95.11 (June 1997), pp. 2573–2584. ISSN: 0009-7322.

[51] J. A. Armour. “Potential clinical relevance of the ’little brain’ on the mammalian heart”. In: *Experimental Physiology* 93.2 (Feb. 2008), pp. 165–176. ISSN: 0958-0670.

[52] J. A. Armour et al. “Gross and Microscopic Anatomy of the Human Intrinsic Cardiac Nervous System”. In: *The Anatomical Record* 247.2 (Feb. 1997), pp. 289–298. ISSN: 0003-276X.

[53] J. A. Armour. “Intrinsic cardiac neurons involved in cardiac regulation possess alpha 1-, alpha 2-, beta 1- and beta 2-adrenoceptors”. In: *The Canadian Journal of Cardiology* 13.3 (Mar. 1997), pp. 277–284. ISSN: 0828-282X.

[54] M. Tsuboi et al. “Inotropic, chronotropic, and dromotropic effects mediated via parasympathetic ganglia in the dog heart”. In: *American Journal of Physiology. Heart and Circulatory Physiology* 279.3 (Sept. 2000), H1201–1207. ISSN: 0363-6135.

[55] Eue-Keun Choi et al. “Ganglionated Plexi as Neuromodulation Targets for Atrial Fibrillation”. In: *Journal of Cardiovascular Electrophysiology* 28.12 (Dec. 2017), pp. 1485–1491. ISSN: 1540-8167.

[56] Alex Y. Tan et al. “Autonomic Innervation and Segmental Muscular Disconnections at the Human Pulmonary Vein-Atrial Junction”. In: *Journal of the American College of Cardiology* 48.1 (July 2006), pp. 132–143. ISSN: 07351097.

[57] Philippe Chevalier et al. “Quantitative study of nerves of the human left atrium”. In: *Heart Rhythm* 2.5 (May 2005), pp. 518–522. ISSN: 1547-5271.

[58] R. C. Arora et al. “Porcine intrinsic cardiac ganglia”. In: *The Anatomical Record. Part A, Discoveries in Molecular, Cellular, and Evolutionary Biology* 271.1 (Mar. 2003), pp. 249–258. ISSN: 1552-4884.

[59] Darius Batulevicius et al. "Topography of the porcine epicardiac nerve plexus as revealed by histochemistry for acetylcholinesterase". In: *Autonomic Neuroscience: Basic & Clinical* 138.1-2 (Feb. 2008), pp. 64–75. ISSN: 1566-0702.

[60] Salim S. Virani et al. "Heart Disease and Stroke Statistics-2021 Update: A Report From the American Heart Association". In: *Circulation* 143.8 (Feb. 2021), e254–e743. ISSN: 1524-4539.

[61] Jordi Heijman et al. "Cellular and molecular electrophysiology of atrial fibrillation initiation, maintenance, and progression". In: *Circulation Research* 114.9 (Apr. 2014), pp. 1483–1499. ISSN: 1524-4571.

[62] Paulus Kirchhof et al. "2016 ESC Guidelines for the management of atrial fibrillation developed in collaboration with EACTS". eng. In: *European Heart Journal* 37.38 (Oct. 2016), pp. 2893–2962. ISSN: 1522-9645.

[63] Sumeet S. Chugh et al. "Worldwide epidemiology of atrial fibrillation: a Global Burden of Disease 2010 Study". In: *Circulation* 129.8 (Feb. 2014), pp. 837–847. ISSN: 1524-4539.

[64] Eloi Marijon et al. "Causes of death and influencing factors in patients with atrial fibrillation: a competing-risk analysis from the randomized evaluation of long-term anticoagulant therapy study". In: *Circulation* 128.20 (Nov. 2013), pp. 2192–2201. ISSN: 1524-4539.

[65] Paul A. Heidenreich et al. "Forecasting the impact of heart failure in the United States: a policy statement from the American Heart Association". In: *Circulation. Heart Failure* 6.3 (May 2013), pp. 606–619. ISSN: 1941-3297.

[66] Renate B. Schnabel et al. "50 year trends in atrial fibrillation prevalence, incidence, risk factors, and mortality in the Framingham Heart Study: a cohort study". In: *Lancet (London, England)* 386.9989 (July 2015), pp. 154–162. ISSN: 1474-547X.

[67] Christopher B. Fordyce et al. "Cardiovascular drug development: is it dead or just hibernating?" In: *Journal of the American College of Cardiology* 65.15 (Apr. 2015), pp. 1567–1582. ISSN: 1558-3597.

[68] E. Braunwald. “Shattuck lecture–cardiovascular medicine at the turn of the millennium: triumphs, concerns, and opportunities”. In: *The New England Journal of Medicine* 337.19 (Nov. 1997), pp. 1360–1369. ISSN: 0028-4793.

[69] Bouwe P. Krijthe et al. “Projections on the number of individuals with atrial fibrillation in the European Union, from 2000 to 2060”. In: *European Heart Journal* 34.35 (Sept. 2013), pp. 2746–2751. ISSN: 1522-9645.

[70] Antonio Di Carlo et al. “Prevalence of atrial fibrillation in the Italian elderly population and projections from 2020 to 2060 for Italy and the European Union: the FAI Project”. In: *Europace: European Pacing, Arrhythmias, and Cardiac Electrophysiology: Journal of the Working Groups on Cardiac Pacing, Arrhythmias, and Cardiac Cellular Electrophysiology of the European Society of Cardiology* 21.10 (Oct. 2019), pp. 1468–1475. ISSN: 1532-2092.

[71] Chern-En Chiang, Kang-Ling Wang, and Gregory Y. H. Lip. “Stroke prevention in atrial fibrillation: an Asian perspective”. In: *Thrombosis and Haemostasis* 111.5 (May 2014), pp. 789–797. ISSN: 2567-689X.

[72] Polychronis E. Dilaveris and Harold L. Kennedy. “Silent atrial fibrillation: epidemiology, diagnosis, and clinical impact”. In: *Clinical Cardiology* 40.6 (June 2017), pp. 413–418. ISSN: 1932-8737.

[73] Emelia J. Benjamin et al. “Prevention of atrial fibrillation: report from a national heart, lung, and blood institute workshop”. In: *Circulation* 119.4 (Feb. 2009), pp. 606–618. ISSN: 1524-4539.

[74] Pyotr G. Platonov et al. “Atrial Fibrillatory Rate in the Clinical Context: Natural Course and Prediction of Intervention Outcome”. In: *Europace: European Pacing, Arrhythmias, and Cardiac Electrophysiology: Journal of the Working Groups on Cardiac Pacing, Arrhythmias, and Cardiac Cellular Electrophysiology of the European Society of Cardiology* 16 Suppl 4 (Nov. 2014), pp. iv110–iv119. ISSN: 1532-2092.

[75] Hamilton Cardiologist Associates. *Atrial Fibrillation*. https://hcahamilton.com/atrial-fibrillation/. 2023.

[76] January Craig T. et al. “2014 AHA/ACC/HRS Guideline for the Management of Patients With Atrial Fibrillation”. In: *Circulation* 130.23 (Dec. 2014), e199–e267.

[77] Hans Kottkamp et al. “Therapeutic Approaches to Atrial Fibrillation Ablation Targeting Atrial Fibrosis”. In: *JACC. Clinical electrophysiology* 3.7 (July 2017), pp. 643–653. ISSN: 2405-5018.

[78] Pyotr G. Platonov et al. “Structural Abnormalities in Atrial Walls are Associated with Presence and Persistency of Atrial Fibrillation but not with Age”. In: *Journal of the American College of Cardiology* 58.21 (Nov. 2011), pp. 2225–2232. ISSN: 1558-3597.

[79] Prashanthan Sanders et al. “Electrical remodeling of the atria in congestive heart failure: electrophysiological and electroanatomic mapping in humans”. In: *Circulation* 108.12 (Sept. 2003), pp. 1461–1468. ISSN: 1524-4539.

[80] M Allessie. “Electrical, contractile and structural remodeling during atrial fibrillation”. In: *Cardiovascular Research* 54.2 (May 2002), pp. 230–246. ISSN: 00086363.

[81] D. George Wyse et al. “Lone Atrial Fibrillation”. en. In: *Journal of the American College of Cardiology* 63.17 (May 2014), pp. 1715–1723. ISSN: 07351097.

[82] Ulrich Schotten et al. “Pathophysiological Mechanisms of Atrial Fibrillation: A Translational Appraisal”. In: *Physiological Reviews* 91.1 (Jan. 2011), pp. 265–325. ISSN: 0031-9333.

[83] Jordi Heijman et al. “The Value of Basic Research Insights into Atrial Fibrillation Mechanisms as a Guide to Therapeutic Innovation: a Critical Analysis”. In: *Cardiovascular Research* 109.4 (Apr. 2016), pp. 467–479. ISSN: 0008-6363, 1755-3245.

[84] A. Boldt et al. “Fibrosis in Left Atrial Tssue of Patients with Atrial Fibrillation With and Without Underlying Mitral Valve Disease”. In: *Heart (British Cardiac Society)* 90.4 (Apr. 2004), pp. 400–405. ISSN: 1468-201X.

[85] Robert S. Oakes et al. “Detection and Quantification of Left Atrial Structural Remodeling with Delayed-Enhancement Magnetic Resonance Imaging in Patients

with Atrial Fibrillation”. In: *Circulation* 119.13 (Apr. 2009), pp. 1758–1767. ISSN: 1524-4539.

[86] Andrew W. Teh et al. “Electroanatomic Remodeling of the Left Atrium in Paroxysmal and Persistent Atrial Fibrillation Patients without Structural Heart Disease”. In: *Journal of Cardiovascular Electrophysiology* 23.3 (Mar. 2012), pp. 232–238. ISSN: 1540-8167.

[87] Sawa Kostin et al. “Structural Correlate of Atrial Fibrillation in Human Patients”. In: *Cardiovascular Research* 54.2 (May 2002), pp. 361–379. ISSN: 0008-6363.

[88] Burstein Brett et al. “Changes in Connexin Expression and the Atrial Fibrillation Substrate in Congestive Heart Failure”. In: *Circulation Research* 105.12 (Dec. 2009), pp. 1213–1222.

[89] Lixia Yue, Jia Xie, and Stanley Nattel. “Molecular Determinants of Cardiac Fibroblast Electrical Function and Therapeutic Implications for Atrial Fibrillation”. In: *Cardiovascular Research* 89.4 (Mar. 2011), pp. 744–753. ISSN: 1755-3245.

[90] Stephan Rohr. “Myofibroblasts in Diseased Hearts: new Players in Cardiac Arrhythmias?” In: *Heart Rhythm* 6.6 (June 2009), pp. 848–856. ISSN: 1556-3871.

[91] Brett Burstein and Stanley Nattel. “Atrial Fibrosis: Mechanisms and Clinical Relevance in Atrial Fibrillation”. In: *Journal of the American College of Cardiology* 51.8 (Feb. 2008), pp. 802–809. ISSN: 1558-3597.

[92] I. Shiraishi et al. “Quantitative histological analysis of the human sinoatrial node during growth and aging”. In: *Circulation* 85.6 (June 1992), pp. 2176–2184. ISSN: 0009-7322.

[93] Patrizia Camelliti et al. “Spatially and temporally distinct expression of fibroblast connexins after sheep ventricular infarction”. In: *Cardiovascular Research* 62.2 (May 2004), pp. 415–425. ISSN: 0008-6363.

[94] Ya-Jean Wang et al. “Contribution of BK(Ca)-channel activity in human cardiac fibroblasts to electrical coupling of cardiomyocytes-fibroblasts”. In: *The Journal of Membrane Biology* 213.3 (2006), pp. 175–185. ISSN: 0022-2631.

[95] P. Kohl and D. Noble. “Mechanosensitive connective tissue: potential influence on heart rhythm”. In: *Cardiovascular Research* 32.1 (July 1996), pp. 62–68. ISSN: 0008-6363.

[96] A. Kamkin et al. “Mechanically induced potentials in fibroblasts from human right atrium”. In: *Experimental Physiology* 84.2 (Mar. 1999), pp. 347–356. ISSN: 0958-0670.

[97] Peter Kohl et al. “Electrical coupling of fibroblasts and myocytes: relevance for cardiac propagation”. In: *Journal of Electrocardiology* 38.4 Suppl (Oct. 2005), pp. 45–50. ISSN: 0022-0736.

[98] Kazuhiko Tanaka et al. “Spatial distribution of fibrosis governs fibrillation wave dynamics in the posterior left atrium during heart failure”. In: *Circulation Research* 101.8 (Oct. 2007), pp. 839–847. ISSN: 1524-4571.

[99] Michele Miragoli, Nicolò Salvarani, and Stephan Rohr. “Myofibroblasts induce ectopic activity in cardiac tissue”. In: *Circulation Research* 101.8 (Oct. 2007), pp. 755–758. ISSN: 1524-4571.

[100] Dawn M. Pedrotty et al. “Cardiac Fibroblast Paracrine Factors Alter Impulse Conduction and Ion Channel Expression of Neonatal Rat Cardiomyocytes”. In: *Cardiovascular Research* 83.4 (Sept. 2009), pp. 688–697. ISSN: 1755-3245.

[101] Natalia A. Trayanova. “Mathematical Approaches to Understanding and Imaging Atrial Fibrillation: Significance for Mechanisms and Management”. In: *Circulation Research* 114.9 (Apr. 2014), pp. 1516–1531. ISSN: 1524-4571.

[102] Vincent Jacquemet and Craig S. Henriquez. “Loading effect of fibroblast-myocyte coupling on resting potential, impulse propagation, and repolarization: insights from a microstructure model”. In: *American Journal of Physiology. Heart and Circulatory Physiology* 294.5 (May 2008), H2040–2052. ISSN: 0363-6135.

[103] Gunnar Seemann, Axel Loewe, and Eike M. Wlfers. “Effects of Fibroblasts coupling on the Electrophysiology of Cardiomyocytes from Different Regions of the Human Atrium: a Simulation Study”. In: Sept. 2017.

[104] David R. Van Wagoner et al. "Atrial L-Type Ca $^{2+}$ Currents and Human Atrial Fibrillation". In: *Circulation Research* 85.5 (Sept. 1999), pp. 428–436. ISSN: 0009-7330, 1524-4571.

[105] A. J. Workman, K. A. Kane, and A. C. Rankin. "The contribution of ionic currents to changes in refractoriness of human atrial myocytes associated with chronic atrial fibrillation". In: *Cardiovascular Research* 52.2 (Nov. 2001), pp. 226–235. ISSN: 0008-6363.

[106] M. Boutjdir et al. "Inhomogeneity of cellular refractoriness in human atrium: factor of arrhythmia?" In: *Pacing and clinical electrophysiology: PACE* 9.6 (Nov. 1986), pp. 1095–1100. ISSN: 0147-8389.

[107] R. F. Bosch et al. "Ionic mechanisms of electrical remodeling in human atrial fibrillation". In: *Cardiovascular Research* 44.1 (Oct. 1999), pp. 121–131. ISSN: 0008-6363.

[108] Niels Voigt et al. "Enhanced sarcoplasmic reticulum Ca2+ leak and increased Na+-Ca2+ exchanger function underlie delayed afterdepolarizations in patients with chronic atrial fibrillation". In: *Circulation* 125.17 (May 2012), pp. 2059–2070. ISSN: 1524-4539.

[109] Samuel Sossalla et al. "Altered Na(+) currents in atrial fibrillation effects of ranolazine on arrhythmias and contractility in human atrial myocardium". In: *Journal of the American College of Cardiology* 55.21 (May 2010), pp. 2330–2342. ISSN: 1558-3597.

[110] Raphael P. Martins et al. "Dominant frequency increase rate predicts transition from paroxysmal to long-term persistent atrial fibrillation". In: *Circulation* 129.14 (Apr. 2014), pp. 1472–1482. ISSN: 1524-4539.

[111] T. Christ et al. "L-type Ca2+ current downregulation in chronic human atrial fibrillation is associated with increased activity of protein phosphatases". In: *Circulation* 110.17 (Oct. 2004), pp. 2651–2657. ISSN: 1524-4539.

[112] Ricardo Caballero et al. “In humans, chronic atrial fibrillation decreases the transient outward current and ultrarapid component of the delayed rectifier current differentially on each atria and increases the slow component of the delayed rectifier current in both”. In: *Journal of the American College of Cardiology* 55.21 (May 2010), pp. 2346–2354. ISSN: 1558-3597.

[113] D. R. Van Wagoner et al. “Outward K+ current densities and Kv1.5 expression are reduced in chronic human atrial fibrillation”. In: *Circulation Research* 80.6 (June 1997), pp. 772–781. ISSN: 0009-7330.

[114] J. B. Grammer et al. “Molecular remodeling of Kv4.3 potassium channels in human atrial fibrillation”. In: *Journal of Cardiovascular Electrophysiology* 11.6 (June 2000), pp. 626–633. ISSN: 1045-3873.

[115] M. C. Brandt et al. “The ultrarapid and the transient outward K(+) current in human atrial fibrillation. Their possible role in postoperative atrial fibrillation”. In: *Journal of Molecular and Cellular Cardiology* 32.10 (Oct. 2000), pp. 1885–1896. ISSN: 0022-2828.

[116] B. J. Brundel et al. “Alterations in potassium channel gene expression in atria of patients with persistent and paroxysmal atrial fibrillation: differential regulation of protein and mRNA levels for K+ channels”. In: *Journal of the American College of Cardiology* 37.3 (Mar. 2001), pp. 926–932. ISSN: 0735-1097.

[117] T. Christ et al. “Pathology-specific effects of the IKur/Ito/IK,ACh blocker AVE0118 on ion channels in human chronic atrial fibrillation”. In: *British Journal of Pharmacology* 154.8 (Aug. 2008), pp. 1619–1630. ISSN: 0007-1188.

[118] B. J. Brundel et al. “Ion channel remodeling is related to intraoperative atrial effective refractory periods in patients with paroxysmal and persistent atrial fibrillation”. In: *Circulation* 103.5 (Feb. 2001), pp. 684–690. ISSN: 1524-4539.

[119] Viviana Muñoz et al. “Adenoviral expression of IKs contributes to wavebreak and fibrillatory conduction in neonatal rat ventricular cardiomyocyte monolayers”. In: *Circulation Research* 101.5 (Aug. 2007), pp. 475–483. ISSN: 1524-4571.

[120] Niels Voigt et al. “Left-to-right atrial inward rectifier potassium current gradients in patients with paroxysmal versus chronic atrial fibrillation”. In: *Circulation. Arrhythmia and Electrophysiology* 3.5 (Oct. 2010), pp. 472–480. ISSN: 1941-3084.

[121] Lasse Skibsbye et al. “Small-Conductance Calcium-Activated Potassium (SK) Channels Contribute to Action Potential Repolarization in Human Atria”. eng. In: *Cardiovascular Research* 103.1 (July 2014), pp. 156–167. ISSN: 1755-3245.

[122] Z. Wang, B. Fermini, and S. Nattel. “Delayed rectifier outward current and repolarization in human atrial myocytes”. In: *Circulation Research* 73.2 (Aug. 1993), pp. 276–285. ISSN: 0009-7330.

[123] Ali El-Armouche et al. “Molecular determinants of altered Ca2+ handling in human chronic atrial fibrillation”. In: *Circulation* 114.7 (Aug. 2006), pp. 670–680. ISSN: 1524-4539.

[124] Stanley Nattel and Dobromir Dobrev. “The multidimensional role of calcium in atrial fibrillation pathophysiology: mechanistic insights and therapeutic opportunities”. In: *European Heart Journal* 33.15 (Aug. 2012), pp. 1870–1877. ISSN: 1522-9645.

[125] Stefan Neef et al. “CaMKII-dependent diastolic SR Ca2+ leak and elevated diastolic Ca2+ levels in right atrial myocardium of patients with atrial fibrillation”. In: *Circulation Research* 106.6 (Apr. 2010), pp. 1134–1144. ISSN: 1524-4571.

[126] Maura Greiser et al. “Tachycardia-induced silencing of subcellular Ca2+ signaling in atrial myocytes”. In: *The Journal of Clinical Investigation* 124.11 (Nov. 2014), pp. 4759–4772. ISSN: 1558-8238.

[127] Mihail G. Chelu et al. “Calmodulin kinase II-mediated sarcoplasmic reticulum Ca2+ leak promotes atrial fibrillation in mice”. In: *The Journal of Clinical Investigation* 119.7 (July 2009), pp. 1940–1951. ISSN: 1558-8238.

[128] Reza Wakili et al. “Recent advances in the molecular pathophysiology of atrial fibrillation”. In: *The Journal of Clinical Investigation* 121.8 (Aug. 2011), pp. 2955–2968. ISSN: 1558-8238.

[129] María S. Guillem et al. “Presence and stability of rotors in atrial fibrillation: evidence and therapeutic implications”. In: *Cardiovascular Research* 109.4 (Apr. 2016), pp. 480–492. ISSN: 1755-3245.

[130] T. Satoh and D. P. Zipes. “Cesium-induced atrial tachycardia degenerating into atrial fibrillation in dogs: atrial torsades de pointes?” In: *Journal of Cardiovascular Electrophysiology* 9.9 (Sept. 1998), pp. 970–975. ISSN: 1045-3873.

[131] Zhen Song et al. “Calcium-voltage coupling in the genesis of early and delayed afterdepolarizations in cardiac myocytes”. In: *Biophysical Journal* 108.8 (Apr. 2015), pp. 1908–1921. ISSN: 1542-0086.

[132] Akiko Shiroshita-Takeshita, Bianca J. J. M. Brundel, and Stanley Nattel. “Atrial fibrillation: basic mechanisms, remodeling and triggers”. eng. In: *Journal of Interventional Cardiac Electrophysiology: An International Journal of Arrhythmias and Pacing* 13.3 (Sept. 2005), pp. 181–193. ISSN: 1383-875X.

[133] Michel Haissaguerre et al. “Driver Domains in Persistent Atrial Fibrillation”. In: *Circulation* 130.7 (Aug. 2014), pp. 530–538. ISSN: 0009-7322, 1524-4539.

[134] M. A. Allessie, F. I. Bonke, and F. J. Schopman. “Circus movement in rabbit atrial muscle as a mechanism of tachycardia. III. The ”leading circle” concept: a new model of circus movement in cardiac tissue without the involvement of an anatomical obstacle”. eng. In: *Circulation Research* 41.1 (July 1977), pp. 9–18. ISSN: 0009-7330.

[135] Miguel Vaquero, David Calvo, and José Jalife. “Cardiac fibrillation: from ion channels to rotors in the human heart”. In: *Heart Rhythm* 5.6 (June 2008), pp. 872–879. ISSN: 1556-3871.

[136] Ravi Mandapati et al. “Stable Microreentrant Sources as a Mechanism of Atrial Fibrillation in the Isolated Sheep Heart”. In: *Circulation* 101.2 (Jan. 2000), pp. 194–199.

[137] G. K. Moe and J. A. Abildskov. “Atrial fibrillation as a self-sustaining arrhythmia independent of focal discharge”. eng. In: *American Heart Journal* 58.1 (July 1959), pp. 59–70. ISSN: 0002-8703.

[138] G. K. Moe, W. C. Rheinboldt, and J. A. Abildskov. “A COMPUTER MODEL OF ATRIAL FIBRILLATION”. eng. In: *American Heart Journal* 67 (Feb. 1964), pp. 200–220. ISSN: 0002-8703.

[139] Ghassen Cheniti et al. “Atrial Fibrillation Mechanisms and Implications for Catheter Ablation”. In: *Frontiers in Physiology* 9 (Oct. 2018), p. 1458. ISSN: 1664-042X.

[140] Paolo Verdecchia, Fabio Angeli, and Gianpaolo Reboldi. “Hypertension and Atrial Fibrillation: Doubts and Certainties From Basic and Clinical Studies”. In: *Circulation Research* 122.2 (Jan. 2018), pp. 352–368. ISSN: 0009-7330, 1524-4571.

[141] Elad Anter, Mariell Jessup, and David J. Callans. “Atrial fibrillation and heart failure: treatment considerations for a dual epidemic”. eng. In: *Circulation* 119.18 (May 2009), pp. 2516–2525. ISSN: 1524-4539.

[142] Ewelina Michniewicz et al. “Patients with atrial fibrillation and coronary artery disease - Double trouble”. In: *Advances in Medical Sciences* 63.1 (Mar. 2018), pp. 30–35. ISSN: 1898-4002.

[143] Jannik L. Pallisgaard et al. “Risk of atrial fibrillation in diabetes mellitus: A nationwide cohort study”. In: *European Journal of Preventive Cardiology* 23.6 (Apr. 2016), pp. 621–627. ISSN: 2047-4881.

[144] Mohammad-Reza Movahed, Mehrtash Hashemzadeh, and M. Mazen Jamal. “Diabetes mellitus is a strong, independent risk for atrial fibrillation and flutter in addition to other cardiovascular disease”. In: *International Journal of Cardiology* 105.3 (Dec. 2005), pp. 315–318. ISSN: 0167-5273.

[145] Dominik Linz et al. “Assessment and interpretation of sleep disordered breathing severity in cardiology: Clinical implications and perspectives”. In: *International Journal of Cardiology* 271 (Nov. 2018), pp. 281–288. ISSN: 1874-1754.

[146] Apoor S. Gami et al. “Association of atrial fibrillation and obstructive sleep apnea”. In: *Circulation* 110.4 (July 2004), pp. 364–367. ISSN: 1524-4539.

[147] Rachel R. Huxley et al. “Physical activity, obesity, weight change, and risk of atrial fibrillation: the Atherosclerosis Risk in Communities study”. In: *Circulation. Arrhythmia and Electrophysiology* 7.4 (Aug. 2014), pp. 620–625. ISSN: 1941-3084.

[148] Yong-Soo Baek et al. “Associations of Abdominal Obesity and New-Onset Atrial Fibrillation in the General Population”. In: *Journal of the American Heart Association* 6.6 (Nov. 2017), e004705. ISSN: 2047-9980.

[149] Kenneth J. Mukamal et al. “Alcohol consumption and risk of atrial fibrillation in men and women: the Copenhagen City Heart Study”. In: *Circulation* 112.12 (Sept. 2005), pp. 1736–1742. ISSN: 1524-4539.

[150] Yan Liang et al. “Alcohol consumption and the risk of incident atrial fibrillation among people with cardiovascular disease”. In: *Canadian Medical Association Journal* 184.16 (Nov. 2012), E857–E866. ISSN: 0820-3946, 1488-2329.

[151] Jens Rokkedal Nielsen, Kristian Wachtell, and Jawdat Abdulla. “The Relationship Between Physical Activity and Risk of Atrial Fibrillation-A Systematic Review and Meta-Analysis”. In: *Journal of Atrial Fibrillation* 5.5 (2013), p. 789. ISSN: 1941-6911.

[152] Jay Chen, Stephen L. Wasmund, and Mohamed H. Hamdan. “Back to the Future: The Role of the Autonomic Nervous System in Atrial Fibrillation”. en. In: *Pacing and Clinical Electrophysiology* 29.4 (Apr. 2006), pp. 413–421. ISSN: 0147-8389, 1540-8159.

[153] Peng-Sheng Chen et al. “Role of the Autonomic Nervous System in Atrial Fibrillation”. In: *Circulation Research* 114.9 (Apr. 2014), pp. 1500–1515.

[154] Ching-Tai Tai. “Role of Autonomic Influences in the Initiation and Perpetuation of Focal Atrial Fibrillation”. In: *Journal of Cardiovascular Electrophysiology* 12.3 (Mar. 2001), pp. 292–293. ISSN: 1045-3873, 1540-8167.

[155] P. Coumel. “Paroxysmal Atrial Fibrillation: a Disorder of Autonomic Tone?” In: *European Heart Journal* 15 Suppl A (Apr. 1994), pp. 9–16. ISSN: 0195-668X.

[156] J. A. Armour, G. R. Hageman, and W. C. Randall. “Arrhythmias induced by local cardiac nerve stimulation”. eng. In: *The American Journal of Physiology* 223.5 (Nov. 1972), pp. 1068–1075. ISSN: 0002-9513.

[157] Masamichi Hirose et al. “Partial vagal denervation increases vulnerability to vagally induced atrial fibrillation”. In: *Journal of Cardiovascular Electrophysiology* 13.12 (Dec. 2002), pp. 1272–1279. ISSN: 1045-3873.

[158] H. P. Brunner-La Rocca et al. “Effect of cardiac sympathetic nervous activity on mode of death in congestive heart failure”. In: *European Heart Journal* 22.13 (July 2001), pp. 1136–1143. ISSN: 0195-668X.

[159] Eugene Patterson et al. “Triggered firing in pulmonary veins initiated by in vitro autonomic nerve stimulation”. In: *Heart Rhythm* 2.6 (June 2005), pp. 624–631. ISSN: 1547-5271.

[160] J. A. Sánchez-Chapula et al. “Blockade of currents by the antimalarial drug chloroquine in feline ventricular myocytes”. In: *The Journal of Pharmacology and Experimental Therapeutics* 297.1 (Apr. 2001), pp. 437–445. ISSN: 0022-3565.

[161] Kazuki Iso et al. “Is Vagal Response During Left Atrial Ganglionated Plexi Stimulation a Normal Phenomenon?” In: *Circulation: Arrhythmia and Electrophysiology* 12.10 (Oct. 2019), e007281.

[162] Yuan Zhang et al. “Comparison of atrial fibrillation inducibility by electrical stimulation of either the extrinsic or the intrinsic autonomic nervous systems”. In: *Journal of Interventional Cardiac Electrophysiology: An International Journal of Arrhythmias and Pacing* 24.1 (Jan. 2009), pp. 5–10. ISSN: 1383-875X.

[163] Mark J. Shen et al. “Neural mechanisms of atrial arrhythmias”. In: *Nature Reviews. Cardiology* 9.1 (Sept. 2011), pp. 30–39. ISSN: 1759-5010.

[164] Shailesh Male and Benjamin J. Scherlag. “Role of neural modulation in the pathophysiology of atrial fibrillation”. In: *The Indian Journal of Medical Research* 139.4 (Apr. 2014), pp. 512–522. ISSN: 0975-9174.

[165] Yinglong Hou et al. “Ganglionated Plexi Modulate Extrinsic Cardiac Autonomic Nerve Input”. In: *Journal of the American College of Cardiology* 50.1 (July 2007), pp. 61–68. ISSN: 07351097.

[166] L. Liu and S. Nattel. “Differing sympathetic and vagal effects on atrial fibrillation in dogs: role of refractoriness heterogeneity”. In: *The American Journal of Physiology* 273.2 Pt 2 (Aug. 1997), H805–816. ISSN: 0002-9513.

[167] Jun Mao et al. “Ablation of epicardial ganglionated plexi increases atrial vulnerability to arrhythmias in dogs”. In: *Circulation. Arrhythmia and Electrophysiology* 7.4 (Aug. 2014), pp. 711–717. ISSN: 1941-3084.

[168] Jing Zhou et al. “Gradients of Atrial Refractoriness and Inducibility of Atrial Fibrillation due to Stimulation of Ganglionated Plexi”. In: *Journal of Cardiovascular Electrophysiology* 18.1 (Jan. 2007), pp. 83–90. ISSN: 1540-8167.

[169] Stephan Rohr, Jan P. Kucera, and André G. Kléber. “Slow Conduction in Cardiac Tissue, I: Effects of a Reduction of Excitability Versus a Reduction of Electrical Coupling on Microconduction”. In: *Circulation Research* 83.8 (Oct. 1998), pp. 781–794. ISSN: 0009-7330, 1524-4571.

[170] S. Nattel, D. Li, and L. Yue. “Basic Mechanisms of Atrial Fibrillation—Very New Insights into Very Old Ideas”. In: *Annual Review of Physiology* 62.1 (Mar. 2000), pp. 51–77. ISSN: 0066-4278, 1545-1585.

[171] Sana M. Al-Khatib et al. “Rate- and rhythm-control therapies in patients with atrial fibrillation: a systematic review”. In: *Annals of Internal Medicine* 160.11 (June 2014), pp. 760–773. ISSN: 1539-3704.

[172] E. Kevin Heist, Moussa Mansour, and Jeremy N. Ruskin. “Rate control in atrial fibrillation: targets, methods, resynchronization considerations”. In: *Circulation* 124.24 (Dec. 2011), pp. 2746–2755. ISSN: 1524-4539.

[173] T. Nikolaidou and K. S. Channer. “Chronic atrial fibrillation: a systematic review of medical heart rate control management”. In: *Postgraduate Medical Journal* 85.1004 (June 2009), pp. 303–312. ISSN: 1469-0756.

[174] Zachary D. Goldberger and G. Caleb Alexander. “Digitalis use in contemporary clinical practice: refitting the foxglove”. In: *JAMA internal medicine* 174.1 (Jan. 2014), pp. 151–154. ISSN: 2168-6114.

[175] Leonardo J. Tamariz and Eric B. Bass. “Pharmacological rate control of atrial fibrillation”. In: *Cardiology Clinics* 22.1 (Feb. 2004), pp. 35–45. ISSN: 0733-8651.

[176] J. B. Segal et al. “The evidence regarding the drugs used for ventricular rate control”. In: *The Journal of Family Practice* 49.1 (Jan. 2000), pp. 47–59. ISSN: 0094-3509.

[177] Kang-Teng Lim et al. “Ablate and pace strategy for atrial fibrillation: long-term outcome of AIRCRAFT trial”. In: *Europace: European Pacing, Arrhythmias, and Cardiac Electrophysiology: Journal of the Working Groups on Cardiac Pacing, Arrhythmias, and Cardiac Cellular Electrophysiology of the European Society of Cardiology* 9.7 (July 2007), pp. 498–505. ISSN: 1099-5129.

[178] M. A. Wood et al. “Clinical outcomes after ablation and pacing therapy for atrial fibrillation : a meta-analysis”. In: *Circulation* 101.10 (Mar. 2000), pp. 1138–1144. ISSN: 1524-4539.

[179] Paulus Kirchhof et al. “Anterior-posterior versus anterior-lateral electrode positions for external cardioversion of atrial fibrillation: a randomised trial”. In: *Lancet (London, England)* 360.9342 (Oct. 2002), pp. 1275–1279. ISSN: 0140-6736.

[180] S. Mittal et al. “Transthoracic cardioversion of atrial fibrillation: comparison of rectilinear biphasic versus damped sine wave monophasic shocks”. In: *Circulation* 101.11 (Mar. 2000), pp. 1282–1287. ISSN: 1524-4539.

[181] Elena Arbelo et al. “The atrial fibrillation ablation pilot study: a European Survey on Methodology and results of catheter ablation for atrial fibrillation conducted by

the European Heart Rhythm Association". In: *European Heart Journal* 35.22 (June 2014), pp. 1466–1478. ISSN: 1522-9645.

[182] Hugh Calkins et al. "2012 HRS/EHRA/ECAS expert consensus statement on catheter and surgical ablation of atrial fibrillation: recommendations for patient selection, procedural techniques, patient management and follow-up, definitions, endpoints, and research trial design". In: *Journal of Interventional Cardiac Electrophysiology: An International Journal of Arrhythmias and Pacing* 33.2 (Mar. 2012), pp. 171–257. ISSN: 1572-8595.

[183] J. L. Cox et al. "Successful surgical treatment of atrial fibrillation. Review and clinical update". In: *JAMA* 266.14 (Oct. 1991), pp. 1976–1980. ISSN: 0098-7484.

[184] C. Lafuente-Lafuente et al. "Antiarrhythmics for maintaining sinus rhythm after cardioversion of atrial fibrillation". In: *The Cochrane Database of Systematic Reviews* 4 (Oct. 2007), p. CD005049. ISSN: 1469-493X.

[185] Ijaz A. Khan. "Oral loading single dose flecainide for pharmacological cardioversion of recent-onset atrial fibrillation". In: *International Journal of Cardiology* 87.2-3 (Feb. 2003), pp. 121–128. ISSN: 0167-5273.

[186] I. A. Khan. "Single oral loading dose of propafenone for pharmacological cardioversion of recent-onset atrial fibrillation". In: *Journal of the American College of Cardiology* 37.2 (Feb. 2001), pp. 542–547. ISSN: 0735-1097.

[187] Denis Roy et al. "Vernakalant hydrochloride for rapid conversion of atrial fibrillation: a phase 3, randomized, placebo-controlled trial". In: *Circulation* 117.12 (Mar. 2008), pp. 1518–1525. ISSN: 1524-4539.

[188] Luz M. Letelier et al. "Effectiveness of amiodarone for conversion of atrial fibrillation to sinus rhythm: a meta-analysis". In: *Archives of Internal Medicine* 163.7 (Apr. 2003), pp. 777–785. ISSN: 0003-9926.

[189] José Francisco Secorun Inácio et al. "Monophasic and biphasic shock for transthoracic conversion of atrial fibrillation: Systematic review and network meta-analysis". In: *Resuscitation* 100 (Mar. 2016), pp. 66–75. ISSN: 1873-1570.

[190] Lucie Valembois et al. “Antiarrhythmics for maintaining sinus rhythm after cardioversion of atrial fibrillation”. In: *The Cochrane Database of Systematic Reviews* 9.9 (Sept. 2019), p. CD005049. ISSN: 1469-493X.

[191] Jens Cosedis Nielsen et al. “Long-term efficacy of catheter ablation as first-line therapy for paroxysmal atrial fibrillation: 5-year outcome in a randomised clinical trial”. In: *Heart (British Cardiac Society)* 103.5 (Mar. 2017), pp. 368–376. ISSN: 1468-201X.

[192] Luigi Di Biase et al. “Ablation Versus Amiodarone for Treatment of Persistent Atrial Fibrillation in Patients With Congestive Heart Failure and an Implanted Device: Results From the AATAC Multicenter Randomized Trial”. In: *Circulation* 133.17 (Apr. 2016), pp. 1637–1644. ISSN: 1524-4539.

[193] Renato De Vecchis. “Is an elevated burden of antiarrhythmic drug (AAD) side-effects the unavoidable price to be traded for a durable suppression of AF relapses in ablated patients? The weaknesses and risks of the AAD suppression algorithm used by current models of AF secondary prevention after catheter ablation”. In: *European Journal of Clinical Pharmacology* 75.6 (June 2019), pp. 873–874. ISSN: 1432-1041.

[194] D. J. MacNeil. “The side effect profile of class III antiarrhythmic drugs: focus on d,l-sotalol”. In: *The American Journal of Cardiology* 80.8A (Oct. 1997), 90G–98G. ISSN: 0002-9149.

[195] Paulus Kirchhof et al. “Short-term versus long-term antiarrhythmic drug treatment after cardioversion of atrial fibrillation (Flec-SL): a prospective, randomised, open-label, blinded endpoint assessment trial”. In: *Lancet (London, England)* 380.9838 (July 2012), pp. 238–246. ISSN: 1474-547X.

[196] James Kneller et al. “Cholinergic Atrial Fibrillation in a Computer Model of a Two-Dimensional Sheet of Canine Atrial Cells With Realistic Ionic Properties”. en. In: *Circulation Research* 90.9 (May 2002). ISSN: 0009-7330, 1524-4571.

[197] Sandeep V. Pandit and José Jalife. “Rotors and the dynamics of cardiac fibrillation”. In: *Circulation Research* 112.5 (Mar. 2013), pp. 849–862. ISSN: 1524-4571.

[198] Sandeep V. Pandit et al. “Ionic determinants of functional reentry in a 2-D model of human atrial cells during simulated chronic atrial fibrillation”. In: *Biophysical Journal* 88.6 (June 2005), pp. 3806–3821. ISSN: 0006-3495.

[199] David G. Jones et al. “A randomized trial to assess catheter ablation versus rate control in the management of persistent atrial fibrillation in heart failure”. In: *Journal of the American College of Cardiology* 61.18 (May 2013), pp. 1894–1903. ISSN: 1558-3597.

[200] J. L. Cox et al. “The surgical treatment of atrial fibrillation. II. Intraoperative electrophysiologic mapping and description of the electrophysiologic basis of atrial flutter and atrial fibrillation”. In: *The Journal of Thoracic and Cardiovascular Surgery* 101.3 (Mar. 1991), pp. 406–426. ISSN: 0022-5223.

[201] T. M. Sundt, C. J. Camillo, and J. L. Cox. “The maze procedure for cure of atrial fibrillation”. In: *Cardiology Clinics* 15.4 (Nov. 1997), pp. 739–748. ISSN: 0733-8651.

[202] M. Haïssaguerre et al. “Spontaneous initiation of atrial fibrillation by ectopic beats originating in the pulmonary veins”. In: *The New England Journal of Medicine* 339.10 (Sept. 1998), pp. 659–666. ISSN: 0028-4793.

[203] Karl-Heinz Kuck et al. “Impact of Complete Versus Incomplete Circumferential Lines Around the Pulmonary Veins During Catheter Ablation of Paroxysmal Atrial Fibrillation: Results From the Gap-Atrial Fibrillation-German Atrial Fibrillation Competence Network 1 Trial”. In: *Circulation. Arrhythmia and Electrophysiology* 9.1 (Jan. 2016), e003337. ISSN: 1941-3084.

[204] Alexander Fürnkranz et al. “Rationale and Design of FIRE AND ICE: A multicenter randomized trial comparing efficacy and safety of pulmonary vein isolation using a cryoballoon versus radiofrequency ablation with 3D-reconstruction”. In: *Journal of Cardiovascular Electrophysiology* 25.12 (Dec. 2014), pp. 1314–1320. ISSN: 1540-8167.

[205] D. E. Haines. “The biophysics of radiofrequency catheter ablation in the heart: the importance of temperature monitoring”. In: *Pacing and clinical electrophysiology: PACE* 16.3 Pt 2 (Mar. 1993), pp. 586–591. ISSN: 0147-8389.

[206] Katsuaki Yokoyama et al. “Novel contact force sensor incorporated in irrigated radiofrequency ablation catheter predicts lesion size and incidence of steam pop and thrombus”. In: *Circulation. Arrhythmia and Electrophysiology* 1.5 (Dec. 2008), pp. 354–362. ISSN: 1941-3084.

[207] Andrea Natale et al. “Paroxysmal AF catheter ablation with a contact force sensing catheter: results of the prospective, multicenter SMART-AF trial”. In: *Journal of the American College of Cardiology* 64.7 (Aug. 2014), pp. 647–656. ISSN: 1558-3597.

[208] Karl-Heinz Kuck et al. “A novel radiofrequency ablation catheter using contact force sensing: Toccata study”. In: *Heart Rhythm* 9.1 (Jan. 2012), pp. 18–23. ISSN: 1556-3871.

[209] Roberto De Ponti. “Cryothermal energy ablation of cardiac arrhythmias 2005: state of the art”. In: *Indian Pacing and Electrophysiology Journal* 5.1 (Jan. 2005), pp. 12–24. ISSN: 0972-6292.

[210] Armin Luik et al. “Cryoballoon Versus Open Irrigated Radiofrequency Ablation in Patients With Paroxysmal Atrial Fibrillation: The Prospective, Randomized, Controlled, Noninferiority FreezeAF Study”. In: *Circulation* 132.14 (Oct. 2015), pp. 1311–1319. ISSN: 1524-4539.

[211] Martin Schmidt et al. “Cryoballoon versus RF ablation in paroxysmal atrial fibrillation: results from the German Ablation Registry”. In: *Journal of Cardiovascular Electrophysiology* 25.1 (Jan. 2014), pp. 1–7. ISSN: 1540-8167.

[212] Douglas L. Packer et al. “Cryoballoon ablation of pulmonary veins for paroxysmal atrial fibrillation: first results of the North American Arctic Front (STOP AF) pivotal trial”. In: *Journal of the American College of Cardiology* 61.16 (Apr. 2013), pp. 1713–1723. ISSN: 1558-3597.

[213] Karl-Heinz Kuck et al. “Cryoballoon or radiofrequency ablation for symptomatic paroxysmal atrial fibrillation: reintervention, rehospitalization, and quality-of-life outcomes in the FIRE AND ICE trial”. In: *European Heart Journal* 37.38 (Oct. 2016), pp. 2858–2865. ISSN: 0195-668X, 1522-9645.

[214] J. J. Gallagher et al. “Catheter technique for closed-chest ablation of the atrioventricular conduction system”. In: *The New England Journal of Medicine* 306.4 (Jan. 1982), pp. 194–200. ISSN: 0028-4793.

[215] Vivek Y. Reddy et al. “Pulsed Field Ablation for Pulmonary Vein Isolation in Atrial Fibrillation”. In: *Journal of the American College of Cardiology* 74.3 (July 2019), pp. 315–326. ISSN: 1558-3597.

[216] Peter Loh et al. “Pulmonary Vein Isolation With Single Pulse Irreversible Electroporation: A First in Human Study in 10 Patients With Atrial Fibrillation”. In: *Circulation: Arrhythmia and Electrophysiology* 13.10 (Oct. 2020). ISSN: 1941-3149, 1941-3084.

[217] Vivek Y. Reddy et al. “Ablation of Atrial Fibrillation With Pulsed Electric Fields”. In: *JACC: Clinical Electrophysiology* 4.8 (Aug. 2018), pp. 987–995. ISSN: 2405500X.

[218] Atul Verma et al. “Approaches to catheter ablation for persistent atrial fibrillation”. In: *The New England Journal of Medicine* 372.19 (May 2015), pp. 1812–1822. ISSN: 1533-4406.

[219] Axel Bauer et al. “Effects of circumferential or segmental pulmonary vein ablation for paroxysmal atrial fibrillation on cardiac autonomic function”. In: *Heart Rhythm* 3.12 (Dec. 2006), pp. 1428–1435. ISSN: 1547-5271.

[220] Carlo Pappone et al. “Pulmonary Vein Denervation Enhances Long-Term Benefit After Circumferential Ablation for Paroxysmal Atrial Fibrillation”. en. In: *Circulation* 109.3 (Jan. 2004), pp. 327–334. ISSN: 0009-7322, 1524-4539.

[221] Benjamin J. Scherlag et al. “Electrical Stimulation to Identify Neural Elements on the Heart: Their Role in Atrial Fibrillation”. en. In: *Journal of Interventional*

Cardiac Electrophysiology 13.S1 (Aug. 2005), pp. 37–42. ISSN: 1383-875X, 1572-8595.

[222] Demosthenes G. Katritsis et al. “Rapid pulmonary vein isolation combined with autonomic ganglia modification: a randomized study”. In: *Heart Rhythm* 8.5 (May 2011), pp. 672–678. ISSN: 1556-3871.

[223] Seongwook Han et al. “Electrophysiological Characteristics of the Marshall Bundle in Humans”. In: *Heart Rhythm* 7.6 (June 2010), pp. 786–793. ISSN: 1556-3871.

[224] Evgeny Mikhaylov et al. “Outcome of Anatomic Ganglionated Plexi Ablation to Treat Paroxysmal Atrial Fibrillation: a 3-Year Follow-Up Study”. In: *Europace: European Pacing, Arrhythmias, and Cardiac Electrophysiology: Journal of the Working Groups on Cardiac Pacing, Arrhythmias, and Cardiac Cellular Electrophysiology of the European Society of Cardiology* 13.3 (Mar. 2011), pp. 362–370. ISSN: 1532-2092.

[225] Mao Jun et al. “Ablation of Epicardial Ganglionated Plexi Increases Atrial Vulnerability to Arrhythmias in Dogs”. In: *Circulation: Arrhythmia and Electrophysiology* 7.4 (Aug. 2014), pp. 711–717.

[226] Kimie Ohkubo et al. “Combined effect of pulmonary vein isolation and ablation of cardiac autonomic nerves for atrial fibrillation”. In: *International Heart Journal* 49.6 (Nov. 2008), pp. 661–670. ISSN: 1349-2365.

[227] Demosthenes G. Katritsis et al. “Autonomic Denervation Added to Pulmonary Vein Isolation for Paroxysmal Atrial Fibrillation”. en. In: *Journal of the American College of Cardiology* 62.24 (Dec. 2013), pp. 2318–2325. ISSN: 07351097.

[228] Qina Zhou, Yuemei Hou, and Shanglei Yang. “A Meta-Analysis of the Comparative Efficacy of Ablation for Atrial Fibrillation with and without Ablation of the Ganglionated Plexi”. In: *Pacing and Clinical Electrophysiology* 34.12 (2011), pp. 1687–1694. ISSN: 1540-8159.

[229] Jiaxiong Lin et al. “Autonomic Mechanism to Explain Complex Fractionated Atrial Electrograms (CFAE)”. In: *Journal of Cardiovascular Electrophysiology* 18.11 (Nov. 2007), pp. 1197–1205. ISSN: 1540-8167.

[230] Jiaxiong Lin et al. “Inducibility of Atrial and Ventricular Arrhythmias Along the Ligament of Marshall: Role of Autonomic Factors”. In: *Journal of Cardiovascular Electrophysiology* 19.9 (Sept. 2008), pp. 955–962. ISSN: 1540-8167.

[231] Evgeny Pokushalov et al. “Left Atrial Ablation at the Anatomic Areas of Ganglionated Plexi for Paroxysmal Atrial Fibrillation: LEFT ATRIAL ABLATION OF GANGLIONATED PLEXI”. en. In: *Pacing and Clinical Electrophysiology* 33.10 (June 2010), pp. 1231–1238. ISSN: 01478389.

[232] Carlos A. Morillo et al. “Radiofrequency ablation vs antiarrhythmic drugs as first-line treatment of paroxysmal atrial fibrillation (RAAFT-2): a randomized trial”. In: *JAMA* 311.7 (Feb. 2014), pp. 692–700. ISSN: 1538-3598.

[233] Pierre Jaïs et al. “Catheter ablation versus antiarrhythmic drugs for atrial fibrillation: the A4 study”. In: *Circulation* 118.24 (Dec. 2008), pp. 2498–2505. ISSN: 1524-4539.

[234] Carlo Pappone et al. “A randomized trial of circumferential pulmonary vein ablation versus antiarrhythmic drug therapy in paroxysmal atrial fibrillation: the APAF Study”. In: *Journal of the American College of Cardiology* 48.11 (Dec. 2006), pp. 2340–2347. ISSN: 1558-3597.

[235] Jens Cosedis Nielsen et al. “Radiofrequency Ablation as Initial Therapy in Paroxysmal Atrial Fibrillation”. In: *New England Journal of Medicine* 367.17 (Oct. 2012), pp. 1587–1595. ISSN: 0028-4793, 1533-4406.

[236] Oussama M. Wazni et al. “Radiofrequency ablation vs antiarrhythmic drugs as first-line treatment of symptomatic atrial fibrillation: a randomized trial”. In: *JAMA* 293.21 (June 2005), pp. 2634–2640. ISSN: 1538-3598.

[237] Evgeny Pokushalov et al. “Progression of atrial fibrillation after a failed initial ablation procedure in patients with paroxysmal atrial fibrillation: a randomized comparison of drug therapy versus reablation”. In: *Circulation. Arrhythmia and Electrophysiology* 6.4 (Aug. 2013), pp. 754–760. ISSN: 1941-3084.

[238] David J. Wilber et al. “Comparison of antiarrhythmic drug therapy and radiofrequency catheter ablation in patients with paroxysmal atrial fibrillation: a randomized controlled trial”. In: *JAMA* 303.4 (Jan. 2010), pp. 333–340. ISSN: 1538-3598.

[239] Joachim R. Ehrlich and Stanley Nattel. “Novel approaches for pharmacological management of atrial fibrillation”. In: *Drugs* 69.7 (2009), pp. 757–774. ISSN: 0012-6667.

[240] Anand N. Ganesan et al. “Long-term outcomes of catheter ablation of atrial fibrillation: a systematic review and meta-analysis”. In: *Journal of the American Heart Association* 2.2 (Mar. 2013), e004549. ISSN: 2047-9980.

[241] A. L. Hodgkin and A. F. Huxley. “A quantitative description of membrane current and its application to conduction and excitation in nerve”. In: *The Journal of Physiology* 117.4 (Aug. 1952), pp. 500–544. ISSN: 0022-3751.

[242] David Adolfo Sampedro Puente. “Theoretical analysis of autonomic nervous system effects on cardiac electrophysiology and its relationship with arrhythmic risk”. PhD thesis. Universidad de Zaragoza, 2020.

[243] Richard B. Colquitt, Douglas A. Colquhoun, and Robert H. Thiele. “In silico modelling of physiologic systems”. In: *Best Practice & Research. Clinical Anaesthesiology* 25.4 (Dec. 2011), pp. 499–510. ISSN: 1521-6896.

[244] Marc Courtemanche, Rafael J. Ramirez, and Stanley Nattel. “Ionic mechanisms underlying human atrial action potential properties: insights from a mathematical model”. In: *American Journal of Physiology-Heart and Circulatory Physiology* 275.1 (July 1998), H301–H321. ISSN: 0363-6135, 1522-1539.

[245] A. Nygren et al. "Mathematical Model of an Adult Human Atrial Cell: The Role of K^+ Currents in Repolarization". In: *Circulation Research* 82.1 (Jan. 1998), pp. 63–81. ISSN: 0009-7330, 1524-4571.

[246] Mathias Wilhelms et al. "Benchmarking Electrophysiological Models of Human Atrial Myocytes". In: *Frontiers in Physiology* 3 (2012), p. 487. ISSN: 1664-042X.

[247] Mary M. Maleckar et al. "Mathematical simulations of ligand-gated and cell-type specific effects on the action potential of human atrium". In: *Progress in Biophysics and Molecular Biology* 98.2-3 (2008), pp. 161–170. ISSN: 0079-6107.

[248] Jussi T. Koivumäki, Topi Korhonen, and Pasi Tavi. "Impact of Sarcoplasmic Reticulum Calcium Release on Calcium Dynamics and Action Potential Morphology in Human Atrial Myocytes: A Computational Study". In: *PLOS Computational Biology* 7.1 (2011), e1001067. ISSN: 1553-7358.

[249] Lasse Skibsbye et al. "Refractoriness in Human Atria: Time and Voltage Dependence of Sodium Channel Availability". en. In: *Journal of Molecular and Cellular Cardiology* 101 (Dec. 2016), pp. 26–34. ISSN: 00222828.

[250] Márcia Vagos et al. "Computational Modeling of Electrophysiology and Pharmacotherapy of Atrial Fibrillation: Recent Advances and Future Challenges". In: *Frontiers in Physiology* 9 (2018). ISSN: 1664-042X.

[251] Jordi Heijman et al. "Computational models of atrial cellular electrophysiology and calcium handling, and their role in atrial fibrillation". In: *The Journal of Physiology* 594.3 (Feb. 2016), pp. 537–553. ISSN: 1469-7793.

[252] C. H. Luo and Y. Rudy. "A dynamic model of the cardiac ventricular action potential. I. Simulations of ionic currents and concentration changes". In: *Circulation Research* 74.6 (June 1994), pp. 1071–1096. ISSN: 0009-7330.

[253] Lixia Yue et al. "Ionic Remodeling Underlying Action Potential Changes in a Canine Model of Atrial Fibrillation". In: *Circulation Research* 81.4 (Oct. 1997), pp. 512–525. ISSN: 0009-7330, 1524-4571.

[254] Jutta Engel, Howard A. Schultens, and Detlev Schild. “Small Conductance Potassium Channels Cause an Activity-Dependent Spike Frequency Adaptation and Make the Transfer Function of Neurons Logarithmic”. en. In: *Biophysical Journal* 76.3 (Mar. 1999), pp. 1310–1319. ISSN: 00063495.

[255] Chia-Hsiang Hsueh et al. “Proarrhythmic Effect of Blocking the Small Conductance Calcium Activated Potassium Channel in Isolated Canine Left Atrium”. In: *Heart Rhythm* 10.6 (June 2013), pp. 891–898. ISSN: 1556-3871.

[256] Chiara Celotto et al. “Calcium-Activated Potassium Channel Inhibition in Autonomically Stimulated Human Atrial Myocytes”. In: vol. 46. Dec. 2019, pp. 1–4.

[257] Zsófia Kohajda et al. “In Vivo and Cellular Antiarrhythmic and Cardiac Electrophysiological Effects of Desethylamiodarone in Dog Cardiac Preparations”. In: *British Journal of Pharmacology* 179.13 (July 2022), pp. 3382–3402. ISSN: 1476-5381.

[258] Jason D. Bayer et al. “Acetylcholine Delays Atrial Activation to Facilitate Atrial Fibrillation”. In: *Frontiers in Physiology* 10 (Sept. 2019), p. 1105. ISSN: 1664-042X.

[259] Marta González de la Fuente et al. “Chronic Atrial Fibrillation Up-Regulates β1-Adrenoceptors Affecting Repolarizing Currents and Action Potential Duration”. In: *Cardiovascular Research* 97.2 (Feb. 2013), pp. 379–388. ISSN: 0008-6363.

[260] Eleonora Grandi, Francesco S. Pasqualini, and Donald M. Bers. “A novel computational model of the human ventricular action potential and Ca transient”. In: *Journal of Molecular and Cellular Cardiology* 48.1 (Jan. 2010), pp. 112–121. ISSN: 1095-8584.

[261] Thomas R. Shannon et al. “A mathematical treatment of integrated Ca dynamics within the ventricular myocyte”. In: *Biophysical Journal* 87.5 (Nov. 2004), pp. 3351–3371. ISSN: 0006-3495.

[262] Angelina Peñaranda et al. “Effects of Small Conductance Calcium Activated Potassium Channels in Cardiac Myocytes”. In: Sept. 2017.

[263] Niels Voigt et al. “Impaired Na-Dependent Regulation of Acetylcholine-Activated Inward-Rectifier K Current Modulates Action Potential Rate Dependence in Patients with Chronic Atrial Fibrillation”. In: *Journal of Molecular and Cellular Cardiology* 61 (Aug. 2013), pp. 142–152. ISSN: 1095-8584.

[264] S Koumi et al. “Alterations in Muscarinic K+ Channel Response to Acetylcholine and to G Protein-Mediated Activation in Atrial Myocytes Isolated from Failing Human Hearts”. In: *Circulation* 90.5 (Nov. 1994), pp. 2213–2224.

[265] Thomas R. Shannon, Fei Wang, and Donald M. Bers. “Regulation of Cardiac Sarcoplasmic Reticulum Ca Release by Luminal [Ca] and Altered Gating Assessed with a Mathematical Model”. In: *Biophysical Journal* 89.6 (Dec. 2005), pp. 4096–4110. ISSN: 0006-3495.

[266] Jussi T. Koivumäki et al. “In Silico Screening of the Key Cellular Remodeling Targets in Chronic Atrial Fibrillation”. In: *PLoS Computational Biology* 10.5 (May 2014). Ed. by Andrew D. McCulloch, e1003620. ISSN: 1553-7358.

[267] B. Hirschberg et al. “Gating of recombinant small-conductance Ca-activated K+ channels by calcium”. In: *The Journal of General Physiology* 111.4 (Apr. 1998), pp. 565–581. ISSN: 0022-1295.

[268] Chuyi Tang et al. “Biophysical characterization of inwardly rectifying potassium currents (I(K1) I(K,ACh), I(K,Ca)) using sinus rhythm or atrial fibrillation action potential waveforms”. In: *General Physiology and Biophysics* 34.4 (Oct. 2015), pp. 383–392. ISSN: 0231-5882.

[269] M Courtemanche. “Ionic targets for drug therapy and atrial fibrillation-induced electrical remodeling: insights from a mathematical model”. In: *Cardiovascular Research* 42.2 (May 1999), pp. 477–489. ISSN: 00086363.

[270] N Voigt et al. “Cellular and Molecular Determinants of Altered Atrial Ca2+ Signaling in Patients With Chronic Atrial Fibrillation”. In: *Circulation* Abstract 2630 (2009).

[271] Madison S. Spach et al. “Mechanism of origin of conduction disturbances in aging human atrial bundles: experimental and model study”. In: *Heart Rhythm* 4.2 (Feb. 2007), pp. 175–185. ISSN: 1547-5271.

[272] Marjorie Letitia Hubbard and Craig S. Henriquez. “A microstructural model of reentry arising from focal breakthrough at sites of source-load mismatch in a central region of slow conduction”. In: *American Journal of Physiology. Heart and Circulatory Physiology* 306.9 (May 2014), H1341–1352. ISSN: 1522-1539.

[273] Joyce Lin and James P. Keener. “Microdomain effects on transverse cardiac propagation”. In: *Biophysical Journal* 106.4 (Feb. 2014), pp. 925–931. ISSN: 1542-0086.

[274] Aslak Tveito et al. “A Cell-Based Framework for Numerical Modeling of Electrical Conduction in Cardiac Tissue”. In: *Frontiers in Physics* 5 (Oct. 2017), p. 48. ISSN: 2296-424X.

[275] S. H. Weinberg. “Ephaptic coupling rescues conduction failure in weakly coupled cardiac tissue with voltage-gated gap junctions”. In: *Chaos (Woodbury, N.Y.)* 27.9 (Sept. 2017), p. 093908. ISSN: 1089-7682.

[276] Karoline Horgmo Jæger et al. “Properties of cardiac conduction in a cell-based computational model”. In: *PLoS computational biology* 15.5 (May 2019), e1007042. ISSN: 1553-7358.

[277] Karoline Horgmo Jæger et al. “From Millimeters to Micrometers; Re-introducing Myocytes in Models of Cardiac Electrophysiology”. In: *Frontiers in Physiology* 12 (2021), p. 763584. ISSN: 1664-042X.

[278] Karoline Horgmo Jæger and Aslak Tveito. “Deriving the Bidomain Model of Cardiac Electrophysiology From a Cell-Based Model; Properties and Comparisons”. In: *Frontiers in Physiology* 12 (Jan. 2022), p. 811029. ISSN: 1664-042X.

[279] Mark Potse. “Integrated electrocardiographic mapping. Combined analysis of multichannel endocardial and body surface ECG data”. PhD thesis. Universiteit van Amsterdam, 2001.

[280] Carlos Sanchez Tapia. “Multiscale Analysis of Atrial Fibrillation Mechanisms”. PhD thesis. Universidad de Zaragoza, 2014.

[281] Jonathan P. Whiteley. “An efficient numerical technique for the solution of the monodomain and bidomain equations”. In: *IEEE transactions on bio-medical engineering* 53.11 (2006), pp. 2139–2147. ISSN: 0018-9294.

[282] Smaill Bruce H., Zhao Jichao, and Trew Mark L. “Three-Dimensional Impulse Propagation in Myocardium”. In: *Circulation Research* 112.5 (Mar. 2013), pp. 834–848.

[283] K.A. MacCannell et al. “A Mathematical Model of Electrotonic Interactions between Ventricular Myocytes and Fibroblasts”. en. In: *Biophysical Journal* 92.11 (June 2007), pp. 4121–4132. ISSN: 00063495.

[284] Kathleen S. McDowell et al. “Mechanistic Inquiry Into the Role of Tissue Remodeling in Fibrotic Lesions in Human Atrial Fibrillation”. In: *Biophysical Journal* 104.12 (June 2013), pp. 2764–2773. ISSN: 1542-0086.

[285] Ana Ferrer et al. “Detailed Anatomical and Electrophysiological Models of Human Atria and Torso for the Simulation of Atrial Activation”. In: *PloS One* 10.11 (2015), e0141573. ISSN: 1932-6203.

[286] R. Wesselink et al. “Does Left Atrial Epicardial Conduction Time Reflect Atrial Fibrosis and the Risk of Atrial Fibrillation Recurrence After Thoracoscopic Ablation? Post Hoc Analysis of the AFACT Trial”. In: *BMJ open* 12.3 (Mar. 2022), e056829. ISSN: 2044-6055.

[287] Konstantinos A Mountris and Esther Pueyo. “The Radial Point Interpolation Mixed Collocation Method for the Solution of Transient Diffusion Problems”. In: *Engineering Analysis with Boundary Elements* 121 (2020), pp. 207–216.

[288] Konstantinos A Mountris and Esther Pueyo. “Next-generation in silico cardiac electrophysiology through immersed grid meshfree modeling: application to simulation of myocardial infarction”. In: *2020 Computing in Cardiology*. IEEE. 2020, pp. 1–4.

[289] Konstantinos A Mountris et al. “Meshfree implementation of the cardiac monodomain model through the Fragile Points Method”. In: *methods* 11 (2021), p. 12.

[290] Elvio A. Heidenreich et al. “Adaptive Macro Finite Elements for the Numerical Solution of Monodomain Equations in Cardiac Electrophysiology”. In: *Annals of Biomedical Engineering* 38.7 (2010), pp. 2331–2345.

[291] K. A. Mountris and E. Pueyo. “A Dual Adaptive Explicit Time Integration Algorithm for Efficiently Solving the Cardiac Monodomain Equation”. In: *International Journal for Numerical Methods in Biomedical Engineering.* Under Review (2020a).

[292] Hung-Yu Chang et al. “Effect of Vagotomy on the Activity of Cardiac Autonomic Ganglia: Insight from Left Atrial High Density Frequency Mapping”. In: *International Journal of Cardiology* 220 (Oct. 2016), pp. 435–439. ISSN: 01675273.

[293] L. Sörnmo, ed. *Atrial Fibrillation from an Engineering Perspective, Series in Bioengineering*. Springer, 2018.

[294] Simona Petrutiu et al. “Atrial Fibrillation and Waveform Characterization. A Time Domain Perspective in the Surface ECG”. eng. In: *IEEE engineering in medicine and biology magazine: the quarterly magazine of the Engineering in Medicine & Biology Society* 25.6 (Dec. 2006), pp. 24–30. ISSN: 0739-5175.

[295] Marianna Meo et al. “Spatial Variability of the 12-Lead Surface ECG as a Tool for Noninvasive Prediction of Catheter Ablation Outcome in Persistent Atrial Fibrillation”. In: *IEEE transactions on bio-medical engineering* 60.1 (Jan. 2013), pp. 20–27. ISSN: 1558-2531.

[296] Theo A. R. Lankveld et al. “The ECG as a Tool to Determine Atrial Fibrillation Complexity”. In: *Heart (British Cardiac Society)* 100.14 (July 2014), pp. 1077–1084. ISSN: 1468-201X.

[297] L. Sörnmo et al. “Characterization of f waves”. In: *Atrial Fibrillation from an Engineering Perspective*. Ed. by L. Sörnmo. Springer, 2018. Chap. 6, pp. 221–280. DOI: `10.1007/978-3-319-68515-1\_6`.

[298] Sten Östenson et al. “Autonomic Influence on Atrial Fibrillatory Process: Head-Up and Head-Down Tilting”. In: *Annals of Noninvasive Electrocardiology: The Official Journal of the International Society for Holter and Noninvasive Electrocardiology, Inc* 22.2 (Mar. 2017). ISSN: 1542-474X.

[299] Junbeom Park et al. “Early differentiation of long-standing persistent atrial fibrillation using the characteristics of fibrillatory waves in surface ECG multi-leads”. In: *Scientific Reports* 9.1 (Feb. 2019), p. 2746. ISSN: 2045-2322.

[300] Mikael Henriksson et al. “Model-Based Assessment of f-Wave Signal Quality in Patients With Atrial Fibrillation”. In: *IEEE Transactions on Biomedical Engineering* 65.11 (Nov. 2018), pp. 2600–2611. ISSN: 0018-9294, 1558-2531.

[301] Mostafa Abdollahpur et al. “Respiratory Induced Modulation in f-Wave Characteristics During Atrial Fibrillation”. In: *Frontiers in Physiology* 12 (2021), p. 653492. ISSN: 1664-042X.

[302] Fumihiko Yasuma and Jun-Ichiro Hayano. “Respiratory Sinus Arrhythmia: why does the Heartbeat Synchronize with Respiratory Rhythm?” In: *Chest* 125.2 (Feb. 2004), pp. 683–690. ISSN: 0012-3692.

[303] Dwain L. Eckberg. “The human respiratory gate”. In: *The Journal of Physiology* 548.Pt 2 (Apr. 2003), pp. 339–352. ISSN: 0022-3751.

[304] J. A. Hirsch and B. Bishop. “Respiratory sinus arrhythmia in humans: how breathing pattern modulates heart rate”. In: *The American Journal of Physiology* 241.4 (Oct. 1981), H620–629. ISSN: 0002-9513.

[305] M. Piepoli et al. “Origin of respiratory sinus arrhythmia in conscious humans. An important role for arterial carotid baroreceptors”. In: *Circulation* 95.7 (Apr. 1997), pp. 1813–1821. ISSN: 0009-7322.

[306] P. G. Katona and F. Jih. “Respiratory sinus arrhythmia: noninvasive measure of parasympathetic cardiac control”. In: *Journal of Applied Physiology* 39.5 (Nov. 1975), pp. 801–805. ISSN: 0021-8987.

[307] D. L. Eckberg. “Human sinus arrhythmia as an index of vagal cardiac outflow”. In: *Journal of Applied Physiology: Respiratory, Environmental and Exercise Physiology* 54.4 (Apr. 1983), pp. 961–966. ISSN: 0161-7567.

[308] D. L. Kunze. “Reflex discharge patterns of cardiac vagal efferent fibres”. In: *The Journal of Physiology* 222.1 (Apr. 1972), pp. 1–15. ISSN: 0022-3751.

[309] Michela Masé, Leon Glass, and Flavia Ravelli. “A model for mechano-electrical feedback effects on atrial flutter interval variability”. In: *Bulletin of Mathematical Biology* 70.5 (July 2008), pp. 1326–1347. ISSN: 1522-9602.

[310] Fredrik Holmqvist et al. “Rapid Fluctuations in Atrial Fibrillatory Electrophysiology Detected During Controlled Respiration”. In: *American Journal of Physiology-Heart and Circulatory Physiology* 289.2 (Aug. 2005), H754–H760. ISSN: 0363-6135, 1522-1539.

[311] Flavia Ravelli, Michela Masè, and Marcello Disertori. “Mechanical modulation of atrial flutter cycle length”. In: *Progress in Biophysics and Molecular Biology* 97.2-3 (June 2008), pp. 417–434. ISSN: 00796107.

[312] Michela Masè, Marcello Disertori, and Flavia Ravelli. “Cardiorespiratory interactions in patients with atrial flutter”. In: *Journal of Applied Physiology (Bethesda, Md.: 1985)* 106.1 (Jan. 2009), pp. 29–39. ISSN: 8750-7587.

[313] Jin Ma, Qiuxiong Chen, and Shiyu Ma. “Left atrial fibrosis in atrial fibrillation: Mechanisms, clinical evaluation and management”. In: *Journal of Cellular and Molecular Medicine* 25.6 (Mar. 2021), pp. 2764–2775. ISSN: 1582-4934.

[314] M. Stridh and L. Sörnmo. “Spatiotemporal QRST cancellation techniques for analysis of atrial fibrillation”. In: *IEEE transactions on bio-medical engineering* 48.1 (Jan. 2001), pp. 105–111. ISSN: 0018-9294.

[315] Raquel Bailón et al. “A Robust Method for ECG-Based Estimation of the Respiratory Frequency during Stress Testing”. In: *IEEE transactions on bio-medical engineering* 53.7 (July 2006), pp. 1273–1285. ISSN: 0018-9294.

[316] Richard Gordan, Judith K. Gwathmey, and Lai-Hua Xie. “Autonomic and endocrine control of cardiovascular function”. In: *World Journal of Cardiology* 7.4 (Apr. 2015), pp. 204–214. ISSN: 1949-8462.

[317] Mostafa Abdollahpur et al. “A subspace projection approach to quantify respiratory variations in the f-wave frequency trend”. In: *Frontiers in Physiology* 13 (2022). ISSN: 1664-042X.

[318] R. Coronel et al. “Left atrial pressure reduction for mitral stenosis reverses left atrial direction-dependent conduction abnormalities”. In: *Cardiovascular Research* 85.4 (Mar. 2010), pp. 711–718. ISSN: 0008-6363.

[319] F. Sachs. “Mechanical transduction by membrane ion channels: a mini review”. In: *Molecular and Cellular Biochemistry* 104.1-2 (June 1991), pp. 57–60. ISSN: 0300-8177.

[320] H. Hu and F. Sachs. “Stretch-activated ion channels in the heart”. In: *Journal of Molecular and Cellular Cardiology* 29.6 (June 1997), pp. 1511–1523. ISSN: 0022-2828.

[321] S. C. Calaghan and E. White. “The role of calcium in the response of cardiac muscle to stretch”. In: *Progress in Biophysics and Molecular Biology* 71.1 (1999), pp. 59–90. ISSN: 0079-6107.

[322] L. Bernardi et al. “Respiratory sinus arrhythmia in the denervated human heart”. In: *Journal of Applied Physiology (Bethesda, Md.: 1985)* 67.4 (Oct. 1989), pp. 1447–1455. ISSN: 8750-7587.

[323] L. Bernardi et al. “Evidence for an intrinsic mechanism regulating heart rate variability in the transplanted and the intact heart during submaximal dynamic exercise?” In: *Cardiovascular Research* 24.12 (Dec. 1990), pp. 969–981. ISSN: 0008-6363.

[324] M. El-Omar, A. Kardos, and B. Casadei. “Mechanisms of respiratory sinus arrhythmia in patients with mild heart failure”. In: *American Journal of Physiology. Heart and Circulatory Physiology* 280.1 (Jan. 2001), H125–131. ISSN: 0363-6135.

[325] B. Casadei et al. “Is respiratory sinus arrhythmia a good index of cardiac vagal tone in exercise?” In: *Journal of Applied Physiology (Bethesda, Md.: 1985)* 81.2 (Aug. 1996), pp. 556–564. ISSN: 8750-7587.

[326] Menashe B. Waxman et al. “Effects of posture, Valsalva maneuver and respiration on atrial flutter rate: An effect mediated through cardiac volume”. In: *Journal of the American College of Cardiology* 17.7 (June 1991), pp. 1545–1552. ISSN: 07351097.

[327] Nico H. L. Kuijpers et al. “Mechanoelectric feedback leads to conduction slowing and block in acutely dilated atria: a modeling study of cardiac electromechanics”. In: *American Journal of Physiology-Heart and Circulatory Physiology* 292.6 (June 2007), H2832–H2853. ISSN: 0363-6135, 1522-1539.

[328] Nico H.L. Kuijpers et al. “Mechanoelectrical coupling enhances initiation and affects perpetuation of atrial fibrillation during acute atrial dilation”. In: *Heart Rhythm* 8.3 (Mar. 2011), pp. 429–436. ISSN: 15475271.

[329] G. A. Reyes del Paso, J. Godoy, and J. Vila. “Respiratory sinus arrhythmia as an index of parasympathetic cardiac control during the cardiac defense response”. In: *Biological Psychology* 35.1 (Jan. 1993), pp. 17–35. ISSN: 0301-0511.

[330] Frida Sandberg et al. “Circadian variation in dominant atrial fibrillation frequency in persistent atrial fibrillation”. In: *Physiological Measurement* 31.4 (Apr. 2010), pp. 531–542. ISSN: 0967-3334, 1361-6579.

[331] Chiara Celotto et al. “Effects of Acetylcholine Release Spatial Distribution on the Frequency of Atrial Reentrant Circuits: a Computational Study”. In: vol. 49, pp. 1–4.

[332] W. H. Cooke et al. “Human responses to upright tilt: a window on central autonomic integration”. In: *The Journal of Physiology* 517 (Pt 2).Pt 2 (June 1999), pp. 617–628. ISSN: 0022-3751.

[333] Raffaello Furlan et al. “Oscillatory Patterns in Sympathetic Neural Discharge and Cardiovascular Variables During Orthostatic Stimulus”. In: *Circulation* 101.8 (Feb. 2000), pp. 886–892. ISSN: 0009-7322, 1524-4539.

[334] Richard S. Whittle et al. “Gravitational Dose-Response Curves for Acute Cardiovascular Hemodynamics and Autonomic Responses in a Tilt Paradigm”. In: *Journal of the American Heart Association* 11.14 (July 2022), e024175. ISSN: 2047-9980.

[335] Alberto Porta et al. “Directionality in cardiovascular variability interactions during head-down tilt test”. In: *Annual International Conference of the IEEE Engineering in Medicine and Biology Society. IEEE Engineering in Medicine and Biology Society. Annual International Conference* 2014 (2014), pp. 6008–6011. ISSN: 2694-0604. DOI: `10.1109/EMBC.2014.6944998`.

[336] Varun Malhotra et al. “Effect of head down tilt on heart rate variability”. In: *Journal of Family Medicine and Primary Care* 10.1 (Jan. 2021), pp. 439–442. ISSN: 2249-4863. DOI: `10.4103/jfmpc.jfmpc_1642_20`.

[337] Farzad Sarmast et al. “Cholinergic Atrial Fibrillation: IK,ACh Gradients Determine Unequal Left/Right Atrial Frequencies and Rotor Dynamics”. In: *Cardiovascular Research* 59.4 (Oct. 2003), pp. 863–873. ISSN: 0008-6363.

[338] Minki Hwang et al. “Inducibility of human atrial fibrillation in an in silico model reflecting local acetylcholine distribution and concentration”. In: *The Korean Journal of Physiology & Pharmacology: Official Journal of the Korean Physiological Society and the Korean Society of Pharmacology* 20.1 (Jan. 2016), pp. 111–117. ISSN: 1226-4512.

[339] Robert Lemery. “How to perform ablation of the parasympathetic ganglia of the left atrium”. en. In: *Heart Rhythm* 3.10 (Oct. 2006), pp. 1237–1239. ISSN: 15475271.

[340] Benjamin J. Scherlag et al. “The Autonomic Nervous System and Atrial Fibrillation:The Roles of Pulmonary Vein Isolation and Ganglionated Plexi Ablation”. In: *Journal of Atrial Fibrillation* 2.2 (Sept. 2009), p. 177. ISSN: 1941-6911.

[341] Stavros Stavrakis et al. “The Role of the Autonomic Ganglia in Atrial Fibrillation”. en. In: *JACC: Clinical Electrophysiology* 1.1-2 (Mar. 2015), pp. 1–13. ISSN: 2405500X.

[342] Edward J. Vigmond et al. “Using Atrial Electrograms to Estimate Vagal Influence”. In: *Heart Rhythm* 2.5 (May 2005), S179. ISSN: 15475271.

[343] Tze-Fan Chao et al. “Clinical Outcome of Catheter Ablation in Patients With Non-paroxysmal Atrial Fibrillation: Results of 3-Year Follow-Up”. en. In: *Circulation: Arrhythmia and Electrophysiology* 5.3 (June 2012), pp. 514–520. ISSN: 1941-3149, 1941-3084.

[344] Carlos Sánchez et al. “Inter-Subject Variability in Human Atrial Action Potential in Sinus Rhythm versus Chronic Atrial Fibrillation”. In: *PLOS ONE* 9.8 (2014), e105897. ISSN: 1932-6203.

[345] Sanne de Jong et al. “Fibrosis and Cardiac Arrhythmias”. In: *Journal of Cardiovascular Pharmacology* 57.6 (June 2011), pp. 630–638. ISSN: 1533-4023.

[346] Martin W. Krueger et al. “Personalization of Atrial Anatomy and Electrophysiology as a Basis for Clinical Modeling of Radio-Frequency Ablation of Atrial Fibrillation”. In: *IEEE transactions on medical imaging* 32.1 (Jan. 2013), pp. 73–84. ISSN: 1558-254X.

[347] Konstantinos Mountris, Carlos Sanchez, and Esther Pueyo. “A Novel Paradigm for In Silico Simulation of Cardiac Electrophysiology Through the Mixed Collocation Meshless Petrov-Galerkin Method”. In: Dec. 2019.

[348] Konstantinos A. Mountris and Esther. Pueyo. “The Radial Point Interpolation Mixed Collocation Method for the Solution of Transient Diffusion Problems”. In: *Engineering Analysis with Boundary Elements* 121 (Dec. 2020), pp. 207–216.

[349] C Sánchez et al. “Cardiac memory in human atria and relation to arrhythmogenesis”. In: *2009 36th Annual Computers in Cardiology Conference (CinC)*. 2009, pp. 81–84.

[350] Ali Baher et al. “Short-term cardiac memory and mother rotor fibrillation”. In: *American Journal of Physiology-Heart and Circulatory Physiology* 292.1 (Jan. 2007), H180–H189. ISSN: 0363-6135, 1522-1539.

[351] Kazutaka Gima and Yoram Rudy. “Ionic Current Basis of Electrocardiographic Waveforms: A Model Study”. en. In: *Circulation Research* 90.8 (May 2002), pp. 889–896. ISSN: 0009-7330, 1524-4571.

[352] Laura C Palacio, Juan P Ugarte, and Catalina Tobón. “In-silico study of the ionic current gradients determining left-to-right atrial frequencies during paroxysmal atrial fibrillation”. In: *SIMULATION* 95.12 (Dec. 2019), pp. 1129–1139. ISSN: 0037-5497, 1741-3133.

[353] I. Chouvarda et al. “Deconvolution and wavelet-based methods for membrane current estimation from simulated fractionated electrograms”. In: *IEEE Transactions on Biomedical Engineering* 48.3 (Mar. 2001), pp. 294–301. ISSN: 00189294.

[354] Bahareh Abdi et al. “Improved Local Activation Time Annotation of Fractionated Atrial Electrograms for Atrial Mapping”. In: *Computers in Biology and Medicine* 117 (Feb. 2020), p. 103590. ISSN: 00104825.

[355] Francisco Sahli Costabal et al. “Interpreting Activation Mapping of Atrial Fibrillation: A Hybrid Computational/Physiological Study”. In: *Annals of Biomedical Engineering* 46.2 (Feb. 2018), pp. 257–269. ISSN: 0090-6964, 1573-9686.

[356] Deborah Nairn et al. “Comparison of Unipolar and Bipolar Voltage Mapping for Localization of Left Atrial Arrhythmogenic Substrate in Patients With Atrial Fibrillation”. In: *Frontiers in Physiology* 11 (2020), p. 575846. ISSN: 1664-042X.

[357] Sascha Rolf et al. “Tailored Atrial Substrate Modification Based on Low-Voltage Areas in Catheter Ablation of Atrial Fibrillation”. In: *Circulation: Arrhythmia and Electrophysiology* 7.5 (Oct. 2014), pp. 825–833. ISSN: 1941-3149, 1941-3084.

[358] Alessandro Blandino et al. “Left Atrial Substrate Modification Targeting Low-Voltage Areas for Catheter Ablation of Atrial Fibrillation: A Systematic Review

and Meta-Analysis". In: *Pacing and clinical electrophysiology: PACE* 40.2 (Feb. 2017), pp. 199–212. ISSN: 1540-8159.

[359] Sahar Avazzadeh et al. "Ganglionated Plexi Ablation for the Treatment of Atrial Fibrillation". In: *Journal of Clinical Medicine* 9.10 (Oct. 2020), p. 3081.

[360] Mário Oliveira et al. "Acute Vagal Modulation of Electrophysiology of the Atrial and Pulmonary Veins Increases Vulnerability to Atrial Fibrillation: Electrophysiological Changes and Vagally Mediated Atrial Fibrillation". In: *Experimental Physiology* 96.2 (Feb. 2011), pp. 125–133. ISSN: 09580670.

[361] Crystal M. Ripplinger, Sami F. Noujaim, and Dominik Linz. "The Nervous Heart". In: *Progress in Biophysics and Molecular Biology* 120.1-3 (Jan. 2016), pp. 199–209. ISSN: 1873-1732.

[362] Rishi Arora. "Recent Insights Into the Role of the Autonomic Nervous System in the Creation of Substrate for Atrial Fibrillation: Implications for Therapies Targeting the Atrial Autonomic Nervous System". In: *Circulation. Arrhythmia and Electrophysiology* 5.4 (Aug. 2012), pp. 850–859. ISSN: 1941-3084.

[363] Paul G. A. Volders. "Novel Insights into the Role of the Sympathetic Nervous System in Cardiac Arrhythmogenesis". In: *Heart Rhythm* 7.12 (Dec. 2010), pp. 1900–1906. ISSN: 1556-3871.

[364] Kunihiro Nishida et al. "The Role of Pulmonary Veins vs. Autonomic Ganglia in Different Experimental Substrates of Canine Atrial Fibrillation". In: *Cardiovascular Research* 89.4 (Mar. 2011), pp. 825–833. ISSN: 1755-3245.

[365] C. W. Chiou and D. P. Zipes. "Selective Vagal Denervation of the Atria Eliminates Heart Rate Variability and Baroreflex Sensitivity while Preserving Ventricular Innervation". In: *Circulation* 98.4 (July 1998), pp. 360–368. ISSN: 0009-7322.

[366] Masayuki Shimano et al. "Reactive Oxidative Metabolites are Associated with Atrial Conduction Disturbance in Patients with Atrial Fibrillation". In: *Heart Rhythm* 6.7 (July 2009), pp. 935–940. ISSN: 1556-3871.

[367] Zhiwei Feng et al. "Neuronal Differentiation and Protection from Nitric Oxide-Induced Apoptosis Require c-Jun-Dependent Expression of NCAM140". eng. In: *Molecular and Cellular Biology* 22.15 (Aug. 2002), pp. 5357–5366. ISSN: 0270-7306.

[368] Yang Yu et al. "Atrial Fibrillation Increases Sympathetic and Parasympathetic Neurons in the Intrinsic Cardiac Nervous System: INTRINSIC NEURONS REMODELING IN ATRIAL FIBRILLATION". In: *Pacing and Clinical Electrophysiology* 37.11 (Nov. 2014), pp. 1462–1469. ISSN: 01478389.

[369] Sunny S. Po et al. "Experimental model for paroxysmal atrial fibrillation arising at the pulmonary vein-atrial junctions". In: *Heart Rhythm* 3.2 (Feb. 2006), pp. 201–208. ISSN: 1547-5271.

[370] Eugene Patterson et al. "Sodium-Calcium Exchange Initiated by the Ca2+ Transient: an Arrhythmia Trigger Within Pulmonary Veins". In: *Journal of the American College of Cardiology* 47.6 (Mar. 2006), pp. 1196–1206. ISSN: 1558-3597.

[371] Sébastien P.J. Krul et al. "Disparate Response of High-Frequency Ganglionic Plexus Stimulation on Sinus Node Function and Atrial Propagation in Patients with Atrial Fibrillation". In: *Heart Rhythm* 11.10 (Oct. 2014), pp. 1743–1751. ISSN: 15475271.

[372] Kristina Rysevaite et al. "Immunohistochemical Characterization of the Intrinsic Cardiac Neural Plexus in Whole-Mount Mouse Heart Preparations". In: *Heart Rhythm* 8.5 (May 2011), pp. 731–738. ISSN: 1556-3871.

[373] Shun-ichiro Sakamoto et al. "Vagal Denervation and Reinnervation after Ablation of Ganglionated Plexi". In: *The Journal of Thoracic and Cardiovascular Surgery* 139.2 (Feb. 2010), pp. 444–452. ISSN: 00225223.

[374] Phang Boon Lim and Prapa Kanagaratnam. "The Left Atrial Neural Network: More Complicated than We Thought?" In: *Future Cardiology* 11.3 (May 2015), pp. 251–254. ISSN: 1479-6678.

[375] Eva M Benito et al. “Preferential regional distribution of atrial fibrosis in posterior wall around left inferior pulmonary vein as identified by late gadolinium enhancement cardiac magnetic resonance in patients with atrial fibrillation”. en. In: *EP Europace* 20.12 (Dec. 2018), pp. 1959–1965. ISSN: 1099-5129, 1532-2092.

[376] Felix Yang et al. “Towards a Mechanistic Understanding and Treatment of a Progressive Disease: Atrial Fibrillation”. en. In: *Journal of Atrial Fibrillation* 10.3 (2017), p. 1627. ISSN: 1941-6911.

[377] Nicolas Lellouche et al. “Functional Characterization of Atrial Electrograms in Sinus Rhythm Delineates Sites of Parasympathetic Innervation in Patients with Paroxysmal Atrial Fibrillation”. In: *Journal of the American College of Cardiology* 50.14 (Oct. 2007), pp. 1324–1331. ISSN: 1558-3597.

[378] Edward J. Vigmond et al. “Estimating Atrial Action Potential Duration from Electrograms”. In: *IEEE transactions on bio-medical engineering* 56.5 (May 2009), pp. 1546–1555. ISSN: 1558-2531.

[379] Jennifer Riccio et al. “Atrial Fibrosis Identification with Unipolar Electrogram Eigenvalue Distribution Analysis in Multi-Electrode Arrays.” In: *Medical & Biological Engineering & Computing* (2022). DOI: `10.1007/s11517-022-02648-3`.

[380] Kathleen S. McDowell et al. “Methodology for Patient-Specific Modeling of Atrial Fibrosis as a Substrate for Atrial Fibrillation”. In: *Journal of Electrocardiology* 45.6 (Dec. 2012), pp. 640–645. ISSN: 1532-8430.

[381] Jaemin Shim et al. “Virtual In-Silico Modeling Guided Catheter Ablation Predicts Effective Linear Ablation Lesion Set for Longstanding Persistent Atrial Fibrillation: Multicenter Prospective Randomized Study”. In: *Frontiers in Physiology* 8 (2017), p. 792. ISSN: 1664-042X.

[382] Florian Jousset. “Characterization of Atrial Repolarization Alternans and Activation Time Kinetics based on Intracardiac Electrograms”. In: (2011).

[383] Florian Jousset et al. “Kinetics of Atrial Repolarization Alternans in a Free-Behaving Ovine Model”. In: *Journal of Cardiovascular Electrophysiology* 23.9 (Sept. 2012), pp. 1003–1012. ISSN: 1540-8167.

[384] Joanna Monigatti-Tenkorang et al. “Intermittent Atrial Tachycardia Promotes Repolarization Alternans and Conduction Slowing during Rapid Rates, and Increases Susceptibility to Atrial Fibrillation in a Free-Behaving Sheep Model”. In: *Journal of Cardiovascular Electrophysiology* 25.4 (Apr. 2014), pp. 418–427. ISSN: 1540-8167.

[385] Richard L. Verrier et al. “Unmasking Atrial Repolarization to Assess Alternans, Spatiotemporal Heterogeneity, and Susceptibility to Atrial Fibrillation”. In: *Heart Rhythm* 13.4 (Apr. 2016), pp. 953–961. ISSN: 1556-3871.

[386] Stanley Nattel. “Calcium-Activated Potassium Current: a Novel Ion Channel Candidate in Atrial Fibrillation”. In: *The Journal of Physiology* 587.7 (Apr. 2009), pp. 1385–1386. ISSN: 00223751.

[387] Lasse Skibsbye et al. “The Duration of Pacing-Induced Atrial Fibrillation is Reduced in Vivo by Inhibition of Small Conductance Ca(2+)-Activated K(+) Channels”. In: *Journal of Cardiovascular Pharmacology* 57.6 (June 2011), pp. 672–681. ISSN: 1533-4023.

[388] Eugene A. Sosunov, Evgeny P. Anyukhovsky, and Michael R. Rosen. “Adrenergic-Cholinergic Interaction that Modulates Repolarization in the Atrium is Altered with Aging”. In: *Journal of Cardiovascular Electrophysiology* 13.4 (Apr. 2002), pp. 374–379. ISSN: 1045-3873.

[389] S. L. Stuesse, D. W. Wallick, and M. N. Levy. “Autonomic Control of Right Atrial Contractile Strength in the Dog”. In: *The American Journal of Physiology* 236.6 (June 1979), H860–865. ISSN: 0002-9513.

[390] K. B. Walsh, T. B. Begenisich, and R. S. Kass. “Beta-Adrenergic Modulation in the Heart. Independent Regulation of K and Ca Channels”. In: *Pflugers Archiv: European Journal of Physiology* 411.2 (Feb. 1988), pp. 232–234. ISSN: 0031-6768.

[391] Jorge A. Negroni et al. “β-adrenergic effects on cardiac myofilaments and contraction in an integrated rabbit ventricular myocyte model”. In: *Journal of Molecular and Cellular Cardiology* 81 (Apr. 2015), pp. 162–175. ISSN: 1095-8584.

[392] Elhacene Matene, Alain Vinet, and Vincent Jacquemet. “Dynamics of Atrial Arrhythmias Modulated by Time-Dependent Acetylcholine Concentration: a Simulation Study”. In: *Europace: European Pacing, Arrhythmias, and Cardiac Electrophysiology: Journal of the Working Groups on Cardiac Pacing, Arrhythmias, and Cardiac Cellular Electrophysiology of the European Society of Cardiology* 16 Suppl 4 (Nov. 2014), pp. iv11–iv20. ISSN: 1532-2092.

[393] Yung-Kuo Lin et al. “Leptin modulates electrophysiological characteristics and isoproterenol-induced arrhythmogenesis in atrial myocytes”. In: *Journal of Biomedical Science* 20.1 (Dec. 2013), p. 94. ISSN: 1423-0127.

[394] Arie O. Verkerk et al. “Effects of Acetylcholine and Noradrenalin on Action Potentials of Isolated Rabbit Sinoatrial and Atrial Myocytes”. In: *Frontiers in Physiology* 3 (2012). ISSN: 1664-042X.

[395] Rui Hua et al. “Effects of Wild-Type and Mutant Forms of Atrial Natriuretic Peptide on Atrial Electrophysiology and Arrhythmogenesis”. In: *Circulation. Arrhythmia and Electrophysiology* 8.5 (Oct. 2015), pp. 1240–1254. ISSN: 1941-3084.

[396] Yanfang Xu et al. “Molecular identification and functional roles of a Ca(2+)-activated K+ channel in human and mouse hearts”. In: *The Journal of Biological Chemistry* 278.49 (Dec. 2003), pp. 49085–49094. ISSN: 0021-9258.

[397] Philippe Comtois et al. “Mechanisms of Atrial Fibrillation Termination by Rapidly Unbinding Na+ Channel Blockers: Insights from Mathematical Models and Experimental Correlates”. In: *American Journal of Physiology. Heart and Circulatory Physiology* 295.4 (Oct. 2008), H1489–1504. ISSN: 0363-6135.

[398] N. Szentandrássy et al. “Role of action potential configuration and the contribution of C²a and K currents to isoprenaline-induced changes in canine ventricular cells”. In: *British Journal of Pharmacology* 167.3 (Oct. 2012), pp. 599–611. ISSN: 1476-5381.

[399] Gong-Xin Liu et al. “Differential conditions for early after-depolarizations and triggered activity in cardiomyocytes derived from transgenic LQT1 and LQT2 rabbits”. In: *The Journal of Physiology* 590.5 (Mar. 2012), pp. 1171–1180. ISSN: 1469-7793.

[400] Yuanfang Xie et al. “β-Adrenergic Stimulation Activates Early Afterdepolarizations Transiently via Kinetic Mismatch of PKA Targets”. In: *Journal of Molecular and Cellular Cardiology* 58 (May 2013), pp. 153–161. ISSN: 1095-8584.

[401] David Adolfo Sampedro-Puente et al. “Time Course of Low-Frequency Oscillatory Behavior in Human Ventricular Repolarization Following Enhanced Sympathetic Activity and Relation to Arrhythmogenesis”. In: *Frontiers in Physiology* 10 (2019), p. 1547. ISSN: 1664-042X.

[402] Esther Pueyo et al. “Interactive Effect of Beta-Adrenergic Stimulation and Mechanical Stretch on Low-Frequency Oscillations of Ventricular Action Potential Duration in Humans”. In: *Journal of Molecular and Cellular Cardiology* 97 (Aug. 2016), pp. 93–105. ISSN: 1095-8584.

[403] Elisa Passini et al. “The Virtual Assay Software for Human in Silico Drug Trials to Augment Drug Cardiac Testing”. In: *Journal of Computational Science* 52 (May 2021), p. 101202. ISSN: 18777503.

List of Publications

Journal Publications

- **C. Celotto**, C. Sánchez, P. Laguna, E. Pueyo, Location of Parasympathetic Innervation Regions From Electrograms to Guide Atrial Fibrillation Ablation Therapy: An *in silico* Modeling Study. *Frontiers in Physiology*, 2021;12:674197.
- **C. Celotto**, C. Sánchez, K. A. Mountris, P. Laguna, E. Pueyo, Steady-state and transient effects of SK channel block and adrenergic stimulation to counteract acetylcholine-induced arrhythmogenic effects in the human atria: A computational study. *Computers in Biology and Medicine*, 2023;157:106719.
- **C. Celotto**, C. Sánchez, M. Abdollahpur, F. Sandberg, J.F. Rodríguez, P. Laguna, E. Pueyo, The Frequency of Atrial Fibrillatory Waves is Modulated by the Spatiotemporal Pattern of Acetylcholine Release: a 3D Computational Study. *Frontiers in Physiology*, *Under review*.
- **C. Celotto***, M. Abdollahpur*, C. Sánchez, P. Laguna, E. Pueyo, F. Sandberg. Tilt Induced changes in f-wave characteristics during atrial fibrillation: an experimental and computational investigation. *In preparation*. * Joint first authorship.

Conference Proceedings

- **C. Celotto**, C. Sánchez, P. Laguna, E. Pueyo, Calcium-Activated Potassium Channel Inhibition in Autonomically Stimulated Human Atrial Myocytes. *International Conference on Computing in Cardiology (CinC)*, 2019, article no. 334.
- **C. Celotto**, C. Sánchez, K. A. Mountris, P. Laguna, E. Pueyo, SK Channel Block and Adrenergic Stimulation Counteract Acetylcholine-Induced Arrhythmogenic Ef-

fects in Human Atria. *Annual International Conference of the IEEE Engineering in Medicine and Biology Society (EMBC)*, 2020.

- **C. Celotto**, C. Sánchez, K. A. Mountris, P. Laguna, E. Pueyo, Relationship between Atrial Oscillatory Acetylcholine Release Pattern and f-wave Frequency Modulation: a Computational and Experimental Study. *International Conference on Computing in Cardiology (CinC)*, 2020, article no. 303.
- **C. Celotto**, C. Sánchez, K. A. Mountris, P. Laguna, E. Pueyo, Rotor Termination in Cholinergic Paroxysmal Atrial Fibrillation by Small-Conductance Calcium-Activated K + Channels Inhibition and Isoproterenol: a Computational Study. *International Conference on Computing in Cardiology (CinC)*, 2021, article no. 166.
- **C. Celotto**, C. Sánchez, M. Abdollahpur, F. Sandberg, J.F. Rodríguez, P. Laguna, E. Pueyo, Effects of Acetylcholine Release Spatial Distribution on the Frequency of Atrial Reentrant Circuits: a Computational Study. *International Conference on Computing in Cardiology (CinC)*, 2022, article no. 396.
- **C. Celotto**, C. Sánchez, M. Abdollahpur, F. Sandberg, P. Laguna, E. Pueyo, Dependence of Atrial Fibrillatory Rate Variations Induced by Head-Up/Down Tilt-Test on Autonomic Action. *International Conference on Computing in Cardiology (CinC)*, 2023, *Submitted*.